Eulerian modeling of reactive gas-liquid flow in a bubble column

Samenstelling promotiecommissie:

Prof. dr. ir. A. Bliek, voorzitter	Universiteit Twente
Prof. dr. ir. J.A.M. Kuipers, promotor	Universiteit Twente
Dr. ir. N.G. Deen, assistent-promotor	Universiteit Twente
Prof. dr-ing. B.H. Hjertager	Aalborg University Esbjerg
Prof. dr. D. Lohse	Universiteit Twente
Prof. dr. R.F. Mudde	TU Delft
Prof. dr. ir. J.J.W. van der Vegt	Universiteit Twente
Prof. dr. ing. M. Wessling	Universiteit Twente
Dr. ir. M.J.V. Goldschmidt	Akzo Nobel

The research in this thesis was financially supported by Akzo Nobel, Shell, Marin, DSM, STW and FOM.

ISBN 978-90-365-2560-2

EULERIAN MODELING OF REACTIVE GAS-LIQUID FLOW IN A BUBBLE COLUMN

PROEFSCHRIFT

ter verkrijging van
de graad van doctor aan de Universiteit Twente,
op gezag van de rector magnificus,
prof. dr. W.H.M. Zijm,
volgens besluit van het College van Promoties
in het openbaar te verdedigen
op donderdag 4 oktober 2007 om 15.00 uur

door

Dongsheng Zhang
geboren op 25 oktober 1974
te Fugu, Shaanxi, China

Dit proefschrift is goedgekeurd door de promoter

Prof. dr. ir. J.A.M. Kuipers

en de assistent promotor

Dr. ir. N.G. Deen

Table of contents

Summary

Despite the widespread application of bubble columns and intensive research efforts devoted to understand their complex behavior, detailed knowledge on the fluid flow, mass transfer and chemical reactions as well as their interactions is currently very limited. Gas-liquid flow in bubble column reactors is characterized by a combination of inherently unsteady complex processes with widely varying spatial and temporal scales. The complicated interactions between the gas and the liquid phases comprising hydrodynamics, mass transfer and chemical reaction cause many challenging modeling problems to be solved.

The Euler–Euler model is adopted throughout this thesis to investigate gas-liquid flow in bubble columns. In this study, efforts have been focused on the assessment of suitable closure laws for interfacial forces and for turbulence in the continuous phase. Furthermore, gas-liquid heterogeneous flow and reactive gas-liquid flows have been studied. All the numerical simulations were carried out with the commercial CFD package CFX-4.4 and all simulation results were compared with the available experimental PIV data of Deen (2001).

In order to study gas-liquid flow in bubble columns, several interfacial closure models reported in the literature were examined. Moreover, both the boundary condition applied at the outlet and the wall boundary condition for the gas phase were investigated. The interfacial closures for single individual bubbles were extensively and systematically studied as well as the performance of bubble swarm interfacial coefficients available in the literature. It is observed that, both the outlet boundary condition and wall boundary condition for the gas phase have minor effect on the flow behavior. It is found that the gas-liquid bubbly flow dynamics depends on the column aspect ratio, and that the lift force is mainly responsible for spreading of the bubble plume towards the confining walls and the virtual mass force only has a small ‘tuning’ effect. The drag coefficient determines the slip velocity and hence the gas holdup. The bubble aspect ratio influences the drag and virtual mass coefficients; however, it has little effect on the flow behavior. The corrections to the drag and lift coefficients as a function of the local gas fraction only show minor effect on the dynamic flow field due to the relatively low gas holdup.

Turbulence modeling is one of the main unresolved problems in the simulation of single as well as multi-phase flows. A detailed survey and study of different multiphase turbulence models was carried out to evaluate the shear-induced turbulence in the continuous phase and different bubble-induced turbulence models in the k-ε turbulence model were assessed as well. When a sub-grid scale (SGS) turbulence model is employed, it is found that the difference between two SGS turbulence models (Smagorinsky, 1963 and Vreman, 2004) in modeling of gas-liquid bubbly flow is very small. However, the model suggested by Vreman (2004) inherently dampens the shear-induced turbulent viscosity near the wall which makes the model better suited than the model of Smagorinsky (1963). It is seen that the liquid phase effective viscosity is sensitive to the model constant, C_S and values of $0.08 \leq C_S \leq 0.10$ are preferable in simulation of gas-liquid bubbly flow. All three bubble-induced

turbulence models (Sato and Sekoguchi, 1975; Troshko and Hassan, 2001 and Pfleger and Becker, 2001) in the k-ε turbulence model could produce good solutions for the time-averaged velocity. Whereas the models proposed by Pfleger and Becker (2001) and Troshko and Hassan (2001) are capable of capturing the dynamics of the bubbly flow. The model of Sato and Sekoguchi (1975) always produces a quasi-steady bubble plume behavior which departs from experimental observation.

The gas-liquid heterogeneous flow regime is characterized by a wide range of bubble sizes and an inherently dynamic flow dominated by the larger bubbles. A small bubble-big bubble-liquid three-phase modeling strategy is adopted to perform a preliminary study of gas-liquid heterogeneous flow. All bubbles are categorized into two groups: spherical/distorted bubbles belonging to the small bubble group and cap/slug/churn-turbulent bubbles belonging to the large bubble group. Each class of bubbles represents a distinct phase that interacts with the liquid. Interaction between bubbles and coalescence and breakup are not accounted for yet. The first objective is to identify a suitable shear-induced turbulence model and bubble-induced turbulence model. The effect of superficial velocity and inlet dispersed phase fractions on the flow patterns was explored. It is found that, first of all, the Sato and Sekoguchi (1975) model for bubble-induced turbulence is not suitable in case of gas-liquid heterogeneous flow, due to the high gas hold-up. The extended multiphase k-ε turbulence model of Pfleger and Becker (2001) is capable to capture the dynamics of the heterogeneous flow. It is observed that the dynamics of the flow as well as the total gas hold-up increase with increasing superficial velocity. It is seen that the big bubble phase predominantly agitates the liquid, while the small bubble phase mainly determines the total gas holdup.

When a chemical reaction is considered in a gas-liquid system, the interactions between the hydrodynamics, mass transfer and chemical reaction processes are very complex and these complex interactions make the overall prediction of the performance and scale-up of the system very difficult. A preliminary study of reactive gas-liquid flow is carried out here to identify a suitable outlet boundary condition. Assuming a constant bubble size, physical and chemical absorption of pure and dilute CO_2 bubbles in water and an aqueous sodium hydroxide (NaOH) solution have been studied respectively. It is found that the overall mass transfer coefficient does not change much with the bubble diameter in the range of 2 to 4 mm. In addition the bubble diameter decreases approximately linearly with time provided that the pH value of the alkaline solution is lower than 12. It is seen that the "Opening" boundary condition is preferred in case of physical or chemical absorption of CO_2. It is noted that when pure CO_2 is absorbed into water, high aqueous CO_2 concentrations are found around the bubble plume. When pure CO_2 is absorbed into aqueous NaOH solution the local hydroxyl concentration decreases in an oscillatory manner. In case dilute CO_2 gas is used in the chemisorption process, the local pH value drops slower compared with pure CO_2 gas.

In the Euler-Euler model, fully coupling of mass transfer, fluid flow and chemical reaction can be achieved when the local bubble size distribution is known. It is most straightforward to use the bubble number density to track the bubble size and therefore, it was incorporated in the Euler-Euler model to obtain the bubble size and achieve full coupling of fluid flow, mass transfer and chemical reaction. The capability of the bubble number density model to predict the bubble size was investigated and physical absorption of pure CO_2 in water and chemisorption of pure CO_2 bubbles in an aqueous NaOH solution were numerically studied. It was verified that the bubble number density equation is capable of predicting the bubble size in the gas-liquid bubbly flow. For the physical absorption of CO_2 in water, it is found that generally, the size of the bubbles in the core of the bubble plume is larger

than the bubbles that are trapped in the down flow along the wall. As time proceeds, the bubble size distribution in the column shifts towards large bubble sizes. It is further seen that when pure CO_2 is absorbed into aqueous NaOH solution with an initial pH value of 12, the pH history resulting from the detailed numerical model agrees well with a simple macroscopic model, whereas the numerical model with constant bubble size assumption underestimates the overall rate of the absorption process.

Samenvatting

Ondanks de vele toepassing van bellenkolommen en onderzoek aan deze systemen, is er momenteel slechts beperkte kennis over stroming, stof- en warmteoverdracht en hun onderlinge interacties. Gas-vloeistof stroming in een bellenkolom wordt gekarakteriseerd door een combinatie van inherent dynamische gecompliceerde stromingsprocessen met wijd uiteenlopende tijd- en lengteschalen. De gecompliceerde interactie tussen stroming, stofoverdracht en chemische reactie biedt veel uitdagende onopgeloste modelleerproblemen.

In dit proefschrift wordt het Euler-Euler model gehanteerd om gas-vloeistof stromingen in bellenkolommen te onderzoeken. Dit werk spitst zich toe op het onderzoek naar geschikte sluitingsrelaties voor de krachten tussen de fasen en de vloeistof fase turbulentie. Verder worden heterogene gas-vloeistof stromingen en reactieve stromingen bestudeerd. Alle numerieke simulaties zijn uitgevoerd met het commerciële CFD pakket CFX-4.4 en alle simulatie resultaten werden vergeleken met de beschikbare experimentele PIV data van Deen (2001).

Om de gas-vloeistof stroming in bellenkolommen te bestuderen, zijn verschillende sluitingsrelaties uit de beschikbare literatuur onderzocht. Bovendien werden de randvoorwaarden aan de uitlaat en de randvoorwaarden voor de gasfase aan de wanden onderzocht. Daarnaast zijn sluitingsrelaties uit de literatuur voor de krachten op zowel enkele bellen als op bellenzwermen onderzocht. Het is vastgesteld dat zowel de randvoorwaarden aan de uitlaat, als de randvoorwaarden voor de gasfase aan de wanden slechts een zeer kleine invloed op het voorspelde stromingsgedrag hebben. Verder is vastgesteld dat het gas-vloeistof stromingsgedrag afhangt van de hoogte/diameter verhouding van de kolom. De lift kracht blijkt voornamelijk verantwoordelijk te zijn voor het uitspreiden van de bellenpluim naar de wanden van de kolom, terwijl de virtuele massakracht voornamelijk een “instellend” effect heeft. De wrijvingscoëfficiënt bepaalt de relatieve belsnelheid en daarmee de volumefractie van de gasfase. De vormfactor van de bel beïnvloedt de wrijvings- en virtuele massacoëfficiënten. Echter, dit heeft slechts een beperkte invloed op het stromingsgedrag. De correcties op de wrijvings- en liftcoëfficiënten als functie van de locale gas volumefractie hebben slechts een kleine invloed op het stromingsgedrag, vanwege de relatief lage gas volumefractie.

Turbulentiemodellering is één van de belangrijkste onopgeloste problemen in de simulatie van zowel één als meer-fasen stroming. Een gedetailleerd overzicht en studie van verschillende meerfasen turbulentie modellen voor de schuifspanninggeïnduceerde turbulentie in de continue fase is uitgevoerd. Verder zijn verschillende bel geïnduceerde turbulentie modellen in het k-ε modellen eveneens geëvalueerd. Na toepassing van een sub-grid schaal (SGS) turbulentie model is gebleken dat het verschil tussen twee SGS modellen (Smagorinsky, 1963 en Vreman, 2004) in de modellering van gas-vloeistof stroming zeer klein is. Echter, het door Vreman (2004) voorgestelde model dempt de turbulente viscositeit nabij de wand op inherente wijze en is daarom beter geschikt dan het model van Smagorinsky (1963). Het is vastgesteld dat de effectieve viscositeit in de vloeistof fase gevoelig is voor de modelconstante, C_S en dat waardes voor $0.08 \leq C_S \leq 0.10$ de voorkeur genieten in de simulatie

van gas-vloeistof stroming. Alle drie de onderzochte belgeïnduceerde turbulentie modellen (Sato en Sekoguchi, 1975; Troshko en Hassan, 2001 en Pfleger en Becker, 2001) in het k-ε model vinden een accurate oplossing van het tijdsgemiddelde stromingsveld. De modellen van Pfleger en Becker (2001) en Troshko en Hassan (2001) zijn bovendien in staat om de dynamica van de stroming op te lossen, terwijl het model van Sato en Sekoguchi (1975) altijd een quasi-stationaire bellenpluim voorspelt, hetgeen afwijkt van experimentele waarnemingen.

Het gas-vloeistof heterogene stromingsregime wordt gekarakteriseerd door een grote verscheidenheid aan belgroottes en een inherent dynamische stroming, die wordt gedomineerd door grote bellen. Voor een eerste studie van het heterogene regime is een kleine bel-grote bel-vloeistof driefasen modelleringstrategie toegepast. Alle bellen zijn onderverdeeld in twee klassen: ronde/vervormde bellen behorende bij de kleine bellen klasse en “cap/slug/churn turbulente” bellen behorende bij de grote bellen klasse. Elke belklasse representeert een afzonderlijke fase, die interacteert met de vloeistoffase. In het model wordt noch rekening gehouden met de interactie tussen de bellen, noch met coalescentie en opbreking. De eerste doelstelling van deze studie is de bepaling van geschikte modellen voor de door schuifspanning en de aanwezigheid van bellen geïnduceerde turbulentie. De invloed van de superficiële gassnelheid en de gedispergeerde fractie verdeling aan de inlaat op het stromingsgedrag is onderzocht. Het is allereerst gebleken dat het belgeïnduceerde turbulentiemodel van Sato en Sekoguchi (1975) vanwege de hoge gas fractie ongeschikt is voor heterogene stromingen. Het uitgebreide k-ε turbulentiemodel van Pfleger en Becker (2001) blijkt daarentegen wel in staat om de dynamiek van de heterogene stroming te beschrijven. Het is vastgesteld dat zowel de stromingsdynamiek, als de totale gasfractie toeneemt bij toenemende superficiële gassnelheid. Het blijkt dat het voornamelijk de grote bellen zijn, die de vloeistof mengen, terwijl de kleine bellen voornamelijk de gasfractie bepalen.

Wanneer een chemische reactie plaatsvindt in een gas-vloeistof systeem, hangen stroming, stofoverdracht en chemische reacties op een ingewikkelde manier met elkaar samen. Deze onderlinge afhankelijkheid maken de voorspelling van de systeemprestaties en opschaling buitengewoon moeilijk. Een inleidende studie van een reactieve gas-vloeistof stroming is verricht om geschikte randvoorwaarden voor de uitlaat te bepalen. Vervolgens zijn zowel fysische en chemische absorptie van zuivere en verdunde CO_2 gasbellen in respectievelijk water en een waterige natronloog (NaOH) oplossing bestudeerd onder aanname van een constante belgrootte. Hieruit bleek dat de overall stofoverdrachtscoëfficiënt weinig verandert voor bellen van tussen de 2 en 4 mm en dat de bel diameter ongeveer lineair afneemt als functie van de tijd voor pH waardes lager dan 12. Het is vastgesteld dat de “Opening” randvoorwaarde de voorkeur geniet in geval van fysische of chemische absorptie. Wanneer zuiver CO_2 in water wordt geabsorbeerd, worden hoge CO_2 concentraties rond de bellenpluim waargenomen. Wanneer zuiver CO_2 in een waterige NaOH oplossing wordt geabsorbeerd, neemt de hydroxyl concentratie op schommelende wijze af. Wanneer verdund CO_2 wordt gebruikt in plaats van zuiver CO_2, daalt de pH waarde langzamer.

Wanneer de locale belgrootte verdeling bekend is, kunnen stofoverdracht, stroming en chemische reactie in het Euler-Euler model volledig aan elkaar worden gekoppeld. Het gebruik van een vergelijking voor de belconcentratie is het meest voor de hand liggend en is daarom toegepast in het Euler-Euler model om een waarde voor de locale belgrootte te verkrijgen en zo de volledige koppeling tussen stofoverdracht, stroming en chemische reactie te bewerkstelligen. De mogelijkheden van de belconcentratie vergelijking voor het voorspellen van de belgrootte zijn onderzocht aan de

hand van numerieke berekeningen voor fysische absorptie van CO_2 in water en chemische absorptie van zuiver CO_2 in een waterige NaOH oplossing. Het is vastgesteld dat de belconcentratie vergelijking in staat is om de belgrootte correct te voorspellen. Voor het geval van fysische absorptie van CO_2 in water is gebleken dat de bellen in het midden van de bellenpluim over het algemeen groter zijn dan de bellen die zijn gevangen in de neerwaartse vloeistofstroming nabij de wanden. Met het verstrijken van de tijd neemt de absorptie af en daarmee de krimpen de bellen minder sterk. In het geval van chemische absorptie van CO_2 in een waterige NaOH oplossing met een initiële pH waarde van 12 blijkt de door het complete numerieke model voorspelde verloop van de pH waarden goed overeen te komen met het pH verloop dat volgt uit een eenvoudig macroscopisch model. Dit in tegenstelling tot het numerieke model, waarin een constante belgrootte wordt verondersteld, welke een te lage stofoverdrachtssnelheid van het gehele proces voorspelt.

1

Introduction

1.1 Bubble column reactors

Bubble-driven flows occur widely in chemical, bio- and/or petrochemical industrial applications. Bubble columns, in which gas bubbles rise through a liquid, are known as excellent reactors for processes which require large interfacial area for gas–liquid mass transfer and efficient mixing for reacting species. Oxidation, hydrogenation, chlorination and alkylation are examples of liquid bulk processes being performed in bubble-column reactors. The distinct advantage of bubble column over other gas-liquid contactors are its simple design and construction, low operation costs, excellent heat and mass transfer characteristics and high mixing ability.

The hydrodynamics in bubble columns is determined by the bubble rise and hence bubble size distribution and gas hold-up. Three regimes (Zahradnik et al., 1997) generally occur in bubble columns. A schematic representation of these three flow regimes is shown in Figure 1.1. The homogeneous regime is obtained at low gas superficial velocities. Its bubble size distribution is mono-modal, narrow and is only influenced by the type of gas sparger used, and coalescence and break-up phenomena are negligible. In aqueous systems, the rise velocity of the spherical and ellipsoidal bubbles is about 0.18-0.3 m. Liquid up flow is found in the wake of bubbles and liquid flows down in between the bubbles and near the walls. When the superficial gas velocity is increased, the heterogeneous regime is obtained, in which coalescence and break-up occur more frequently. Bubbles with different shapes and sizes are observed in the column. Large bubbles travel in the center of the column whereas smaller bubbles move along the walls or are tracked in the wakes of large bubbles. The undesirable slug flow regime is observed at even higher superficial gas velocity and/or in particular, when the column diameter is smaller than 0.15 m. In this regime, very large bubbles, i.e., slugs span the entire cross section of the bubble column. The slug flow regime is frequently encountered in pipelines used to transport gas-oil mixtures. In this thesis, only the first two flow regimes will be considered.

To increase the predictability of the bubble column reactor design and to improve the efficiency of the processes detailed knowledge of the local hydrodynamics is required. In order to develop design tools for engineering purposes, a large amount of experimental and numerical (computational fluid dynamics) research has been carried out to study and analyze gas–liquid flows processes. From a practical point of view, the development of general models that are capable of predicting the mean and dynamic flow fields and phase distribution is of great interest for the design, control and improvement of gas–liquid systems. From a scientific point of view, the study of two-phase flows raises a number of challenging questions that still require theoretical advances and new experimental investigations.

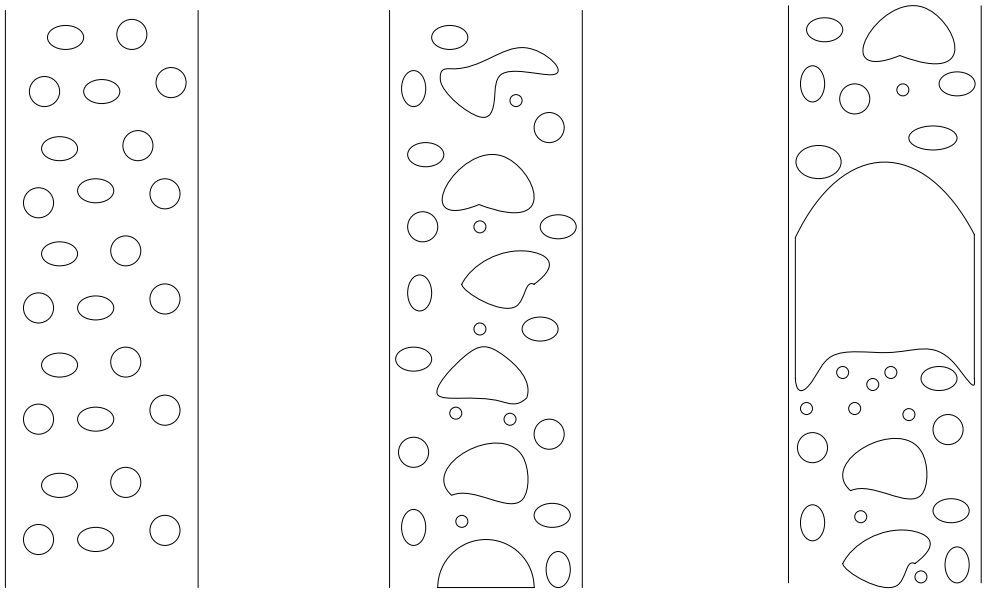

Figure 1.1: The flow regime observed in gas-liquid bubble column reactors: bubbly flow or homogeneous regime (left); heterogeneous regime (middle) and slug flow regime (right).

1.2 Hierarchy of models

Gas-liquid flow in bubble column reactors are characterized by a combination of inherently unsteady complex flow processes with widely varying spatial and temporal scales. Furthermore, the complex interactions between the gas and the liquid phases cause many modeling problems to be solved. It is not possible to develop a generalized computational fluid dynamics (CFD) model to describe all hydrodynamic phenomena across all time and length scales. Therefore, a 'hierarchy of models' is adopted in which each model is used to study specific hydrodynamic phenomena, prevailing at a particular scale (Delnoij, 1999). The 'hierarchy of models' is a set of three CFD models as shown in Figure 1.2: an interface tracking model, an Euler-Lagrange model and an Euler-Euler model. The spatial resolution decreases from $O(10^{-4}$ m) for the interface tracking model to $O(10^{-2}$ m) for the Euler-Euler model.

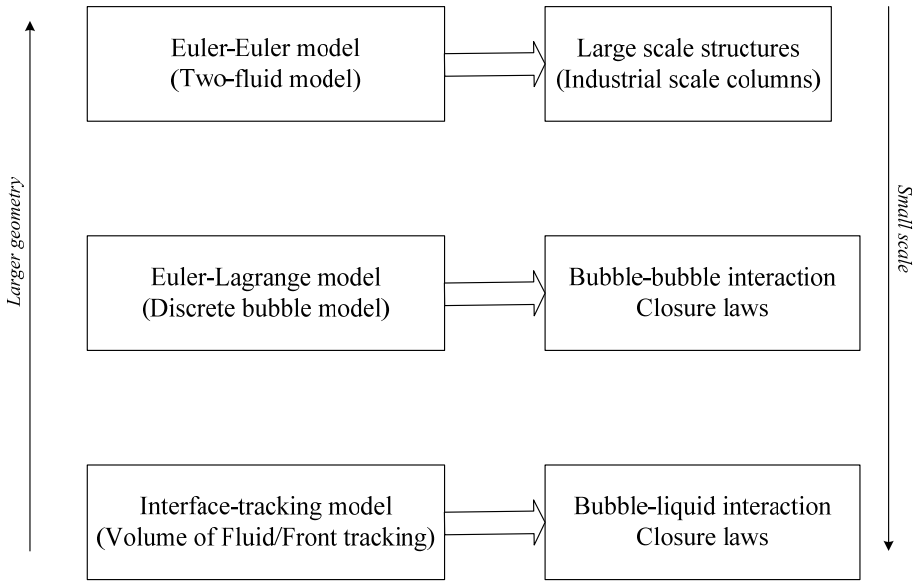

Figure 1.2: Multi-level modeling concept for fundamental hydrodynamic models of gas-liquid flow in bubble columns.

Within this multi-scale modeling strategy, information is exchanged among the three levels: the detailed interface-tracking model requires no empirical closures and it provides detailed information for Euler-Lagrange and Euler-Euler models about bubble-liquid interactions, bubble shapes and interfacial closure laws. The Euler-Lagrange model is used to obtain closures for bubble-bubble interaction required by the Euler-Euler model.

Each of these models is briefly introduced.

Detailed information of bubble motion and deformation as well as interfacial closure laws can be obtained by interface tracking models, which solve the instantaneous Navier-Stokes equations to obtain the gas and liquid flow field with a very high spatial resolution with no empirical constitutive equations. The disadvantage of this model is that the number of bubbles that can be simulated simultaneously is limited (<100 bubbles). Different methods were used for this interface tracking technique: Delnoij (1999) and van Sint Annaland et al. (2005) used a volume of fluid (VOF) technique (Youngs, 1982; Rudman, 1997) that is based on interface reconstruction and volume tracking. Dijkhuizen et al. (2005) used a front tracking technique (Tryggvason et al., 2001) that tracks the gas-liquid interface.

In the Euler-Lagrange approach (Delnoij, et al., 1997; Laín et al., 2001; Darmana et al., 2005), also called discrete bubble model (DBM), the continuous liquid phase is described as a continuum in an Eulerian framework. The dispersed gas phase on the other hand is treated in a Lagrangian way. That is, each individual bubble in the system is tracked by solving Newton's second law. The model has a two-way coupling for the exchange of momentum between the gas and liquid phase, which can be obtained from interface tracking model based closure relations. As each individual bubble is tracked in the computational domain, breakup and coalescence can be easily implemented in this approach, which makes the E-L method well suited for fundamental investigations of the bubbly flow. The main disadvantage of the E-L approach is the limitation of the numbers of bubbles (10^6) and the required computational effort.

In the Euler–Euler approach, also called two-fluid model, both the gas and liquid phases are regarded as two interpenetrating phases, and each phase has its own set of conservation equations of mass,

momentum and energy, coupled with some phase interaction terms. The governing equations are derived from various averaging techniques (time averaging, Ishii, 1975; volume averaging, Nigmatulin, 1979 and ensemble averaging, Buyevich and Schchelchkova, 1978). Closure equations for the required interfacial exchange terms can be derived using the interface tracking models. The breakup and coalescence should be accounted for through a proper model rather than relatively simple constitutive equations as in the E-L model. The advantage of this approach is that the computational demands are much lower compared to the Euler–Lagrange approach. Thus the Euler-Euler model is preferred in high gas holdup and churn turbulent flows or in industrial scale bubble columns. As this thesis aims to numerically study gas-liquid flows in bubble column with industrial relevance, the Euler-Euler model will be used in this thesis.

1.3 Objective and Outline

The objective of this thesis is to further develop and improve the Euler-Euler model in the study of fluid dynamics, mass transfer and chemical reaction in gas-liquid bubble column reactors. The emphasis will be devoted to investigate and study the performance of the available interfacial force closures and turbulence models. The model is then employed to investigate the heterogeneous flow regime in a bubble column. Next, with the proven interfacial closure laws and turbulence model, the Euler-Euler model is used to explore a gas-liquid bubble column reactor under reactive conditions with the aim to achieve a full coupling between hydrodynamics, mass transfer and chemical reaction. The contributions to these topics are organized in chapters as follows:

Chapter 2 will mainly investigate the interfacial closures. Different boundary conditions for the outlet as well as the different wall boundary conditions for the gas phase will be studied. Interfacial closure laws for single isolated bubbles are discussed in detail and finally, available bubble swarm drag, lift and virtual mass coefficients are investigated.

Chapter 3 focuses on the investigation of turbulence models in bubble columns. Both sub-grid scale (SGS) and k-ε turbulence models are studied in detail. Three different bubble-induced turbulence models in the k-ε turbulence model are explored.

Chapter 4 presents a three-phase Eulerian model to describe the motion of small bubbles-large bubbles and the continuous liquid phase for the case of heterogeneous flow in a square cross-sectioned bubble column. Different approaches to account for the bubble-induced turbulence are tested. The effect of superficial velocity and the inlet phase fraction of the big bubbles on the flow field are studied.

Chapter 5 concentrates on the numerical simulation of gas-liquid bubbly flow with mass transfer and chemical reaction in bubble columns with the use of an Euler-Euler model. Under the assumption of the constant bubble size, physical absorption of pure CO_2 bubbles in water and chemisorption of pure and dilute CO_2 bubbles in aqueous NaOH solution are numerically studied.

Chapter 6 presents the detailed numerical simulation of gas-liquid bubbly flow with mass transfer and chemical reaction in a bubble column. Mass transfer, fluid flow and chemical reaction are fully coupled by employing a bubble number density equation. Chemisorption of CO_2 into an aqueous NaOH solution with an initial pH of 12 is studied.

1.4 Bibliography

Buyevich, Y. A. and Schchelchkova, I. N., 1978. Flow of dense suspensions. *Prog. Aerospace Sc.*, 18, 121-150.

Darmana, D., Deen, N. G. and Kuipers, J. A. M., 2005. Detailed modeling of hydrodynamics, mass transfer and chemical reactions in a bubble column using a discrete bubble model. *Chem. Eng. Sci.*, 60, 3383-3404.

Delnoij, E., Kuipers, J. A. M. and Van Swaaij, W. P. M., 1997. Dynamic simulation of gas-liquid two-phase flow: effect of column aspect ratio on the flow structure. *Chem. Eng. Sci.*, 52, 3759-3772.

Delnoij, E., 1999. Fluid dynamics of gas-liquid bubble columns. A theoretical and experimental study. PhD thesis, University of Twente, Enschede, The Netherlands.

Dijkhuizen, W., Van den Hengel, E.I.V., Deen, N.G., van Sint Annaland, M. and Kuipers, J. A. M., 2005. Numerical investigation of closures for interface forces acting on single air-bubbles in water using Volume of Fluid and Front Tracking models, *Chem. Eng. Sci.*, 60, 6169-6175.

Ishii, M., 1975. Thermo-fluid dynamic theory of two-phase flow. Paris: Eyrolles (ed). Collection de la Direction des Etudes et Recherches d'Electricité de France, No. 22, 275

Laín, S., Bröder, D. and Sommerfeld, M., 2001. Numerical simulation of the hydrodynamics in a bubble column: quantitative comparisons with experiments. *4th Int. Conf. on Multiphase Flow, ICMF-2001*, New Orleans, USA.

Nigmatulin, R., 1979. Spatial averaging in the mechanics of heterogeneous and dispersed systems. *Int. J. Multiphase Flow*, 4, 353-385.

Rudman, M., 1997. Volume-tracking methods for interfacial flow calculations. *Int. J. Num. Methods in Fluids*, 24, 671-691.

Tryggvason, G., Bunner, B., Esmaeeli, A., Julic, D., Al-Rawahi, N., Tauber, W., Han, J., Nas, S. and Jan, Y. J., 2001. A front-tracking method for the computations of multiphase flow. *J. Comp. Phys*., 169, 708-759.

van Sint Annaland, M., Deen, N. G. and Kuipers, J.A.M., 2005. Numerical simulation of gas bubbles behaviour using a three-dimensional volume of fluid method. *Chem. Eng. Sci*., 60, 2999-3011.

Youngs, D. L., 1982. Time-dependent multi-material flow with large fluid distortion. *Numerical methods for Fluid Dynamics*, in Morton, K. W. and Baines, M. J. (eds), New York, 273-285.

Zahradnik, J., Fiavola, M., Ruzicka M. Drahos, J., Kastanek, F., and Thomas, N., 1997. Duality of the gas-liquid flow regimes in bubble column reactors. *Chem. Eng. Sci.*, 52, 3811-3826.

2

Study of interfacial closure laws in modeling of gas-liquid flow in bubble columns

Abstract

In this chapter, numerical simulations of the bubbly flow in two bubble columns of different aspect ratios are performed. Both the sub-grid scale model proposed of Vreman (2004) and extended k-ε turbulence models (Pfleger and Becker, 2001) were employed to describe the shear-induced turbulence in the liquid phase. Both "Pressure" and "Opening" boundary conditions applied at the outlet were explored and the difference between free slip and no slip wall boundary conditions for the gas phase was also investigated. Two sets of interfacial closure models, one used by Deen (2001) and the other, proposed by Tomiyama (2004) were investigated and compared. The interfacial closures for the drag, lift and virtual mass forces as well as the effect of the bubble aspect ratios were studied extensively. Furthermore, the performance of the available bubble swarm interfacial coefficients was assessed. Finally, with the selected proper interfacial closure models, numerical simulations of gas–liquid bubbly at high superficial velocity (Vs = 1.5 cm/s) were carried out. All simulated mean and fluctuating velocities were compared with the available PIV experimental data of Deen (2001). It is observed that there is hardly any difference between the simulated results obtained from "Pressure" and "Opening" outlet boundary conditions. Except along the wall, the numerical results obtained from free slip wall boundary condition do not differ from those obtained from no slip wall boundary condition. For the column with an aspect ratio of 3, the set of closures of Deen (2001) performs the best. Whereas, for an aspect ratio of 6, the closures proposed by Tomiyama (2004) perform the best. It turns out that the dynamics differs as function of the column aspect ratio. This leads to the unsatisfactory conclusion that the closure model is system dependent. To better understand the influence of several aspects of the closure model, each of the force coefficients was varied independently. It is found that the bubble plume spreads less in the tall column, which can be captured by lowering the lift coefficient. Furthermore, the slip velocity can be directly controlled through the drag coefficient. The latter is shown to depend on the size aspect ratio of the bubble. The bubble aspect ratio also influences the virtual mass coefficient. However, this has little effect on the flow behavior.

It is believed that swarm effects can explain the different behavior in both columns. However, corrections to the drag and lift coefficients as a function of the local gas fraction only show minor

effect. The applied corrections were based on empirical data and still contain a large uncertainty. Further work on these corrections, for instance through detailed front tracking simulations, is still required to improve the closures and shed more light on the found differences.

This chapter is based on: Zhang, Deen and Kuipers [2005, 2006]

2.1 Introduction

Bubble column reactors are widely used in chemical, petrochemical and biochemical processes. The ability to predict fluid flow dynamics is of paramount important in designing and developing bubble column reactors. Experimental investigation and numerical simulations are widely used to carry out predictions and analyze gas-liquid fluid flow process.

Two approaches are widely used to simulate the flow in bubble columns: the Euler-Euler (E-E) (Becker et al., 1994) and Euler-Lagrange (E-L) approach (Delnoij et al., 1997). The E-L method is more suited for fundamental investigations of the bubbly flow while the E-E method is preferred in high gas holdup and churn turbulent flows

A correct description of the closure laws for the drag, lift and virtual mass forces is of great importance in numerical simulation of bubbly flows. Despite extensive research (Clift et al., 1978; Ervin and Tryggvason, 1997; Magnaudet and Eames, 2000; Tomiyama et al., 2002), accurate modeling of the interfacial forces remains an open question in numerical simulations of bubbly flow. Based on the study of Becker (1994) case, Oey et al. (2003) concluded that the drag force is decisive while turbulent diffusion force, the added mass force only have “tuning” effect, and they suggested that further research should be conducted to study the effect of the lift force. For a single bubble, its shape varies with the bubble size, continuous phase flow field, and the physical properties of the system, which turns the interfacial force closures into a complex function of the bubble Reynolds number (*Re*), the Eötvös number (*Eö*), and the Morton number (*M*). Consequently, different drag correlations (Clift et al., 1978; Ishii and Zuber, 1979; Tomiyama, 1998, 2002) and lift coefficients (Svendsen et al., 1992; Tomiyama et al., 1995, 2002) are found in literature. Recently, Tomiyama (2004) proposed a set of closures for the drag, lift and virtual mass forces based on a large body of experimental data. In his work, for a single bubble, the drag and virtual mass coefficients as well as the lift coefficient not only depend on the bubble Reynolds (*Re*), the Eötvös number (*Eö*), but also on the bubble aspect ratio (*E*, defined as $E = b/a$ as shown in Figure 2.1). With an equivalent bubble diameter of 4 *mm* in the air-water system, *E* is about 0.77 according to Wellek et al. (1966). Recent front tracking results of Dijkhuizen et al. (2005) show that the bubble is considerably flatter, where *E* is 0.375. In this chapter, both bubble aspect ratios were adopted to investigate the effect of the bubble shape on the numerical results.

Unfortunately, all the aforementioned correlations are only valid for single isolated bubbles and therefore only applicable for dilute systems. When the gas hold-up is elevated, it is desirable to introduce the effects of the gas hold-up on the interfacial force closures. In the work of Ishii and

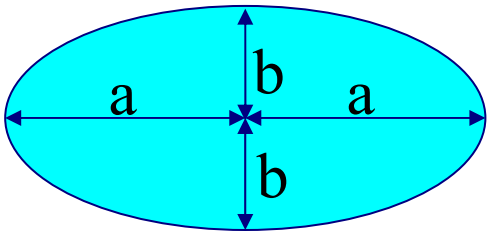

Figure 2.1: Schematic representation of a distorted oblate bubble.

Zuber (1979), through a detailed analysis and based on amounts of experimental data, the derived expressions of the swarm bubble drag coefficient were formulated as the product of a correction factor times the individual bubble drag coefficient for all three flow regimes. In the Newton and distorted bubble regimes, with increasing void fraction the relative bubble velocity decreases, while in the spherical cap regime, an increase in the void fraction increases the relative bubble velocity. This approach is similar to the correction found in the most recent experimental work of Simonnet et al. (2007), who suggested that when local gas holdup is lower than 15%, the void fraction has a hindrance effect on the relative bubble velocity; beyond this critical value, the aspiration of bubbles in the wake of the leading bubbles dominates the hindrance effect and the relative velocity thus increases suddenly. Contrary to this, Behzadi et al. (2004) found that in all three regimes, the void fraction increases the drag coefficient. Furthermore, Behzadi et al. (2004) stated that the unsatisfactory situation that different lift coefficients were used in different flow configurations lies in the strong dependence of the lift coefficient on the void fraction but not with the lift force itself. Except the work of Beyerlein et al. (1985) and Behzadi et al. (2004), no other studies on the influence of the gas hold-up on the lift coefficient have been found. In the work of Behzadi et al. (2004), the lift coefficient of the bubble swarm is a simple expression, the bubble shape and local Reynolds number were not considered. This is quite different from the work of Tomiyama (2004), who suggested that the lift coefficient for a single bubble is a function of the bubble shape factor and local Reynolds number. The virtual mass coefficient of the bubble swarm could be obtained from the work of van Wijngaarden (1976). Both the correlations resulted from a bulk of experimental data, but their validity have not been systematically tested for the simulation of gas-liquid flow. So the performance of the corrections of Ishii and Zuber (1979) and Behzadi et al. (2004) are studied here.

Turbulence modeling is one of the main unresolved problems in the simulation of gas-liquid two-phase flow. Extended k-ε (Beckeret al., 1994; Sokolichin and Eigenberger, 1999; Pfleger and Becker, 2001) and sub-grid scale (SGS) models (Deen et al., 2001; Milelli et al., 2001; Lakehal et al., 2002) have been employed to model the turbulence in gas-liquid two-phase flows. According to previous work (Zhang et al., 2005, 2006), both SGS and extended k-ε (Pfleger and Becker, 2001) turbulence models are used in this chapter. More details and differences of different SGS and k-ε turbulence models are addressed in the Chapter 3.

In the previous studies (Zhang, 2005), the outlet of the bubble column was simply treated as a 'pressure' boundary, which allows both phases to flow in or out, and as a consequence, the simulated results in the upper part of the column ($y/H > 0.72$) do not agree with the measurements. However, in reality, the column is not entirely filled with water. There is a gas cap above the liquid in the upper part of the column. Thus, an 'opening' boundary condition was implemented at the outlet as well. This boundary condition only allows the gas to flow in or out of the column, but the liquid phase is kept inside the bubble column.

In the numerical simulation of gas-liquid two-phase flow, free slip and no slip boundary conditions can in principle be used for the gas phase at the wall. In principle, in the Euler-Euler frame, the gas phase is treated as a continuous phase, which implies that a no slip boundary should be applied for the gas phase on the wall. But in reality, as the gas phase is presented as a dispersed phase, the bubbles can move freely along the wall, so a partial free slip boundary condition is more suitable for the gas phase on the wall. The difference between the above two boundary conditions for the gas phase on the wall is investigated in this chapter.

This chapter presents three-dimensional dynamic simulations of gas-liquid bubbly flow in two square cross-sectioned bubble columns with the Euler-Euler model. This chapter is organized as follows, first of all, different boundary conditions for the outlet, "Opening" and "Pressure" are studied; followed with the comparison of different wall boundary conditions (free slip and no slip) for the gas phase. The sensitivity of the two sets of the interfacial closure laws in gas-liquid bubbly flow simulations are discussed in detail. Finally, available bubble swarm drag, lift and virtual mass coefficients are investigated and gas-liquid bubbly flow in bubble columns with high superficial velocity is numerically studied. All the numerical results are compared with experimental measurement data of Deen et al. (2001).

2.2 Governing equations

The equations of the two-fluid formulation are derived by ensemble averaging the local instantaneous equations of single-phase flow (Drew, 1999). Two sets of balance equations for mass and momentum are obtained. Ignoring the interfacial mass transfer, the generic conservation equations for mass and momentum respectively take the following form:

$$\frac{\partial(\alpha_k \rho_k)}{\partial t} + \nabla \cdot (\alpha_k \rho_k \mathbf{u}_k) = 0 \tag{2.1}$$

$$\frac{\partial(\alpha_k \rho_k \mathbf{u}_k)}{\partial t} + \nabla \cdot (\alpha_k \rho_k \mathbf{u}_k \mathbf{u}_k + \alpha_k \boldsymbol{\tau}_k) = \alpha_k \rho_k \mathbf{g} - \alpha_k \nabla p_k + \mathbf{M}_k \tag{2.2}$$

where the indices k refers to the phase (L for liquid, G for gas). The volume fraction of each phase is denoted by α and $\mathbf{u} = (u, v, w)$ is the velocity vector.

The term $\boldsymbol{M}_k$ in Eq. 2.2, describing the interface forces, is given as follows

$$\mathbf{M}_L = -\mathbf{M}_G = \mathbf{M}_{D,L} + \mathbf{M}_{L,L} + \mathbf{M}_{VM,L} \tag{2.3}$$

where the terms on the right hand side represent forces due to drag, lift and virtual mass, respectively. They are calculated as:

$$\mathbf{M}_{D,L} = \frac{3}{4} \alpha_G \rho_L \frac{C_D}{d_B} |\mathbf{u}_G - \mathbf{u}_L| (\mathbf{u}_G - \mathbf{u}_L) \tag{2.4}$$

$$\mathbf{M}_{L,L} = \alpha_G \rho_L C_L (\mathbf{u}_G - \mathbf{u}_L) \times \nabla \times \mathbf{u}_L \tag{2.5}$$

$$\mathbf{M}_{VM,L} = \alpha_G \rho_L \mathbf{C}_{\mathbf{VM}} \left(\frac{D_G \mathbf{u}_G}{Dt} - \frac{D_L \mathbf{u}_L}{Dt}\right) \tag{2.6}$$

For the drag force, it is argued by Mudde and Simonin(1999), that a so-called 'drift' velocity should appear in Eq. 2.4. But in other studies (Gosman et al., 1992), this is accounted for through a turbulent dispersion force.

In this chapter, an equivalent bubble diameter of 4 *mm* is used, which was obtained from visual observation. Models for the drag coefficient that are normally used in CFD calculations are listed by Hjertager (1998) and Jakobsen et al. (1997). Here, three drag correlations for a single bubble are investigated first.

The drag coefficient can be modeled with the correlation of Ishii-Zuber (1979):

$$C_D = \frac{2}{3}\sqrt{E\ddot{o}} \tag{2.7}$$

An alternative C_D correlation was proposed by Tomiyama (2004):

$$C_D = \frac{8}{3}\frac{E\ddot{o}(1-E^2)}{E^{2/3}E\ddot{o}+16(1-E^2)E^{4/3}}F(E)^{-2} \tag{2.8}$$

where

$$F(E) = \frac{\sin^{-1}\sqrt{1-E^2} - E\sqrt{1-E^2}}{1-E^2} \tag{2.9}$$

E is the bubble aspect ratio as define by b/a, which is shown in Figure 2.1. According to Wellek et al. (1966), it is given by

$$E = \frac{1}{1+0.163E\ddot{o}^{0.757}} \tag{2.10}$$

For $d_B = 4$ *mm*, Front Tracking (Dijkhuizen, et al. 2005) results show that the bubble is much flatter and gives rise to provide a bubble aspect ratio E of 0.375; furthermore, they suggested $C_D = 1.071$.
In the previous work of Deen (2001), a standard lift coefficient of $C_L = 0.5$ was used. In Tomiyama's closures (2004), C_L was calculated as:

$$C_L = \min[0.288\tanh(0.121\,\mathrm{Re}), f(Eo_d)] \tag{2.11}$$

where the modified Eötvös number, $Eo_d = E\ddot{o}/E^{2/3}$ and $f(Eo_d)$ was given by:

$$f(Eo_d) = 0.00105Eo_d^3 - 0.0159Eo_d^2 - 0.0204Eo_d + 0.474 \tag{2.12}$$

According to Tomiyama (2004), the virtual mass coefficient vector $\mathbf{C}_{VM}$ takes the form ($C_{VM,h}$, $C_{VM,V}$, $C_{VM,h}$). For a spherical bubble in potential flow and in Stokes flow $\mathbf{C}_{VM}$ is known to be 0.5 in all three co-ordinate directions; for ellipsoidal bubbles, the virtual mass coefficients in the horizontal ($C_{VM,h}$) and vertical ($C_{VM,V}$) directions are given as:

$$C_{VM,h} = \frac{E\cos^{-1}E - \sqrt{1-E^2}}{E^2\sqrt{1-E^2} - E\cos^{-1}E} \quad C_{VM,V} = \frac{\cos^{-1}E - E\sqrt{1-E^2}}{(2E^{-1}-E)\sqrt{1-E^2} - \cos^{-1}E} \tag{2.13}$$

As mentioned earlier, all the above correlations are valid for single bubble or dilute systems. When the void fraction is elevated, it is important to account for the effect of the gas volume fraction in the interfacial closures. The available corrections are listed in Table 2.1.

Table 2.1: Available corrections for interfacial force closures.

$C_{D,Swa}$	$C_{L,Swa}$	$C_{VM,Swa}$
$C_{D,Swa} = C_{D,\sin gle} / \sqrt{\alpha_L}$ Ishii-Zuber (1979)	$C_{L,Swa} = \min(0.5, 6.51\times10^{-4} / \alpha_G^{1.2})$ Behzadi, Issa and Rusche (2004)	$\mathbf{C}_{VM,Swa} = \mathbf{C}_{VM,Single}(1+2.78\alpha_G)$ Van Wijngaarden (1976)
$C_{D,Swa} = C_{D,\sin gle}(e^{3.64\alpha_G} + \alpha_G^{0.864})$ Behzadi, Issa and Rusche (2004)		

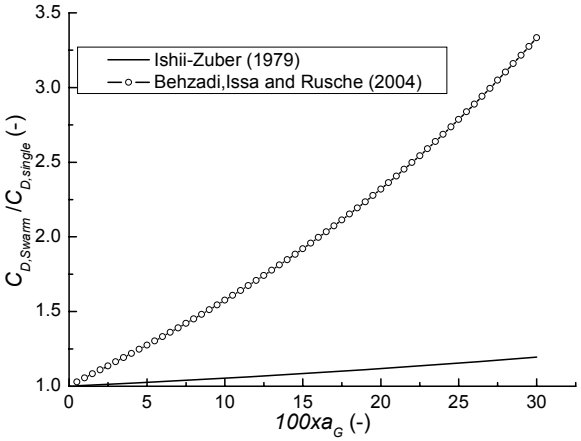

Figure 2.2: $C_{D,Swarm}$ correction factor as a function of α_G .

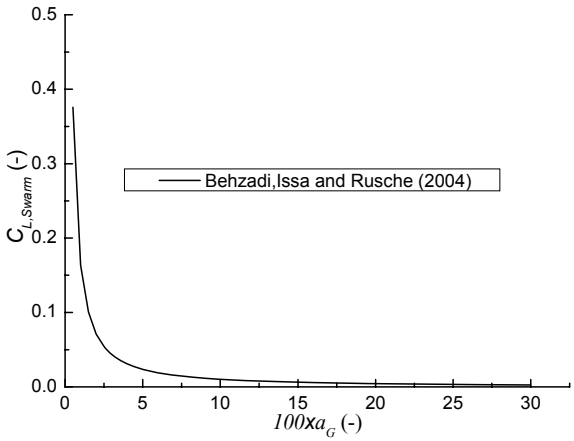

Figure 2.3: Variation of $C_{L,Swarm}$ with α_G.

Figure 2.2 illustrates the comparison of two available correction factors for the drag coefficient as a function of α_G. The correction of Behzadi, Issa and Rusche (2004) increases faster compared with the correction of Ishii and Zuber (1979). Figure 2.3 shows how the lift coefficient of a swarm bubbles varies with respect to the gas phase volume fraction (α_G). It is also seen in Figure 2.3 that the bubble swarm lift coefficient decays quickly to 0 with increasing gas phase volume fraction.
For phase k, the stress tensor $\boldsymbol{\tau}_k$ is given by:

$$\boldsymbol{\tau}_k = -\mu_{eff}(\nabla \mathbf{u}_k + (\nabla \mathbf{u}_k)^T - \frac{2}{3} I \nabla \cdot \mathbf{u}_k) \tag{2.14}$$

The effective viscosity of the liquid phase, $\mu_{L,eff}$ is composed of three contributions: the molecular viscosity $\mu_{L,Lam}$, the shear-induced turbulent viscosity $\mu_{L,Tur}$ and an extra term due to bubble induced turbulence, μ_{BIT}:

$$\mu_{L,eff} = \mu_{L,Lam} + \mu_{L,Tur} + \mu_{BIT} \tag{2.15}$$

In this chapter, both the sub-grid model (SGS) and the k-ε model are employed to evaluate the shear-induced turbulent viscosity in the liquid phase. In both cases, the effective viscosity of the gas phase is calculated as follows according to Jakobsen et al. (1997):

$$\mu_{G,eff} = \frac{\rho_G}{\rho_L}\mu_{L,eff} \tag{2.16}$$

When the SGS model proposed by Vreman (2004) is adopted, the liquid phase shear-induced turbulent viscosity is calculated as:

$$\mu_{L,Tur} = 2.5\rho C_S^2\sqrt{\frac{B_\beta}{S_{ij}S_{ij}}} \tag{2.17}$$

where $S_{ij} = \partial u_j / \partial x_i$, $\beta_{ij} = \Delta_m^2 S_{mi} S_{mj}$ and $B_\beta = \beta_{11}\beta_{22} - \beta_{12}^2 + \beta_{11}\beta_{33} - \beta_{13}^2 + \beta_{22}\beta_{33} - \beta_{23}^2$. Δ_i is the filter width in i direction. C_S is a model constant, which typically ranges between 0.08 and 0.22 (Canuto and Cheng, 1997) and its effect will be studied later in Chapter 3. In this chapter, C_S = 0.1 is used based on previous studies.

Bubble-induced turbulent viscosity appearing in Eq. 2.15 is accounted for through the model proposed by Sato and Sekoguchi (1975):

$$\mu_{BIT} = \rho_L \alpha_G C_{\mu,BIT} d_B |\mathbf{u}_G - \mathbf{u}_L| \tag{2.18}$$

where $C_{\mu,BIT}$ is a model constant which is set to 0.6.

When the extended k-ε turbulence model proposed by Pfleger and Becker (2001) is employed, the gas phase influences the turbulence in the liquid phase by a bubble-induced turbulence model; consequently, the bubble-induce turbulent viscosity appearing in Eq. 2.15 is set to 0. The shear-induced turbulent viscosity of the liquid phase is calculated by:

$$\mu_{L,Tur} = C_\mu \rho_L \frac{{k_L}^2}{\varepsilon_L} \tag{2.19}$$

The conservation equations for k and ε are respectively given by

$$\frac{\partial(\alpha_L\rho_L k_L)}{\partial t} + \nabla\cdot(\alpha_L\rho_L\mathbf{u}_L k_L - \alpha_L(\mu_{L,Lam} + \frac{\mu_{L,Tur}}{\sigma_k})\nabla k_L) = \alpha_L(G_L - \rho_L\varepsilon_L) + S_{k,BIT} \tag{2.20}$$

$$\begin{aligned}\frac{\partial(\alpha_L\rho_L\varepsilon_L)}{\partial t} + \nabla\cdot(\alpha_L\rho_L\mathbf{u}_L\varepsilon_L - \alpha_L(\mu_{L,Lam} + \frac{\mu_{L,Tur}}{\sigma_\varepsilon})\nabla\varepsilon_L) \\ = \alpha_L\frac{\varepsilon_L}{k_L}(C_{\varepsilon 1}G_L - C_{\varepsilon 2}\rho_L\varepsilon_L) + S_{\varepsilon,BIT}\end{aligned} \tag{2.21}$$

$S_{k,BIT}$ and $S_{\varepsilon,BIT}$ are source terms due to presence of bubbles, detailed discussion about these source terms is presented in the following chapter. According to Pfleger and Becker (2001), they are given by:

$$S_{k,BIT} = \alpha_L C_k \,|\mathbf{M}_L|\cdot|\mathbf{u}_G - \mathbf{u}_L| \qquad S_{\varepsilon,BIT} = \frac{\varepsilon_L}{k_L} C_\varepsilon S_{k,BIT} \tag{2.22}$$

with $C_k = C_{\varepsilon 1} = 1.44$, $C_\varepsilon = C_{\varepsilon 2} = 1.92$, $C_\mu = 0.09$, $\sigma_k = 1.0$ and $\sigma_\varepsilon = 1.217$. It is noted that these constants are not universal, even in the case of single-phase flow. For multiphase flows they are still under debate.

2.3 Physical problems

In this chapter, two bubble columns of different aspect ratio were used. The bubble columns are schematically displayed in Figure 2.4. The columns are initially filled with water to a height (H_{sta}) of either 0.45 or 0.90 m. Air is used as the dispersed gas phase and is introduced into the column in the center of the bottom plane with $A_{in} = 0.03\times0.03$ m^2 at a superficial gas velocity of V_S ranging from 0.5 to 1.5 cm/s.

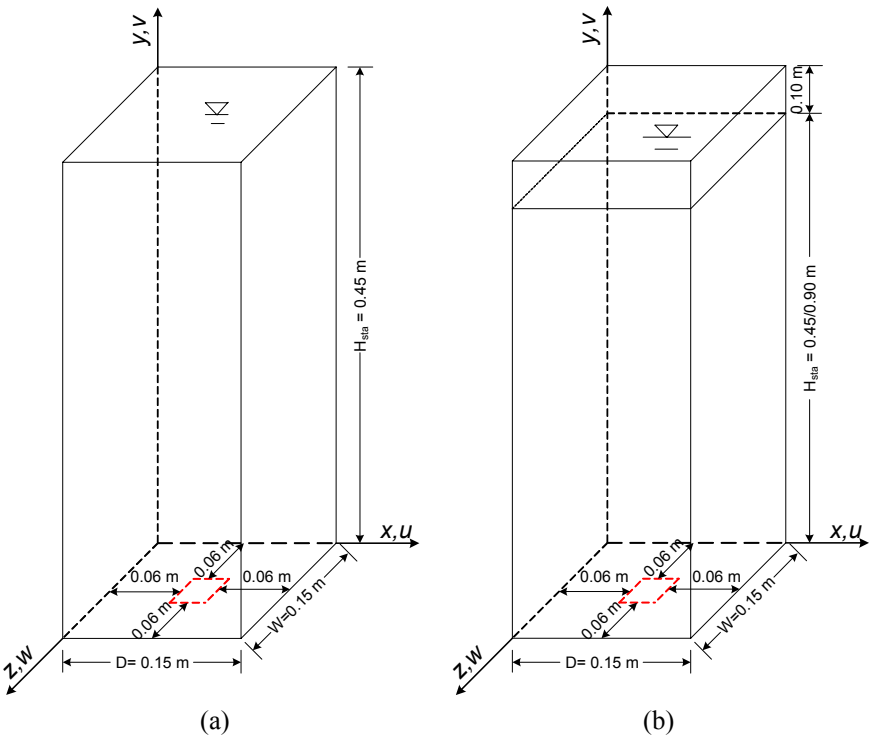

Figure2.4: Schematic representation of the investigated bubble columns: (a), pressure boundary; (b), opening boundary.

Table 2.2: Simulation and case parameters used in the base cases.

Case	Outlet boundary condition	Wall boundary condition (gas)
0A3P	"Pressure"	No slip
0A3	"Opening"	No slip
0A3N	"Opening"	Free slip
$\rho_L = 1000$ kg/m^3, $\mu_{L,Lam} = 0.001$ kg/(m.s), $\sigma = 0.07275$ N/m, $\rho_G = 1.29$ kg/m^3, $d_B = 4$ *mm*, $\mu_G = 1.812\times10^{-5}$ kg/(m.s). *Eö* = 2.15. $C_D = 0.978$, $C_L = 0.50$, ($C_{vm,h}$, $C_{vm,v}$) = (0.5, 0.5), $H_{Sta}/D = 3$.		

Table 2.3: Simulation and case parameters used in the simulations.

Case	$\mu_{L,tur}$	C_D	C_L	($C_{vm,h}$, $C_{vm,v}$)	*Vs* (cm/s)	*E*	H_{sta}/D
0A3	*SGS*	0.98	0.5	(0.5, 0.5)	0.5	0.77	3
0A3CDT		1.52	0.5	(0.5, 0.5)	0.5	0.77	
0A3CLT		0.98	Tomiyama (2004)	(0.5, 0.5)	0.5	0.77	
0A3VM0		0.98	0.5	(0, 0)	0.5	0.77	
0A3VMT		0.98	0.5	(0.43, 0.68)	0.5	0.77	
0A3E1		1.071	0.5	(0.25, 1.53)	0.5	0.38	
0A3E2		1.52	0.5	(0.43, 0.68)	0.5	0.77	
0A310		1.071	0.5	(0.25, 1.53)	1.0	0.38	
0A310A		$C_{D,a}^{Swa}$	0.5	($C_{VM,h}^{Swa}$, $C_{VM,v}^{Swa}$)	1.0	0.38	
0A310B		$C_{D,b}^{Swa}$	0.5	($C_{VM,h}^{Swa}$, $C_{VM,v}^{Swa}$)	1.0	0.38	
0A315		$C_{D,b}^{Swa}$	0.5	($C_{VM,h}^{Swa}$, $C_{VM,v}^{Swa}$)	1.5	0.38	
0B3		1.52	Tomiyama (2004)	(0.43, 0.68)	0.5	0.77	
0A6		0.98	0.5	(0.5, 0.5)	0.5	0.77	6
0A6CLT		0.98	Tomiyama (2004)	(0.5, 0.5)	0.5	0.77	
0A6CDT		1.52	0.5	(0.5, 0.5)	0.5	0.77	
0B6		1.52	Tomiyama (2004)	(0.43, 0.68)	0.5	0.77	
0B6E		1.071	Tomiyama (2004)	(0.25, 1.53)	0.5	0.77	
0B610		$C_{D,a}^{Swa}$	C_L^{Swa}	($C_{VM,h}^{Swa}$, $C_{VM,v}^{Swa}$)	1.0	0.38	
0B610B		$C_{D,b}^{Swa}$	C_L^{Swa}	($C_{VM,h}^{Swa}$, $C_{VM,v}^{Swa}$)	1.0	0.38	
0B615		$C_{D,b}^{Swa}$	C_L^{Swa}	($C_{VM,h}^{Swa}$, $C_{VM,v}^{Swa}$)	1.5	0.38	
2A6	*k- ε*	0.98	0.5	(0.5, 0.5)	0.5	0.77	
2B6		1.52	Tomiyama (2004)	(0.43, 0.68)	0.5	0.77	
2B615		$C_{D,b}^{Swa}$	C_L^{Swa}	($C_{VM,h}^{Swa}$, $C_{VM,v}^{Swa}$)	1.5	0.77	
2A315		$C_{D,b}^{Swa}$	0.5	($C_{VM,h}^{Swa}$, $C_{VM,v}^{Swa}$)	1.5	0.38	3

ρ_L = 1000 kg/m^3, $\mu_{L,Lam}$ = 0.001 kg/(m.s), σ = 0.073 N/m, ρ_G=1.29 kg/m^3, d_B = 4 *mm*, $\mu_G = 1.812\times10^{-5}$ kg/(m.s), *Eö* = 2.2.

$C_{D,a}^{Swa} = 1.071(1-\alpha_G)^{-0.5}$, $C_{D,b}^{Swa} = 1.071(e^{3.64\alpha_G} + \alpha_G^{0.864})$, $C_L^{Swa} = \min(0.5, 6.51\times\alpha_G^{-1.2}\times10^{-4})$.

$C_{VM,h}^{Swa} = 0.25(1+2.68\alpha_G)$, $C_{VM,v}^{Swa} = 1.53(1+2.68\alpha_G)$

The gas-liquid flow is assumed to be homogeneous (bubbly) flow, break-up and coalescence are not accounted for. The columns have the following dimensions: width (*W*) 0.15 m, depth (*D*) 0.15 m and height (*H*) 0.45/0.55/1.0 m. The gas distributor is mounted at the bottom at a distance of 0.06 m from

the confining walls. All the simulation parameters and physical properties are presented in Tables 2.2 and 2.3.

2.4 Data processing

In order to compare the numerical results with the experimental data, the time-averaged quantities are calculated as defined in the following expressions. The time-averaged mean velocity is calculated as:

$$\overline{u}_n = \frac{n-n_0-1}{n-n_0}\overline{u}_{n-1} + \frac{1}{n-n_0}u_n \tag{2.23}$$

where the averaging is started at time step n_0 = 7500, corresponding to 37.5 s. All simulations were carried out for n = 10^5 corresponding to a period of 500 s.
The large-scale velocity fluctuations are calculated during the calculation as follows:

$$\overline{u_{rms,n}}^2 = \overline{u_n^2} - \overline{u}_n^2 \tag{2.24}$$

All the presented quantitative results are time-averaged quantities, which are selected in a plane at a width of z/W = 0.50.

2.5 Numerical solution method

All the numerical simulations are carried out with the commercial CFD package CFX-4.4 of AEA Technology, Harwell, UK. The total domain is subdivided into uniform computational grid cells with $\Delta x = \Delta y = \Delta z = 0.01$ m. Eqs. 2.1 and 2.2 are solved in a transient fashion with a time step of 0.005 s. It is found in previous work (Zhang, 2005) that good space and time resolutions are obtained with the above grid size and time step. The curvature compensated convective transport (CCCT) scheme is used for the discretization of all convective terms. Standard boundary conditions employing wall functions are used for k and ε.
For the "opening" boundary condition at the outlet, the following conditions are imposed:

$$\alpha_G = 1.0 \qquad \alpha_L = 0.0 \tag{2.25}$$

In the gas cap, special measures need to be taken to prevent numerical problem due to the high gas volume fraction. This is accomplished as follows:

$$\alpha_L < 0.55 \quad \begin{cases} C_D = 0.05 \\ C_L = 0 \\ C_{VM} = 0 \end{cases} \tag{2.26}$$

With these measures, Eqs. 2.1 and 2.2 approximately reduce to single phase flow. A finite value for C_D is required in Eq. 2.26 to guarantee proper coupling of the two phases.

2.6 Results and Discussion

In this section, numerical results obtained from the Euler – Euler model are presented and compared with the corresponding PIV experimental data of Deen et al. (2001). Two different outlet boundary conditions ("Pressure" and "Opening") are investigated first, followed with a comparison of two different wall boundary conditions for the gas phase (free slip and no slip). Then, two sets of interfacial closure laws: one used by Deen (2001) and the other proposed by Tomiyama (2004), are studied. The effect of drag, lift and virtual mass forces in gas-liquid bubbly flow are evaluated as well. Furthermore, the influence of the bubble aspect ratio on the numerical simulation of gas-liquid bubbly flow is investigated. Subsequently, the applicability and performance of the available bubble swarm interfacial force coefficients are assessed and finally, numerical simulations of gas-liquid bubbly flow with high superficial velocity (Vs = 1.5 cm/s) in two bubble columns are carried out. All test cases are summarized in Tables 2.2 and 2.3.

2.6.1 The outlet boundary condition

First of all, different outlet boundary conditions are explored with the help of Case 0A3P and 0A3. Figure 2.5 shows snapshots of gas fraction iso-surface and liquid velocity fields in the mid-plane of x/W = 0.5. Clearly, it is seen that the SGS turbulence model resolves the details of the flow. Large vortices are observed along both walls of the bubble column. The liquid phase rises in the center of the column and flows down along the wall. Furthermore, when the "Opening" boundary condition applied at the outlet, the free surface in the top part of the column is captured.

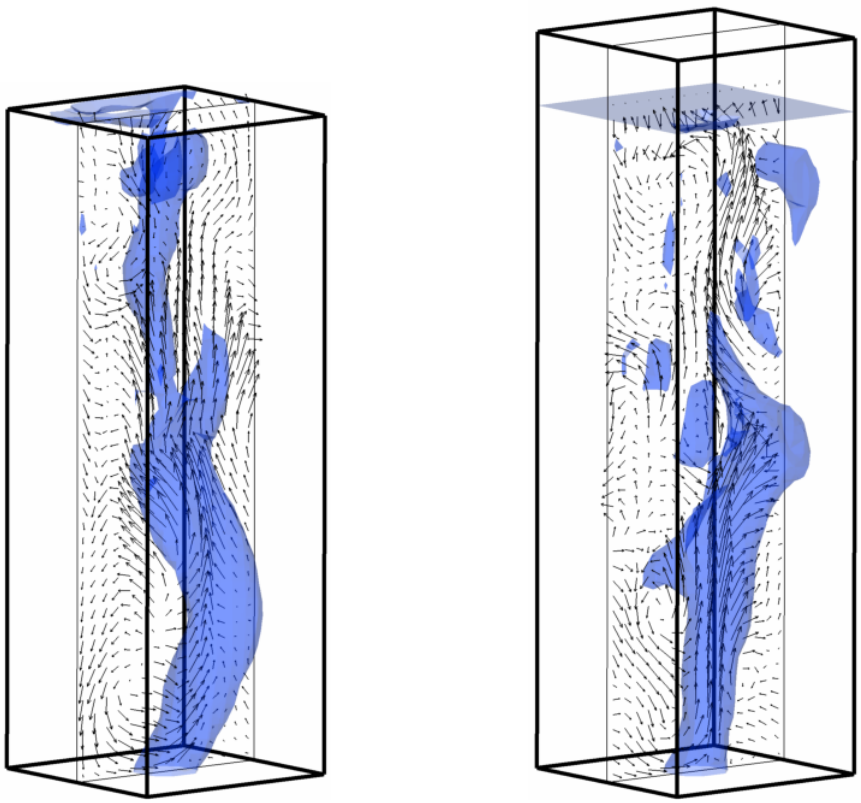

Figure 2.5: Snapshots of the instantaneous iso-surface of α_G = 0.05 and liquid velocity fields with "Pressure" and "Opening" boundary conditions. Left corresponds to Case 0A3P and right is 0A3.

A more quantitative comparison between the two outlet boundary conditions is shown in Figure 2.6. As found in Figure 2.6, the liquid phase flows up in the centre of the column and down along the wall. The gas phase rises up across the column but has a higher velocity in the column center. At the middle height of the column, the predicted results, obtained from both outlet boundary conditions, fit well with the available PIV measurements. However, at the top part of the column, the numerical results over-predict the PIV data. That is, at y/H_{sta} = 0.90, the numerical results do not agree with the experimental data. At this height, as deduced from Figure 2.6, the maximum difference in the simulation is 0.226 m/s ($V_{G,max} - V_{L,max}$), while in the experimental data, $V_{G,max} - V_{L,max}$ = 0.054 m/s. This difference might be due to the use of the standard drag force coefficient; or, as mentioned by Millies and Mewes (1999), in this upper part of column, coalescence and breakup are not negligible anymore, but no coalescence and breakup are assumed in the simulation. Nevertheless, the difference between the simulated velocity profiles obtained from these two different outlet boundary conditions is very small, except that with the "Opening" boundary, the dynamic free surface can be captured. It is concluded that both boundary conditions are equally well suited to describe the top boundary of the bubble column. More work is still needed to improve the prediction quality in the top of the bubble column.

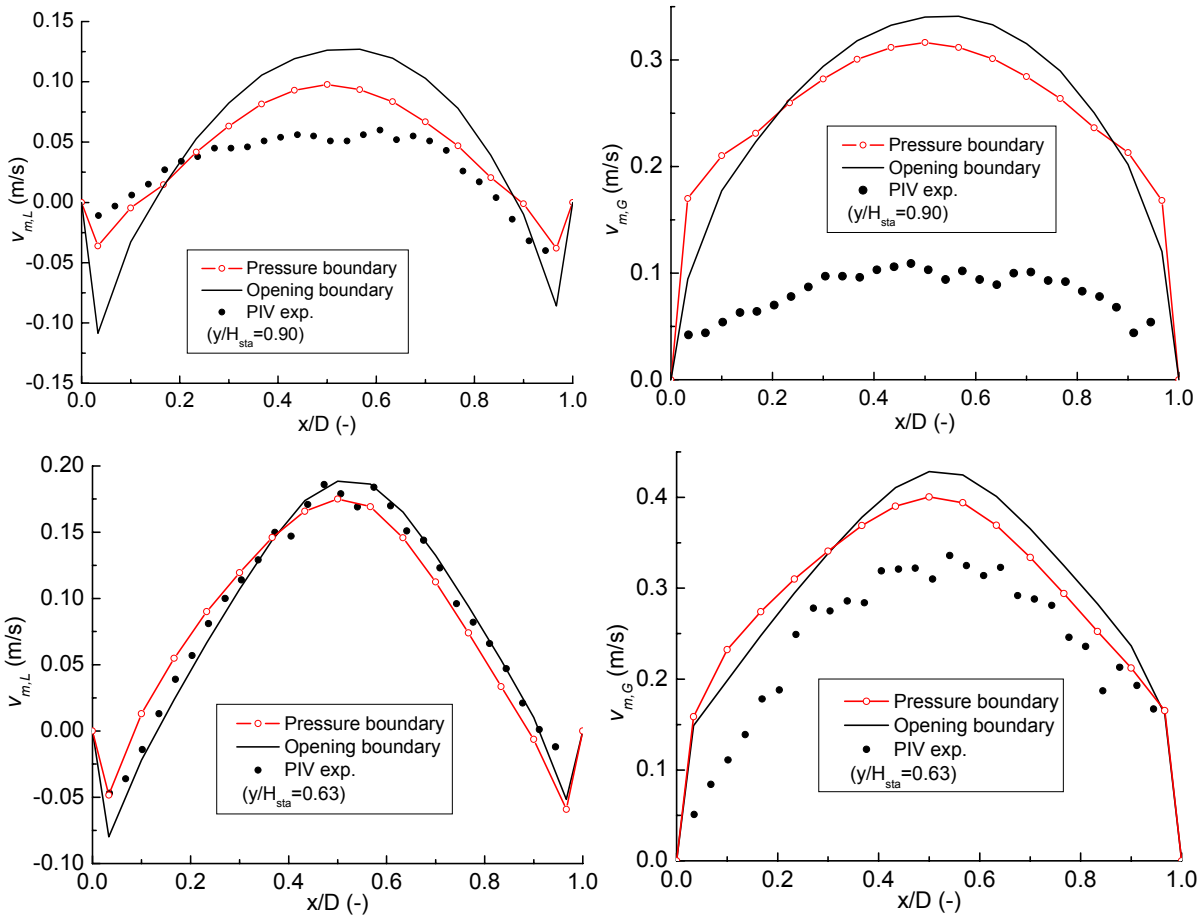

Figure 2.6: Comparison of the simulated time-averaged vertical velocity profiles of both phases with the experimental data at different heights. Pressure boundary corresponds to Case 0A3P and Opening boundary is Case 0A3.

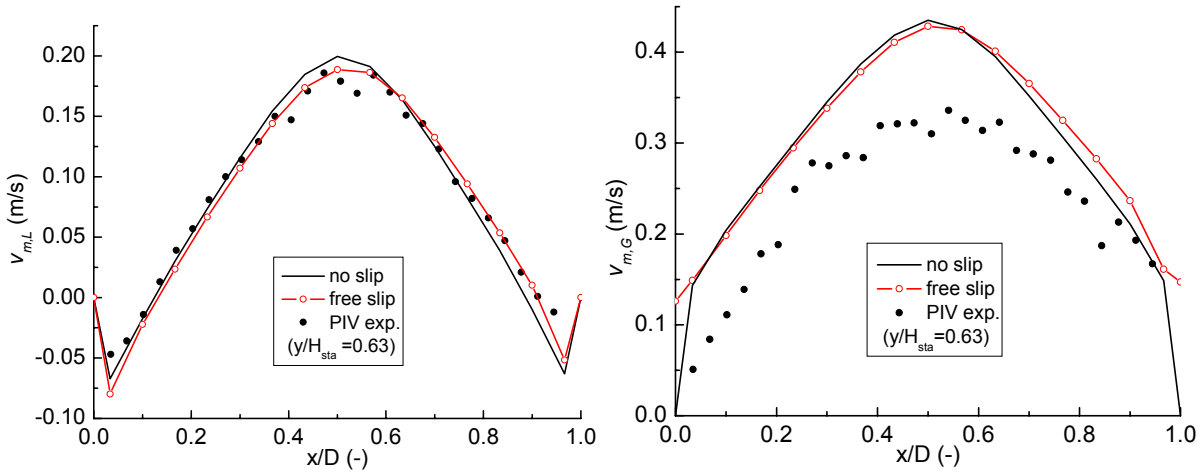

Figure 2.7: Comparison of the simulated and the experimental profiles of the vertical velocity for both phases. Here, free slip corresponds to Case 0A3 and no slip is Case 0A3N.

2.6.2 The wall boundary condition

With the help of Case 0A3 and 0A3N, the differences between free slip and no slip boundary condition for the gas at the confining walls is explored. Figure 2.7 presents the comparison of the predicted velocity profiles of both phases with the experimental data. Numerical results obtained with the no slip boundary condition slightly differ from those obtained with free slip boundary condition. Except along the wall, the gas phase approximately possesses the same velocity when either of the two boundary conditions is used for the gas phase at the wall. As found in Figure 2.7, near the wall, $v_G > 0$; the liquid phase flows down near the wall, which implies that $\partial v_L/\partial x > 0$; thus, according to Eq. 2.5, gas phase is pushed away from the wall, consequently, the gas phase volume fraction near the wall is very small, which in turn decreases the effect of the gas phase wall boundary condition.

As it hardly makes any difference between two wall boundary conditions for the gas phase, and furthermore, Euler – Euler model treats both phases as continuous phase, which implies that the gas phase does not move along the wall, so in the following numerical simulations, no slip boundary condition is applied for the gas phase along the wall. Since the "Opening" boundary condition captures the bulk liquid phase free surface, it is also adopted in the following numerical study of gas-liquid bubbly flow.

2.6.3 Interfacial closures of Tomiyama

The interfacial closures proposed by Tomiyama (2004) are tested for bubble columns of two different aspect ratios. First we will discuss a bubble column with $H_{sta}/D = 6$, i.e., cases 0A6, 0B6, 2A6 and 2B6 (see Table 2.3). Followed by a bubble column with $H_{sta}/D = 3$, i.e., cases 0A3 and 0B3. In these cases, "A" refers to the closures employed by Deen et al. (2001) and "B" refers to the closures suggested by Tomiyma (2004). Figure 2.8 provides the comparison of the time-averaged vertical velocity profiles for both phases. When the standard interfacial coefficients used by Deen (2001) (Cases 0A6 and 2A6) is employed, relatively flat vertical velocity profiles are predicted in the upper part of the column, which reflects that the bubble plume is spread out to the entire cross-sectional area of the column and consequently a uniform velocity profile is obtained. When the interfacial closure model proposed by Tomiyama is adopted (Cases 0B6 and 2B6), though the liquid phase vertical velocity is under-predicted, the simulated gas phase vertical velocity distribution agrees well with the experimental data. The under-prediction of the liquid vertical velocity may come from the drag correlation or the experimental error as the experimentally measured slip velocity (0.13 m/s) is

smaller than the predicted slip velocity (0.18 m/s). Contrary to the results of the standard model, the vertical velocity profiles obtained from Tomiyama's interfacial closures appear to be parabolic, which can be attributed to the relatively low lift force. In Tomiyama's model, the value of C_L is relatively small ($C_L \approx 0.29$) compared to that in Deen's case ($C_L = 0.5$). Consequently, the bubble plume is dispersed less, which leads to a relatively steep velocity profile. Related to this, it is found in Figure 2.9 that compared to the interfacial closure used by Deen (2001), the interfacial models of Tomiyama increase the height where the bubble plume is spread throughout the cross section of the column.

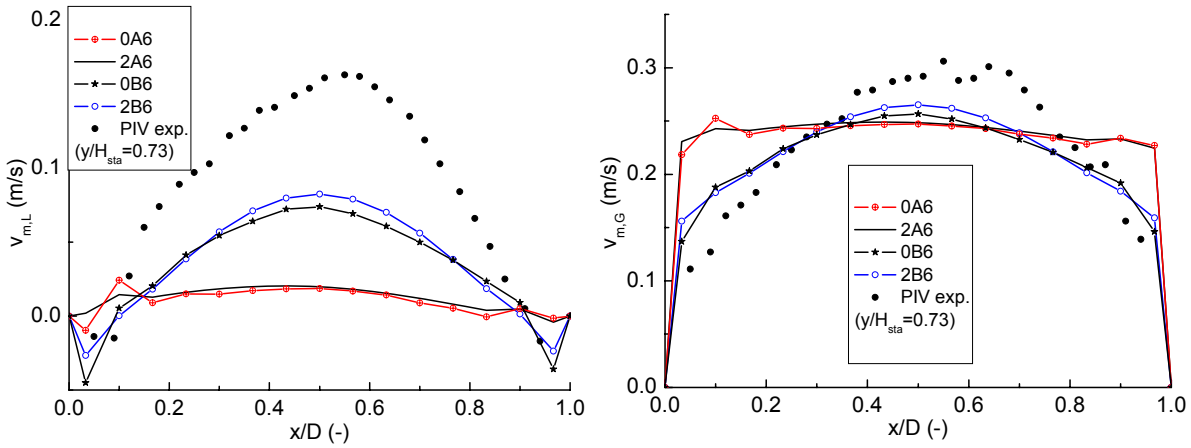

Figure 2.8: Comparison of the simulated time-averaged vertical velocity profiles of both phases with the experimental data using different interfacial closures in a taller column.

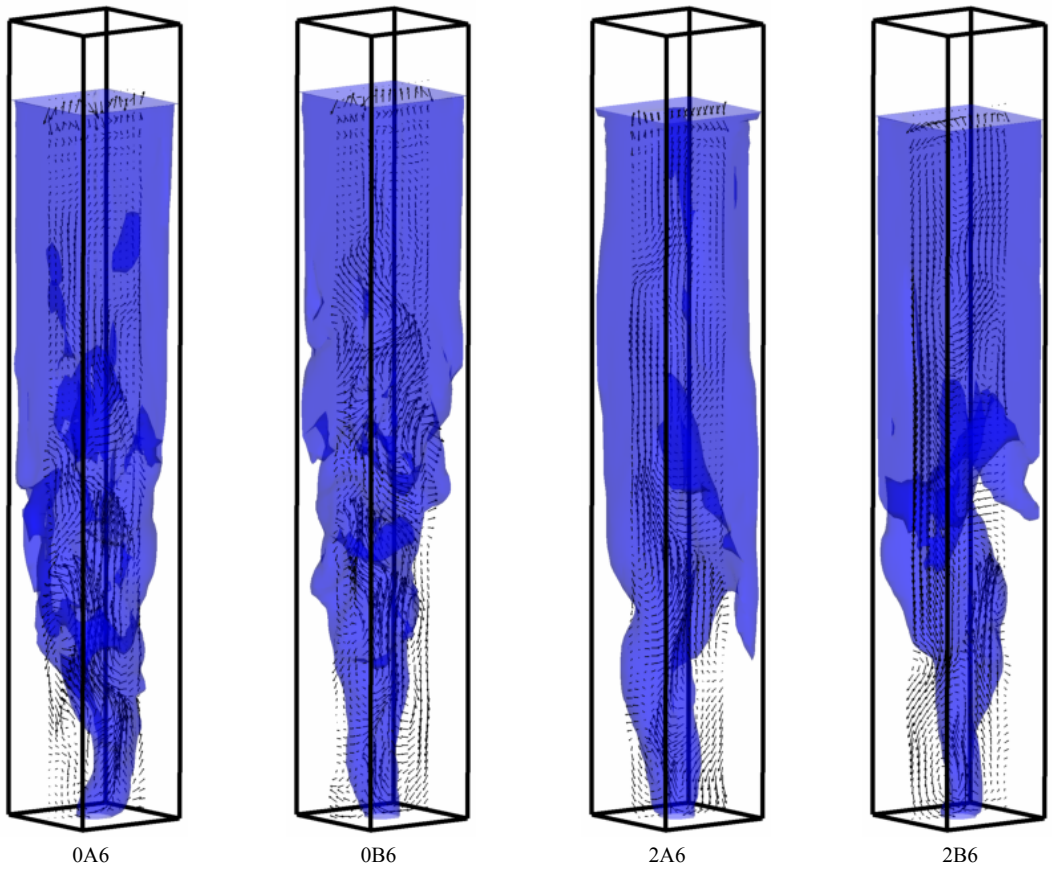

Figure 2.9: Snapshots of the instantaneous iso-surface of $\alpha_G = 0.01$ and liquid velocity field after 500 s for different bubble-induced turbulence models and interfacial closure models.

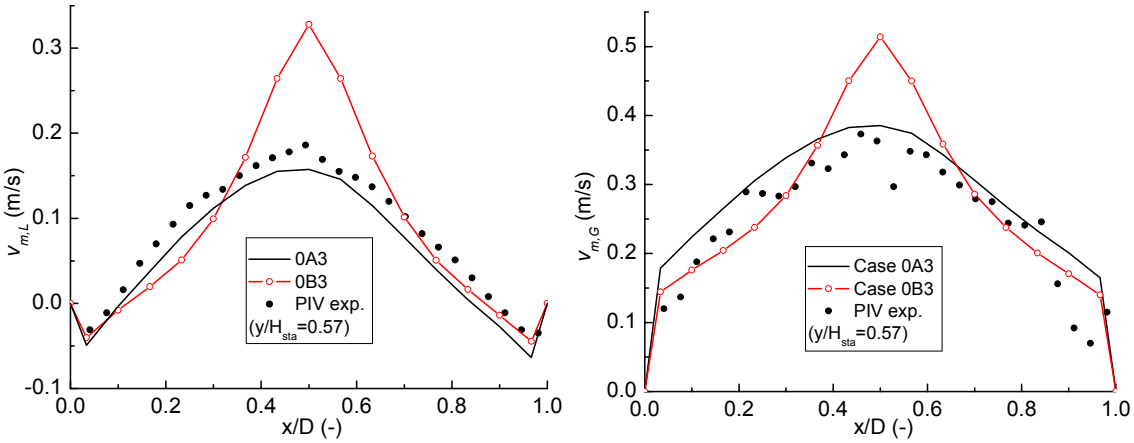

Figure 2.10: Comparison of the simulated time-averaged vertical velocity profiles of both phases with the experimental data using different interfacial closures in a lower column.

However, when Tomiyama's interfacial closures are adopted in the simulation of the lower column ($H_{Sta}/D = 3$), very steep vertical velocity profiles are found as demonstrated in Figure 2.10. In this case the large C_D and small C_L lead to a plume that is only meandering in the column centre, which is not in agreement with the experimental observations.

Combining the observations in Figures 2.8 – 2.10, it is concluded that the spreading behavior of the bubble plume and therefore also the underlying interfacial closure model depends on the column aspect ratio. In order to investigate the nature of the contradictory results obtained for different aspect ratios, some additional cases will be discussed in which only one of the interfacial forces was changed.

2.6.4 Tomiyama drag coefficients

Case 0A3 (C_D = 0.98), 0A3CDT (C_D = 1.52), 0A6 and 0A6CDT are employed to assess the performance of the drag correlation proposed by Tomiyama (2004). In these cases all of the model parameters are kept constant except for the drag force closure model, which is varied for each of the cases. Figure 2.11 exhibits a comparison of the simulated vertical velocity components from different drag models with the experimental data in two columns. In the lower column, the correlation of Ishii and Zuber (1979) gives better time-averaged vertical velocity profiles than the drag model of Tomiyama (2004), although, as can be deduced from Figure 2.11, the slip velocity predicted by the latter model agrees better with the measured value ($v_{rel} \approx 0.18$ m/s). From Figure 2.12 it can be seen that as a result of the increase of C_D and the consequent decrease in the slip velocity the gas hold-up is increased. When the drag model of Tomiyama (2004) is used, the drag force, which mainly works in the vertical direction, between the gas and the liquid phase is increased. On the other hand, the lift force, which is mainly responsible for the lateral spreading of the gas, is not or only slightly affected by the change of C_D. The ratio of these two forces, i.e. the ratio of the drag force in the vertical direction to the lift force in the horizontal direction, roughly determines the amount of spreading of the bubble plume as a function of height. This explains why, as found in both columns, the predicted vertical velocity profiles are steeper when a higher drag coefficient is used. When comparing Figure 2.11 with Figures. 2.8 and 2.10, it is concluded that the differences in bubble plume spreading behavior predicted by models used by Deen (2001) and Tomiyama (2004) can only partially be attributed to the applied drag force model. Most of the observed differences are due to the lift force

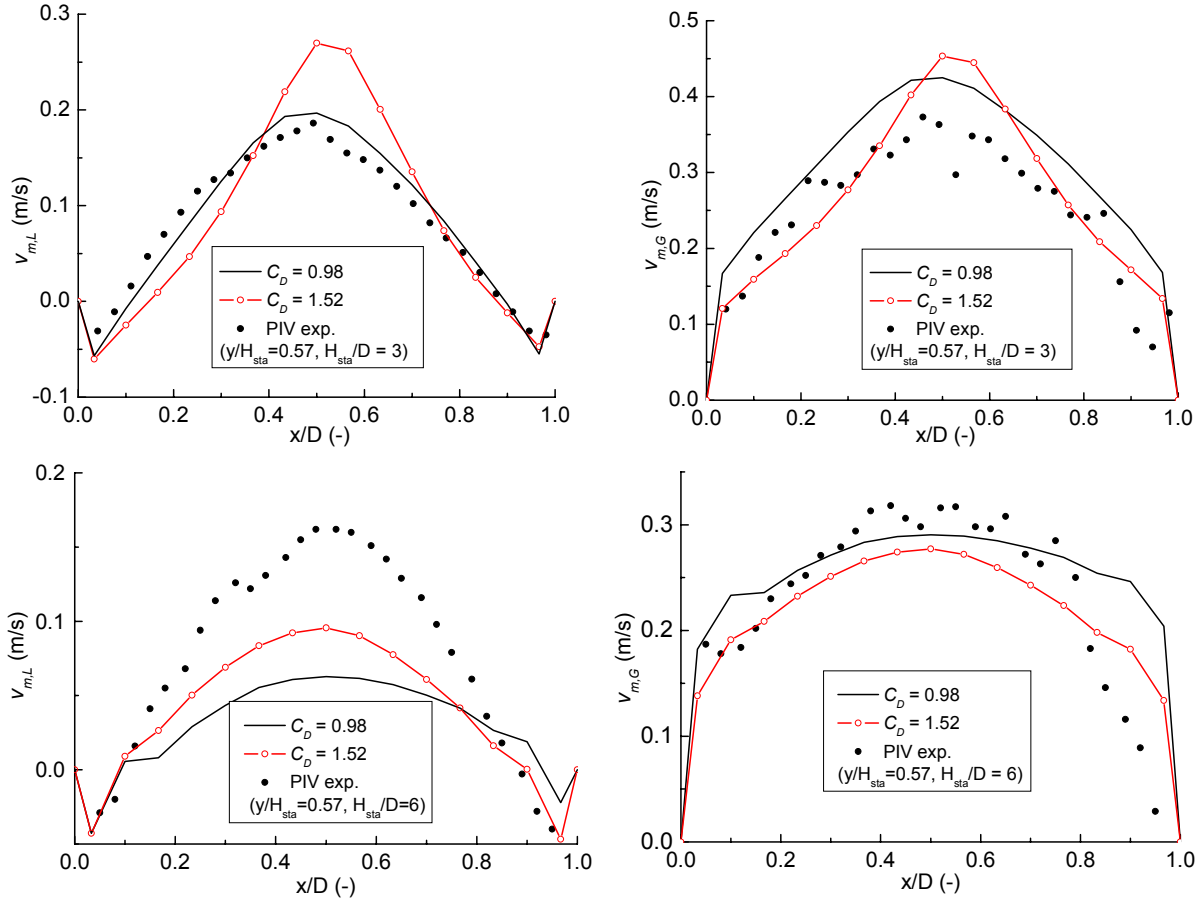

Figure 2.11: Comparison of the time-averaged vertical velocity profiles obtained from two different drag models with experimental data of Deen et al. (2001) in two columns. Here, C_D = 0.98 corresponds to Case 0A3 or 0A6 and C_D = 1.52 is Case 0B3 or 0B6, according to the column ratio, H_{sta}/D.

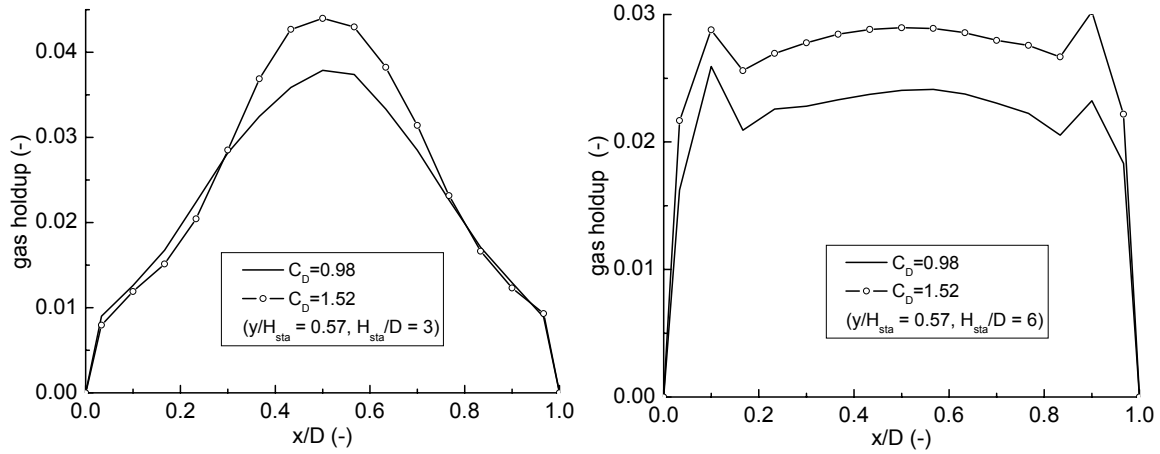

Figure 2.12: Comparison of the simulated gas holdup profiles with different drag models in two columns. Here, C_D = 0.98 corresponds to Case 0A3 or 0A6 and C_D = 1.52 is Case 0B3 or 0B6, according to the column ratio, H_{sta}/D.

model. Furthermore, as an increased drag force reduces the gas phase (bubble) velocity, the residence time of the gas phase increases, which directly leads to an increase of the gas hold up, as can be seen in Figure 2.12. It is further observed in Figure 2.11 that in the taller column, as the bubble plume is spread to the sides, wall peaking is predicted.

2.6.5 Effect of the lift force

The influence of the lift force on the bubble column dynamics is evaluated through Case 0A3 (C_L = 0.5), 0A3CLT (Tomiyama C_L), 0A6 and 0A6CLT (see Table 2.3). In these cases only C_L is varying, whereas C_D and $\mathbf{C}_{VM}$ are kept constant. Figure 2.13 provides the comparison of the simulated time-averaged vertical velocity and the experimental data. Clearly, the lift force has a significant impact on the velocity distribution: with the increase of the lift force the bubble plume becomes more dynamic leading to a decrease of the vertical velocity of both phases and subsequently to a flatter velocity profile. It appears that the results with $C_L = 0.5$ fit better with the experimental data in the lower column, while in the taller column, simulation results obtained with the lift closure of Tomiyama (2004) agree best with the measurements. This implies that the bubble plume spreading mechanism varies with the column aspect ratio. As mentioned earlier, the ratio of the vertical drag force to the horizontal lift force roughly determines the amount of gas spreading. The lift coefficient of Tomiyama (2004) is approximately 0.29 in both columns; consequently, it leads to less spreading and a steeper vertical velocity distribution. Due to the reduced spreading of the plume the dynamics of the plume are reduced. Consequently, as displayed in Figure 2.14, the velocity fluctuations in the horizontal direction are slightly reduced, whereas in the vertical direction, the velocity fluctuations are enhanced only in the column center where the bubble plume is present (see also Figure 2.5). Though in the work of Pan et al. (1999) and Pfleger and Becker (2001), satisfactory results were obtained without lift force, a very steep velocity profile and quasi-steady bubble plume were observed in a numerical

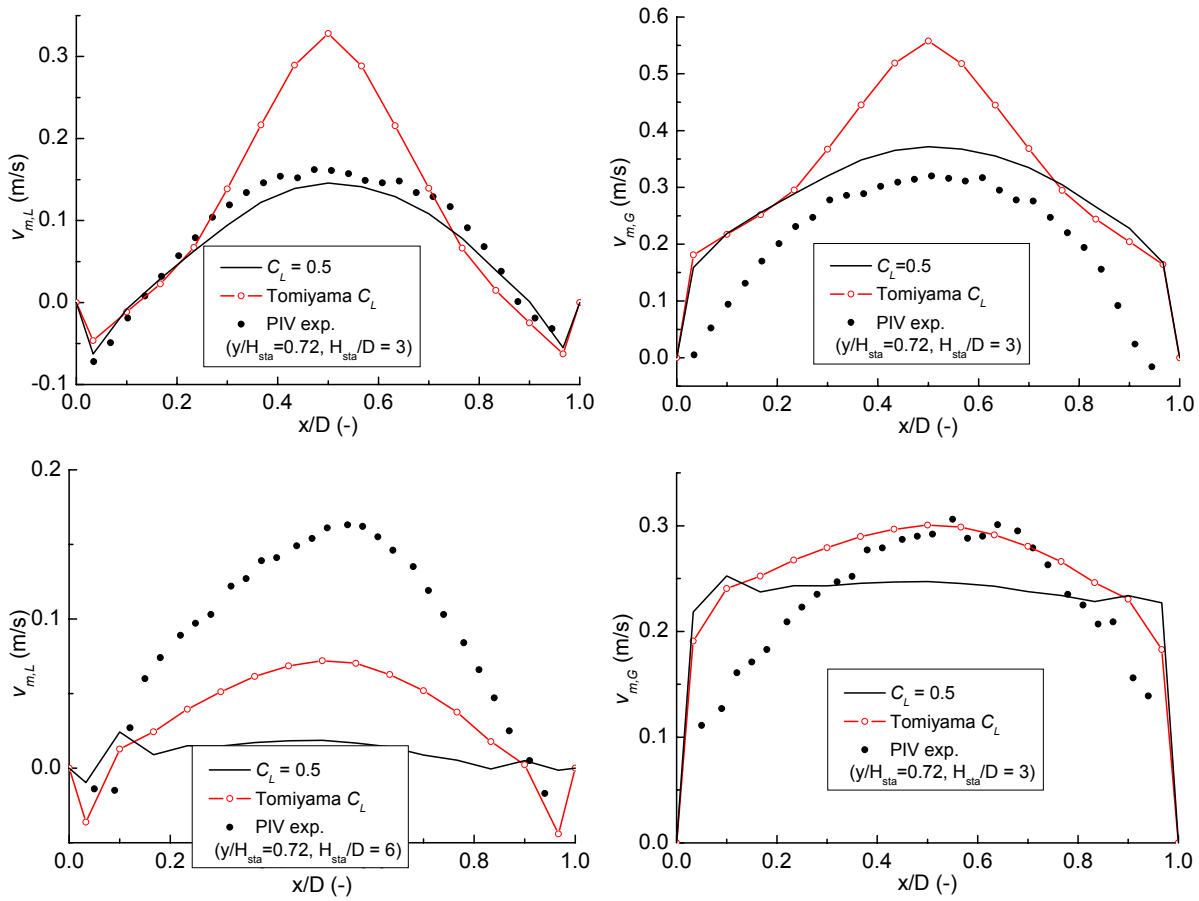

Figure 2.13: Comparison of the vertical velocity profile of the experimental data and those simulated with different C_L in two bubble columns. Cases 0A3 or 0A6 corresponds to C_L = 0.5 and Cases 0A3CLT or 0A6CLT, correspond to the C_L of Tomiyama (2004).

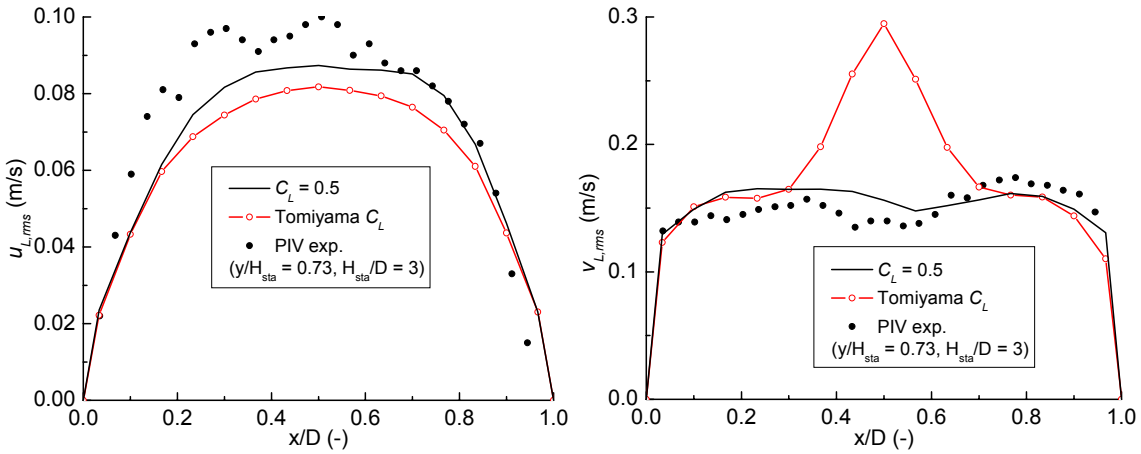

Figure 2.14: Comparison of the simulated and experimental liquid velocity fluctuations. Different C_L were used in the simulations. Cases 0A3 corresponds to C_L = 0.5 and Cases 0A3CLT corresponds to the C_L of Tomiyama (2004).

simulation with C_L = 0 conducted by the authors, which is in agreement with the findings of Deen et al. (2001). It is therefore concluded that the lift force plays a critical role in the prediction of the lateral behavior of the bubble plumes. Unfortunately, the different results for the two columns are not conclusive on the best lift closure. Possibly other aspects, such as the local gas fraction (hold-up effect) determine the exact value of the lift coefficient as found in the work of Behzadi, Issa and Rusche (2004). Recent Front Tracking simulation by Dijkhuizen et al. (2007) reveals that the lift coefficient also depends on the shear rate in the liquid phase, which may also vary as a function of the applied column geometry.

2.6.6 Effect of virtual mass force

The effect of the virtual mass force was investigated with the aid of Cases 0A3, 0A3VMT and 0A3VM0, in which the vertical and horizontal virtual mass coefficients ($C_{VM,v}$, $C_{VM,h}$) are (0.5, 0.5), (0.68, 0.43) and (0, 0), respectively. Based on the work of Lopez de Bertodano (1992), the bubble relaxation time τ_{BIT} can be estimated to be about 0.006 s. So, gas bubbles requires about 1 mm to accelerate to a velocity of 0.2 m/s. Therefore, comparisons of simulation results employing different virtual mass coefficients were only made at the very bottom and top of the column, where the most important acceleration effects can be expected. Figure 2.15 demonstrates the comparisons among three simulated profiles of the mean vertical velocity of both phases at two heights. As shown in the figure, the virtual mass force slightly suppresses the acceleration of the gas phase and increases the liquid velocity in the bottom part of the column, whereas at the very top of the column, it increases both the gas and liquid vertical velocities. From Figure 2.15 as well as from the definition of the virtual mass force in Eq. 2.6, it is seen that the effect of the virtual mass force is to keep the slip velocity to be constant. In the very bottom part of the column, the bubbles experience acceleration, but the virtual mass force impedes this acceleration, that is why with a bigger virtual mass coefficient, the gas phase velocity is lower as seen in Figure 2.15. In the very top part of the column, y/H_{sta} = 0.99, a hindrance effect of the virtual mass force is not found. Maybe this is because the bulk liquid phase free surface is elevated, so at this height, the gas phase does not tend to decelerate. At both bottom and top of the column, the differences among these three numerical results are quite small,

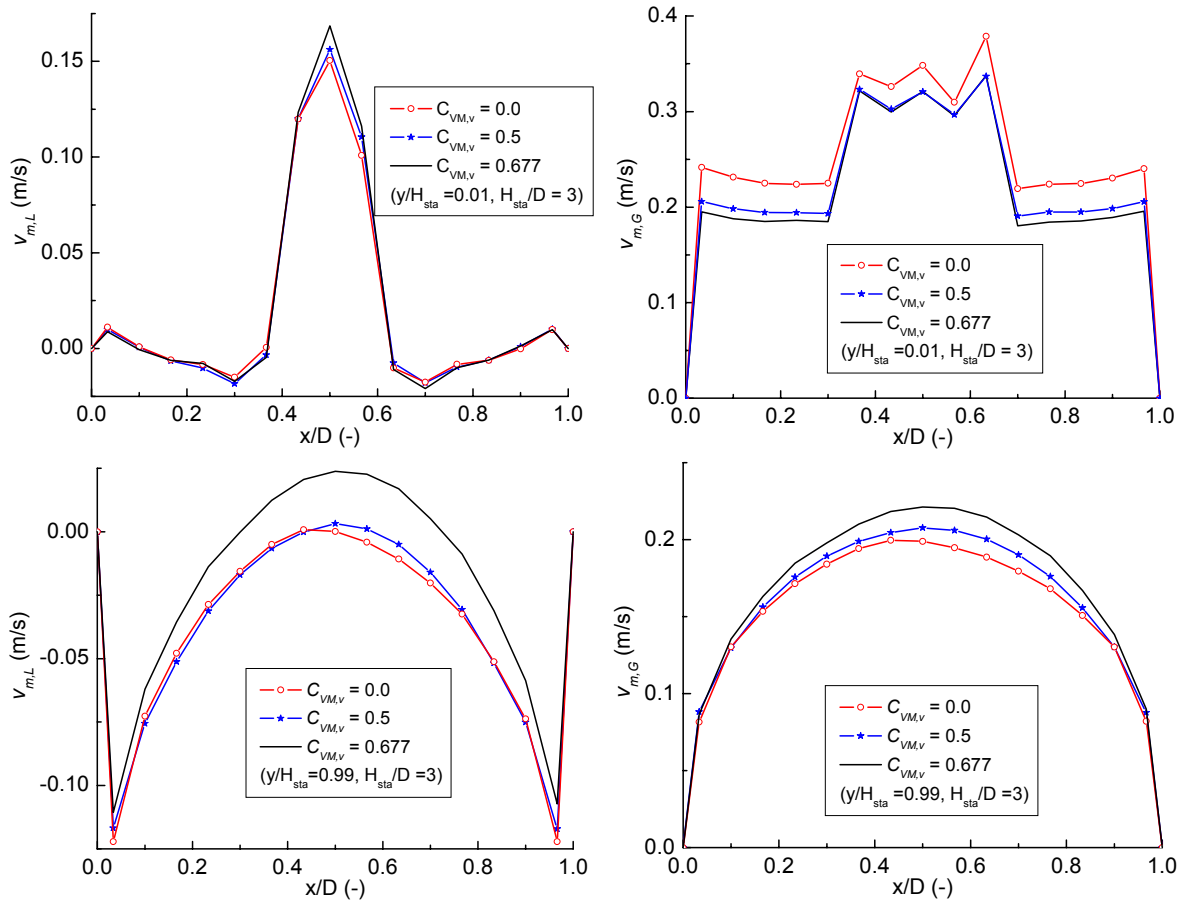

Figure 2.15: Comparison of the simulated and experimental profiles of the vertical velocity. Different virtual mass coefficients are tested. $C_{VM,V}$ = 0.5 corresponds to Case 0A3, $C_{VM,V}$ = 0.0 refers to Case 0A3VM0 and $C_{VM,V}$ = 0.677 corresponds to Case 0A3VMT.

which was also found in further comparisons at different heights. this means that the influence of the virtual mass force on the flow is really weak.

2.6.7 Effect of bubble aspect ratio

The influences of the bubble aspect ratio, E, on the numerical simulation of bubbly flow is investigated by employing Case 0A3, 0A3E1, 0A3E2 and 0B6 and 0B6E. The bubble aspect ratio influences both the closures for drag and virtual mass forces. Proper values for E, C_D, C_L and $\mathbf{C}_{VM}$ can be obtained from Front Tracking simulation data. As discussed earlier, C_L = 0.5 is preferred in the simulation of the lower column (H_{sta}/D = 3) so the lift coefficient is fixed in the study of the lower column. Figure 2.16 shows a comparison of the simulated time-averaged vertical velocity profiles of both phases obtained from different interfacial coefficient settings and the experimental data. As seen in Figure 2.16, the numerical results obtained from standard setting (case 0A3) differ slightly with those simulated with larger drag coefficient (C_D = 1.07) and virtual mass coefficient ($C_{VM,v}$ = 1.53) (case 0A3E1). With a larger drag coefficient (C_D = 1.52), the velocity profiles of both phases become steeper and over-predict the PIV measurements. The difference in the liquid phase velocity fluctuations among these three interfacial coefficient settings is quite small as observed in Figure 2.17, except for Case 0A3E2, in which the bubble plume is more pronounced in the column centre due to high the drag coefficient (C_D = 1.52). Figure 2.18 presents the comparison of the simulated

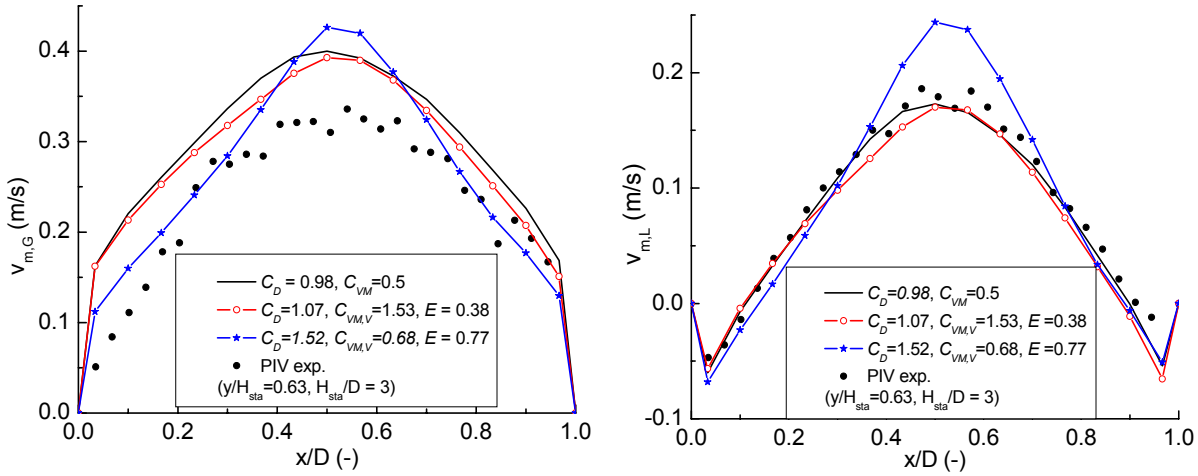

Figure 2.16: Comparison of the simulated and experimental profiles of the vertical velocity. Different interfacial closure coefficients are employed. $C_{VM,V}$ = 0.5 corresponds to Case 0A3, $C_{VM,V}$ = 1.53 refers to Case 0A3E and $C_{VM,V}$ = 0.68 corresponds to Case 0B3.

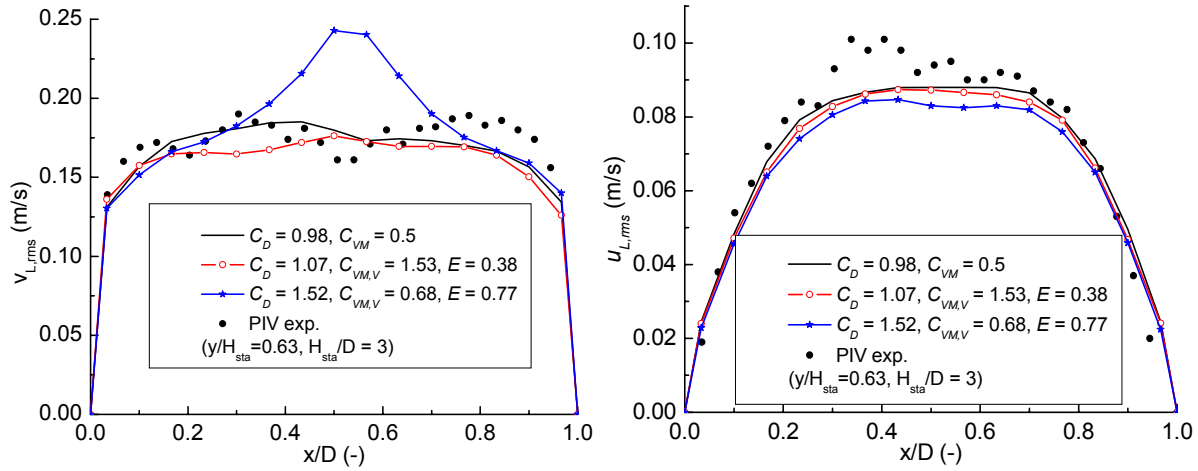

Figure 2.17: Comparison of the simulated and experimental profiles of the liquid velocity fluctuations. The simulated profiles were obtained from different interfacial closures.

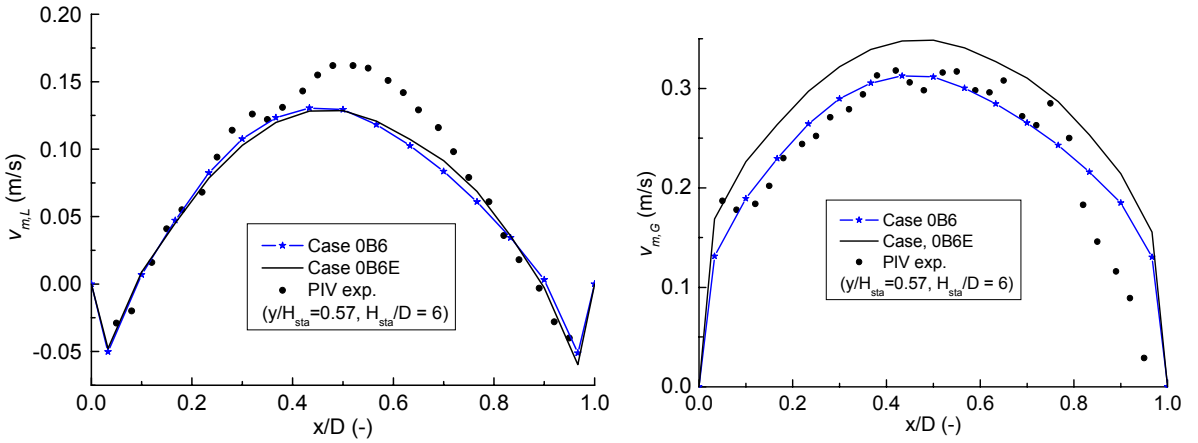

Figure 2.18: Comparison of the simulated time-averaged vertical velocity profiles of both phases with the experimental data using different interfacial closures in a taller column.

time-averaged vertical velocity profiles of both phases obtained from different interfacial coefficient settings and the experimental data in a taller column. Though the drag coefficient is different between case 0B6 (C_D = 1.52) and 0B6E (C_D = 1.07), the simulated liquid phase vertical velocity profiles differ very little. Because of the smaller drag coefficient in case 0B6E, the predicted gas phase vertical velocity profile is higher than that of case 0B6. From Figures 2.16 and 2.18, it is found that when the interfacial coefficients obtained from the Front Tracking results are used in the numerical simulation, a better solution could be obtained.

2.6.8 Bubble swarm interfacial closure models

In principal, the gas phase fraction has some influence on the interfacial closure models. In most previous studies of dilute bubbly flow, drag, lift and virtual mass coefficients were taken those from a single, isolated bubble. When the gas hold-up is elevated, it is desirable to introduce the effects of the gas hold-up on the interfacial force closures. Here, the performance and applicability of the bubble swarm interfacial closure models are tested and investigated by employing Cases 0A310, 0A310A, 0A310B, 0B610 and 0B610B.

First of all, Figure 2.19 illustrates the time averaged vertical velocity profiles of two cases for both phases. The predicted liquid phase vertical velocities fit well with the PIV measurements, while the simulated gas phase vertical velocities overestimate the experimental data. Further comparisons of the measured liquid velocity fluctuations with those obtained from the numerical simulation display a very small difference, as seen in Figure 2.20. The overestimation of the gas vertical velocity may have three reasons: the experimental data are not accurate enough as it is difficult to accurately measure the bubble velocities when the gas hold-up is high; the drag coefficient used in the numerical simulation is too low; and/or the physical properties used in the experiment are different from those in the numerical simulations.

Figure 2.21 shows the comparison of the simulated time-averaged vertical velocity profiles for both phases obtained from the different drag models in the tall column. First of all, it is seen in Figure 2.21 that the simulated velocity profiles match the PIV measurements, though, the predicted gas phase vertical velocity profiles obtained from both drag models overpredict the measurements. Furthermore, the simulated vertical velocity profiles with the drag coefficient correction suggested by Behzadi et al.

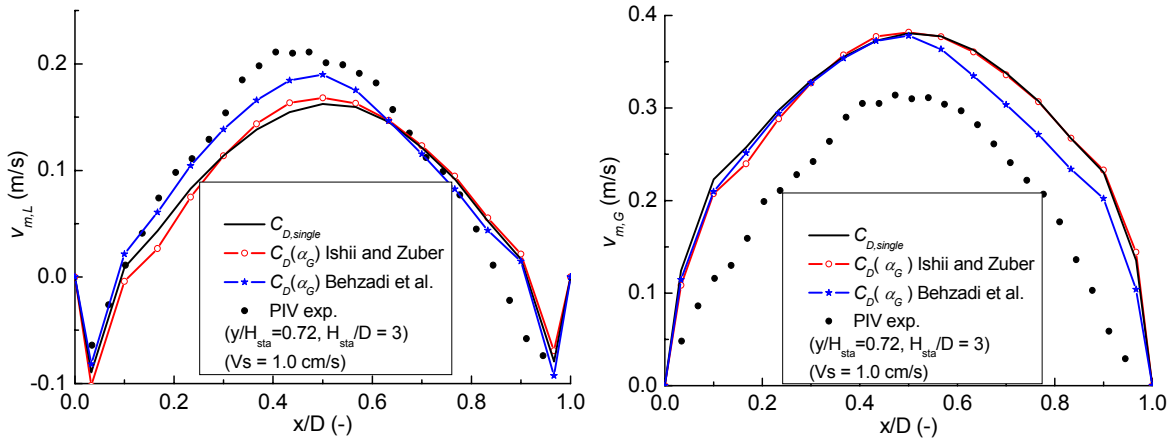

Figure 2.19: Comparison of the simulated time-averaged vertical velocity profiles of both phases with the experimental data in a smaller column. Here, different drag corrections are employed. $C_{D,single}$ refers to Case 0A310, Ishii and Zuber corresponds to 0A310A and Behzadi et al. is 0A310B.

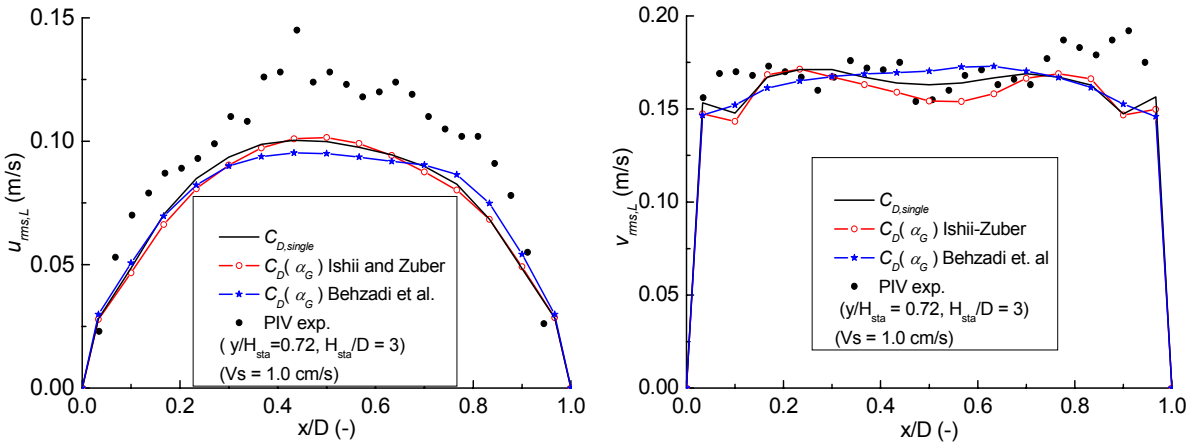

Figure 2.20: Comparison of the simulated and experimental profiles of the liquid phase velocity fluctuations. The simulated profiles were obtained from different drag corrections. $C_{D,single}$ refers to Case 0A310, Ishii and Zuber corresponds to 0A310A and Behzadi et al. is 0A310B.

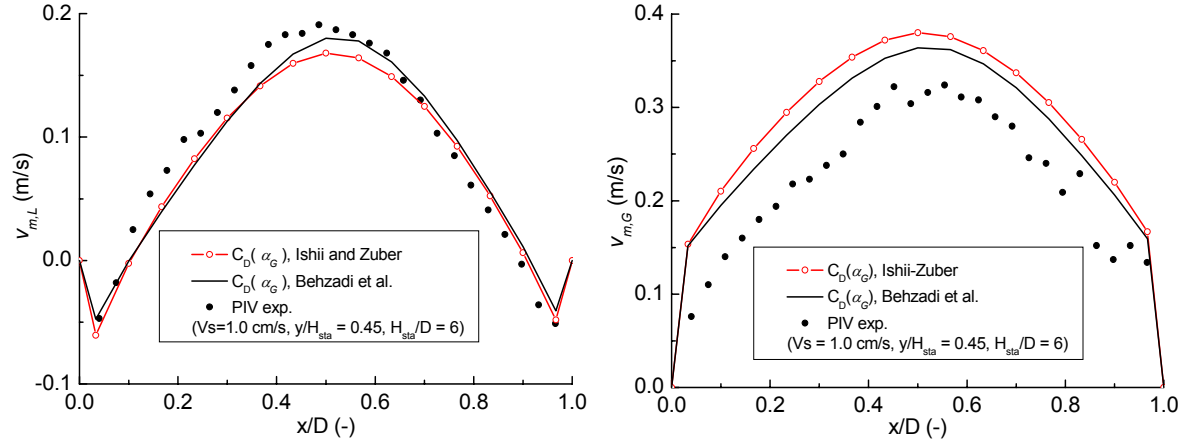

Figure 2.21: Comparison of the simulated time-averaged vertical velocity profiles of both phases with the experimental data in the tall column. Here, different drag corrections are tested. Ishii and Zuber refers to Case 0B610 and Behzadi et al. is 0B610B.

(2005) agree better with the experimental data as the drag enhancement factor given by Behzadi et al. (2005) is higher than that of Ishii and Zuber (1979).

Based on the results shown in Figures 2.19-2.21, the drag coefficient enhancement correction provided by Behzadi et al. (2005) will be adopted in the study of the superficial gas velocity.

2.6.9 Simulation of bubbly flow with high superficial velocity

Numerical simulations are conducted for case 0A315, 2A315 and 0B615 and 2B615 with the selected suitable interfacial closure models. In all of these simulations, the superficial gas velocity is increased to 1.5 cm/s. Figure 2.22 shows a comparison of the simulated vertical velocity profiles with the experimental data. As found earlier, the liquid phase vertical velocity agrees fairly well with the measurements, and this agreement is also found in the comparison of the liquid phase velocity fluctuations as presented in Figure 2.23. However, the predicted gas phase velocity is much larger than observed in the experimental data. These phenomena are also observed in case of the tall column (H_{sta}/D =6) as shown in Figure 2.24. Furthermore, it is found that the two different turbulence models

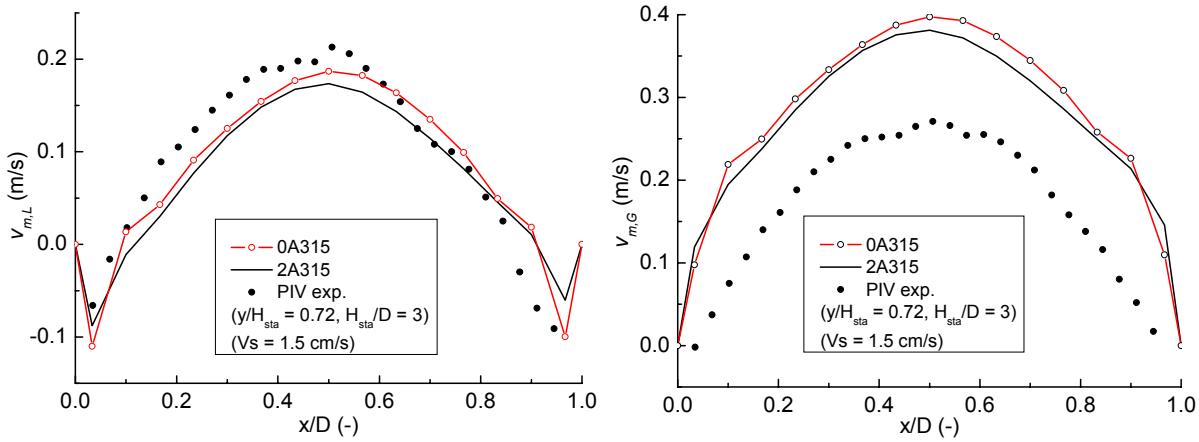

Figure 2.22: Comparison of the simulated time-averaged vertical velocity profiles of both phases with the experimental data in the low column. Here, different turbulence models (SGS and k-ε) are employed.

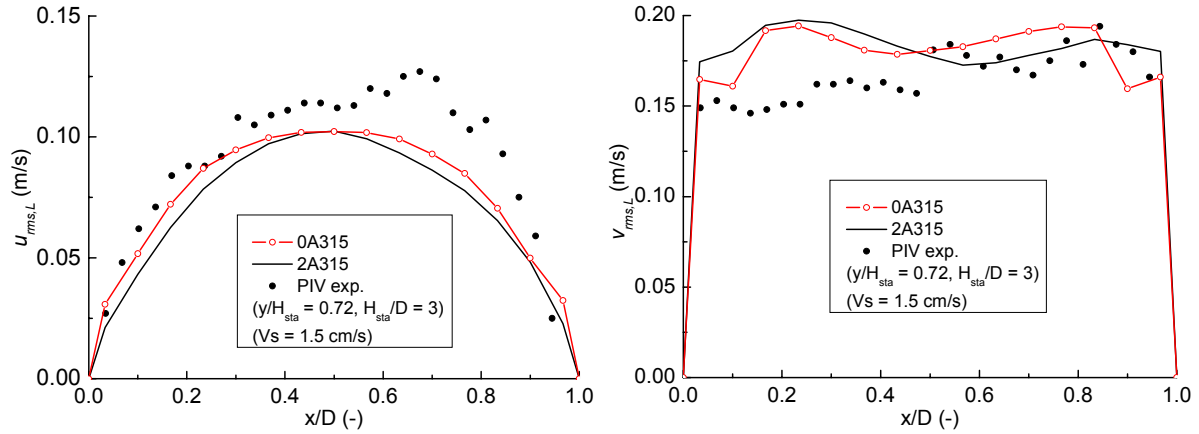

Figure 2.23: Comparison of the simulated and experimental profiles of the liquid phase velocity fluctuations. The simulated profiles were obtained from different turbulence models (SGS and k-ε).

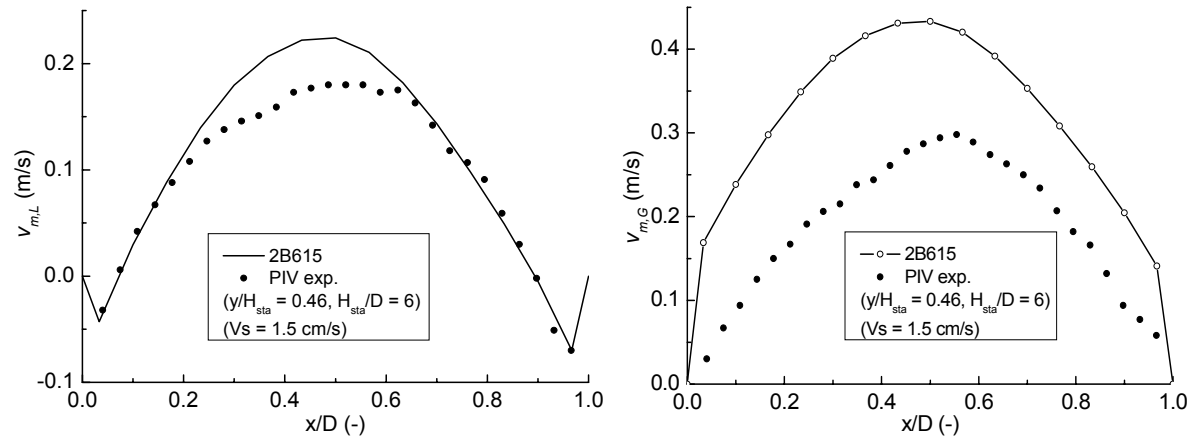

Figure 2.24: Comparison of the simulated time-averaged vertical velocity profiles of both phases with the experimental data in the tall column.

give only small differences in the simulation results and both of them are capable of solving the bubbly flow with high superficial velocity. The disagreement of the simulated gas phase vertical velocity with the experimental data found in case 0A315, 2A315 and 2B615 requires further study both from the experimental and numerical view point. Figure 2.25 presents a comparison of the gas

phase volume fraction distributions obtained from different superficial velocities in both columns. As expected, the gas volume fraction increases correspondingly with the increase of the superficial velocity. When the superficial velocity *Vs* = 1.5 cm/s, the local gas hold-up reaches a value of 0.09. In this situation, according to Ishii and Zuber (1979), the enhancement factor of the swarm bubbles drag coefficient is about 1.05, while it is about 1.51 according to Behzadi et al. (2004). Consequently, as shown in Figure 2.26, that predicted slip velocity obtained from Behzadi et al. (2004) is lower than that of Ishii and Zuber (1979). In a further comparison of the slip velocity, it is observed that the slip velocity decreases with the increase of the superficial velocity. Due to the non-uniform distribution of gas phase volume fraction, the slip velocity profiles vary constant across the column. It is further observed that the simulated slip velocity is about 0.20 m/s for all superficial velocities, while in the experiment, the slip velocity decreases from 0.23 m/s to 0.10 m/s when the superficial velocity is increased from 0.5 cm/s to 1.5 cm/s. This in turn implies that the current drag coefficient is still not suitable to predict gas phase velocity, or the homogeneous flow assumption is not valid and coalescence and breakup should be accounted for in the simulation at high superficial velocities.

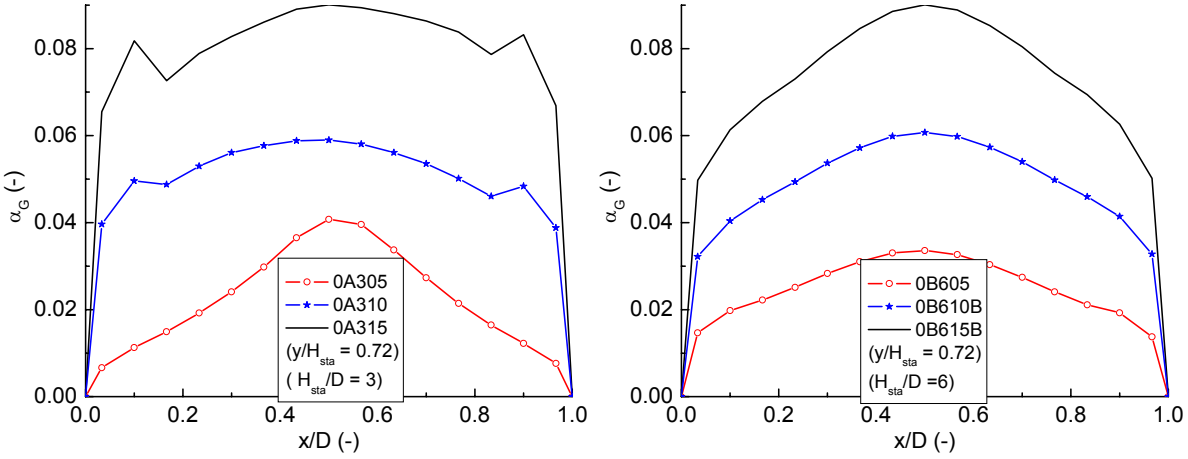

Figure 2.25: Comparison of the simulated time-averaged void fraction profiles in low (left) and tall (right) bubble columns. Here, different superficial velocities are tested.

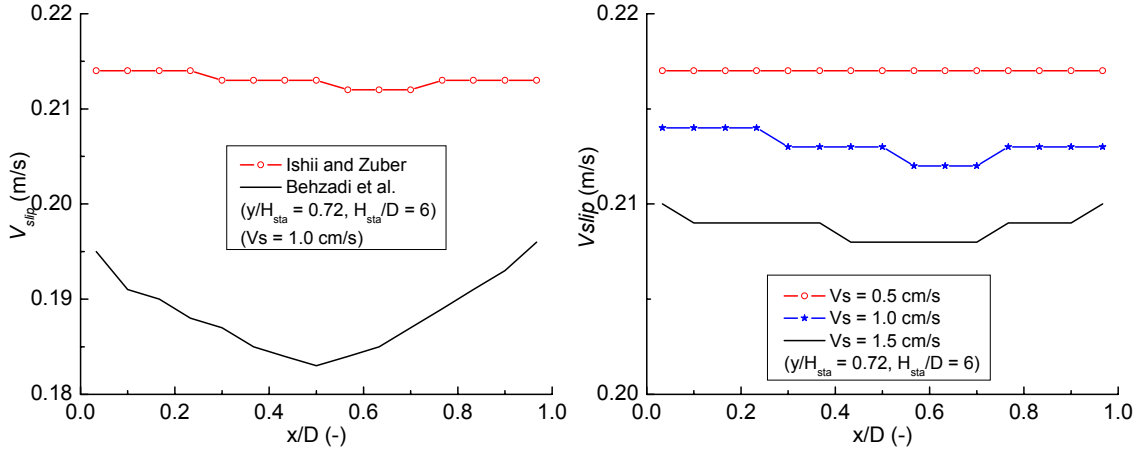

(a) (b)

Figure 2.26: Comparison of the simulated time-averaged slip velocity profiles in the tall column: (a) effect of different drag coefficient corrections, (b): effect of different superficial velocities. Here, Ishii and Zuber refers to Case 0B610 and Behzadi et al. corresponds to 0B610B; *Vs* = 0.5 cm/s corresponds to Case 0B605, *Vs* = 1.0 cm/s is case 0B610b and *Vs* = 1.5 cm/s refers to Case 0B615.

2.7 Conclusions

Numerical simulations of the gas-liquid two-phase flow in two squared-sectioned bubble columns were carried out with the use of the commercial software package CFX4.4. Sub-grid scale (SGS) and k-ε turbulence models were employed to evaluate the shear-induced turbulent viscosity in the liquid phase. Different interfacial closure models were extensively and systematically studied. Both "Pressure" and "Opening" boundary conditions applied at the outlet were explored. The effect of the gas phase wall boundary condition was also investigated.

It is observed that, through the "Opening" can capture the free surface, there is hardly any difference between the simulated results obtained from "Pressure" and those obtained from "Opening" outlet boundary conditions. Except along the wall, the numerical results obtained from the free slip boundary condition do not differ from those obtained from the no slip wall boundary condition.

Both the SGS and the k-ε turbulence models can produce a good solution in modeling of gas-liquid bubbly flow in bubble columns. Though simulated results obtained from Tomiyama's interfacial force closures (Tomiyama, 2004) do not satisfy the experimental data in the lower bubble column ($H_{sta}/D = 3$), in a taller column ($H_{sta}/D = 6$), these closures produce a good solution. This observation implies that the way the bubble plume spreads over the column varies with the column aspect ratio and apparently there is not yet a universal interfacial closure model available. With a higher value for C_D and smaller value for C_L, Tomiyama's interfacial force closures increase the height where the bubble plume is spread out over the entire cross section of the column.

It is found that the closure model for the drag force strongly affects the vertical velocity profiles and the gas hold-up distribution. In the lower column, the drag coefficient of Ishii and Zuber (1979) provides a better solution than that of Tomiyama (2004), though the latter model yields a better prediction of the slip velocity. In the taller column however, the drag correlation of Tomiyama produces a better solution than that of Ishii and Zuber.

It was observed that the virtual mass force has a small influence on the investigated bubbly flow as the zone at which the virtual mass force is active is quite small. The lift force, on the contrary has a large impact on the flow dynamics, as it determines the dispersion of the bubble plume towards the bubble column walls and subsequently influences the shape of the vertical velocity profile. The lift coefficient of Tomiyama is preferred for the taller column. As indicated earlier, it was found that the spreading mode of the plume varies with the column aspect ratio. This finding implies that the lift coefficient should also depend on the local gas hold-up and/or the local gradient of the gas hold-up.

The bubble aspect ration, E, affects the drag, lift and virtual mass force coefficients. With an equivalent bubble diameter of 4 *mm*, the bubble aspect ratio is 0.77 according to Wellek et al. (1966), while recent front tracking results (Dijkhuizen et al., 2005) show it is considerably flatter ($E = 0.38$). Numerical simulations reveal that though the bubble aspect ratio significantly influences the drag coefficient, differences between the numerical results obtained from interfacial coefficients calculated from Wellek et al. (1966) and those predicted with the Front Tracking result are quite small. It was found that a better solution could be obtained when the drag and virtual mass coefficients are simultaneously taken from Front Tracking data.

When the superficial velocity is higher, it is desirable to employ bubble swarm interfacial coefficients in the modeling of gas-liquid bubbly flow. Two corrections proposed by Ishii-Zuber (1979) and Behzadi et al. (2004) to account for the influence of the local gas hold up on the drag coefficient are studied and compared. The lift correlation suggested by Behzadi et al. (2004) is tested as well. The correction suggested by van Wijngaarden (1976) is adopted to account for the bubble swarm effect on the virtual mass coefficients. It is found in this study that both drag corrections perform better than the

single bubble closures and display small differences in the simulation with relatively high superficial velocity. The lift correction suggested by Behzadi et al. (2004) performs better in the simulation of the taller column. In the simulations at the high superficial velocity, the predicted mean and fluctuating liquid phase vertical velocity profiles agrees well with the experimental data, whereas the gas phase vertical velocity is somewhat overestimated. It is believed that the discrepancy can be attributed to the measurement uncertainty which increases with the gas holdup. This disagreement needs further experimental and numerical study, especially with respect to the correction for the lift coefficient.

2.8 Notation

B	model notation
C	model coefficient
D	bubble column depth, m
E	bubble aspect ration
$Eö$	Eötvös number, = $(\rho_L-\rho_G)g\,d_B^2\,/\sigma$
Eo_d	modified Eötvös number, = $Eö\,/E^{2/3}$
H	bubble column height, m
$\mathbf{M}$	interfacial force vector
S	source terms
W	bubble column width, m
X	Cartesian coordinate axis, x direction
Y	Cartesian coordinate axis, y direction
Z	Cartesian coordinate axis, z direction
a	horizontal dimension of an ellipsoidal bubble, m
b	vertical dimension of an ellipsoidal bubble, m
d	bubble diameter, m
n	time step number
p	pressure, N m^{-2}
k	turbulent kinetic energy, m^2 s^{-2}
$\boldsymbol{g}$	gravity acceleration, 9.81 m s^{-2}
S	strain tensor
t	time, s
$\mathbf{u}$	phase velocity, m s^{-1}

Greek letters

α	phase volume fraction, dimensionless
β	model notation
ε	turbulent dissipation rate m^2 s^{-3}
μ	viscosity, kg m^{-1} s^{-1}
ρ	density, kg m^{-3}
σ	interfacial tension, N m^{-1}
τ	characteristic time, s
τ	stress tensor, N s^{-1}
Δ	filter width, m

Indices

B	bubble
BIT	bubble induced turbulence
D	drag force
L	liquid phase, lift
Lam	laminar
G	gas phase
VM	virtual mass force
S	superficial velocity
S	SGS model constant
Sta	static liquid level
Swa	bubble swarm
Tur	shear-induced turbulence
a	bubble swarm virtual mass correlation, type a
b	bubble swarm virtual mass correlation, type b
c	bubble swarm virtual mass correlation notation
eff	effective
h	horizontal direction
i	Cartesian coordinate index
k	phase notation
m	Cartesian coordinate index
max	maximum
rms	root of mean square
v	vertical direction

2.9 Bibliography

Becker, S., Sokolichin, A. and Eigenberger, G., 1994.Gas-liquid flow in bubble columns and loop reactors:Part II. Comparison of detailed experiments and flow simulations. *Chem. Eng. Sci.,* 49, 5747-5762.

Behzadi, A, Issa, R. I. and Rusche, H., 2004. Modeling of dispersed bubble and droplet flow at high phase fractions. *Chem. Eng. Sci*, 59: 759-770.

Beyerlein, S. W., Cossmann, R. K. and Richter, H., 1985. Prediction of bubble concentration profiles in vertical turbulent two-phase flow. *Int. J. Multiphase Flow*,11 , 629-641.

Canuto, V. M. and Cheng, Y., 1997. Determination of the Smagorinsky-Lilly constant. *Phys. Fluids*, 9, 1368-1378.

Clift, R., Grace, J. R. and Weber, M. E., 1978. Bubbles, Drops and Particles. *Academic Press*. New York.

Deen, N, G., 2001. An experimental and computational study of fluid dynamics in gas-liquid chemical reactors. Ph.D thesis,Aalborg University, Esbjerg, Denmark.

Deen, N. G., Solberg, T., and Hjertager, B. H., 2001. Large eddy simulation of the Gas-Liquid flow in a square cross-sectioned bubble column. *Chem. Eng. Sci.*, 56, 6341-6349.

Delnoij, E., Kuipers, J. A. M. and Van Swaaij, W. P. M., 1997. Dynamic simulation of gas-liquid two-phase flow: effect of column aspect ratio on the flow structure. *Chem. Eng. Sci.*, 52, 3759-3772.

Dijkhuizen, W., Van den Hengel, E.I.V., Deen, N.G., van Sint Annaland, M. and Kuipers, J. A. M., 2005. Numerical investigation of closures for interface forces acting on single air-bubbles in water using Volume of Fluid and Front Tracking models, *Chem. Eng. Sci.*, 60, 6169-6175.

Drew, D. A. and Passman, S. L., 1999. Theory of multicomponent fluids, Applied Mathematical Sciences 135, Springer.

Ervin, E. A. and Tryggvason, G., 1997. The rise of bubbles in a vertical shear flow, *J. Fluids Eng,* 119, 443-449.

Gosman, A. D., Issa, R. I., Lekakou, C., Looney, M. K. and Politis, S., 1992. Multidimensional modeling of turbulent two-phase flows in stirred vessels. *AIChE J.*, 38, 1946-1955.

Hjertager, B.H., 1998. Computational fluid dynamics (CFD) analysis of multiphase chemical reactors. Trends in Chemical Engineering, 4, 45–92.

Ishii, M. and Zuber, N., 1979. Drag coefficient and relative velocity in bubbly, droplet or particulate flows. *AIChE J.,* 25, 843-855.

Jakobsen, H.A., Sannæs, B. H., Grevskott, S. and Svendsen, H.F., 1997. Modeling of vertical bubble-driven flows. *Ind. Eng. Chem. Res*., 36, 4052-4074.

Lakehal, D., Smith, B. L. and Milelli, M., 2002. Large-eddy simulation of bubbly turbulent shear flows. *Journal of Turbulence*. 3, 1-21.

Lopez de Bertodano, M.A., 1992. Turbulent bubbly two-phase flow in a triangular duct, Ph.D dissertation, Rensselaer Polytechnic Institute.

Magnaudet, J. and Eames, I., 2000. The Motion of High-Reynolds Number Bubbles in inhomogeneous Flows. *Ann. Rev. Fluid Mech.*, 32, 659-708.

Milelli M., Smith, B. L. and Lakehal D., 2001. Large-eddy simulation of turbulent shear flows laden with bubbles. *Direct and Large-Eddy Simulation IV*. Geurts, B. J., Friedrich R. and Metais O., 461–470, Amsterdam: Kluwer Acadmic.

Mudde, R. F. and Simonin, O., 1999. Two- and three dimensional simulations of a bubble plume using a two-fluid model. *Chem. Eng. Sci.*, 54, 5061-5069.

Oey, R.S., Mudde, R.F., and Van Den Akker, H.E.A., 2003. Sensitivity study on interfacial closure laws in two-fluid bubbly flow simulations, *AIChE J.*, 49, 1621-1636.

Pfleger, D. and Becker, S., 2001. Modeling and simulation of the dynamic flow behavior in a bubble column. *Chem. Eng. Sci.*, 56, 1737-1747.

Sato, Y. and Sekoguchi, K.,1975. Liquid velocity distribution in two-phase bubble flow. *Int. J. Multiphase Flow*, 2, 79-95.

Smagorinsky, J., 1963. General circulation experiments with the primitive equations. *Mon. Weather Rev.*, 91, 99-165.

Simonnet, M., Gentric, C., Olmos, E. and Midoux, N., 2007. Experimental determination of the drag coefficient in a swarm of bubbles. *Chem. Eng. Sci*., 62, 858-866.

Sokolichin, A. and Eigenberger, G., 1999. Applicability of the standard turbulence model to the dynamic simulation of bubble columns: Part I. Detailed numerical simulations. *Chem. Eng. Sci*., 52, 611-626.

Svendsen, H. F., Jakobsen, H. A. and Torvik, R., 1992. Local flow structures in internal loop and bubble column reactors. *Chem. Eng. Sci*., 47, 3297-3304.

Tomiyama, A., Sou, A., Zun, I., Kanami, N. and Sakaguchi, T., 1995. Effect of Eötvös number and dimensionless liquid volumetric flux on lateral motion of a bubble in a laminar duct flow. Proceedings of the 2nd international conference on Multiphase Flow, Kyoto, Japan.

Tomiyama, A. 1998. Struggle with computational bubble dynamics. 1998. 3rd international conference on multiphase flow, ICMF, Lyon, France.

Tomiyama, A., Celata, G. P., Hosokawa S. and Yoshida S., 2002. Terminal velocity of single bubbles in surface tension force dominant regime. *Int. J. Multiphase Flow*, 28, 1497-1519.

Tomiyama, A., 2004. Drag, lift and virtual mass forces acting on a single bubble. 3rd International Symposium on Two-Phase Flow Modeling and Experimentation. Pisa, Italy. 22-24 Sept.

Van Wijngaarden, L., 1976. Hydrodynamic interaction between gas bubbles in liquid. *J. Fluid Mech*., 77: 27-44

Vreman, A. W., 2004. An eddy-viscosity sub grid-scale model for turbulent sher flow: Algebraic theory and applications. *Phys. Fluids*, 16, 3670-3681.

Wellek, R.M., Agrawal, A.K. and Skelland, A.H.P., 1966. Shape of liquid drops moving in liquid media. *AIChE J*., 12, 854–862.

Zhang, D., 2005. Numerical simulation of dynamic flow behavior in a bubble column: grid and time-independent solution. *Technical report*. University of Twente, March.

Zhang, D., Deen, N. G., Kuipers, J. A. M., 2005. Numerical simulation of dynamic flow behavior in a bubble column: Comparison of the bubble-induced turbulence models in the k-ε model. Fourth International Conference on CFD in the Oil and Gas, Metallurgical & Process Industries. Trondheim, Norway. 6-8 June 2005.

Zhang, D., Deen, N. G., Kuipers, J. A. M., 2006. Numerical simulation of dynamic flow behavior in a bubble column: A study of closures for turbulence and interface forces. *Chem. Eng. Sci.*, 61, 7593-7608.

3

Study of multiphase turbulence models in modeling of gas-liquid flow in bubble columns

Abstract

Numerical simulations of the bubbly flow in bubble columns were carried out with the commercial CFD package CFX4.4. The Euler-Euler model is adopted to study the gas-liquid bubbly flow in this chapter. Both a sub-grid scale and k-ε turbulence models were employed to evaluate the shear-induced turbulence in the continuous phase. The effect of the model constant used in the sub-grid scale (SGS) model, C_S, as well as the difference between two SGS turbulence models (Smagorinsky, 1963 and Vreman, 2004) were investigated. Furthermore, the performance of three models (Pfleger and Becker, 2001; Sato and Sekoguchi, 1975; Troshko and Hassan, 2001) to account for the bubble-induced turbulence in the k-ε model was assessed as well. All simulated mean and fluctuating velocities were compared with the available PIV experimental data of Deen (2001). It is found that the difference between two SGS turbulence model in modeling of gas-liquid bubbly flow is very small. Only near the wall, the model suggested by Vreman (2004) inherently dampens the shear-induced turbulent viscosity. It is seen that when a SGS turbulence model is used, the simulation results with $C_S = 0.08$ and $C_S = 0.10$ agree well with the measurements. Furthermore, when C_S is increased, the effective viscosity increases and consequently the bubble plume becomes less dynamic. All three bubble-induced turbulence models could produce good solutions for the time-averaged velocity. The models of Troshko and Hassan (2001) and Pfleger and Becker (2001) reproduce the dynamics of the bubbly flow in a more accurate way than the model of Sato and Sekoguchi (1975). Based on the comparison of the results, it was found that the model of Pfleger and Becker (2001) performs slightly better than the model of Troshko and Hassan (2001), while the model of Sato and Sekoguchi (1975) performs the worst.

This chapter is based on: Zhang, Deen and Kuipers [2005, 2006]

3.1 Introduction

Bubble column reactors are widely used in chemical, petrochemical and biochemical processes. The ability to predict fluid flow dynamics is of paramount important in designing and developing bubble

column reactors. Experimental investigation and numerical simulations are widely used to carry out predictions and analyze gas-liquid fluid flow process.

Two approaches are mostly used to simulate the flow in bubble columns: the Euler-Euler model (E-E) (Becker, Sokolichin and Eigenberger, 1994) and Euler-Lagrange (E-L) approach (Delnoij, Kuipers and Van Swaaij, 1997). The E-L method is more suited for fundamental investigations of the bubbly flow while the E-E method is preferred in high gas holdup and churn turbulent flows

Turbulence modeling is one of the main unresolved problems in the simulation of gas-liquid two-phase flow. Zero equation turbulence model has been used (Pan, Dudukovic and Chang, 1999), as well as the k-ε (Becker, Sokolichin and Eigenberger, 1994; Lopez de Bertodano, Lahey and Jones, 1994; Sokolichin, Eigenberger, 1999; Becker et al., 1994; Pfleger and Becker, 2001) and sub-grid scale (SGS) models (Deen et al., 2001; Milelli et al., 2001; Lakehal et al., 2002). Through a thorough study of the k-ε and sub-grid scale (SGS) models used in the simulation of bubbly flow, Deen (2001) found that good agreement was obtained with the k-ε model in the simulation of the Becker case (Becker et al., 1994), while in the simulation of a three-dimensional bubble column, the SGS model produces a better solution. When the SGS model of Smagorinsky (1963) is used, it is noted that the predicted effective viscosity is not damped near the wall, which is unphysical. This can be improved by applying a damping function, as suggested by Van Driest (1956) or by using an alternative SGS model, such as the simple algebraic model suggested by Vreman (2004). The eddy-viscosity SGS model proposed by Vreman (2004) inherently damps the turbulent viscosity near the wall. Furthermore, Deen et al. (2001) used a fixed value for the model constant appearing in the SGS model (Smagorinksky , 1963), C_S, based on single-phase flow conditions. However, the sensitivity of the model results with respect to this model constant is not clear.

When the k-ε model is employed to evaluate the shear-induced turbulent viscosity, the bubble-induced turbulence is generally accounted for through two different approaches: Sato and Sekoguchi (1975) directly added an extra term to the effective viscosity, whereas in the other approach, the turbulence induced by the bubbles is accounted for by source terms appearing in the equations of k and ε (Mudde and Simonin, 1999; Pfleger and Becker, 2001; Troshko and Hassan, 2001). There exist several models for the source terms due to bubble-induced turbulence (Bel F'dhila and Simonin, 1992; Gosman et. al., 1992; Kataoka and Serizawa, 1989; Lopez de Bertodano et al., 1994; Pfleger and Becker, 2001; Troshko and Hassan, 2001). In the model of Gosman et. al. (1992), these terms in the equation for the liquid turbulent kinetic energy, k originates from the gas fluctuation and dispersion, whereas the bubble-induced production term in the equation for the liquid turbulence dissipation rate, ε comes from the gas dissipation rate. In other models (Kataoka and Serizawa, 1989; Pfleger and Becker, 2001; Troshko and Hassan, 2001), the production of bubble-induced turbulent kinetic energy is calculated as the work of the bubble, i.e., the interfacial force multiplied with the local slip velocity. In this case, the associated energy dissipation rate is scaled with a time scale, τ_{BIT}. Oey et al. (2003) found that in the simulation of the Becker case (Becker et al., 1994), the model of Gosman et al. (1992) and that of Bel F'dhila and Simonin (1992) do not yield a large difference in the global column dynamics. The main difference among the bubble-induced turbulence models of Pfleger and Becker (2001) and Troshko and Hassan (2001) lies in the time scale of the bubble-induced turbulence dissipation. In the model of Pfleger and Becker (2001), the smallest eddy time scale of the shear-induced turbulence was used as the characteristic time scale of the bubble-induced turbulence. Lopez de Bertodano (1992) found that when the shear-induced turbulence time scale is used as an estimate for the time scale of the bubble-induced turbulence, the turbulence decay depends on the initial dissipation rate, which is unphysical. For this reason he proposed a new expression for the bubble-

induced turbulence time scale, which depends on the bubble relaxation time. Troshko and Hassan (2001) also adopted this time scale. In the simulations of Pfleger and Becker (2001) and Troshko and Hassan (2001), numerical results fit well with the experiments, though the time scale used to calculate the bubble-induced turbulence production in the liquid phase turbulence dissipation rate equation is quite different. Although all these models can provide good solutions for the time-averaged velocities, to the best of our knowledge, neither the validity of the predicted sub-grid scale quantities, nor the difference between these models has been investigated systematically before. In this chapter, the performance of these two models, along with the model of Sato and Sekoguchi (1975) are investigated for the case of a square cross-sectioned bubble column.

A correct description of the closure laws for the drag, lift and virtual mass forces is of great importance in numerical simulation of bubbly flows. Despite considerable research efforts on this topic (Clift et al., 1978, Ervin and Tryggvason, 1997; Magnaudet and Eames, 2000; Tomiyama., 2004; Dijkhuizen et al., 2005), accurate modeling of the interfacial forces remains an open question in numerical simulations of bubbly flow. As found in the work of Deen et al. (2001), even with constant drag, lift and virtual mass coefficients, numerical simulated results still agree well with the available Particle Image Velocimetry (PIV) measurements in a small column. In the study addressed in Chapter 2, it was found that there is no universal set of interfacial coefficients available which is valid for all kinds of bubble columns. So in this chapter, the most suitable interfacial closure laws found in the previous chapter are employed. Detailed discussion and investigation of the interfacial closure laws can be found in Chapter 2.

This chapter presents three-dimensional dynamic simulations of gas-liquid bubbly flow, employing the Euler-Euler approach for the case of square cross-sectioned bubble columns. An “Opening” boundary condition is applied at the outlet and no slip boundary conditions are applied for both phases along the wall. The sensitivity of the sub-grid scale (SGS) model to the model constant C_S and the difference between the SGS models of Smagorinsky (1963) and Vreman (2004) as well as the applicability and performance of three different bubble-induced turbulence models proposed by Sato and Sekoguchi (1975), Pfleger and Becker (2001) and Troshko and Hassan (2001) are investigated in detail. All the numerical results are compared with experimental measurement data of Deen et al. (2001).

3.2 Governing equations

The equations of the two-fluid formulation are derived by ensemble averaging the local instantaneous equations of single-phase flow (Drew, 1999). Two sets of balance equations for mass and momentum are obtained. Ignoring the interfacial mass transfer, the generic conservation equations for mass and momentum respectively take the following form:

$$\frac{\partial(\alpha_k \rho_k)}{\partial t} + \nabla \cdot (\alpha_k \rho_k \mathbf{u}_k) = 0 \tag{3.1}$$

$$\frac{\partial(\alpha_k \rho_k \mathbf{u}_k)}{\partial t} + \nabla \cdot (\alpha_k \rho_k \mathbf{u}_k \mathbf{u}_k + \alpha_k \boldsymbol{\tau}_k) = \alpha_k \rho_k \mathbf{g} - \alpha_k \nabla p_k + \mathbf{M}_k \tag{3.2}$$

where the indices k refers to the phase (L for liquid, G for gas). The volume fraction of each phase is denoted by α and $\mathbf{u} = (u, v, w)$ is the velocity vector.

The term $\boldsymbol{M}_k$ in Eq. 3.2, describing the interface forces, is given as follows

$$\mathbf{M}_L = -\mathbf{M}_G = \mathbf{M}_{D,L} + \mathbf{M}_{L,L} + \mathbf{M}_{VM,L} \tag{3.3}$$

where the terms on the right hand side represent forces due to drag, lift and virtual mass, respectively. They are calculated as:

$$\mathbf{M}_{D,L} = \frac{3}{4}\alpha_G \rho_L \frac{C_D}{d_B} |\mathbf{u}_G - \mathbf{u}_L| (\mathbf{u}_G - \mathbf{u}_L) \tag{3.4}$$

$$\mathbf{M}_{L,L} = \alpha_G \rho_L C_L (\mathbf{u}_G - \mathbf{u}_L) \times \nabla \times \mathbf{u}_L \tag{3.5}$$

$$\mathbf{M}_{VM,L} = \alpha_G \rho_L \mathbf{C}_{\mathbf{VM}} (\frac{D_G \mathbf{u}_G}{Dt} - \frac{D_L \mathbf{u}_L}{Dt}) \tag{3.6}$$

As discussed in Chapter 2, virtual mass coefficient takes a form as ($C_{VM,h}$, $C_{VM,V}$, $C_{VM,h}$), which means in different Cartesian directions, virtual mass takes different values. In this chapter, a bubble size of 4 *mm* is used, Based on Chapter 2, the suitable interfacial coefficients C_D, C_L and ($C_{VM,h}$, $C_{VM,V}$) for each tested cases are listed in Table 3.1 .

For phase *k*, the stress tensor $\boldsymbol{\tau}_k$ is given by:

$$\boldsymbol{\tau}_k = -\mu_{eff} (\nabla \mathbf{u}_k + (\nabla \mathbf{u}_k)^T - \frac{2}{3} I \nabla \cdot \mathbf{u}_k) \tag{3.7}$$

The effective viscosity of the liquid phase, $\mu_{L,eff}$ is composed of three contributions: the molecular viscosity $\mu_{L,Lam}$, the shear-induced turbulent viscosity $\mu_{L,Tur}$ and an extra term due to bubble induced turbulence, μ_{BIT}:

$$\mu_{L,eff} = \mu_{L,Lam} + \mu_{L,Tur} + \mu_{BIT} \tag{3.8}$$

Here, the model proposed by Sato and Sekoguchi (1975) is used to account for the bubble-induced turbulence in Eq. 3.8:

$$\mu_{BIT} = \rho_L \alpha_G C_{\mu,BIT} d_B |\mathbf{u}_G - \mathbf{u}_L| \tag{3.9}$$

where $C_{\mu,BIT}$ is a model constant which is set to 0.6.

Sometimes, the bubble-induced turbulence is considered by including extra source terms in the turbulent models. In that case, the liquid phase effective viscosity ,$\mu_{L,eff}$ consists of the molecular viscosity $\mu_{L,Lam}$ and the shear-induced turbulent viscosity $\mu_{L,Tur}$:

$$\mu_{L,eff} = \mu_{L,Lam} + \mu_{L,Tur} \tag{3.10}$$

In this chapter, both the sub-grid model (SGS) and the *k*-ε model are employed to evaluate the shear-induced turbulent viscosity in the liquid phase. In both cases, the effective viscosity of the gas phase is calculated as follows according to Jakobsen et al. (1997):

$$\mu_{G,eff} = \frac{\rho_G}{\rho_L}\mu_{L,eff} \tag{3.11}$$

When the SGS model of Smagorinsky (1963) is employed, the shear-induced turbulent viscosity in the liquid phase is assessed as:

$$\mu_{L,Tur} = \rho_L (C_S \Delta)^2 |\mathbf{S}| \tag{3.12}$$

where $\mathbf{S}$ is the characteristic filtered rate of strain and $\Delta = (\Delta_i \Delta_j \Delta_k)^{1/3}$ is the filter width. C_S is a model constant, which is typically between 0.08 and 0.22 (Canuto and Cheng, 1997) and its effect is studied later in this chapter. When the SGS model suggested by Vreman (2004) is adopted, the liquid phase shear-induced turbulent viscosity is calculated as:

$$\mu_{L,Tur} = 2.5\rho C_S^2 \sqrt{\frac{B_\beta}{S_{ij}S_{ij}}} \tag{3.13}$$

where $S_{ij} = \partial u_j / \partial x_i$, $\beta_{ij} = \Delta_m^2 S_{mi} S_{mj}$ and $B_\beta = \beta_{11}\beta_{22} - \beta_{12}^2 + \beta_{11}\beta_{33} - \beta_{13}^2 + \beta_{22}\beta_{33} - \beta_{23}^2$. Δ_i is the filter width in i direction.

When the k-ε turbulence model is employed, the gas phase influences the turbulence in the liquid phase by a bubble-induced turbulence model. The shear-induced turbulent viscosity of the liquid phase is calculated by:

$$\mu_{L,Tur} = C_\mu \rho_L \frac{{k_L}^2}{\varepsilon_L} \tag{3.14}$$

The conservation equations for k and ε are respectively given by

$$\frac{\partial(\alpha_L \rho_L k_L)}{\partial t} + \nabla \cdot (\alpha_L \rho_L \mathbf{u}_L k_L - \alpha_L (\mu_{L,Lam} + \frac{\mu_{L,Tur}}{\sigma_k})\nabla k_L) = \alpha_L (G_L - \rho_L \varepsilon_L) + S_{k,BIT} \tag{3.15}$$

$$\frac{\partial(\alpha_L \rho_L \varepsilon_L)}{\partial t} + \nabla \cdot (\alpha_L \rho_L \mathbf{u}_L \varepsilon_L - \alpha_L (\mu_{L,Lam} + \frac{\mu_{L,Tur}}{\sigma_\varepsilon})\nabla \varepsilon_L) = \alpha_L \frac{\varepsilon_L}{k_L}(C_{\varepsilon 1} G_L - C_{\varepsilon 2}\rho_L \varepsilon_L) + S_{\varepsilon,BIT} \tag{3.16}$$

with $C_{\varepsilon 1}$ = 1.44, $C_{\varepsilon 2}$ = 1.92, C_μ = 0.09, σ_k = 1.0 and σ_ε = 1.217. It is noted that these constants are not universal, even in the case of single-phase flow. For multiphase flows they are still under debate.

$S_{k,BIT}$ and $S_{\varepsilon,BIT}$ are source terms due to the presence of bubbles, which are discussed in detail below. There are two approaches to account for the bubble-induced turbulence when the k-ε turbulence model is used in the simulation of multiphase flow. One is to use the standard k-ε turbulence model, *i.e.*, $S_{k,BIT}$ and $S_{\varepsilon,BIT}$ in Eqs. 3.15 and 3.16 are 0, but the bubble-induced turbulence is contained in the

effective viscosity, $\mu_{L,eff}$, as in Eq. 3.8. Another approach to account for the bubble-induced turbulence in the k-ε turbulence model is to include extra source terms in the turbulence model as found in the available literatures (Bel F'dhila and Simonin, 1992; Gosman et. al., 1992; Kataoka and Serizawa, 1989; Lopez de Bertodano et al., 1994; Pfleger and Becker, 2001; Troshko and Hassan, 2001). Here, only the model of Pfleger and Becker (2001) and Troshko and Hassan (2001) are investigated.
According to Pfleger and Becker (2001), the extra terms, $S_{k,BIT}$ in Eq. 3.15 and $S_{\varepsilon,BIT}$ in Eq. 3.16 are given by:

$$S_{k,BIT} = \alpha_L C_k |\mathbf{M}_L| \cdot |\mathbf{u}_G - \mathbf{u}_L| \tag{3.17}$$

$$S_{\varepsilon,BIT} = \frac{\varepsilon_L}{k_L} C_\varepsilon S_{k,BIT} \tag{3.18}$$

where $C_k = 1.44$, $C_\varepsilon = 1.92$.
Note that in Eq. 3.18 ε_L/k_Lrepresents the characteristic time scale of the bubble-induced turbulence dissipation rate. Base on the work of Lopez de Bertodano (1992), Troshko and Hassan (2001) proposed another model to account for the bubble-induced turbulence in the k and ε equations. In their model, $S_{k,BIT}$ and $S_{\varepsilon,BIT}$ were calculated as:

$$S_{k,BIT} = \frac{3}{4}\frac{C_D}{d}\alpha_G \rho_L |\mathbf{u}_G - \mathbf{u}_L|^3 = |\mathbf{M}_D||\mathbf{u}_G - \mathbf{u}_L| \tag{3.19}$$

$$S_{\varepsilon,BIT} = \frac{3C_D |\mathbf{u}_G - \mathbf{u}_L|}{2C_{VM} d_B} C_3 S_{k,BIT} \tag{3.20}$$

here $C_3 = 0.45$ and $\frac{3C_D |\mathbf{u}_G - \mathbf{u}_L|}{2C_{VM} d_B}$ is the characteristic time scale of the bubble-induced turbulence.
In the approach of Pfleger and Becker (2001), $|\mathbf{M}_L|.|\mathbf{U}_G\text{-}\mathbf{U}_L|$ represents the rate of energy input of the bubbles resulting from the total interfacial forces and the slip velocity into the liquid phase and $\tau_{BIT} = \varepsilon_L/k_L$. In the approach of Troshko and Hassan (2001), only the drag force is considered in the energy input of the bubbles. The characteristic time-scale of bubble-induced turbulence is set equal to the bubble response time, $\tau_{BIT} = 2C_{VM}d_B/(3C_D|\mathbf{u}_G\text{-}\mathbf{u}_L|)$. It is noted that the drag is the main source of energy input. Consequently the difference between the above two models is mainly expressed through the characteristic time scale of the bubble-induced turbulence.

3.3 Numerical solution method

All the numerical simulations are carried out with the commercial CFD package CFX-4.4 of AEA Technology, Harwell, UK. The total domain is subdivided into uniform computational grid cells with $\Delta x = \Delta y = \Delta z = 0.01$ m. Eqs. 3.1 and 3.2 are solved in a transient fashion with a time step of 0.005 s. It was previously found (Zhang, 2005) that good space and time resolutions are obtained with the above grid size and time step. The curvature compensated convective transport (CCCT) scheme is used for the discretization of all convective terms. Standard boundary conditions employing wall functions are used for k and ε.
For the "opening" boundary condition at the outlet, the following conditions are imposed:

$$\alpha_G = 1.0 \qquad \alpha_L = 0 \tag{3.21}$$

In the gas cap, special measures are taken. That is, in case $\alpha_L < 0.55$

$$\alpha_L < 0.55 \quad \begin{cases} C_D = 0.05 \\ C_L = 0 \\ C_{VM} = 0 \end{cases} \tag{3.22}$$

With such a measure, Eqs. 3.1 and 3.2 in approximation reduce to single phase flow equation. A small, finite value of $C_D = 0.05$ in Eq. 3.22 is required to guarantee the coupling of the two phases.

3.4 Physical problem

Sketches of the bubble columns used in this chapter are shown in Figure 3.1. The columns are initially filled with water to a height (H_{sta}) of 0.45/0.90 m, which acts as the continuous liquid phase; air is used as the dispersed gas phase and is injected in the center of the bottom plane with $A_{in} = 0.03 \times 0.03$ m^2 at a superficial gas velocity of $V_S = 4.9$ mm/s. The gas-liquid flow is assumed to be homogeneous (bubbly) flow, break-up and coalescence are not accounted for. The columns have the following dimensions: width (W) 0.15 m, depth (D) 0.15 m and height (H) 0.55 m. The gas distributor is mounted at the bottom at a distance of 0.06 m from both the left and backside of the column. All the simulation parameters and physical properties are presented in Tables 3.1 and 3.2.

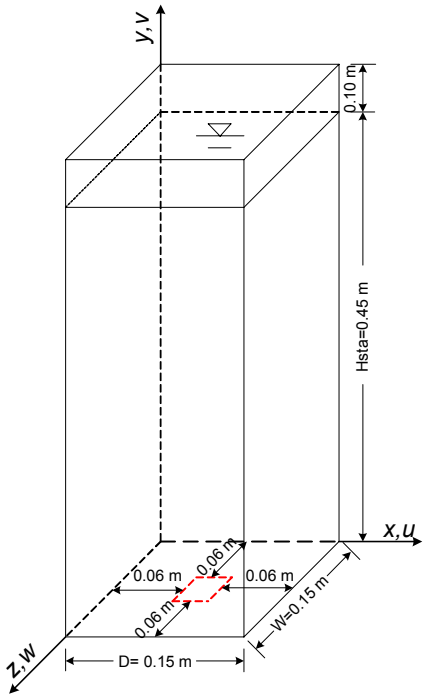

Figure 3.1: Schematic representation of the investigated bubble columns.

Table 3.1: Simulation and case parameters when SGS turbulence model is employed.

Case	$\mu_{L,Tur}$	C_D	C_L	($C_{VM,h}$, $C_{VM,V}$)	C_S
0A3S	Eq. 3.12	1.071	0.5	(0.25, 1.53)	0.1
0A3	Eq. 3.13				0.1
0A3S					0.1
0A3V08					0.08
0A3V15					0.15
0A3V20					0.20
ρ_L = 1000 kg/m^3, $\mu_{L,Lam}$ =0.001 kg/(m.s), σ = 0.07275 N/m, ρ_G = 1.29 kg/m^3, d_B = 4 mm, μ_G =1.812×10^{-5} kg/(m.s). $Eö$ = 2.15. $\mu_{BIT} = \alpha_G \rho_L C_{\mu,BIT} \lvert \mathbf{u}_G - \mathbf{u}_L \rvert$ Outlet boundary condition: "Opening"					

Table 3.2: Simulation and case parameters when k-ε turbulence mode is adopted.

Case	μ_{BIT}	$S_{k,BIT}$	$S_{\varepsilon,BIT}$	C_D	C_L	($C_{VM,h}$, $C_{VM,V}$)
1A3	Eq. 3.10	0	0	1.071	0.5	(0.25, 1.53)
2A3	0	Eq. 3.17	Eq. 3.18			
3A3	0	Eq. 3.19	Eq. 3.20			
ρ_L = 1000 kg/m^3, $\mu_{L,Lam}$ = 0.001 kg/(m.s), σ = 0.07275 N/m, ρ_G = 1.29 kg/m^3, d_B = 4 mm, μ_G =1.812×10^{-5} kg/(m.s). $Eö$ = 2.15. $\mu_{L,Tur} = C_\mu \rho_L \frac{k_L^2}{\varepsilon_L}$ Outlet boundary condition: "Opening"						

3.5 Data processing

In order to compare the numerical results with the experimental data, the time-averaged quantities are calculated as defined in the following expressions. The time-averaged mean velocity is calculated as:

$$\overline{u_n} = \frac{n - n_0 - 1}{n - n_0} \overline{u_{n-1}} + \frac{1}{n - n_0} u_n \tag{3.23}$$

where the averaging is started at time step n_0 = 7500, corresponding to 37.50 s. All simulations were carried out for n = 10^5 corresponding to a period of 500 s.
The large-scale velocity fluctuations are calculated during the calculation as follows:

$$\overline{u_{rms,n}}^2 = \overline{u_n^2} - \overline{u_n}^2 \tag{3.24}$$

The resolved, grid-scale turbulent kinetic energy, k_{gs}, is calculated as:

$$k_{gs} = \frac{1}{2}[\overline{(u')^2} + \overline{(v')^2} + \overline{(w')^2}] = \frac{1}{2}(u_{rms}^2 + v_{rms}^2 + w_{rms}^2) \tag{3.25}$$

As there is no data available for w_{rms} in the experiment, is assumed that $u_{\mathrm{rms}} = w_{\mathrm{rms}}$.

When the *SGS* turbulence model is used to evaluate the shear-induced turbulent viscosity, the sub-grid scale turbulence kinetic energy, k_{sgs}, is calculated according to

$$k_{sgs} = C_k (C_s \Delta)^2 \, |\mathbf{S}|^2 \tag{3.26}$$

with C_k a constant with the value of 5 (Mason and Callen, 1986).
All the presented quantitative results are time-averaged quantities, which are selected in a plane at a width of $z/W = 0.50$.

3.6 Results and Discussion

The difference of two SGS turbulence models in simulation of gas-liquid two-phase flow is explored first and followed with the study of the effect of model constant C_S. Finally, the evaluation of the performance and capacity of three different bubble-induced turbulence models in the k-ε turbulence model is carried out. All test cases are summarized in Tables 3.1 and 3.2.

3.6.1 Different sub-grid scale turbulence models

The difference between the two SGS turbulence models proposed by Smagorinsky (1963) and Vreman (2004) in the numerical study of gas-liquid bubbly flow is investigated in detail here. Figure 3.2 displays the comparison of the vertical velocity profiles obtained from two different SGS models. $C_S = 0.10$ is used in both models; the corresponding cases are 0A3 and 0A3S. As seen in Figure 3.2, both models are capable of producing a good solution for the vertical velocity profiles for both phases. It is found that, the model overpredicts the gas phase vertical velocity in the column center: as deduced from Figure 3.2, the measured slip velocity is approximately 0.18 m/s, while the predicted one is 0.23 m/s. Apparently the C_D employed in the simulations is somewhat too low. Nevertheless, the difference between the simulated velocity profiles is quite small. This is also observed in the comparison of the liquid phase velocity fluctuations profiles, which is shown in Figure 3.3. From this figure, it is observed that the velocity fluctuation in the vertical direction is almost twice of that in the horizontal direction, which implies the isotropic turbulence assumption is invalid. In a further investigation, it is found that the main difference between the two SGS models lies in the predicted liquid phase effective viscosity as shown in Figure 3.4. It is clearly seen in Figure 3.4 that the liquid phase effective viscosity is dampened near the wall with the model of Vreman (2004). This makes sense from a physical point of view. Furthermore, it is seen that in the near wall region, the liquid phase effective viscosity mainly comes from the shear-induced turbulent viscosity. Due to the fact that the local gas-holdup is higher in the column center, the predicted bubble-induced turbulent viscosity as well as the total liquid phase effective viscosity from both SGS models is relatively large in the column center.

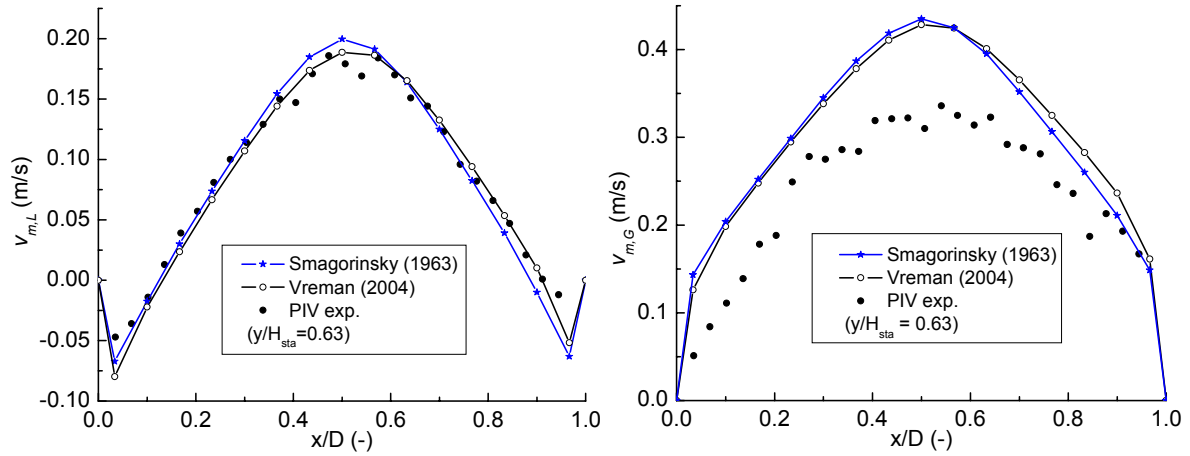

Figure 3.2: Comparison of the simulated time-averaged vertical velocity profiles of both phases with the experimental data. Here, different sub-grid scale turbulence models were used to evaluate the shear-induced turbulent viscosity in the liquid phase. Vreman corresponds to case 0A3, Smagorinsky refers to case 0A3S.

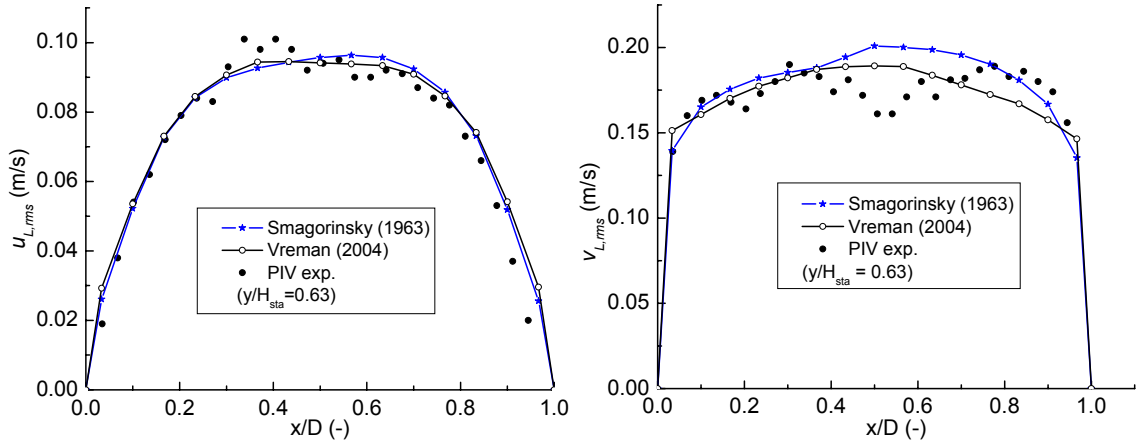

Figure 3.3: Comparison of the simulated and experimental profiles of the liquid velocity fluctuations. The simulated profiles were obtained from different SGS models. Vreman corresponds to case 0A3, Smagorinsky refers to case 0A3S.

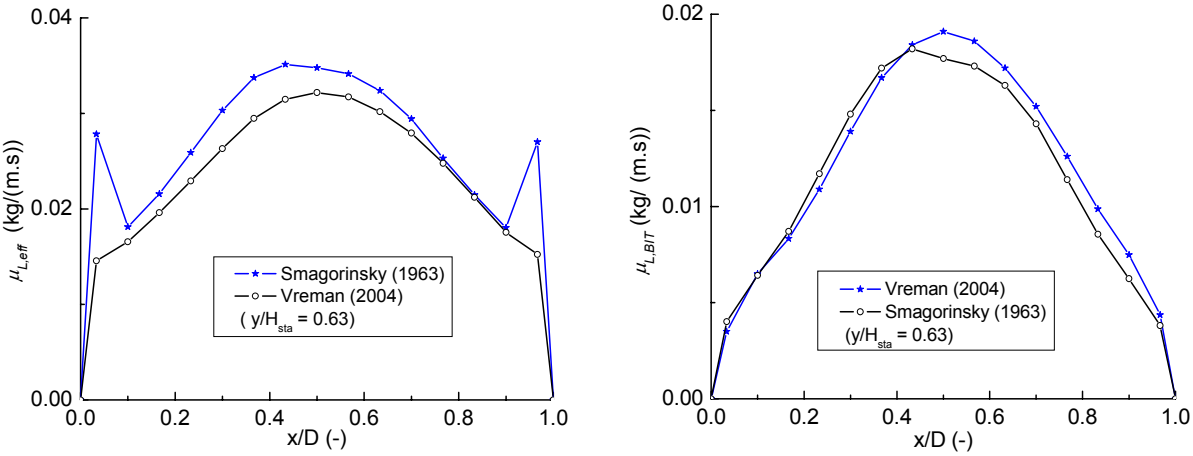

(a) (b)

Figure 3.4: Time-averaged liquid phase effective viscosity (a) and bubble-induced turbulent viscosity (b) obtained from different SGS models. Vreman corresponds to case 0A3, Smagorinsky refers to case 0A3S.

According to Canuto and Cheng (1997), SGS model constant, C_S , ranges between 0.08 and 0.22; in the original paper of Vreman (2004), a model constant C_S = 0.17 was recommended for the case of turbulent channel flow (shear flow). Here, C_S = 0.08, C_S = 0.10, C_S = 0.15 and C_S = 0.20 are selected to explore the sensitivity of the SGS model proposed by Vreman (2004) to the model constant C_S, corresponding cases are Case 0A308, 0A3, 0A315 and 0A320. Figure 3.5 shows the comparison between the experimental and predicted profiles of the mean vertical velocity of both phases for various values of C_S. It is easily observed that with a higher value of C_S, the vertical velocity profiles become steeper, and it is found that the cases with C_S= 0.08 and C_S= 0.10 produce the best solutions, while the case with C_S = 0.20 provides the worst solution. This can be attributed to the fact that, as illustrated in Figure 3.6, with the increase of C_S, the liquid phase effective viscosity (which mainly comes from the shear-induced turbulence) increases as well, that is, bigger C_S makes the liquid more viscous, dampening the bubble plume dynamics and hence the vertical velocity profiles become increasingly steeper. Figure 3.7 gives the comparison between the experimental and simulated profiles of the liquid phase velocity fluctuations. First of all, it is apparent that, as C_S increases, the velocity fluctuation in the horizontal direction drops because of the increase of the viscosity; meanwhile v_{rms} increases in the center and decreases towards the column walls. This is due to the fact that with higher values of C_S the bubble plume fluctuates strongly only in the center of the column. Based on the above comparisons, it can be concluded that the SGS model of Vreman (2004) performs slightly better than that of Smagorinsky (1963) in the simulation of gas-liquid bubbly flow in bubble column, and with a model constant C_S = 0.10, both models produce a good solution.

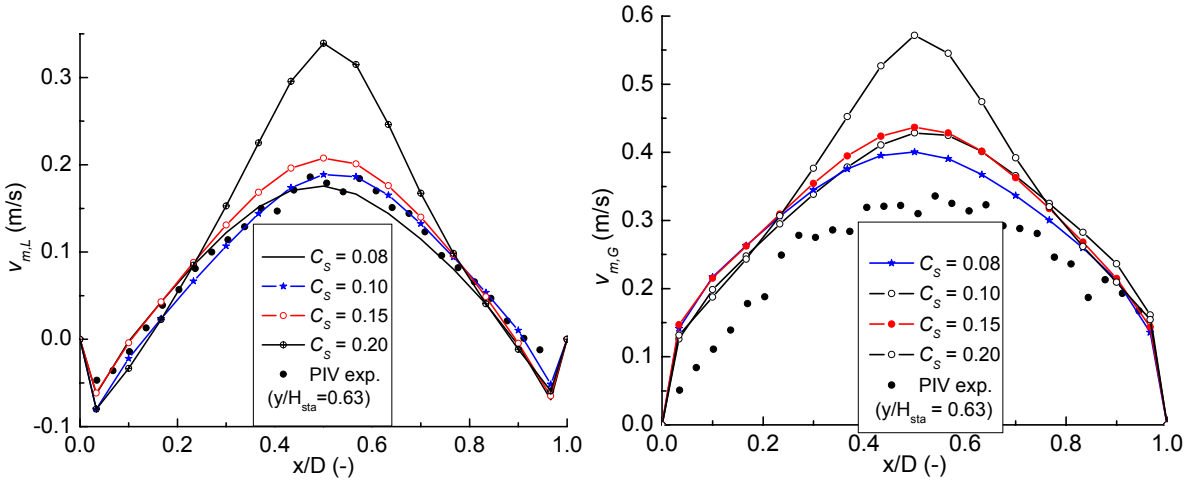

Figure 3.5: Comparison of the experimental and predicted profiles of the mean vertical velocity of the both phases at a height of y/H$_{sta}$ = 0.63. Different C_S values were used in the SGS model of Vreman (2004): C_s = 0.08 refers to case 0A308, C_s = 0.10 is case 0A3 and C_s = 0.15 corresponds to Case 0A315 and C_s = 0.20 refers to Case 0A320.

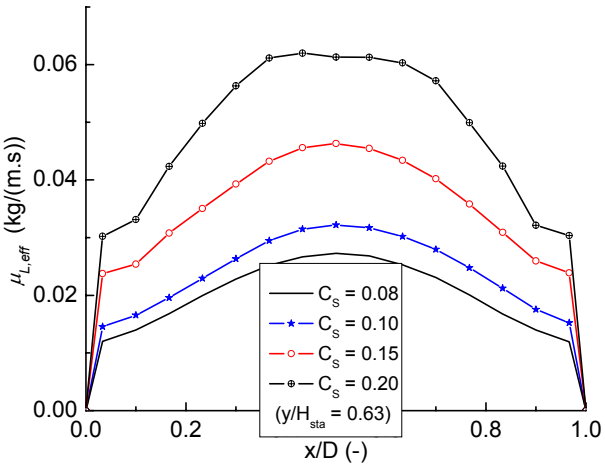

Figure 3.6: Time-averaged liquid phase effective viscosity obtained from SGS model of Vreman (2004). Different C_S were used: C_s = 0.08 refers to case 0A308, C_s = 0.10 is case 0A3 and C_s = 0.15 corresponds to Case 0A315 and C_s = 0.20 refers to Case 0A320.

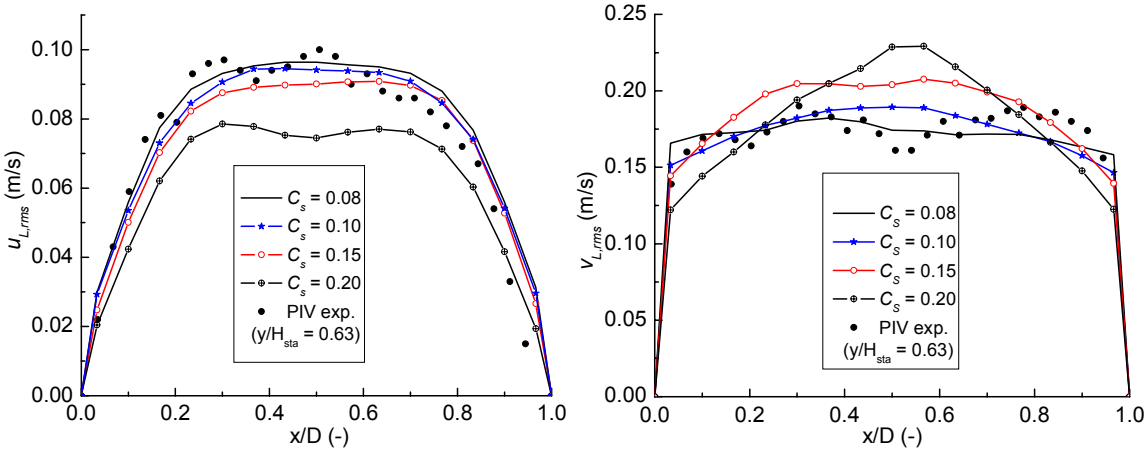

Figure 3.7: Comparison of the simulated and experimental profiles of the liquid velocity fluctuations. The simulated profiles were obtained from different C_S values used in the SGS model of Vreman (2004). C_s = 0.08 refers to case 0A308, C_s = 0.10 is case 0A3 and C_s = 0.15 corresponds to Case 0A315 and C_s = 0.20 refers to Case 0A320.

3.6.2 Different bubble-induced turbulence models in the *k-ε* turbulence model

In this section three different models to account for the bubble-induced turbulence are compared. Figure 3.8 presents the time-averaged vertical velocity profiles for the cases employing the bubble-induced turbulence closures proposed by Sato and Sekoguchi (1975), Pfleger and Becker (2001) and Troshko and Hassan (2001), i.e. cases 1A3, 2A3 and 3A3 in Table 3.2. The numerical results of case 2A3 and 3A3 slightly under-predict the experimental data for the liquid phase, but still fit reasonably well with the experimental data for the gas phase. It is clearly found in this figure that the vertical velocity profiles obtained from the model of Sato and Sekoguchi (1975) (Case 1A3) are higher than those obtained in the other two cases. This can be attributed to the higher effective viscosity predicted by the model of Sato and Sekoguchi (1975), which is shown in Figure 3.9. It is noted in Figure 3.9 that, BIT model of Troshko and Hassan (2001) (Case 3A3) exhibits a local maximum near the wall, which is unphysical. This is most probably due to the use of standard wall functions in the current work. Comparing the bubble-induced turbulent viscosity with the local effective viscosity in BIT

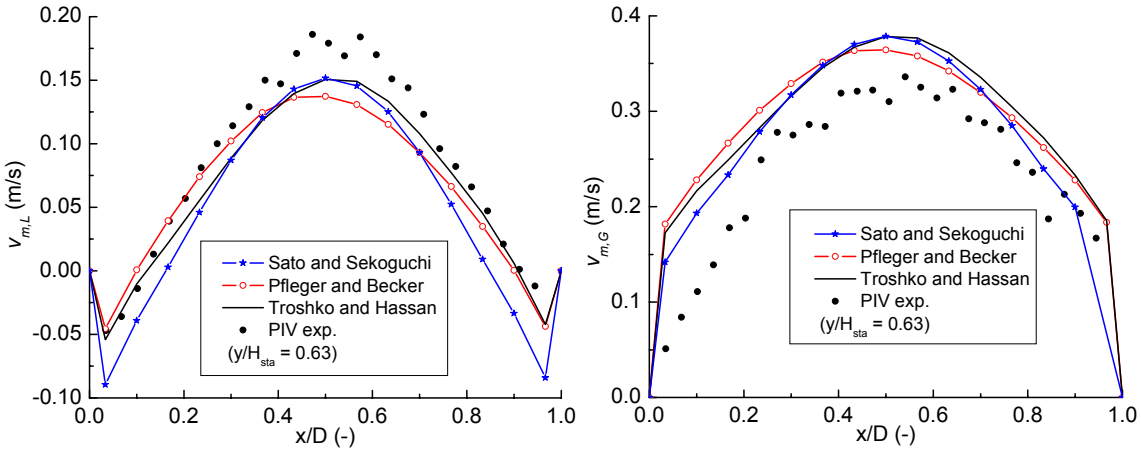

Figure 3.8: Comparison of the simulated time-averaged axial velocity profiles of both phases with the experimental data. Here, different bubble-induced turbulence models in the k-ε model were employed. Sato and Sekoguchi refers to Case 1A3, Pfleger and Becker is 2A3 and Troshko and Hassan corresponds to 3A3.

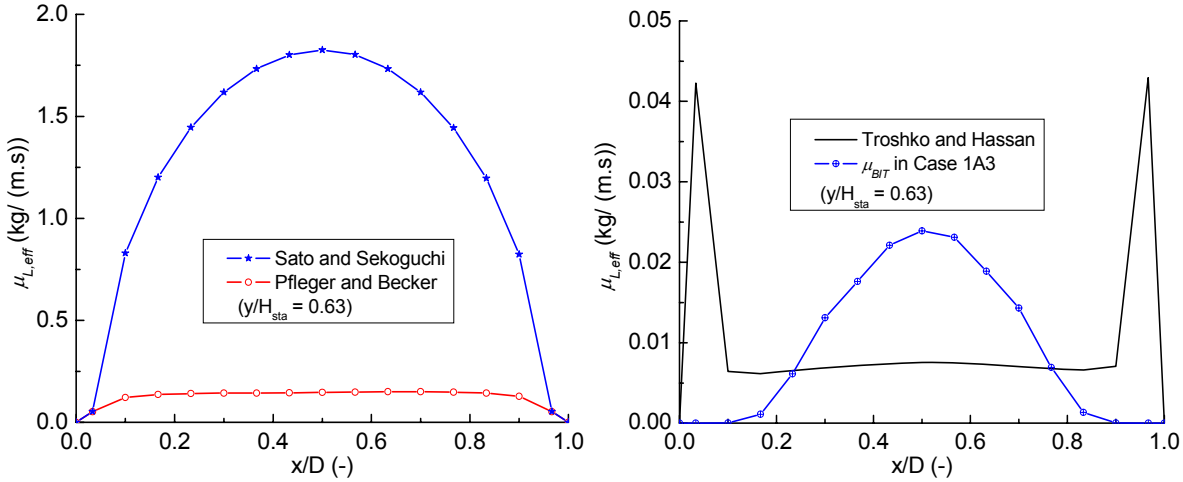

Figure 3.9: Time-averaged profiles of liquid phase effective viscosity obtained from different bubble-induced turbulence models. Sato and Sekoguchi refers to Case 1A3, Pfleger and Becker is 2A3 and Troshko and Hassan corresponds to 3A3.

model of Sato and Sekoguchi (1975) (Case 1A3), it is seen that the bubble-induced turbulent viscosity is negligible compared to the shear-induced contribution, this means that with BIT model of Sato and Sekoguchi (1975), the bubble plume has hardly any influence on the liquid phase turbulence. This finding is consistent with the analysis made by Sokolichin et al. (2004). They found that the bubble-induced viscosity is almost two orders of magnitude smaller than the shear-induced part of the effective viscosity and therefore, it can hardly have any influence on the simulation results. The high eddy viscosity predicted by the k-ε model without extra source terms leads to a quasi-steady state predicted bubble plume as observed in Figure 3.10, while with the other two BIT models, (cases 2A3 and 3A3), a dynamic bubble plume is obtained, which is in much better agreement with the experimental observations.

With the BIT model of Sato and Sekoguchi (1975) (Case 1A3), where the velocity fluctuations are implicitly contained in the turbulent kinetic energy k rather than captured in the standard k-ε model, the simulated velocity fluctuations underpredict the PIV measurements, whereas the models of Troshko and Hassan (2001) and Pfleger and Becker (2001) produce good solutions for the velocity

fluctuations as demonstrated in Figure 3.11. From Figures 3.9-3.11, it is seen that in the simulation of gas-liquid bubbly flow, the k-ε turbulence model can be improved when the bubble-induced turbulence is accounted for through additional source terms as suggested by Pfleger and Becker (2001) and Troshko and Hassan (2001).

As can be deduced from Figure 3.8, the experimental slip velocity is about 0.18 m/s, while the predicted slip velocity is approximately 0.23 m/s, which directly follows from the applied drag model. Based on the drag model and the related slip velocity, the time scale of the bubble-induced turbulence, according to Lopez de Bertodano (1992), $\tau_{BIT} = 2C_{VM}d_B/(3C_D|\mathbf{u_G}-\mathbf{u_L}|)$, is about 0.006 s for the studied cases. This time scale is much smaller than the time scale of the smallest eddy dissipation in the liquid phase ($\tau_{SIT} = k/\varepsilon \approx 0.8$ s) as displayed in Figure 3.12. This implies that the bubble-induced turbulence decays much faster than the shear-induced turbulence in the bubbly flow. Though the extra source term introduced in the ε equation in the model of Troshko and Hassan (2001) is approximately 60 times larger than that in the model of Pfleger and Becker (2001), it is noted in Figure 3.12 that both the turbulent kinetic energy, k and turbulence dissipation rate, ε obtained are smaller with the former model.

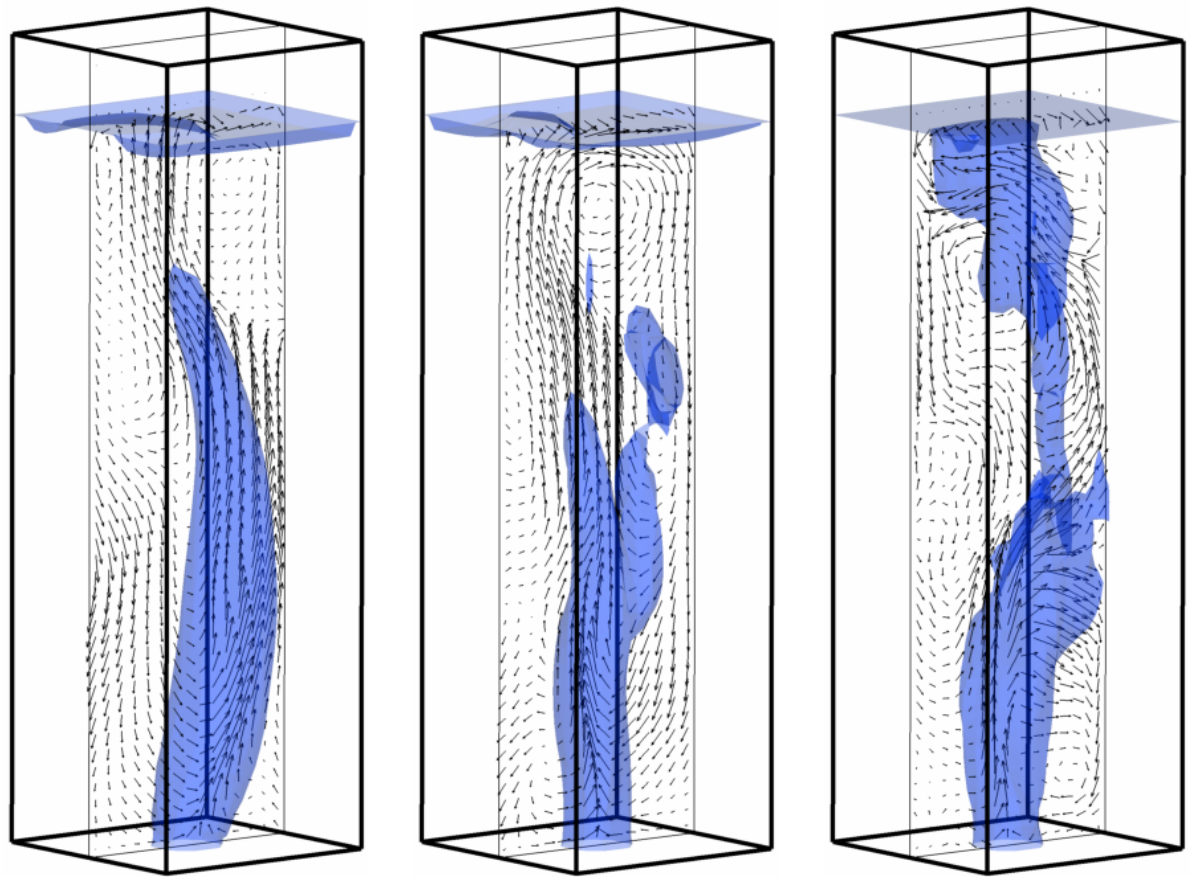

Figure 3.10: Snapshots of the instantaneous iso-surfaces of $\alpha_G = 0.05$ and liquid velocity fields for different cases after 200 s.

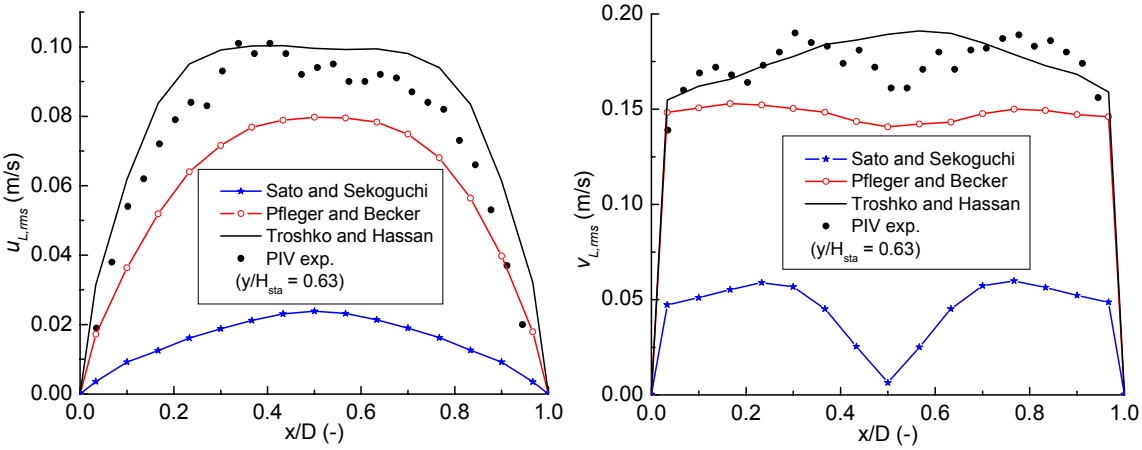

Figure 3.11: Time-averaged plot of the liquid phase velocity fluctuations in horizontal and vertical directions. Different bubble-induced turbulence models in the k-ε turbulence model are used. Sato and Sekoguchi refers to Case 1A3, Pfleger and Becker is 2A3 and Troshko and Hassan corresponds to 3A3.

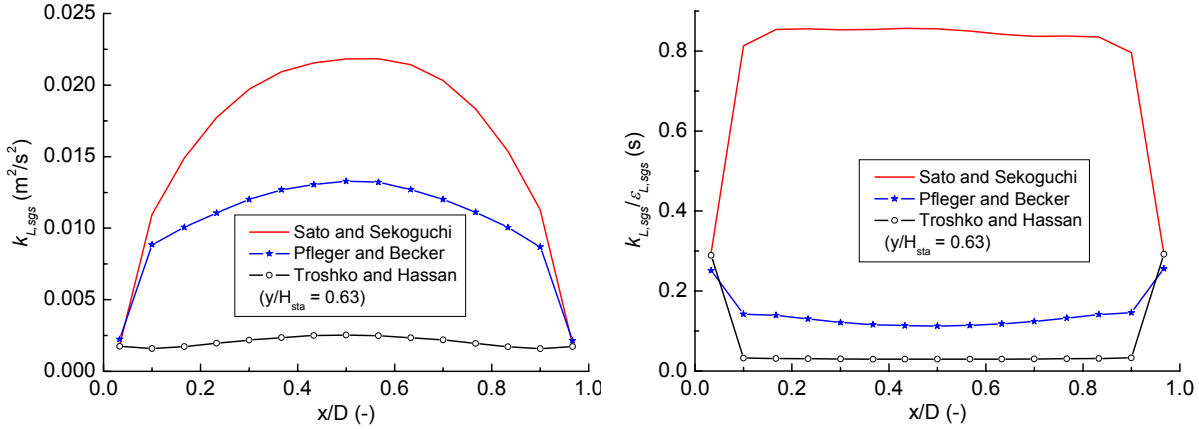

(a) (b)

Figure 3.12: Time-averaged liquid phase distributions of turbulent quantities with different bubble-induced turbulence models: (a) turbulent kinetic energy; (b) time scale of the shear-induced turbulence. Sato and Sekoguchi refers to Case 1A3, Pfleger and Becker is 2A3 and Troshko and Hassan corresponds to 3A3.

3.6.3 Liquid phase resolved and unresolved turbulence energy

Time-averaged liquid phase resolved (grid scale) and unresolved (sub-grid scale) turbulence energy distributions are provided in Figure 3.13. Apparently, much more details of the bubbly flow are implicitly contained in the sub-grid scale turbulence energy when Sato and Sekoguchi (1975) model is employed to account for the bubble-induced turbulence whereas most transient details of the bubbly flow can be resolved by the k-ε turbulence model when the bubble-induced turbulence model of Pfleger and Becker (2001) or Troshko and Hassan (2001) is employed. Furthermore, the SGS turbulence model well resolves the details of the gas-liquid bubbly flow. This again explains why in Figure 3.11, the simulated velocity fluctuations obtained with the k-ε turbulence model and Sato and Sekoguchi (1975) bubble-induced turbulence model are under-predicted in comparison with the measurements.

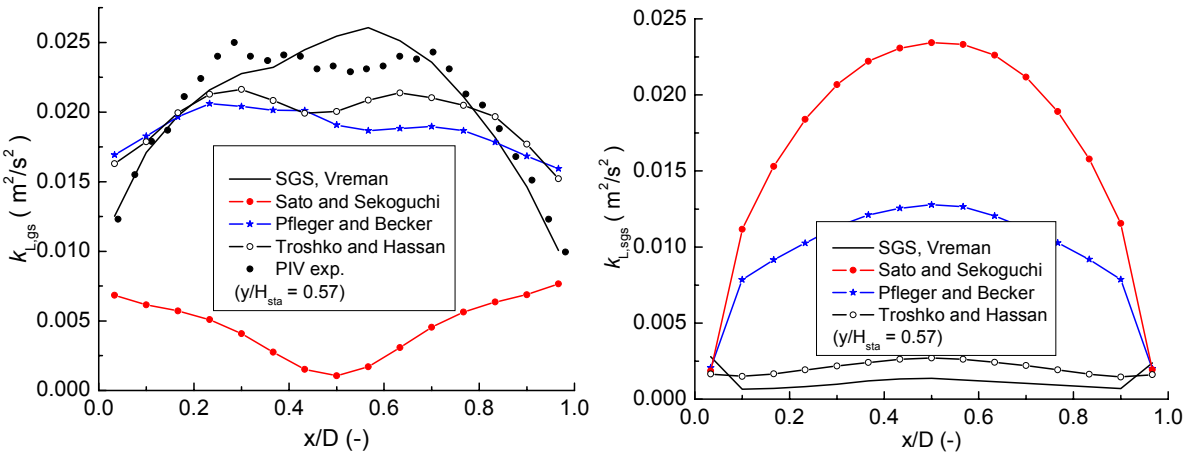

Figure 3.13: Time- averaged liquid phase turbulence energy distributions with different turbulence models: the SGS and k-ε model. (a) resolved (grid scale); (b) unresolved (sub-grid scale). SGS, Vreman is Case 0A3, Sato and Sekoguchi refers to Case 1A3, Pfleger and Becker is 2A3 and Troshko and Hassan corresponds to 3A3.

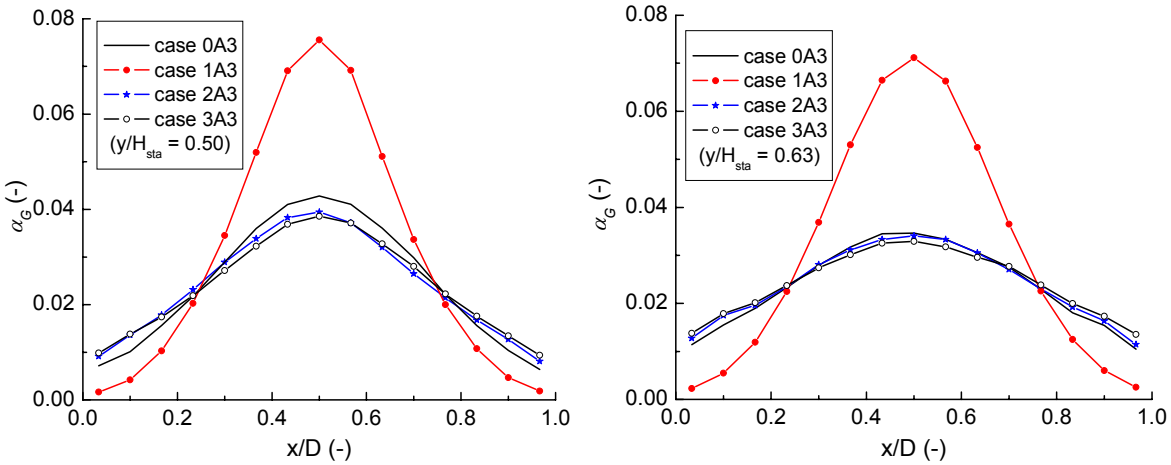

Figure 3.14: Time-averaged gas phase volume fraction distributions at two different heights with different turbulence models.

3.6.4 Time-averaged gas hold-up

Figure 3.14 displays the time-averaged gas hold-up distributions at two different heights. It is illustrated in this figure that the simulated time averaged gas hold-up profiles from Case 1A3 are steeper than those from the other cases. This is due to the over-estimation of the effective viscosity for this case as shown previously in Figure 3.9.

3.7 Conclusions

Numerical simulations of the gas-liquid two-phase flow in two squared-sectioned bubble columns were conducted with the use of the commercial software package CFX4.4. Sub-grid scale (SGS) and *k*-ε turbulence models were employed to evaluate the shear-induced turbulent viscosity in the liquid phase. The difference among three investigated bubble-induced turbulence models in the *k*-*ε* turbulence model was studied in detail.

It is seen that both SGS models suggested by Smagorinsky (1963) and Vreman (2004) perform well in the simulation of gas-liquid bubbly flow. Both SGS turbulence models not only produce good

solutions for the velocity field, they also resolve the transient details of the gas-liquid bubbly flow. The difference between the simulated results obtained from both SGS model is quite small. However, near the wall, the SGS model proposed by Vreman (2004) inherently dampens the shear-induced viscosity, whereas an unphysical high liquid phase effective viscosity profile is obtained from the model of Smagorinsky (1963). It is found that with increasing value of the sub-grid scale model constant C_S, the turbulent viscosity increases, and consequently the mean velocity profiles become steeper, as the bubble plume dynamics are reduced. From this study, it is shown that with a value of C_S = 0.08-0.10, numerical results agree well with the experimental data.

For the k-ε turbulence model different approaches were employed to assess the bubble-induced turbulence. The simulated liquid phase velocity fluctuations predicted with the models of Troshko and Hassan (2001) and Pfleger and Becker (2001) agree well with the measurements. The model of Sato and Sekoguchi (1975) leads to a considerably higher turbulent viscosity and only resolves the overall flow pattern. Most of the transient details of the bubbly flow are implicitly contained in the sub-grid scale turbulence kinetic energy, k_L. As a consequence, a quasi-steady bubble plume behaviour is predicted with this model. On the contrary, both the models of Pfleger and Becker (2001) and Troshko and Hassan (2001) can correctly reproduce dynamic bubble plume behaviour.

For the chosen operating conditions, according to Lopez de Bertodano (1992), the characteristic time scale of the bubble-induced turbulence is about 0.006 s for the studied column, which is much smaller than the time scale of shear-induced turbulences (≈ 0.8 s for the standard k-ε model). The BIT model of Troshko and Hassan produces a near wall peak profile of the liquid phase effective viscosity, which is not very realistic and further work is still needed to improve it.

Both the SGS and the k-ε turbulence models can produce good solution for the time-averaged vertical velocity. When extra source terms are added in the equations of k and ε, not only the resolved velocity fluctuations agree with the measurements, the predicted bubble plume is as dynamic as that obtained from the SGS model, and additionally the mean and fluctuating velocities are in good agreement with the experimental observations. Based on all comparisons and findings, it can be concluded that for the cases studied in this work the k-ε turbulence model extended with the bubble-induced turbulence model of Pfleger and Becker (2001) and the SGS model proposed by Vreman (2004) should be preferred for the simulation of bubbly flow.

3.8 Notation

B	model notation
C	model coefficient
D	bubble column depth, m
$Eö$	Eötvös number, = $(\rho_L-\rho_G)g\,d_B^2\,/\sigma$
H	bubble column height, m
$\mathbf{M}$	interfacial force vector
S	source terms
$\mathbf{S}$	strain tensor
W	bubble column width, m
X	Cartesian coordinate axis, x direction
Y	Cartesian coordinate axis, y direction
Z	Cartesian coordinate axis, z direction
a	horizontal dimension of an ellipsoidal bubble, m

b	vertical dimension of an ellipsoidal bubble, m
d	bubble diameter, m
n	time step number
p	pressure, N m^{-2}
k	turbulent kinetic energy, m^2 s^{-2}
$\boldsymbol{g}$	gravity acceleration, 9.81 m s^{-2}
t	time, s
$\mathbf{u}$	phase velocity, m s^{-1}

Greek letters

α	phase volume fraction, dimensionless
β	model notation
ε	turbulent dissipation rate m^2 s^{-3}
μ	viscosity, kg m^{-1} s^{-1}
ρ	density, kg m^{-3}
σ	interfacial tension, N m^{-1}
τ	characteristic time, s
τ	stress tensor, N s^{-1}
Δ	filter width, m

Indices

B	bubble
BIT	bubble induced turbulence
D	drag force
L	liquid phase, lift
Lam	laminar
G	gas phase
VM	virtual mass force
S	superficial velocity
S	SGS model constant
Sta	static liquid level
Tur	shear-induced turbulence
a	bubble swarm virtual mass correlation, type a
b	bubble swarm virtual mass correlation, type b
c	bubble swarm virtual mass correlation notation
eff	effective
h	horizontal direction
i	Cartesian coordinate index
k	phase notation
m	Cartesian coordinate index
max	maximum
rms	root of mean square
v	vertical direction

3.9 Bibliography

Becker, S., Sokolichin, A. and Eigenberger, G., 1994.Gas-liquid flow in bubble columns and loop reactors:Part II. Comparison of detailed experiments and flow simulations. *Chem. Eng. Sci.,* 49, 5747-5762.

Bel F'dhila, R. and Simonin, O., 1992. Eulerian predictions of a turbulent bubbly flow downstream a sudden pipe expansion. *Sixth Workshop on Two-Phase Flow Predictions, Erlangen, Germany, M. Sommerfeld, ed.,* 264.

Canuto, V. M. and Cheng, Y., 1997. Determination of the Smagorinsky-Lilly constant. *Phys. Fluids*, 9, 1368-1378.

Clift, R., Grace, J. R. and Weber, M. E., 1978. Bubbles, Drops and Particles. *Academic Press*. New York.

Deen, N, G., 2001. An experimental and computational study of fluid dynamics in gas-liquid chemical reactors. Ph.D thesis,Aalborg University, Esbjerg, Denmark.

Deen, N. G., Solberg, T., and Hjertager, B. H., 2001. Large eddy simulation of the Gas-Liquid flow in a square cross-sectioned bubble column. *Chem. Eng. Sci.*, 56, 6341-6349.

Delnoij, E., Kuipers, J. A. M. and Van Swaaij, W. P. M., 1997. dynamic simulation of gas-liquid two-phase flow: effect of column aspect ratio on the flow structure. *Chem. Eng. Sci.*, 52, 3759-3772.

Dijkhuizen, W., Van den Hengel, E.I.V., Deen, N.G., van Sint Annaland, M. and Kuipers, J. A. M., 2005. Numerical investigation of closures for interface forces acting on single air-bubbles in water using Volume of Fluid and Front Tracking models, *Chem. Eng. Sci.*, 60, 6169-6175.

Drew, D. A. and Passman, S. L., 1999. Theory of multicomponent fluids, Applied Mathematical Sciences 135, Springer.

Ervin, E. A. and Tryggvason, G., 1997. The rise of bubbles in a vertical shear flow, *J. Fluids Eng,* 119, 443-449.

Gosman, A. D., Issa, R. I., Lekakou, C., Looney, M. K. and Politis, S., 1992. Multidimensional modeling of turbulent two-phase flows in stirred vessels. AIChE J., 38, 1946-1955.

Ishii, M. and Zuber, N., 1979. Drag coefficient and relative velocity in bubbly, droplet or particulate flows. *AIChE J.,* 25, 843-855.

Kataoka I. and Serizawa, A., 1989. Basic equations of turbulence in gas-liquid two-phase flow. *Int. J. Multiphase Flow*, 15, 843-855.

Jakobsen, H.A., Sannæs, B. H., Grevskott, S. and Svendsen, H.F., 1997. Modeling of vertical bubble-driven flows. *Ind. Eng. Chem. Res*., 36, 4052-4074.

Lakehal, D., Smith, B. L. and Milelli, M., 2002. Large-eddy simulation of bubbly turbulent shear flows. *Journal of Turbulence*. 3, 1-21.

Lopez de Bertodano, M.A., 1992. Turbulent bubbly two-phase flow in a triangular duct, Ph.D dissertation, Rensselaer Polytechnic Institute.

Lopez de Bertodano, M.A., Lahey, R.T. and Jones, O.C., 1994. Development of a k-ε model for bubbly two-phase flow, *J. Fluids Eng.*, 116, 128-134.

Magnaudet, J. and Eames, I., 2000. The Motion of High-Reynolds Number Bubbles in inhomogeneous Flows. *Ann. Rev. Fluid Mech.*, 32, 659-708.

Mason, P. J., Callen, N. S., 1986. on the magnitude of the subgrid-scale eddy coefficient in large-eddy simulations of turbulent channel flow. *J. Fluid Mech.*, 162, 439-462.

Milelli M., Smith, B. L. and Lakehal D., 2001. Large-eddy simulation of turbulent shear flows laden with bubbles. *Direct and Large-Eddy Simulation IV*. Geurts, B. J., Friedrich R. and Metais O., 461–470, Amsterdam: Kluwer Acadmic.

Mudde, R. F. and Simonin, O., 1999. Two- and three dimensional simulations of a bubble plume using a two-fluid model. Chem. Eng. Sci., 54, 5061-5069.

Oey, R.S., Mudde, R.F., and Van Den Akker, H.E.A., 2003. Sensitivity study on interfacial closure laws in two-fluid bubbly flow simulations, *AIChE J.*, 49, 1621-1636.

Pan, Y., Dudukovic, M. P. and Chang, M., 1999. Dynamic simulation of bubbly flow in bubble columns. *Chem. Eng. Sci.*, 54, 2481-2489.

Pfleger, D. and Becker, S., 2001. Modeling and simulation of the dynamic flow behavior in a bubble column. *Chem. Eng. Sci.*, 56, 1737-1747.

Sato, Y. and Sekoguchi, K.,1975. Liquid velocity distribution in two-phase bubble flow. *Int. J. Multiphase Flow*, 2, 79-95.

Smagorinsky, J., 1963. General circulation experiments with the primitive equations. *Mon. Weather Rev.*, 91, 99-165.

Sokolichin, A. and Eigenberger, G., 1999. Applicability of the standard turbulence model to the dynamic simulation of bubble columns: Part I. Detailed numerical simulations. *Chem. Eng. Sci*., 52, 611-626.

Sokolichin, A., Eigenberger, G. and Lapin, A., 2005. Simulation of buoyancy driven bubbly flow: Established simplifications and open questions. *AIChE J.*, 50, 24-45.

Tomiyama, A., 2004. Drag, lift and virtual mass forces acting on a single bubble. 3rd International Symposium on Two-Phase Flow Modeling and Experimentation. Pisa, Italy. 22-24 Sept.

Troshko, A.A. and Hassan, Y.A., 2001. A two-equation turbulence model of turbulent bubbly flows. *Int. J. Multiphase Flow*, 27, 1965-2000.

Van Driest, E. R., 1956. On the Turbulent Flow Near a Wall, *J. Aeronaut. Sci.*, 23, 1007-1011.

Vreman, A. W., 2004. An eddy-viscosity subgrid-scale model for turbulent sher flow: Algebraic theory and applications. *Phys. Fluids*, 16, 3670-3681.

Zhang, D., 2005. Numerical simulation of dynamic flow behavior in a bubble column: grid and time-independent solution. *Technical report*. University of Twente, March.

Zhang, D., Deen, N. G., Kuipers, J. A. M., 2005. Numerical simulation of dynamic flow behavior in a bubble column: Comparison of the bubble-induced turbulence models in the k-ε model. Fourth International Conference on CFD in the Oil and Gas, Metallurgical & Process Industries. Trondheim, Norway. 6-8 June 2005.

Zhang, D., Deen, N. G., Kuipers, J. A. M., 2006. Numerical simulation of dynamic flow behavior in a bubble column: A study of closures for turbulence and interface forces. *Chem. Eng. Sci.*, 61, 7593-7608.

4

Three-fluid modeling of heterogeneous flow in a bubble column

Abstract

Numerical simulations of the small bubble-big bubble-liquid three-phase heterogeneous flow in a square cross-sectioned bubble column were carried out with the commercial CFD package CFX-4.4 to explore the effect of superficial velocity and inlet dispersed phase fractions on the flow patterns. The approach of Krishna et al. (2000) was adopted in the Euler-Euler framework to numerically simulate the gas-liquid heterogeneous flow in bubble columns. On basis of an earlier study (Zhang et al. 2005a), Both the SGS (Vreman, 2004) and the extended multiphase k-ε turbulence model (Pfleger and Becker, 2001) were chosen to model the turbulent viscosity in the liquid phase. The obtained results suggest that, first of all, the Sato and Sekoguchi (1975) model for bubble-induced turbulence is not suitable in simulation of gas-liquid heterogeneous flow due to high gas hold-up while the extended multiphase k-ε turbulence model of Pfleger and Becker (2001) is capable of capturing the dynamics of the heterogeneous flow. With increasing superficial velocity, the dynamics of the flow, as well as the total gas hold-up increases. It is observed that with increasing inlet phase fraction of the big bubbles, the total gas holdup decreases while the dynamic nature of the flow increases, which indicates that the small bubble phase mainly determines the total gas holdup while the big bubble phase predominantly agitates the liquid.

This chapter is based on: Zhang, Deen and Kuipers [2006]

4.1 Introduction

Bubble column reactors are widely used in chemical, petrochemical and biochemical processes. Proper understanding of the fluid dynamics is essential to arrive at an optimum design and operation of such processes. Experimental investigations and numerical simulations are widely used to gain more knowledge and detailed physical understanding of complex gas-liquid flow processes.

Bubble columns can be operated in several regimes: at low superficial velocities, the bubbly flow or homogeneous flow regime prevails. In this regime, small, spherical and equally sized gas bubbles are distributed more or less uniformly over the columns' cross section. At higher superficial velocities, a transition to the heterogeneous flow regime can be observed. In this flow regime, a wide range of

bubble diameters develops as a result of break-up and coalescence, thus leading to an inherently dynamic flow that is dominated by the larger bubbles. At even higher superficial velocities, the gas bubbles grow so large that they occupy the whole width of the column, resulting in an alternating passage of liquid phase and gas phase through the column, this regime is called the slug flow regime. In this study, only the heterogeneous flow regime will be considered.

In the heterogeneous flow regime, the large bubbles rise through the column at high velocities (in the range of 1-2 m/s) while the bubble size ranges from 20 to 70 mm (Krishna and Ellenberger, 1996). Two strategies have been used in the literature to model the heterogeneous flow regime: one approach is to model the gas-liquid flow with a multiple-size group (MUSIG) model (Lo, 1996), in which both the coalescence and breakup are accounted for by dedicated models. A major and critical assumption in the MUSIG model is that the different bubble size groups possess the same slip velocity. Another approach is according to Krishna et al. (1996, 2000), Tomiyama (2002) and Sun et al. (2003), in which the gas phase is divided into two or more classes of bubbles. Each class of bubbles represents a distinct phase that interacts with the liquid. Interaction between bubbles and coalescence and breakup are not accounted for. In the work of Krishna et al.(2000) and Sun et al. (2003), the bubbles are categorized into two groups: spherical/distorted bubbles belong to small bubble group and cap/slug/churn-turbulent bubbles belong to large bubble group. The latter model sounds more promising and physical meaningful, it is therefore adopted in this work. A schematic representation of the small bubble-big bubble-liquid heterogeneous flow is given in Figure 4.1.

Turbulence modeling is one of the main unresolved problems in the simulation of gas-liquid two-phase flow. In the numerical simulation of the gas–liquid two-phase flow, zero equation turbulence models (Pan et al., 1999), the k-ε model (Becker et al., 1994; Pfleger and Becker, 2001) and sub-grid scale (SGS) models (Deen et al., 2001; Milelli et al., 2001; Lakehal et al., 2002) were extensively used. Through a thorough study of the k-ε and sub-grid scale (SGS) models used in the simulation of bubbly flow, Deen (2001) found that good agreement was obtained with the k-ε model in the simulation of the Becker case (Becker et al., 1994). Furthermore, in the simulation of a three-dimensional bubble column, the SGS model produces a better solution as was presented earlier in

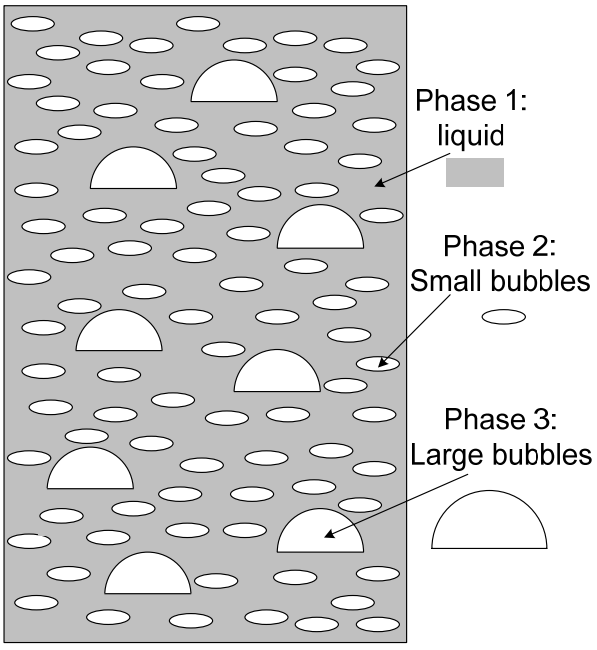

Figure 4.1: Flow picture of heterogeneous gas-liquid flow in a bubble column.

Chapter 3, it was observed that in the numerical simulation of gas–liquid two-phase flow, the results obtained from the extended multiphase k-ε turbulence model of Pfleger and Becker (2001) differ slightly from those obtained with the SGS turbulence model (Vreman, 2004) and both of them agree well with experimental data. Therefore, in this study, both the extended multiphase k-ε turbulence model used by Pfleger and Becker (2001) and SGS turbulence model proposed by Vreman (2004) are employed to evaluate the shear-induced turbulence in the liquid phase.

In a preliminary numerical study of gas (small bubble)-gas (big bubble)-liquid three phases flow, we found that when the model proposed by Sato and Sekoguchi (1975) was employed to account for the bubble induced turbulence in combination with the SGS turbulence model, a very stable flow pattern was obtained, which contradicts experimental observations.

A correct description of the closures for drag, lift and virtual mass forces is of great importance in numerical simulation of bubbly flows. At high gas hold-ups (i.e., α_G >10%), it is desirable to introduce the effects of the gas hold-up on the interfacial force closures. In the work of Ishii and Zuber (1979), the derived expressions of the swarm bubble drag coefficient were formulated as the drag coefficient of individual bubbles multiplied with a phase fraction correction for each of the three flow regimes. This approach is similar to the corrections found in the work of Behzadi, Issa and Rusche (2004). Only Beyerlein et al. (1985) and Behzadi, Issa and Rusche (2004) investigated the influence of the gas hold-up on the lift coefficient. Based on our previous studies (Zhang, 2005b), it is found that in the simulation of bubbly flow at high superficial velocity, the swarm bubble drag coefficient according to Ishii and Zuber (1979) and the bubble swarm lift coefficient proposed by Behzadi et al. (2004) are preferable. So, these two corrections were adopted as well in this work.

This chapter presents Euler-Euler three-dimensional dynamic simulations of small bubble-big bubble-liquid heterogeneous flow in a square cross-sectioned bubble column. The primary purpose of this study is to investigate the applicability of the two approaches (Pfleger and Becker,2001 and Sato and Sekoguchi, 1975) to account for the bubble-induced turbulence in the numerical simulation of small bubble–big bubble–liquid three-phase heterogeneous flow. Furthermore, the performance of the interfacial closure correlations studied in Chapter 2 is also explored. Based on the suitability bubble-induced turbulence model and interfacial closures, the effect of superficial velocity and the inlet phase fraction of the big bubbles on the flow field are studied.

4.2 Governing equations

The equations of the Euler-Euler formulation of the multiphase flow are derived by ensemble averaging the local instantaneous equations of single-phase flow (Drew, 1999). A set of balance equations for mass and momentum are obtained for each of the phases. Ignoring the interfacial mass transfer, the generic conservation equations for mass and momentum respectively take the following form:

$$\frac{\partial(\alpha_k \rho_k)}{\partial t} + \nabla \cdot (\alpha_k \rho_k \mathbf{u}_k) = 0 \tag{4.1}$$

$$\frac{\partial(\alpha_k \rho_k \mathbf{u}_k)}{\partial t} + \nabla \cdot (\alpha_k \rho_k \mathbf{u}_k \mathbf{u}_k + \alpha_k \tau_k) = \alpha_k \rho_k \mathbf{g} - \alpha_k \nabla p_k + \mathbf{M}_k \tag{4.2}$$

where the indices k refers to the phase (L for liquid, SB for small bubbles and BB for big bubbles). The volume fraction of each phase is denoted by α and $\mathbf{u}$ = (u, v, w) is the velocity vector of phase k.

τ_k represents the stress tensor of phase k and will be discussed later. $\mathbf{M}_k$ represents the inter-phase momentum exchange between phase k and all other phases. In this study, only the drag, lift and virtual mass forces are accounted for. For each phase, the inter-phase momentum exchange term, $\mathbf{M}_k$, is represented as follows:

$$\mathbf{M}_L = -\sum_{k\in(SB,BB)} \mathbf{M}_k \tag{4.3}$$

$$\mathbf{M}_k = \mathbf{M}_{k,D} + \mathbf{M}_{k,L} + \mathbf{M}_{k,VM} \qquad \forall k \in (SB, BB) \tag{4.4}$$

The forces are respectively calculated from the following expressions:

$$\mathbf{M}_{k,D} = -\frac{3}{4}\alpha_k \rho_L \frac{C_{D,k}}{d_{B,k}} |\mathbf{u}_k - \mathbf{u}_L| (\mathbf{u}_k - \mathbf{u}_L) \qquad \forall k \in (SB, BB) \tag{4.5}$$

$$\mathbf{M}_{k,L} = -\alpha_k \rho_L C_{L,k} (\mathbf{u}_k - \mathbf{u}_L) \times \nabla \times \mathbf{u}_L \qquad \forall k \in (SB, BB) \tag{4.6}$$

$$\mathbf{M}_{k,VM} = -\alpha_k \rho_L \mathbf{C}_{VM,k} \cdot \left(\frac{D_k \mathbf{u}_k}{Dt} - \frac{D_L \mathbf{u}_L}{Dt}\right) \qquad \forall k \in (SB, BB) \tag{4.7}$$

According to Tomiyama (2004), the virtual mass coefficient vector $\mathbf{C}_{VM}$ takes the form ($C_{VM,h}$, $C_{VM,v}$, $C_{VM,h}$).

In this study, the interfacial force closure models of Tomiyama (2004) were employed for the individual force closures. The bubble aspect ratio was taken from front tracking results of Dijkhuizen et al. (2005). Detailed information on the applied closures can be found in Chapter 2. At high gas volume fractions, bubbles can no longer be considered as isolated and therefore, it is desirable to account for the effect of the volume fraction on the interfacial closures. The available corrections are listed in Table 2.1. In this work we apply the drag corrections suggested by Ishii and Zuber (1979). It is noted that due to the differences in size and shape, different corrections are applied for the two size classes. Unfortunately very little is known on the volume fraction correction for the lift force. The model applied here is inspired by the work of Behzadi et al. (2004), who derived an expression for small bubbles. From the work of Tomiyama (2004) it is known that the lift coefficient of large bubbles changes sign. For this reason, we apply the relation of Behzadi et al. (2004), however, with a different sigh. Finally the lift coefficient was limited to ±0.5 at low gas volume fractions. Figure 4.2 presents the how the drag coefficients of small and big bubbles changes with the local gas hold-up. Unfortunately, when the original corrections suggested by Ishii and Zuber (1979) were used in the simulation of small bubble–big bubble–liquid three-phase heterogeneous flow at a high superficial velocity (V_{sup} = 7.0 cm/s), it introduces some numerical convergence problems. That is, the small bubble phase mainly accounts for the total gas hold-up and its drag coefficient correction factor is $(\alpha_L)^{-0.5}$. So with increasing gas hold-up, C_D increases, yielding a higher gas hold-up, etc. This leads to divergence, and produces numerical problems. Hence, it was decided to introduce a cut-off, that is, the applicable range of the total gas hold-up correction should have an upper limit. After several numerical experiments, it was found that $\alpha_{G,max}$ = 0.30 is suitable and no numerical problems were experienced, so it is adopted in the remaining part of this work. Figure 4.3 illustrates how the lift coefficients of small and big bubbles vary with respect of the gas phase volume fraction (α_G).

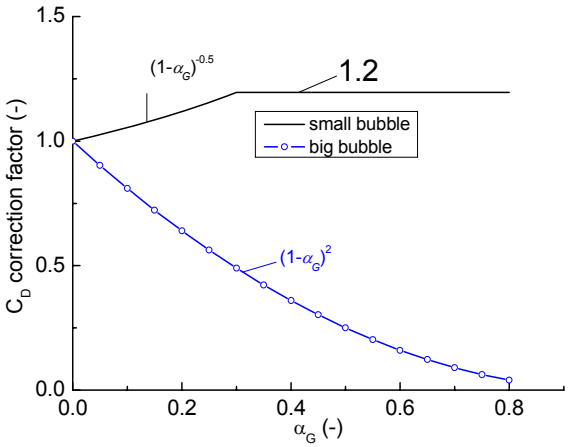

Figure 4.2: Correction factor of drag coefficient of small and big bubbles as a function of local voidage.

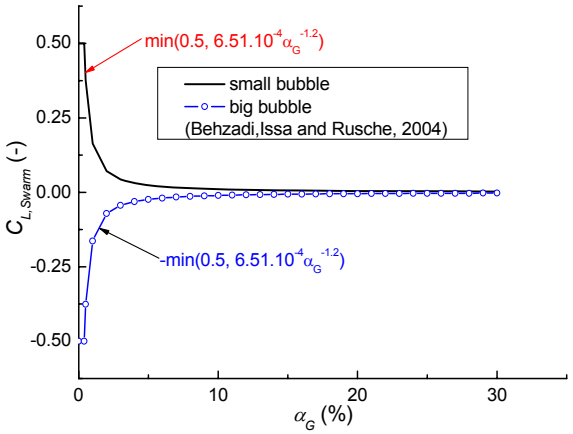

Figure 4.3: Variation of the lift coefficients of small and big bubbles with the local gas hold-up.

For phase k, the stress tensor, $\boldsymbol{\tau}_k$ is given by:

$$\tau_k = -\mu_{eff}(\nabla \mathbf{u}_k + (\nabla \mathbf{u}_k)^T - \frac{2}{3} I \nabla \cdot \mathbf{u}_k) \tag{4.8}$$

where the liquid phase effective viscosity, $\mu_{L,eff}$ is composed of three contributions: the molecular viscosity $\mu_{L,Lam}$, the shear-induced turbulent viscosity $\mu_{L,Tur}$ and an extra term due to bubble-induced turbulence μ_{BIT}:

$$\mu_{L,eff} = \mu_{L,Lam} + \mu_{L,Tur} + \mu_{BIT} \tag{4.9}$$

As stated in Chapter 3, sometimes, the bubble-induced turbulence is accounted for through including extra source terms in the turbulent models. In that case, the liquid phase effective viscosity ,$\mu_{L,eff}$ consists of the molecular viscosity $\mu_{L,Lam}$ and the shear-induced turbulent viscosity $\mu_{L,Tur}$:

$$\mu_{L,eff} = \mu_{L,Lam} + \mu_{L,Tur} \tag{4.10}$$

Following Jakobsen et al. (1997), the effective viscosity of the dispersed gas phases are calculated as follows:

$$\mu_{k,eff} = \frac{\rho_k}{\rho_L} \mu_{L,eff} \qquad \forall k \in (SB, BB) \tag{4.11}$$

When the SGS model suggested by Vreman (2004) is adopted, the liquid phase shear-induced turbulent viscosity is calculated as:

$$\mu_{L,Tur} = 2.5 \rho C_S^2 \sqrt{\frac{B_\beta}{S_{ij} S_{ij}}} \tag{4.12}$$

where $S_{ij} = \partial u_j / \partial x_i$, $\beta_{ij} = \Delta_m^2 S_{mi} S_{mj}$ and $B_\beta = \beta_{11}\beta_{22} - \beta_{12}^2 + \beta_{11}\beta_{33} - \beta_{13}^2 + \beta_{22}\beta_{33} - \beta_{23}^2$. Δ_i is the filter width in i direction. $\Delta = (\Delta_i \Delta_j \Delta_k)^{1/3}$ is the filter width. C_S is a model constant, which takes a value of 0.1 as concluded in Chapter 3.

When a SGS model is used, the model proposed by Sato and Sekoguchi (1975) is applied to account for the bubble-induced turbulence in Eq. 4.9:

$$\mu_{BIT} = \rho_L \alpha_G C_{\mu,BIT} d_B |\mathbf{u}_G - \mathbf{u}_L| \tag{4.13}$$

where $C_{\mu,BIT}$ is a model constant that is set to 0.6.

When the k- ε turbulence model is employed, the gas phase influences the turbulence in the liquid phase by a bubble-induced turbulence model. The shear-induced turbulent viscosity of the liquid phase is calculated by:

$$\mu_{L,Tur} = C_\mu \rho_L \frac{{k_L}^2}{\varepsilon_L} \tag{4.14}$$

The conservation equations for k and ε are respectively given by:

$$\frac{\partial(\alpha_L \rho_L k_L)}{\partial t} + \nabla \cdot (\alpha_L \rho_L \mathbf{u}_L k_L - \alpha_L (\mu_{L,Lam} + \frac{\mu_{L,Tur}}{\sigma_k}) \nabla k_L) = \alpha_L (G_L - \rho_L \varepsilon_L) + S_{k,BIT} \tag{4.15}$$

$$\begin{aligned} \frac{\partial(\alpha_L \rho_L \varepsilon_L)}{\partial t} + \nabla \cdot (\alpha_L \rho_L \mathbf{u}_L \varepsilon_L - \alpha_L (\mu_{L,Lam} + \frac{\mu_{L,Tur}}{\sigma_\varepsilon}) \nabla \varepsilon_L) \\ = \alpha_L \frac{\varepsilon_L}{k_L} (C_{\varepsilon 1} G_L - C_{\varepsilon 2} \rho_L \varepsilon_L) + S_{\varepsilon,BIT} \end{aligned} \tag{4.16}$$

The bubble-induced turbulence is implicitly accounted for through the source terms $S_{k,BIT}$ in Eq. 4.15 and $S_{\varepsilon,BIT}$ in Eq. 4.16. These terms are calculated from:

$$S_{k,BIT} = \alpha_L C_k \sum_{h \in (SB,BB)} |\mathbf{M}_h| |\mathbf{u}_h - \mathbf{u}_L| \tag{4.17}$$

$$S_{\varepsilon,BIT} = \frac{\varepsilon_L}{k_L} C_\varepsilon S_{k,BIT} \tag{4.18}$$

with C_k = $C_{\varepsilon 1}$ = 1.44, C_ε = $C_{\varepsilon 2}$ = 1.92, C_μ = 0.09, σ_k = 1.0 and σ_ε = 1.217. It is noted that these constants are not universal, even in the case of single-phase flow. For multiphase flows they are still under debate.

Note that ε_L/k_L represents the time scale for the dissipation of the bubble-induced turbulence.

4.3 Numerical solution method

All the numerical simulations are carried out with the commercial CFD package CFX-4.4 of AEA Technology, Harwell, UK. The total domain is subdivided into uniform computational grid cells with

$\Delta x = \Delta y = \Delta z = 0.01$ m. The governing equations are solved in a transient fashion with a time step of 0.0025 s. It is found in the previous work (Zhang, 2005c) that good space and time resolutions are obtained with the above grid size and time step. The curvature compensated convective transport (CCCT) scheme is used for the discretization of all convective terms. Standard boundary conditions employing wall functions are used for k and ε. No-slip conditions were used for all three phases along the walls as it was observed in Chapter 2 that numerical results obtained from the free slip wall boundary condition for the dispersed phase hardly differ with those obtained from the no slip wall boundary conditions.

As stated in Chapter 2, the difference between the so-called "Pressure" and "Opening" boundary condition at the outlet is very small in predicting hydrodynamics of the gas-liquid flow. Because the "Opening" boundary condition requires more computational effort, a "Pressure" boundary condition is used for all the test cases in the current chapter.

4.4 Physical problem

A schematic representation of the bubble column geometry studied in this work is shown in Figure 4.2. Air is used as the dispersed gas phase and homogeneously injected into quiescent water through the entire bottom plane of the column. The superficial gas velocity was varied from 4.5 to 7.0 cm/s. Water is used as the continuous liquid phase and initially fills the column to a height of 0.90 m. The dispersed phase is assumed to consist of small and big bubbles as illustrated in Figure 4.1. The small bubbles have an equivalent diameter of 4 mm and are ellipsoidal in shape. The big bubbles fall into the spherical cap regime and the equivalent diameter is set to 20 mm. Break-up and coalescence are not accounted for and it is assumed that there is no direct interaction between the small and large bubbles. The column has the following dimensions: width (W) 0.15 m, depth (D) 0.15 m and height (H) 0.90 m. All the simulation parameters and physical properties are presented in Tables 4.1 and 4.2.

Table 4.1: Interfacial closures and fluid physical peroperties.

Parameters		Interfacial closures set	
		Closure set A	Closure set B
Small bubble	drag coefficient, $C_{D,SB}$	1.071	$1.071(1-\alpha_G)^{-0.5}$
	lift coefficient, $C_{L,SB}$	0.5	$\min(0.5, 6.51\times10^{-4}\alpha_G^{-1.2})$
	virtual mass coefficient, $\mathbf{C}_{VM,SB}$	(0.25, 1.53, 0.25)	(0.25, 1.53, 0.25)
Big bubble	drag coefficient, $C_{D,BB}$	8/3.	$8(1-\alpha_G)^2/3$
	lift coefficient, $C_{L,BB}$	-0.5	$-\min(0.5, 6.51\times10^{-4}\alpha_G^{-1.2})$
	virtual mass coefficient, $\mathbf{C}_{VM,BB}$	(0.35, 1.12, 0.35)	(0.35, 1.12, 0.35)
$d_{B,BB} = 20$ mm, $d_{B,SB} = 4$ mm. $\mu_{L,Lam} = 0.001$ kg/(m.s), $\mu_{G,Lam} = 1.812\times10^{-5}$ kg/(m.s), $\rho_L = 1000$ kg/m^3, $\rho_G = 1.29$ kg/m^3, $\sigma = 0.073$ N/m.			

Table 4.2: Simulation and case parameters.

Case	$\mu_{L,Tur}$	μ_{BIT}	Interfacial closures	V_{Sup} (cm/s)	$\alpha_{BB,in}$
S1	SGS	Sato and Sekoguchi (1975)	Closure set A	4.5	0.3
1	k-ε	Pfleger and Becker (2001)	Closure set A	4.5	0.3
2	k-ε	Pfleger and Becker (2001)	Closure set B	4.5	0.3
3	k-ε	Pfleger and Becker (2001)	Closure set B	7.0	0.3
4	k-ε	Pfleger and Becker (2001)	Closure set B	7.0	0.1
$\alpha_{SB,in} = 1\text{-}\alpha_{BB,in}$, $V_{SB,in} = V_{Sup}$, $V_{BB,in} = V_{Sup}$					

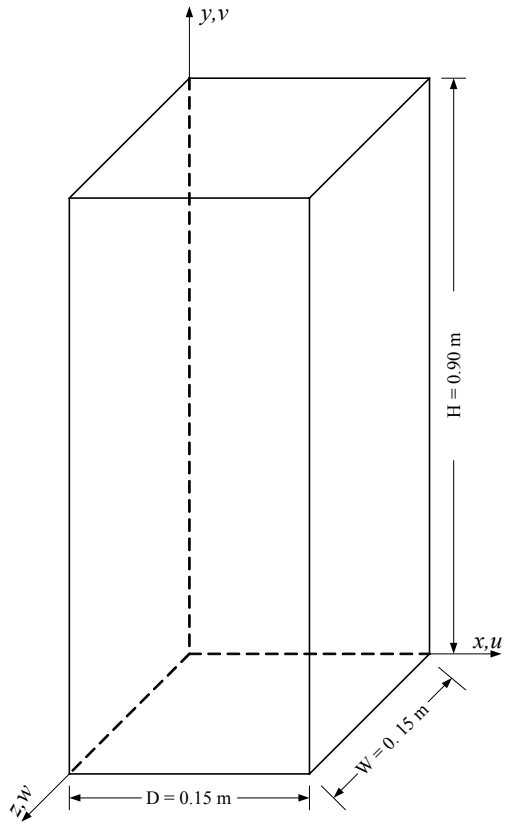

Figure 4.2: Schematic representation of the investigated bubble columns.

4.5 Data processing

In order to get statistical results, the time-averaged quantities are calculated as defined in the following expressions. The time-averaged mean velocity is calculated as:

$$\overline{u}_n = \frac{n-n_0-1}{n-n_0}\overline{u}_{n-1} + \frac{1}{n-n_0}u_n \tag{4.19}$$

where the averaging is started at time step n_0 = 7500, corresponding to 18.75 s. All simulations were carried out for n = 200000 corresponding to a period of 500 s.

The large-scale velocity fluctuations are calculated during the calculation as follows:

$$\overline{u^2_{rms,n}} = \overline{u^2_n} - \overline{u}^2_n \tag{4.20}$$

All the presented quantitative results are time-averaged quantities, which are selected in a plane at a width of $z/W = 0.50$.

4.6 Results and Discussion

In Chapter 3, it was found that both the bubble-induced turbulence model of Sato and Sekoguchi (1975) along with the SGS turbulence model proposed by Vreman (2004), and the extended k-ε turbulence model proposed by Pfleger and Becker (2001), work well for numerical simulation of gas-liquid flow. The first aim of this chapter is to investigate the feasibility and applicability of these two bubble-induced turbulence models for the simulation of gas-gas-liquid "three-phase flow" in the commercial software package CFX4.4. Case S1, S2 and 1 listed in Table 4.2 were implemented in CFX-4.4. Then, the influence of the interfacial coefficient corrections is studied. Finally, the effects of the superficial velocity and inlet big bubble volume fraction on the flow are investigated.

4.6.1 Bubble-induced turbulence model of Sato and Sekoguchi

Case S1 was employed (see Tables 4.1 and 4.2 for all relevant simulation settings) to investigate the applicability and performance of Sato and Sekoguchi (1975) model for bubble-induced turbulence in simulation of gas-liquid heterogeneous flow. The SGS turbulence model was used to model the shear-induced turbulence in the liquid phase. Figure 4.4 shows the time-averaged vertical velocity profiles for the liquid and the small bubble phase. It is found that the predicted the flow field in the column is almost stationary. The obtained stationary flow field does not agree with the experimental observation as the flow regime is heterogeneous. This is mainly caused by the high effective viscosity in the liquid phase as observed in Figure 4.5. In the simulations, it is found that $\alpha_{SB} \approx 0.15$, $\alpha_{BB} \approx 0.05$, $V_{slip,SB} \approx 0.20$ m/s, $V_{slip,BB} \approx 0.28$ m/s, $d_{SB} = 0.004$ m and $d_{BB} = 0.02$ m. Employing Eq. 4.13, it is easily obtained that, $\mu_{BIT,SB} \approx 0.08$ *kg*/(m.s) and $\mu_{BIT,BB} \approx 0.16$ *kg*/(m.s). Consequently, the total bubble-induced turbulent viscosity is about 0.24 kg/(m.s), which is so high that it effectively dampens all fluctuations. As linearly with the gas fraction, such behavior can be expected for all heterogeneous flows, implying that the Sato model is not suited for this flow regime.

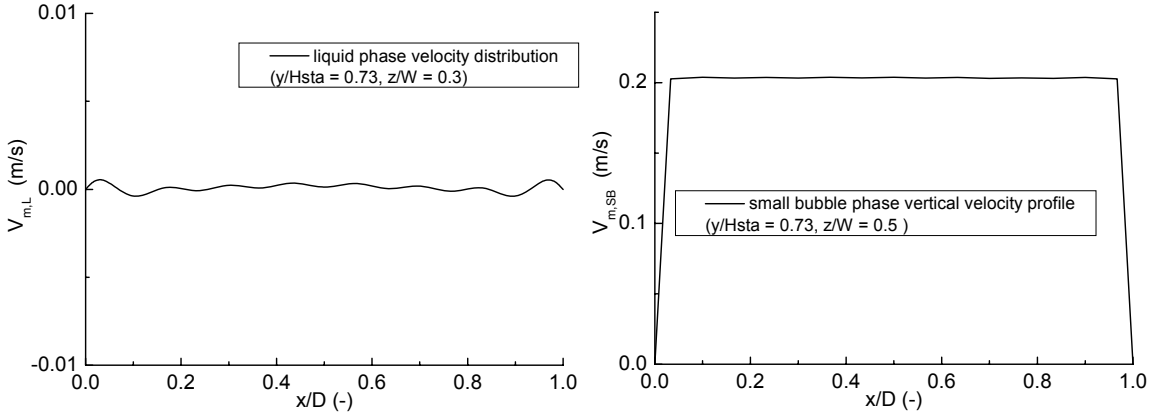

Figure 4.4: Time averaged vertical velocity profiles of liquid (a) and small bubble (b) phase. Different interfacial closures were employed.

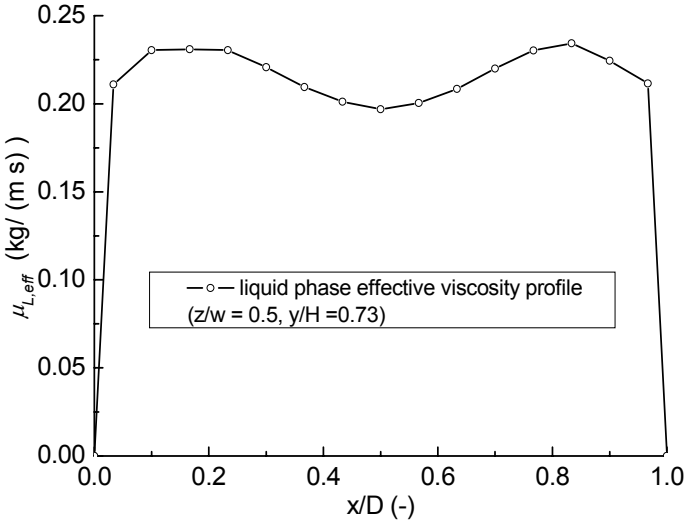

Figure 4.5: Time-averaged liquid phase effective viscosity obtained from different interfacial closures; SGS turbulence model was used.

Due to the high superficial velocity and local gas volume fraction, it is desirable to account for the bubble-induced turbulence in a different manner. To this end, the extended k-ε model is used, which will be discussed in the next section.

4.6.2 Numerical simulation of three-phase flow with k-ε turbulence model

The performance of the extended k-ε model to describe heterogeneous flows is tested in cases 1 and 2 (see Table 4.2). Figure 4.7 shows the instantaneous velocity profiles for all three phases at two different heights for each of the cases. Clearly, it is observed here that the predicted gas-gas-liquid three phase flow pattern is dynamic. In case 2, the influence of gas holdup on the interfacial coefficients (C_D, C_L,$\mathbf{C}_{VM}$) is taken into account leading to a more dynamic solution. When the individual bubble interfacial coefficients are used, the flow is dynamic only in the bottom part of the column. The remainder of the column turns out to be stable, whereas in Case 2, the liquid phase velocity varies throughout the column with most of the liquid phase down flow prevailing near the wall. Figure 4.8 gives the time-averaged velocity fluctuation profiles of the liquid phase in both horizontal and vertical directions. The velocity fluctuations of the liquid phase are very small, which is caused by two factors: first of all, as the entire bottom plane is used as the inlet sparger, a homogeneous flow pattern is obtained; the other reason is that due to the high gas hold-up, bubbles have limited space to rise. Consequently, the liquid agitation is less pronounced. The vertical velocity profiles of the small and big bubbles are presented in Figure 4.9. It can be clearly seen that when the gas hold-up correction is accounted for in the interfacial coefficients, both bubble phases travel up faster near the column centre.

In the remainder of this chapter we will focus on exploring the effects of the superficial velocity and inlet volume fraction on fluid flow patterns (Cases 3 and 4 respectively in Table 4.2). First of all, the effect of the superficial velocity on the flow field was studied, where the gas hold-up corrections were accounted for in the interfacial closures. As expected, the total gas hold-up increases with increasing superficial velocity, which is illustrated in Figure 4.10. Furthermore, it was found that the small bubble phase mainly accounts for the total gas hold-up. This is caused by its lower slip velocity. Figure 4.11 compares the time-averaged vertical velocity profiles of the two dispersed phases. It is

found that the vertical velocity of both dispersed phases possesses a parabolic distribution across the column, which indicates that all bubbles rise faster in the column center. However, as the superficial velocity increases, the total gas phase volume fraction increases. In such a case, the drag coefficient of the small bubble phase increases. Subsequently, the vertical velocity of small bubble phases drops. For the big bubble phase, the drag coefficient drops dramatically with increasing local gas hold-up. Hence, its vertical velocity increases.

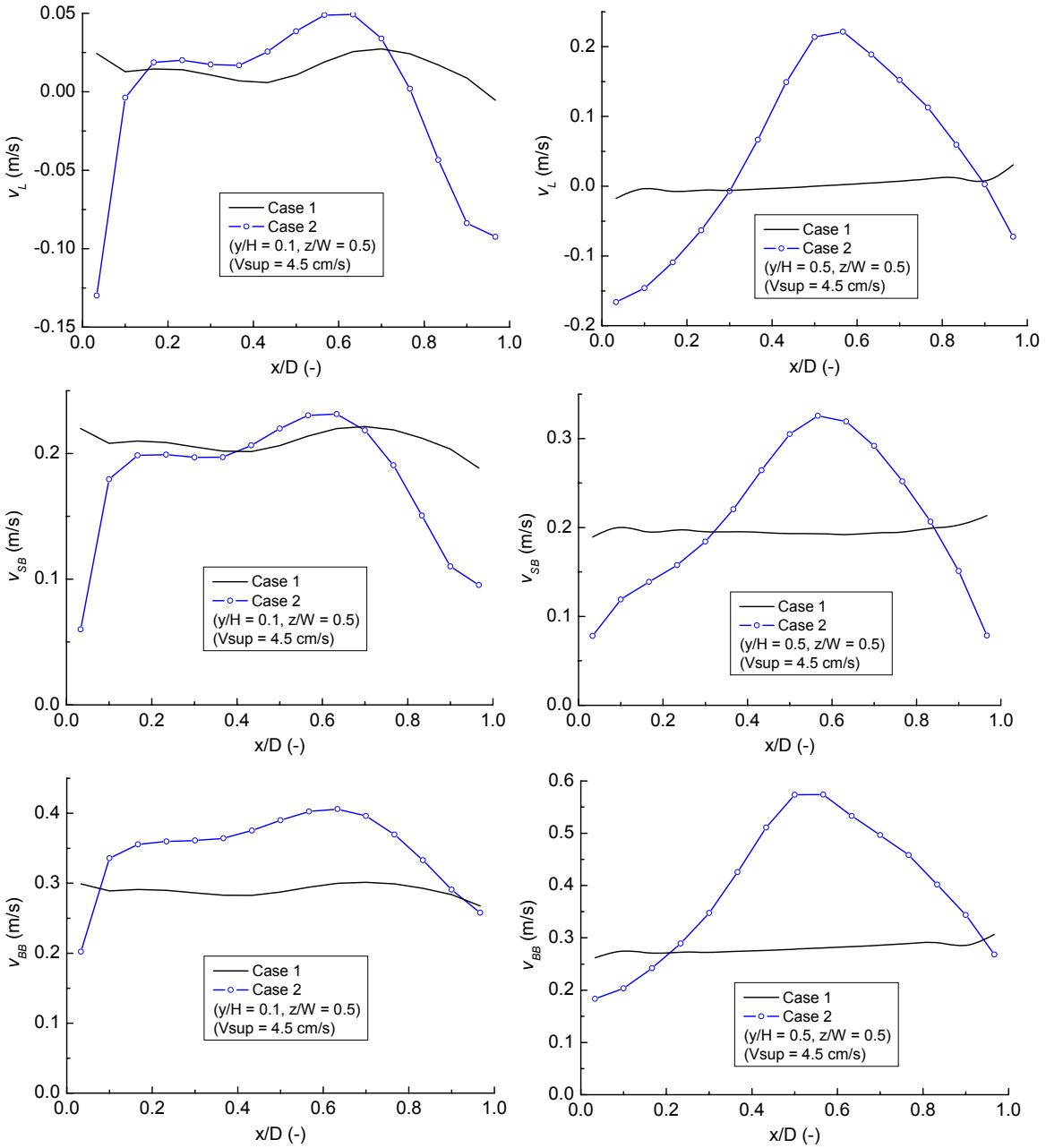

Figure 4.7: Instantaneous velocity profiles for liquid (top), small bubble (middle) and big bubble (bottom) phases at different heights at time = 100 s. Different interfacial coefficients were used in the simulations.

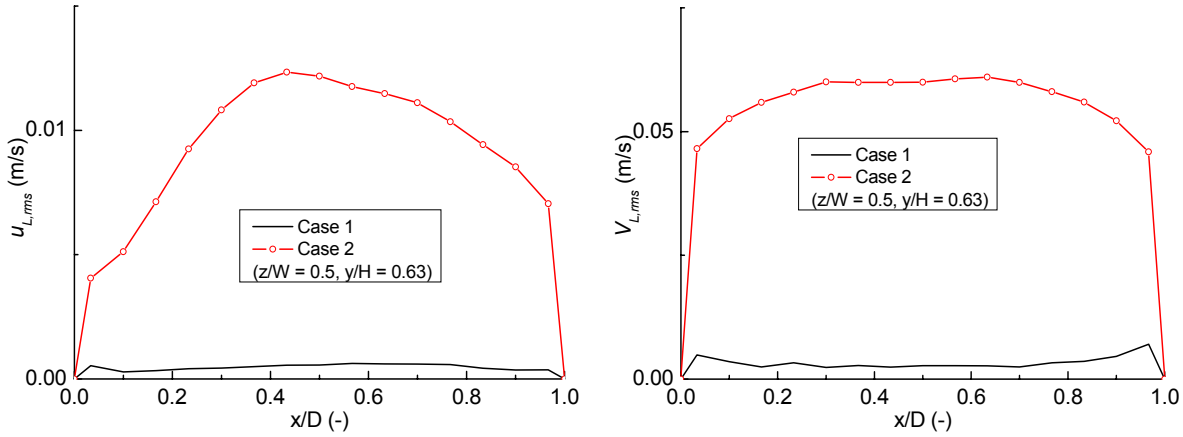

Figure 4.8: Comparison of the velocity fluctuations of the liquid phase obtained from different interfacial closures. The *k-ε* turbulence model is employed in the simulations.

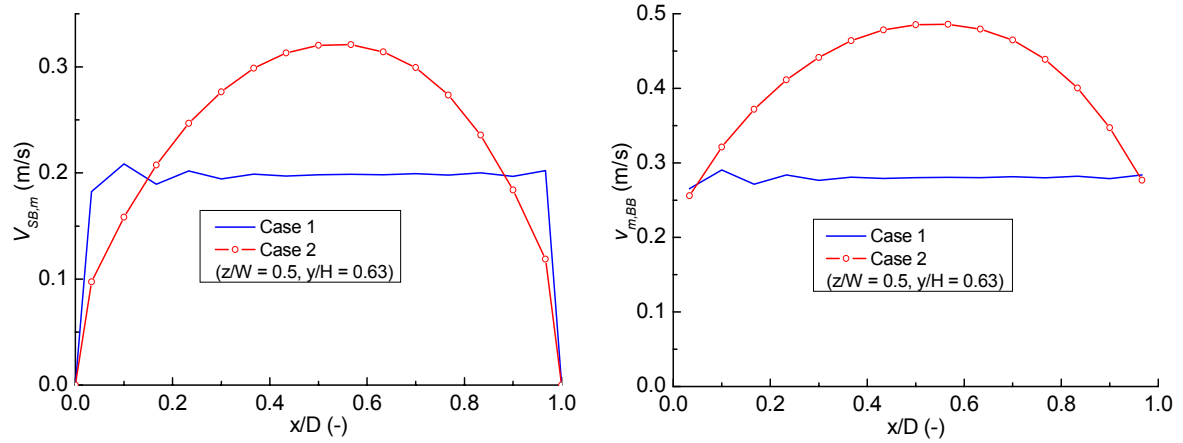

(a) (b)

Figure 4.9: Comparison of the mean dispersed phases' vertical velocity obtained from different interfacial coefficients: (a): small bubble phase; (b): big bubble phase. The *k-ε* turbulence model is employed in the simulations.

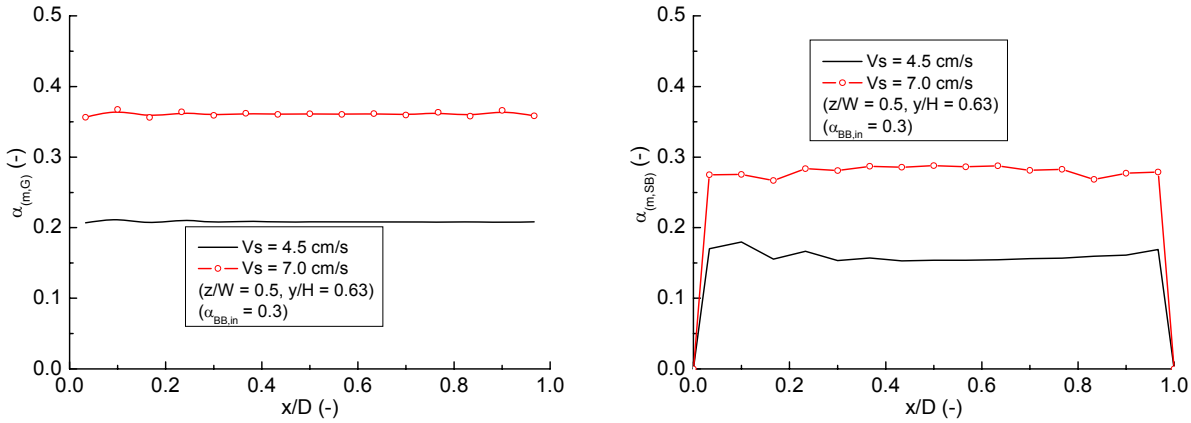

(a) (b)

Figure 4.10: Comparison of the mean phase volume fraction obtained from different superficial velocities: (a): total gas phase volume fraction; (b): small bubble phase volume fraction.

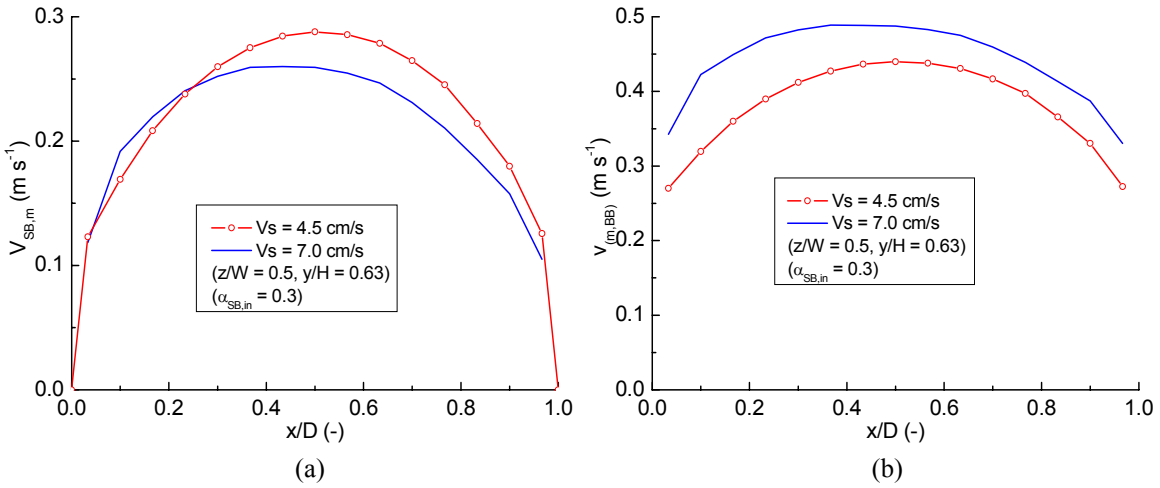

Figure 4.11: Comparison of the mean dispersed phases' vertical velocity obtained from different superficial velocities; (a): small bubble phase; (b): big bubble phase. The corresponding cases are Case 1 and 3.

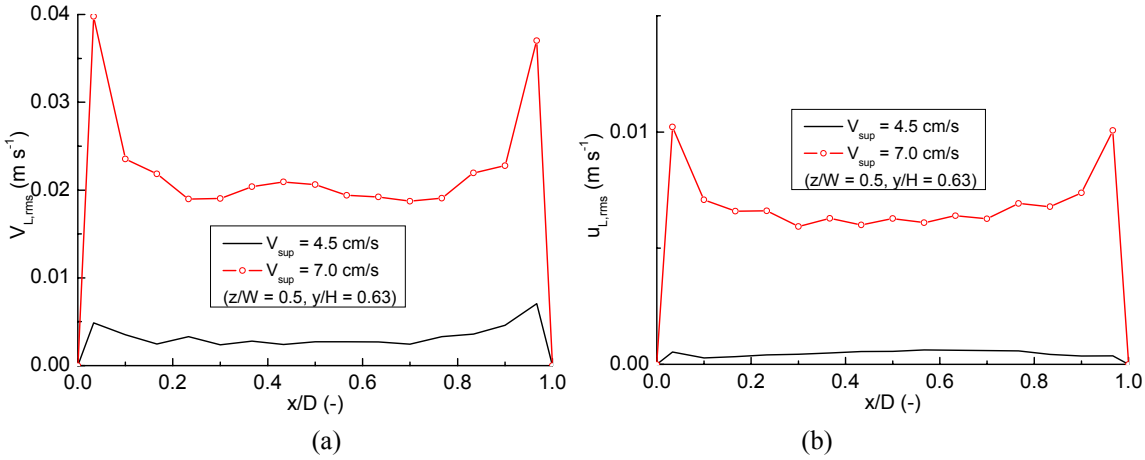

Figure 4.12: Comparison of the time-average liquid phase velocity fluctuations in vertical and horizontal directions. Different superficial velocities were used: (a): vertical direction; (b): horizontal direction.

Figure 4.12 provides the comparison of the liquid phase velocity fluctuations in vertical and horizontal directions for both superficial gas velocities. Clearly, it can be concluded that the dynamics of the flow increases with increasing of the superficial velocity.

Cases 3 and 4 were employed to investigate the influence of the big bubble phase on the flow field. As shown in Figure 4.13, it is observed that only at high inlet volume fraction of the big bubbles, the vertical velocity profiles of both the small and big bubble phase become parabolic. Consequently, as can be seen in Figure 4.14a, much higher liquid phase circulation is obtained. Furthermore, it is seen that the liquid phase velocity fluctuations increase with increasing big bubble phase inlet volume fraction. Thus it can be concluded from Figure 4.13 and 4.14 that the big bubble phase tends to predominantly agitate the liquid phase.

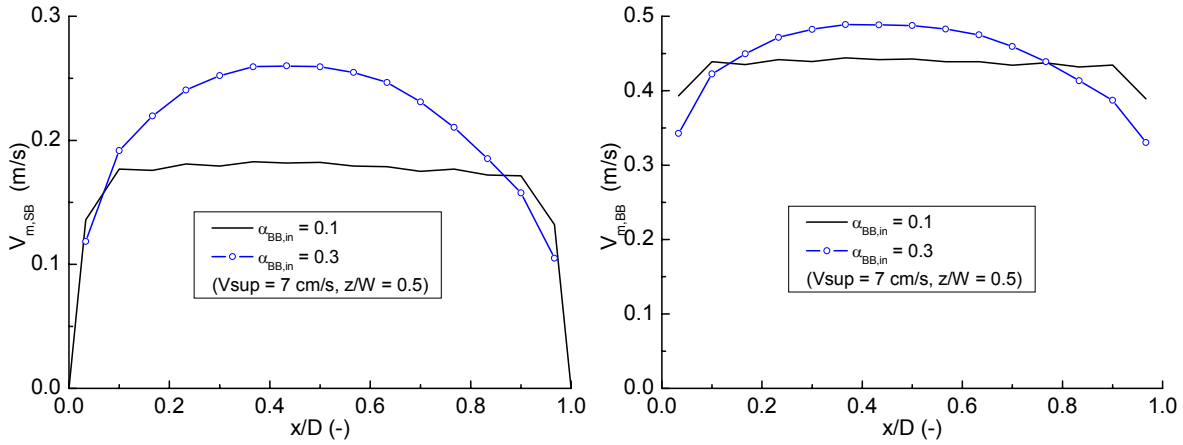

Figure 4.13: Comparison of the vertical velocities of both bubble phases. Here different inlet volume fractions of the big bubbles are used. Test cases 3 and 4 are employed here. See Table 4.2.

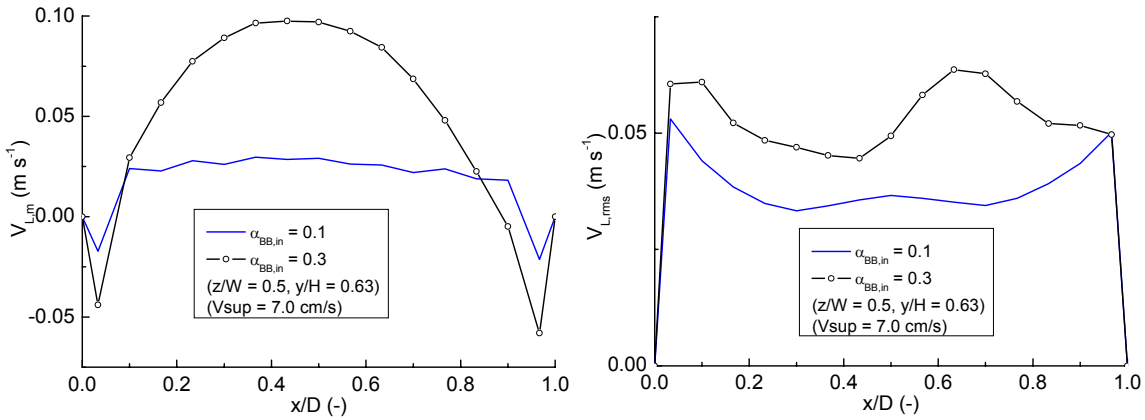

(a) (b)

Figure 4.14: Comparison of the time-averaged liquid phase velocity (a) and velocity fluctuations (b) in vertical direction obtained from simulations with different inlet phase fractions of the big bubbles. The corresponding cases are Case 3 and 4.

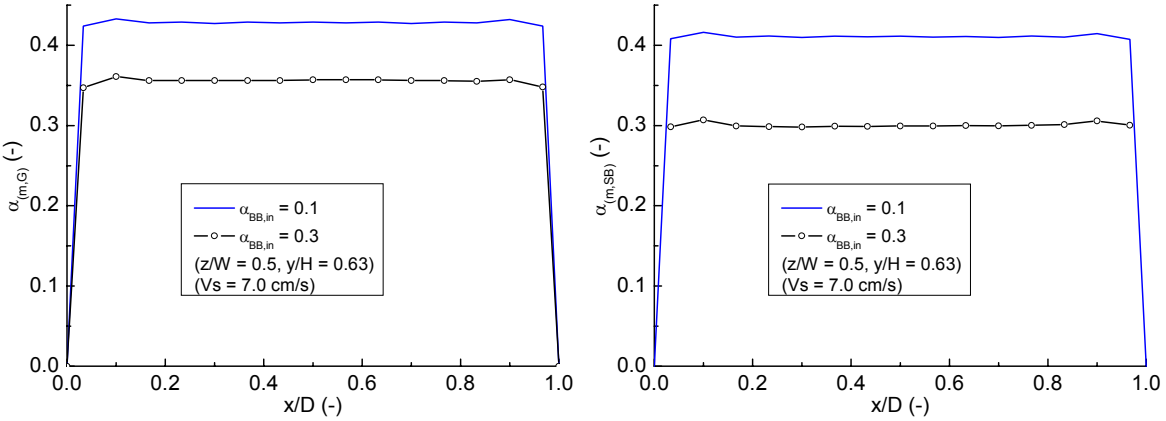

(a) (b)

Figure 4.15: Comparison of the mean phase volume fraction obtained from simulations with different inlet phase fraction of the big bubbles. Test Cases 3 and 4 are shown: (a): total gas phase volume fraction and (b): small bubble phase volume fraction.

Figure 4.15 shows a comparison of the total gas holdup and small bubble phase volume fraction obtained from the simulations with different inlet volume fractions of the big bubbles. It can be deduced from Figure 4.15 that the small bubble phase mainly accounts for the total gas hold-up (more than 85% for both cases).

4.7 Conclusions

Numerical simulations of the gas-gas-liquid three-phase (small bubble-big bubble-liquid) flow in a square cross-sectioned bubble column were carried out with the use of the commercial software package CFX-4.4. The three-phase approach of Krishna et al. (2000) was used in the Euler-Euler frame to numerically simulate the gas-liquid heterogeneous flow in the bubble columns. Both a SGS model (Vreman, 2004) and an extended multiphase k-ε turbulence model (Pfleger and Becker, 2001) were adopted to model the shear-induced turbulent viscosity in the liquid phase. When the gas holdup is accounted for in the interfacial coefficients, it is suggested to introduce a cut-off for the small bubble drag correction at α_g = 30%. The slip velocity of the big bubbles dramatically increases with the gas holdup when the interfacial coefficients are corrected with the local total gas holdup. The obtained results suggest that, first of all, when the bubble-induced turbulence model of Sato and Sekoguchi (1975) is used to account for the bubble-induced turbulent viscosity, an unphysical stationary solution is produced due to high effective viscosity in the liquid phase. It appears that the extended multiphase k-ε turbulence model used by Pfleger and Becker (2001) in gas-liquid flow is better suited for the numerical study of small bubble-big bubble-liquid three-phase flow. A more dynamic solution can be obtained when the correction for the total gas hold-up is accounted for in the interfacial coefficients. The interfacial force corrections have hardly any influence on the total gas hold-up when the superficial velocity is high (V_{sup} > 4.5 cm/s). It is also found that with increasing of the superficial velocity, the total gas hold-up as well as the dynamics of the flow increases. Furthermore, it is observed that, the total gas holdup decreases when the inlet fraction of the big bubble increases, while the flow dynamics increases. It is the small bubble phase that mainly accounts for the total gas holdup, while the big bubble phase mainly is responsible for the agitation of the liquid phase. The small bubble phase mainly accounts for the total gas hold-up, not only because of its high inlet volume fraction, but also due to its lower slip velocity. As this work merely presents first results of the applied gas-gas-liquid model, further validation and incorporation of breakup and coalescence models are still needed.

4.8 Notation

B	model notation
C	model coefficient
D	bubble column depth, m
E	bubble aspect ration
$Eö$	Eötvös number, = $(\rho_L$-$\rho_G)g\,d_B^2\ /\sigma$
Eo_d	modified Eötvös number, = $Eö\ /E^{2/3}$
H	bubble column height, m
M	interfacial force vector
S	source terms
W	bubble column width, m
X	Cartesian coordinate axis, x direction

Y	Cartesian coordinate axis, y direction
Z	Cartesian coordinate axis, z direction
a	horizontal dimension of an ellipsoidal bubble, m
b	vertical dimension of an ellipsoidal bubble, m
d	bubble diameter, m
n	time step number
p	pressure, N m^{-2}
k	turbulent kinetic energy, m^2 s^{-2}
$\boldsymbol{g}$	gravity acceleration, 9.81 m s^{-2}
S	strain tensor
t	time, s
$\mathbf{u}$	phase velocity, m s^{-1}

Greek letters

α	phase volume fraction, dimensionless
β	model notation
ε	turbulent dissipation rate m^2 s^{-3}
μ	viscosity, kg m^{-1} s^{-1}
ρ	density, kg m^{-3}
σ	interfacial tension, N m^{-1}
σ	model constant
τ	characteristic time, s
τ	stress tensor, N s^{-1}
Δ	filter width, m

Indices

B	bubble
BB	big bubble
BIT	bubble induced turbulence
D	drag force
L	liquid phase, lift
Lam	laminar
G	gas phase
VM	virtual mass force
S	superficial velocity
S	SGS model constant
SB	small bubble
Sta	static liquid level
Swa	bubble swarm
Tur	shear-induced turbulence
a	bubble swarm virtual mass correlation, type a
b	bubble swarm virtual mass correlation, type b
c	bubble swarm virtual mass correlation notation
eff	effective
h	horizontal direction
h	phase notation

i	Cartesian coordinate index
k	phase notation
k	model constant
m	Cartesian coordinate index
max	maximum
rms	root of mean square
v	vertical direction

4.9 Bibliography

Becker, S., Sokolichin, A., Eigenberger, G., 1994.Gas-liquid flow in bubble columns and loop reactors: Part II. Comparison of detailed experiments and flow simulations. *Chem. Eng. Sci.,* 49, 5747-5762.

Behzadi, A, Issa, R. I. and Rusche, H., 2004. Modeling of dispersed bubble and droplet flow at high phase fractions. *Chem. Eng. Sci*, 59: 759-770.

Beyerlein, S. W., Cossmann, R. K. and Richter, H., 1985. Prediction of bubble concentration profiles in vertical turbulent two-phase flow. *Int. J. Multiphase Flow*, 11, 629-641.

Deen, N, G., 2001. An experimental and computational study of fluid dynamics in gas-liquid chemical reactors. Ph.D thesis, Aalborg University, Esbjerg, Denmark.

Dijkhuizen, W., van Sint Annaland, M. and Kuipers, J. A. M., 2005. Numerical investigation of closures for interface forces acting on single air-bubbles in water using Volume of Fluid and Front Tracking models. Trondheim, Norway. 6-8 June.

Drew, D. A. and Passman, S. L., 1999. Theory of multicomponent fluids, Applied Mathematical Sciences 135, Springer.

Ishii, M. and Zuber, N., 1979. Drag coefficient and relative velocity in bubbly, droplet or particulate flows. *AIChE J.,* 25, 843-855.

Jakobsen, H.A., Sannæs, B. H., Grevskott, S. and Svendsen, H.F., 1997. Modeling of vertical bubble-driven flows. *Ind. Eng. Chem. Res*., 36, 4052-4074.

Krishna, R. and Ellenberger, J., 1996. Gas hold-up in bubble column reactors operating in the churn-turbulent flow regime. *AIChE J.*, 42, 2627-2634.

Krishna, R., van Baten, J.M. and Urseanu, M.I., 2000. Three-phase Eulerian simulations of bubble column reactors operating in the churn-turbulent flow regime: A scale up strategy. *Chem. Eng. Sci.*, 55, 3275-3286.

Lakehal, D., Smith, B. L. and Milelli, M., 2002. Large-eddy simulation of bubbly turbulent shear flows. *Journal of Turbulence*. 3, 1-21.

Lo, S., 1996. Application of Population Balance to CFD Modelling of Bubbly Flow via the MUSIG model, AEA Technology, *AEAT-1096*.

Milelli M., Smith, B. L. and Lakehal D., 2001. Large-eddy simulation of turbulent shear flows laden with bubbles. *Direct and Large-Eddy Simulation IV*. Geurts, B. J., Friedrich R. and Metais O., 461–470, Amsterdam: Kluwer Acadmic.

Pan, Y., Dudukovic, M. P. and Chang, M., 1999. Dynamic simulation of bubbly flow in bubble columns. *Chem. Eng. Sci.*, 54, 2481-2489.

Pfleger, D, Becker, S., 2001. Modeling and simulation of the dynamic flow behavior in a bubble column. *Chem. Eng. Sci*, 56: 1737-1747.

Sato, Y. and Sekoguchi, K., 1975. Liquid velocity distribution in two-phase bubble flow. *Int. J. Multiphase Flow*, 2, 79-95.

Sun, X., Ishii, M. and Kelly, J. M., 2003. Modified two-fluid model for the two-group interfacial area transport equation. Annals of Nuclear Energy, 30, 1601–1622.

Tomiyama, A., 2002. Some Attempts for the Improvement of Computational Bubble Dynamics. *Proc. 10th Workshop on Two-Phase Flow Predictions*, Merseburg, Germany, April 9-12, 2002, 125-136.

Tomiyama, A., 2004. Drag, lift and virtual mass forces acting on a single bubble. 3rd International Symposium on Two-Phase Flow Modeling and Experimentation. Pisa, Italy. 22-24 Sept. 2004.

Zhang, D., 2005(a). Numerical simulation of dynamic flow behavior in a bubble column: study of two SGS turbulence models and the effect of bubble aspect ratios. *Technical report*. University of Twente, October.

Zhang, D., 2005(b). Numerical simulation of dynamic flow behavior in a bubble column: Numerical simulation of bubbly flows with high superficial velocity. *Technical report*. University of Twente, October.

Zhang, D., 2005(c). Numerical simulation of dynamic flow behavior in a bubble column: grid and time- independent solution. *Technical report*. University of Twente, March.

Zhang, D., Deen, N. G., Kuipers, J. A. M., 2005. Numerical simulation of the dynamic flow behaviour in a bubble column: comparison of the bubble-induced turbulence models in k-ε model. CFD 2005 - fourth International Conference on Computational Fluid Dynamics in the Oil and Gas, Metallurgical and Process Industries, Trondheim, Norway.

5

Numerical modeling of flow, mass transfer and chemical reaction in bubble columns

Abstract

Physical and chemical absorption of pure and dilute CO_2 bubbles in water and aqueous sodium hydroxide (NaOH) solution has been studied in a squared-sectioned bubble column using the commercial software package CFX-4.4. The sub-grid scale (SGS) turbulence model of Vreman (2004) was employed to evaluate the shear-induced turbulent viscosity in the liquid phase. An "Opening" boundary condition was applied at the outlet, whereas the previously studied interfacial coefficients (Zhang et al., 2006) were used in the simulations. The dependence of the overall mass transfer coefficient on the bubble diameter as well as the decrease of the bubble size under a given condition were theoretically analyzed. Subsequently, physical absorption of pure CO_2 in water and chemisorption of pure and dilute CO_2 bubbles in aqueous NaOH solution were numerically studied.

It is found that the overall mass transfer coefficient does not change much with the bubble diameter in the range of 2 to 4 mm, and provided that the pH value of the alkaline solution is lower than 12, the bubble diameter decreases approximately linearly with time. During their rise in the column, the bubble diameter reduces from 4 to 2 mm, which is still acceptable for assuming a constant mass transfer coefficient.

When pure CO_2 is absorbed into water or aqueous NaOH solution, the "Pressure" boundary condition at the outlet is not suitable, since this boundary condition allows CO_2 gas or chemical species in the liquid to enter the column from the outlet. The "Opening" boundary condition is preferred in case of physical or chemical absorption of CO_2, because it does not suffer from these problems.

When pure CO_2 is absorbed into water, the hydrodynamics is similar to the case without mass transfer. High aqueous CO_2 concentrations are found around the bubble plume. After the bubble plume arrives at the free surface, the aqueous CO_2 is transported from the top part of the column to the bottom along the walls due to the down flow of the liquid phase.

When pure CO_2 is absorbed into aqueous NaOH solution with an initial pH value of 12, initially, the local pH value drops sharply in a short period and accordingly carbonate is produced rapidly. Subsequently the local hydroxyl concentration decreased slowly due to the chemical reaction. Finally, the local hydroxyl concentration decreases in an oscillatory manner, which depends on the chemical reaction rate and the convective mixing.

In case dilute CO_2 gas is used in the chemisorption process, the local pH value drops slower compared with pure CO_2 gas, whereas the flow structure and hydrodynamics are similar to the chemisorption of pure CO_2 into aqueous NaOH solution.

All the numerical results are only qualitatively presented, a more detailed comparison of the E-E results with the available E-L simulated results or experimental data is still needed.

This chapter is based on: Zhang, Deen and Kuipers [2007]

5.1 Introduction

Bubble column reactors are widely used in chemical, petrochemical and biological processes. Many processes involve gas-liquid mass transfer with accompanying reactions between the gas and the liquid phase itself or with components dissolved or suspended in it. Despite the widespread application of bubble columns and intensive research efforts devoted to understand their complex behaviour, detailed knowledge on the fluid flow, mass transfer and chemical reactions as well as their interactions is currently very limited.

Experimental investigation and numerical simulations are widely used to study and analyze gas-liquid flow processes. In the last two decades, two approaches were frequently used to simulate the flow in bubble columns: the Euler-Euler model (E-E) (Becker et al., 1994; Deen et al., 2001) and Euler-Lagrange model (E-L) (Delnoij et al., 1997,1999; Darmana et al. 2005). The E-L model, solves the flow field of the liquid phase in an Eulerian way and computes the motion of each individual bubble from the Newtonian equations of motion, which makes it possible to directly consider the bubble-bubble and bubble-liquid interactions. Consequently, it is more suited for fundamental investigations of the bubbly flow. The E-E method, describes the motion of both phases through the volume-averaged or ensemble averaged mass and momentum conservation equations. Bubble-liquid interaction is accounted for through the interfacial exchange terms whereas the number of bubbles that are present in a computational cell is represented by the volume fraction. Detailed information of the bubble size distribution can only be obtained by solving additional population balance equations which account for the breakage and coalescence of bubbles as well as the growth or shrinkage of bubbles due to mass transfer. Figure 5.1 schematically shows how the two models account for the bubble shrinkage due to physical absorption or chemisorption. In the Euler-Lagrange approach bubble shrinkage can be monitored for each individual bubble, while accounting for the properties of the individual bubbles. In the Euler-Euler approach, the information of individual bubbles is lost in the averaging of the equations. As a constant bubble size is assumed at the level of the computational cell, gas-liquid mass transfer leads to a decrease in gas volume fraction, and, due to the constant bubble size, a decrease in the number of bubbles. Clearly this leads to a rather crude approximation. This implies that a standard Euler-Euler model, in the absence of population balance models, may only be applied if the mass transfer rate is relatively low or, more precisely, in case the change in the bubble size is small.

Though it is easier to track the bubble size change in the E-L model, due to its high computational effort and memory requirements, it is less suited to study gas-liquid flow in large-scale bubble columns or at high gas hold-up. In this study, the E-E model is adopted to investigate mass transfer in bubbly flows.

When a chemical reaction is considered in a gas-liquid system, the interactions between the prevailing processes are very complex as schematically depicted in Figure 5.2: the chemical reaction rate depends on the local concentration of the species, which is determined by the inter-phase mass transfer process and the mixing induced by the dispersed bubbles. The interphase mass transfer rate depends on the mass transfer coefficient, the specific interfacial area and chemical reaction rate;

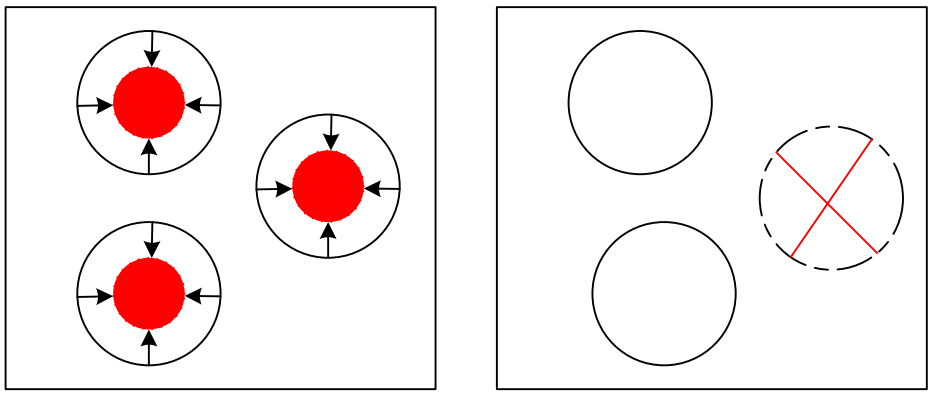

(a) reality (E-L) (b) E- E model

Figure 5.1: Treatment of bubble shrinkage due to mass transfer.

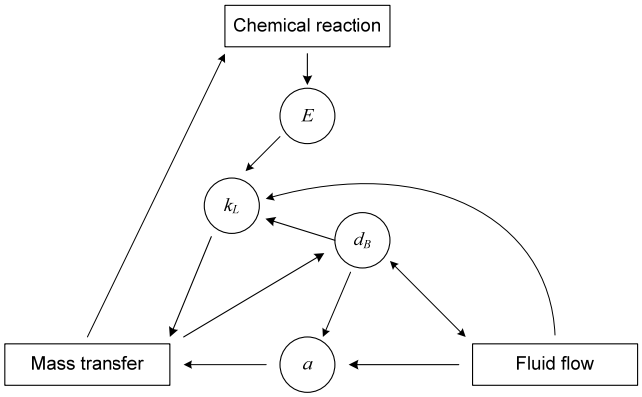

Figure 5.2: Schematic representation of inter-dependency of fluid flow, mass transfer and chemical reaction.

meanwhile the mass transfer coefficient is a function of the local hydrodynamics, which itself is influenced by the bubble shrinkage due to physical or chemical absorption and variation of physical properties due to the inhomogeneous distributions of the chemical species. These complex interactions make the overall prediction of the performance and scale-up of this kind of reactor very difficult. Most numerical studies of gas-liquid flow (Mudde and Simonin, 1999) are devoted to the simulation of the hydrodynamics and improving the closures required by the model to achieve a better prediction of the hydrodynamics.

Due to the complexity of gas-liquid systems, some researchers have simplified the modeling in the E-E approach to steady state conditions or adopted one-dimensional or two-dimensional models (Fleischer et al., 1996; Márquez et al., 1999a, b); the so-called hybrid method is used as well to solve these kinds of problems, in which CFD is employed only for the simulation of hydrodynamics, and the chemical reactions are accounted for by a custom-build compartment models (Bauer and Eigenberger, 1999, 2001; Rigopoulos and Jones, 2003). Though the model of Fleischer et al. (1996) is capable to qualitatively predict the transient behaviour of a chemisorption process in a slender bubble column, many authors (Becker et al., 1994; Delnoij et al., 1997, 1999; Deen et al., 2001; Darmana et al., 2005) found that bubble columns inherently exhibit unsteady three-dimensional flow characteristics. In the so-called hybrid model, the interactions between hydrodynamics, mass transfer, chemical reactions is decoupled, each sub-problem is solved with a separate model, and consequently, the interaction among hydrodynamics, mass transfer and chemical reaction process are not necessarily accounted for. Furthermore, the influence of the mass transfer and chemical reaction on the

hydrodynamics is not accounted for and due to limitations to represent a change in bubble size the predictive capabilities will be limited.

As the chemisorption of CO_2 into aqueous NaOH solution exhibits all important phenomena encountered in practice while its reaction mechanism is well understood and the reaction kinetics are well established, it is chosen as the test case for this work. In order to avoid the problem arising from the constant mean bubble size assumption, the bubble diameter is limited to vary in a range of 2 to 4 mm, in which the drag coefficient is almost constant according to the well-known drag closures.

Due to the inherent drawback of the E-E model in simulating gas-liquid flows with mass transfer, i.e. bubble size change or distribution is not directly provided, the back feeding of the chemical reaction on the mass transfer is not accounted for at this stage in the E-E model. In order to make the numerical study physically meaningful, it is essential to know the dependence of the overall mass transfer coefficient on the bubble size.

When the initial pH value of the alkaline solution is high, it is known that in the beginning of the chemical reaction stage, all the dispersed bubbles are consumed in the liquid mixture. As shown in Figure 5.1, the E-E model conceptually accounts for the decrease of the local gas volume fraction through a decrease in the numbers of bubbles. So, in order to use the E-E model for modeling of chemisorption of the dispersed phase into liquid mixtures, it should be ensured that the bubble size change is small enough that it does not greatly affect other computational parameters. It is therefore important to evaluate the dispersed bubble size change under a given condition to obtain meaningful simulation results.

In this work, simulations were performed with the use of a E-E model for the flow with mass transfer and chemical reaction in two square cross-sectioned gas-liquid bubble columns ($W \times D \times H$ = $0.15 \times 0.15 \times 0.45/0.55$ m^3) that was aerated with pure CO_2 or diluted CO_2 gas through the bottom plane with a superficial gas velocity of V_S = 0.005 m/s. Drag, virtual mass and lift forces are considered for the interfacial momentum transfer. The Sub-grid scale (SGS) turbulence model proposed by Vreman (2004) was employed to evaluate the turbulent viscosity in the continuous phase. Specifically, we study the feasibility of the current model for the numerical simulation of gas-liquid flow with mass transfer. To obtain physically meaningful results, we studied the effect of bubble size on the overall mass transfer rate and the variation of the bubble size with time under a given condition. Based on the obtained results, we designed three simulations to study the gas-liquid flow with mass transfer. Numerical simulations were implemented in the commercial software package CFX-4.4.

5.2 Governing equations

The equations of the two-fluid model can be obtained by ensemble-averaging of the local instantaneous equations for single-phase flow (Drew, 1999). Two sets of balance equations for mass and momentum are obtained. The generic conservation equations for mass and momentum respectively take the following form:

$$\frac{\partial(\alpha_k \rho_k)}{\partial t} + \nabla \cdot (\alpha_k \rho_k \mathbf{u}_k) = -\dot{m}_{k \to l} \tag{5.1}$$

$$\frac{\partial(\alpha_k \rho_k \mathbf{u}_k)}{\partial t} + \nabla \cdot (\alpha_k \rho_k \mathbf{u}_k \mathbf{u}_k + \alpha_k \boldsymbol{\tau}_k) = \alpha_k \rho_k \mathbf{g} - \alpha_k \nabla p_k + \mathbf{M}_k - \dot{m}_{k \to l} \mathbf{u}_k \tag{5.2}$$

where the index k refers to the phase under consideration (L for liquid, G for gas) and l to the other phase. $\mathbf{u} = (u,v,w)$ is the velocity vector. The volume fraction of each phase is denoted by α, whereas $\dot{m}_{k\to l}$ is the mass transfer rate from phase k to phase l. $\mathbf{M}_k$ represents the inter-phase momentum exchange between phase k and all other phases, and accounts for the interface forces.
For phase k, the stress tensor τ_k appearing in Eq. 5.2 reads:

$$\tau_k = -\mu_{k,eff}(\nabla \mathbf{u}_k + (\nabla \mathbf{u}_k)^T - \tfrac{2}{3} I \nabla \cdot \mathbf{u}_k) \tag{5.3}$$

$\mu_{k,eff}$ for the liquid phase ($k = L$) is composed of three contributions: the molecular viscosity $\mu_{L,L}$, the shear-induced turbulent viscosity $\mu_{L,Tur}$, and an extra term due to bubble-induced turbulence μ_{BIT} :

$$\mu_{L,eff} = \mu_{L,L} + \mu_{L,Tur} + \mu_{BIT} \tag{5.4}$$

According to Jakobsen et al. (1997), the effective viscosity of the gas phase ($k = G$) is calculated as follows:

$$\mu_{G,eff} = \frac{\rho_G}{\rho_L} \mu_{L,eff} \tag{5.5}$$

The liquid phase shear-induced turbulent viscosity is evaluated by the SGS model proposed by Vreman (2004):

$$\mu_{L,Tur} = 2.5 \rho_L C_S^2 \sqrt{\frac{B_\beta}{S_{ij} S_{ij}}} \tag{5.6}$$

where $B_\beta = \beta_{11}\beta_{22} - \beta_{12}^2 + \beta_{11}\beta_{33} - \beta_{13}^2 + \beta_{22}\beta_{33} - \beta_{23}^2$, $S_{ij} = \partial u_j / \partial x_i$, $\beta_{ij} = \Delta_m^2 S_{mi} S_{mj}$ and Δ_i is the filter width in the i^{th} direction. C_S is a model constant, and $C_S = 0.1$ is used based on the work of Zhang et al. (2006).
The bubble-induced turbulent viscosity appearing in Eq. 5.4 is accounted for through the model of Sato and Sekoguchi (1975):

$$\mu_{BIT} = \rho_L \alpha_G C_{\mu,BIT} d_B |\mathbf{u}_G - \mathbf{u}_L| \tag{5.7}$$

where $C_{\mu,BIT}$ is a model constant which is set to 0.6.
The term $\mathbf{M}_k$ in Eq. 5.2, describing the interface forces, is given by the following expression:

$$\mathbf{M}_L = -\mathbf{M}_G = \mathbf{M}_{L,D} + \mathbf{M}_{L,L} + \mathbf{M}_{L,VM} \tag{5.8}$$

where the terms on the right hand side represent forces due to drag, lift and virtual mass, respectively. They are calculated as:

$$\mathbf{M}_{L,D} = \frac{3}{4}\alpha_G \rho_L \frac{C_D}{d_B} |\mathbf{u}_G - \mathbf{u}_L| (\mathbf{u}_G - \mathbf{u}_L) \tag{5.9}$$

$$\mathbf{M}_{L,L} = \alpha_G \rho_L C_L (\mathbf{u}_G - \mathbf{u}_L) \times \nabla \times \mathbf{u}_L \tag{5.10}$$

$$\mathbf{M}_{L,VM} = \alpha_G \rho_L \mathbf{C}_{VM} \left(\frac{D_G \mathbf{u}_G}{Dt} - \frac{D_L \mathbf{u}_L}{Dt}\right) \tag{5.11}$$

According to Tomiyama (2004), the virtual mass coefficient vector $\mathbf{C}_{VM}$ takes the form ($C_{VM,h}$, $C_{VM,v}$, $C_{VM,h}$). Based on our previous study, the following interfacial coefficients are used in this work:

$$C_D = 1.071 \tag{5.12}$$

$$C_L = 0.5 \tag{5.13}$$

$$C_{VM,h} = 0.25 \quad C_{VM,v} = 1.53 \tag{5.14}$$

The chemisorption of CO_2 in aqueous alkaline solutions takes place via two reactions. Before these reactions take place, CO_2 gas has to be absorbed in water physically first:

$$CO_2(g) \rightarrow CO_2(aq) \tag{5.15}$$

Subsequently, the elementary reactions then proceed as follows:

$$CO_2(aq) + OH^- \underset{k_{12}}{\overset{k_{11}}{\rightleftharpoons}} HCO_3^- \tag{5.16}$$

$$HCO_3^- + OH^- \underset{k_{22}}{\overset{k_{21}}{\rightleftharpoons}} CO_3^{2-} + H_2O \tag{5.17}$$

Where k_{11} and k_{12} respectively are the forward and backward rate constants for the first reaction (Eq. 5.16) and k_{21} and k_{22} represent the forward and backward rate constants for the second reaction (Eq. 5.17). The reaction rates are consequently written as follows:

$$R_{11} = k_{11}[CO_2(aq)][OH^-] \tag{5.18}$$

$$R_{12} = k_{12}[HCO_3^-] \tag{5.19}$$

$$R_{21} = k_{21}[HCO_3^-][OH^-] \tag{5.20}$$

$$R_{22} = k_{22}[CO_3^{2-}] \tag{5.21}$$

The expressions for the rate constants are provided in appendix A.

The mass fraction of a chemical species A in the liquid mixture is represented by Y_L^A. The chemical species transport equations for the liquid phase are given by:

$$\frac{\partial(\alpha_L \rho_L Y_L^A)}{\partial t} + \nabla \cdot (\alpha_L \rho_L \mathbf{u}_L Y_L^A - \alpha_L \Gamma_L^A \nabla Y_L^A) = S_A \tag{5.22}$$

Table 5.1: Source terms used in the species transport equations.

Species	Sources (kg/(m^3 s))
CO_2 (aq)	$\dot{m}_{G\to L} + \alpha_L (R_{12} - R_{11}) M_{CO_2}$
OH^-	$\alpha_L (R_{12} - R_{11} + R_{22} - R_{21}) M_{OH^-}$
HCO_3^-	$\alpha_L (R_{11} - R_{12} + R_{22} - R_{21}) M_{HCO_3^-}$
CO_3^{2-}	$\alpha_L (R_{21} - R_{22}) M_{CO_3^{2-}}$
CO_2 (g)	$-\dot{m}_{G\to L}$

whereas the gas phase transport equation for CO_2 is given by:

$$\frac{\partial(\alpha_G \rho_G Y_G^{CO_2})}{\partial t} + \nabla \cdot (\alpha_G \rho_G \mathbf{u}_G Y_G^{CO_2} - \alpha_G \Gamma_G^{CO_2} \nabla Y_G^{CO_2}) = S_G^{CO_2} \tag{5.23}$$

The relevant chemical species and source terms are listed in Table 5.1.
The mass transfer rate of species CO_2 per unit volume, $\dot{m}_{G\to L}$, from the dispersed phase to the continuous phase, is defined as:

$$\dot{m}_{G\to L} = k_L a E \rho_L (Y_{GL,e}^{CO_2} - Y_L^{CO_2}) \tag{5.24}$$

where k_L is the overall mass transfer coefficient for the chemical species CO_2(aq); $a = 6\alpha_G/d_B$ is the interfacial area per unit volume; E is the enhancement factor due to the chemical reaction; $Y_{GL,e}^{CO_2}$ is the mass fraction of CO_2(aq) in the liquid phase that would be in equilibrium with the concentration in the gas phase, which is determined by Henry's law:

$$Y_{GL,e}^{CO_2} = H^{CO_2} Y_G^{CO_2} \frac{\rho_G}{\rho_L} \tag{5.25}$$

The overall mass transfer coefficient, k_L is obtained from the following Sherwood relation of Brauer (1981):

$$Sh = \frac{k_L d_B}{D_{CO_2}} = 2 + 0.015 \,\mathrm{Re}^{0.89} Sc^{0.7} \tag{5.26}$$

whereas the enhancement factor is calculated using the relation given by Westerterp et al. (1984):

$$E = \begin{cases} -\dfrac{Ha^2}{2(E_\infty - 1)} + \sqrt{\dfrac{Ha^4}{4(E_\infty - 1)^2} + \dfrac{E_\infty Ha^2}{E_\infty - 1} + 1} & E_\infty > 1 \\ 1 & E_\infty \le 1 \end{cases} \tag{5.27}$$

where

$$E_\infty = (1 + \frac{[OH^-]D_{OH^-}}{2D_{CO_2}H[CO_2(g)]}) \times \sqrt{\frac{D_{CO_2}}{D_{OH^-}}} \tag{5.28}$$

$$Ha = \frac{\sqrt{k_{11}D_{CO_2}[OH^-]}}{k_L} \tag{5.29}$$

The solubility of CO_2 in aqueous electrolytic solutions was estimated using the method presented by Weisenberger and Schumpe (1996):

$$\log(\frac{H^w}{H}) = \sum (h_i + h_g)c_i \tag{5.30}$$

H^w is the solubility coefficient of CO_2 in pure water; it is taken from Versteeg and van Swaaij (1988):

$$H^w = 3.59.10^{-7} RTe^{\frac{2044}{T}} \tag{5.31}$$

For the parameters h_i and h_g, the interested reader is referred to Weisenberger and Schumpe (1996) or the work of Darmana (2006), c_i is the molar concentration of the corresponding ion or gas.
The diffusivity of CO_2 in pure water, $D^w_{CO_2}$ was taken from Versteeg and van Swaaij (1988):

$$D^w_{CO_2} = 2.35.10^{-6} e^{\frac{-2119}{T}} \tag{5.32}$$

The diffusion of gases into aqueous electrolyte solutions was estimated by the method suggested by Ratcliff and Holdcroft (1963):

$$\frac{D_{CO_2}}{D^w_{CO_2}} = 1 - 1.29.10^{-4}[OH^-] \tag{5.33}$$

5.3 Numerical solution method

All the numerical simulations are carried out with the commercial CFD package CFX-4.4 of AEA Technology, Harwell, UK. The total domain is subdivided into uniform computational grid cells with $\Delta x = \Delta y = \Delta z = 0.01$ m. Eqs. 5.1 and 5.2 are solved in a transient fashion with a time step of 0.0005 s. It was previously found (Zhang, 2005) that good spatial and temporal resolutions are obtained with this grid size and time step. The curvature compensated convective transport (CCCT) scheme is used for the discretization of all convective terms. Both "Pressure" and "Opening" boundaries are applied at the outlet. The "opening" boundary condition requires that:

$$\alpha_L = 0 \;\; \alpha_G = 1 \tag{5.34}$$

In the gas cap, special measures need to be taken to prevent numerical problems due to the high gas volume fraction. This is accomplished as follows:

$$\alpha_L < 0.55 \quad \begin{cases} C_D = 0.05 \\ C_L = 0 \\ C_{VM} = 0 \end{cases} \tag{5.35}$$

With these measures, Eqs. 5.1 and 5.2 in approximation reduce to those for single phase flow. A small finite value for C_D is required in Eq. 5.35 to guarantee proper coupling of the two phases.

5.4 Physical problem

A sketch of the bubble column studied in this work is shown in Figure 5.3. The column is initially filled to a height of 0.45 m with pure water or aqueous NaOH solution (initial pH value of 12). Pure CO_2 or diluted CO_2 is used as the dispersed gas phase and injected in the center of the bottom plane with $A_{in} = 0.03 \times 0.03$ m^2 and $V_{G,in} = 0.1225$ m/s corresponding to a superficial gas velocity of 4.9 mm/s. Initially, the gas cap above the liquid is filled with inert N_2 gas. The gas-liquid flow is assumed to be homogeneous (bubbly) flow and break-up and coalescence are not accounted for.

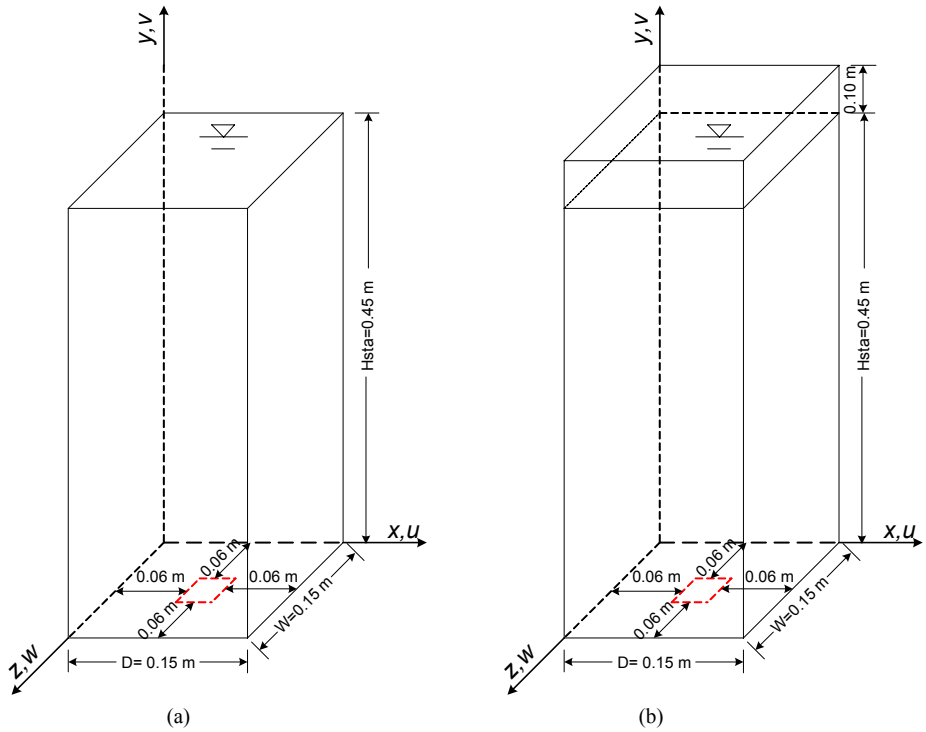

Figure 5.3: Schematic representation of the investigated bubble columns. "Pressure" (a) and "Opening" boundary conditions are applied at the outlet.

The width, depth and height of the column are respectively set to W = 0.15 m, D = 0.15 m, and H = 0.55 m. The gas distributor is located in the bottom wall of the column at a distance of 0.06 m from eachof the surrounding walls of the column. All the simulation parameters and physical properties are presented in Table 5.2. Diffusivities of the four species were obtained from the work of Bauer (2001). A constant bubble size of 4 mm is used currently as it was found that other parameters are not greatly affected by the bubble diameter in the range of $d_B \in [2, 4]$ mm.

Table 5.2: Case definition and involved parameters.

Case	Liquid mixture	Initial pH of liquid mixture	inlet gas	Outlet boundary condition
1	pure water	7	Pure CO_2	"Pressure"
2	pure water	7	Pure CO_2	"Opening"
3	aqueous *NaOH* solution	12	Pure CO_2	"Pressure"
4	aqueous *NaOH* solution	12	Pure CO_2	"Opening"
5	aqueous *NaOH* solution	12	80% N_2 + 20% CO_2 (Mass fraction)	"Opening"
C_D = 1.071, C_L = 0.50, ($C_{VM,h}$, $C_{VM,v}$) = (0.25, 1.53) ρ_L = 1000 kg/m^3, ρ_G = 1.29 kg/m^3, $\mu_{L,Lam}$ = 0.001 kg/(m.s), $\mu_{G,Lam}$ = 1.812×10^{-5} kg/(m.s). σ = 0.07275 N/m, d_B = 4 *mm*, $Eö$ = 2.15. $D_{CO_2} = 1.699.10^{-9}$ m^2/s; $D_{OH^-} = 5.3.10^{-9}$ m^2/s; $D_{HCO_3^-} = 1.1.10^{-9}$ m^2/s; $D_{CO_3^{2-}} = 1.5.10^{-9}$ m^2/s				

5.5 Results and Discussion

The dependence of the overall mass transfer coefficient, k_L on the bubble size d_B and the variation of the bubble size d_B with time for given pH values were investigated first. Then, the performance of "Pressure" and "Opening" boundary conditions at the outlet is investigated; after this, within the acceptable range of bubble shrinkage, physical absorption of pure CO_2 into pure water was studied; followed by the chemisorption of pure CO_2 bubbles into aqueous sodium hydroxide NaOH solution with an initial pH value of 12. Finally, chemisorption of dilute CO_2 bubbles in aqueous sodium hydroxide solution was also modeled.

5.5.1 Variation of the overall mass transfer coefficient with bubble diameter

According to Eq. 5.26, the following expression can be obtained for the mass transfer coefficient:

$$k_L = \frac{D_{CO_2}(2 + 0.015\,\mathrm{Re}^{0.89}\,Sc^{0.7})}{d_B} \tag{5.36}$$

which can be re-written as:

$$k_L = \frac{D_{CO_2}(2 + 0.015(\frac{\rho_L \mathrm{v}_{rel} d_B}{\mu_l})^{0.89}\,Sc^{0.7})}{d_B} \tag{5.37}$$

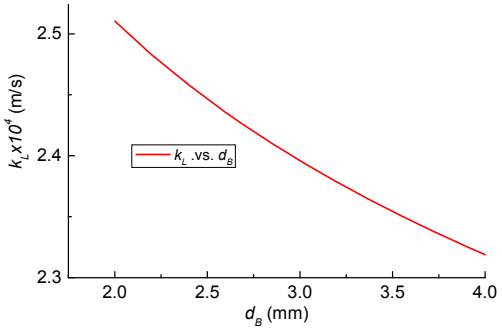

Figure 5.4: Variation of overall mass transfer coefficient, k_L, with bubble diameter, d_B.

As found in Eq. 5.33, the diffusivity of CO_2 in aqueous electrolyte solutions, D_{CO_2} does not change much with the pH value, so, a constant diffusivity $D_{CO_2} = D^w_{CO_2}$ is assumed. Furthermore, it is assumed that the bubble size ranges from 2 to 4 mm, and that in this regime, bubbles approximately possess a constant slip velocity of 0.2 m/s. Based on the aforementioned assumptions, the overall mass transfer coefficient, k_L changes less than 10% with bubble diameter in the range of $d_B \in [2, 4]$ mm as can be seen in Figure 5.4.

5.5.2 Shrinkage of the bubble diameter with time

In the present work, we analyze the change of the diameter of pure CO_2 bubbles due to chemical absorption. As reported by Darmana (2006), for pH>12, the enhancement factor, E increases dramatically. Here, to avoid large changes of the bubble size, an initial pH value, pH = 12 is chosen, hence $E \approx 1$.

For a single CO_2 bubble, its mass change due to inter-phase mass transfer is expressed as:

$$\dot{m}_B^{CO_2} = k_L \mathrm{A}_B \rho_L E (Y_{GL,e}^{CO_2} - Y_L^{CO_2}) \tag{5.38}$$

In case of fast reaction, $Y_L^{CO_2}$ in Eq. 5.38 is very small and it is safe to take it as zero, $Y_{GL,e}^{CO_2}$ is obtained from Eq. 5.25 and the Henry constant takes a value of about 0.92 according to Eq. 5.30. Meanwhile, the initial mass of a single CO_2 bubble is given by:

$$m_B^{CO_2} = \rho_G \frac{\pi d_B^3}{6} \tag{5.39}$$

After some algebraic manipulations, the following relation is obtained for the change in bubble size:

$$\frac{dd_B}{dt} = -2Ek_L H \tag{5.40}$$

Substituting Eq. 5.37 into Eq. 5.40 gives:

$$\frac{dd_B}{dt} = -2H \frac{D^{CO_2}(2 + 0.015(\frac{\rho_L v_{rel} d_B}{\mu_l})^{0.89} Sc^{0.7})}{d_B} \tag{5.41}$$

Figure 5.5 presents the variation of bubble size with time under the aforementioned conditions, which is obtained by numerically integrating Eq. 5.41. It can be seen that the bubble size decreases almost linearly with the residence time. When the residence time is less than 4 s, the bubble size stays between 2 and 4 mm. In the systems studied in this work, a bubble column with a liquid height of 0.45 m was examined. A very conservative estimate of the gas velocity of 0.2 m gives rise to a residence time of about 2 s. This implies that it is safe to assume a constant bubble size in this work.

5.5.3 Pressure and Opening boundary conditions

In this section, we investigate the performance of "Pressure" and "Opening" boundary conditions applied at the outlet for the modeling of physical and chemical absorption of pure CO_2 in respectively water or aqueous NaOH solution. Pure CO_2 gas is introduced into the bubble column through the sparger mounted in the center of the bottom plane. Two species transport equations are solved to compute the mass fraction of CO_2 in the liquid mixture and gas mixture respectively.

First of all, the "Pressure" boundary condition is investigated. That is, pure CO_2 bubbles are introduced into bubble column (see Figure 5.3a). Figure 5.6 displays snapshots of the transient behavior in the column after the CO_2 bubbles are introduced into the column. It is observed that both CO_2 gas and CO_2 liquid solution enter the column at the outlet. Consequently, it alters the components in the liquid mixture, which is unphysical. This phenomenon is more evident during the chemisorption of CO_2 into aqueous NaOH solution, as shown in Figure 5.7. From Figure 5.6 and 5.7, it is concluded that the "Pressure" boundary condition at the outlet is not suitable in the simulation of physical or chemical absorption of CO_2 and so in the remaining part of this chapter, the so-called "Opening" boundary is applied at the outlet.

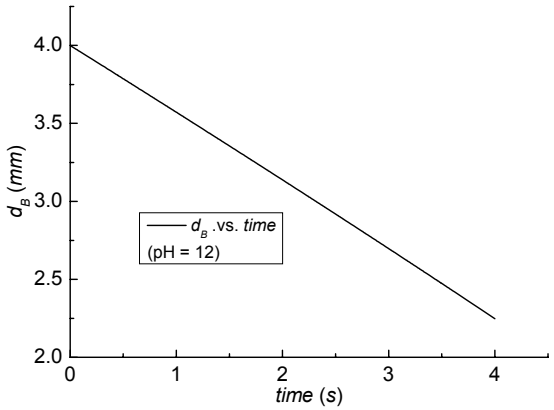

Figure 5.5: Variation of pure CO_2 bubble diameter with time. pH = 12 is used in the analysis.

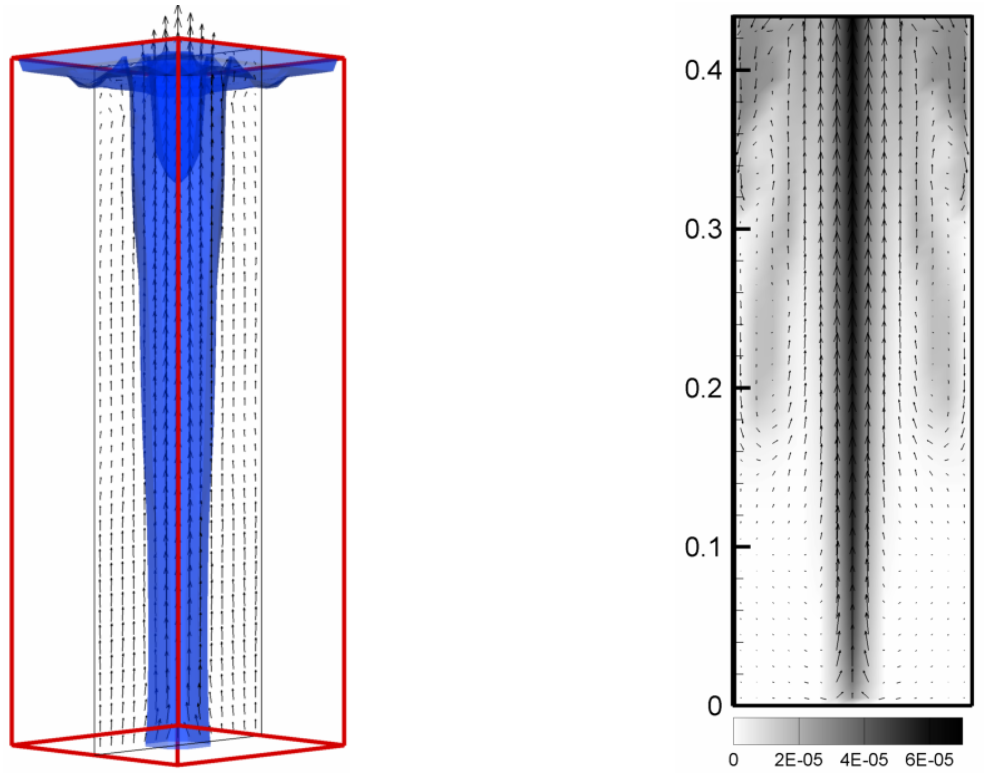

Figure 5.6: Snapshots of the simulated iso-surface of $\alpha_G = 0.05$ and gas phase velocity field in the plane of z/W = 0.5 (left) and contour of aqueous CO_2 and liquid phase velocity field in the plane of x/D = 0.5 (right). Pressure boundary condition is applied at the outlet during numerical modeling of physical absorption of pure CO_2 into water.

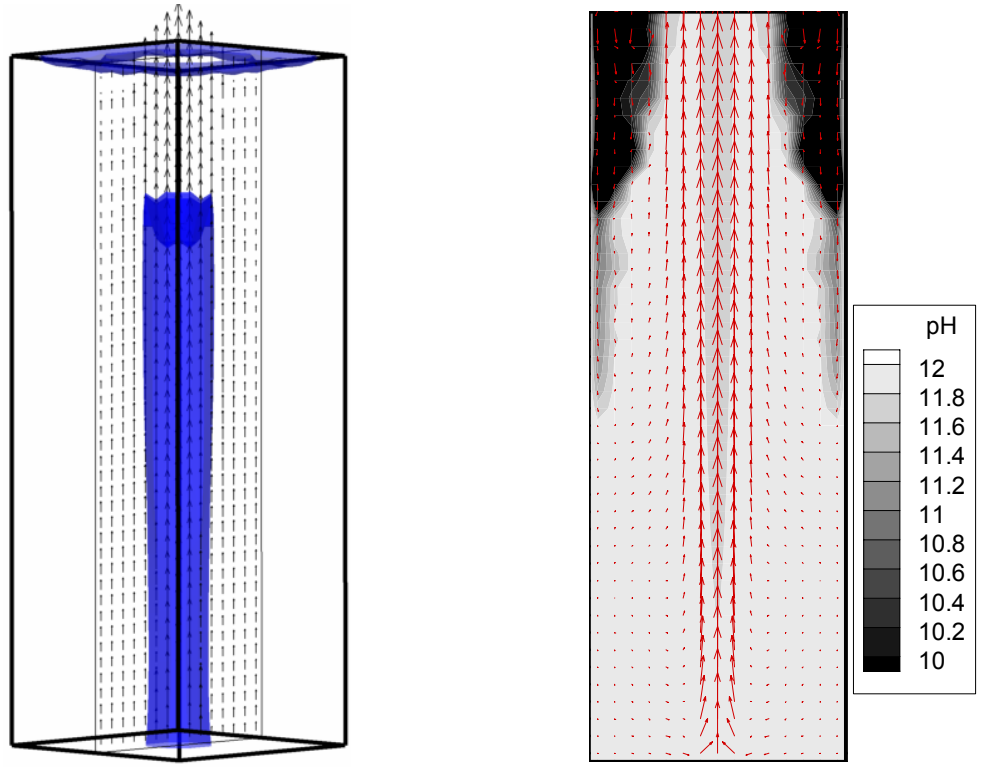

Figure 5.7: Snapshots of the simulated iso-surface of $\alpha_G = 0.05$ and gas phase velocity field in the plane of z/W = 0.5 (left) and contour of aqueous CO_2 and liquid phase velocity field in the plane of x/D = 0.5 (right). Pressure boundary condition is applied at the outlet during numerical modeling of chemisorption of pure CO_2 into aqueous NaOH solution.

5.5.4 Physical absorption of pure CO_2 bubbles in water

In this case, we study the physical absorption of pure CO_2 in water. Pure CO_2 gas is introduced into the bubble column through the sparger mounted in the center of the bottom plane. Two species transport equations are solved to compute the mass fraction of CO_2 in the liquid mixture and gas mixture respectively.

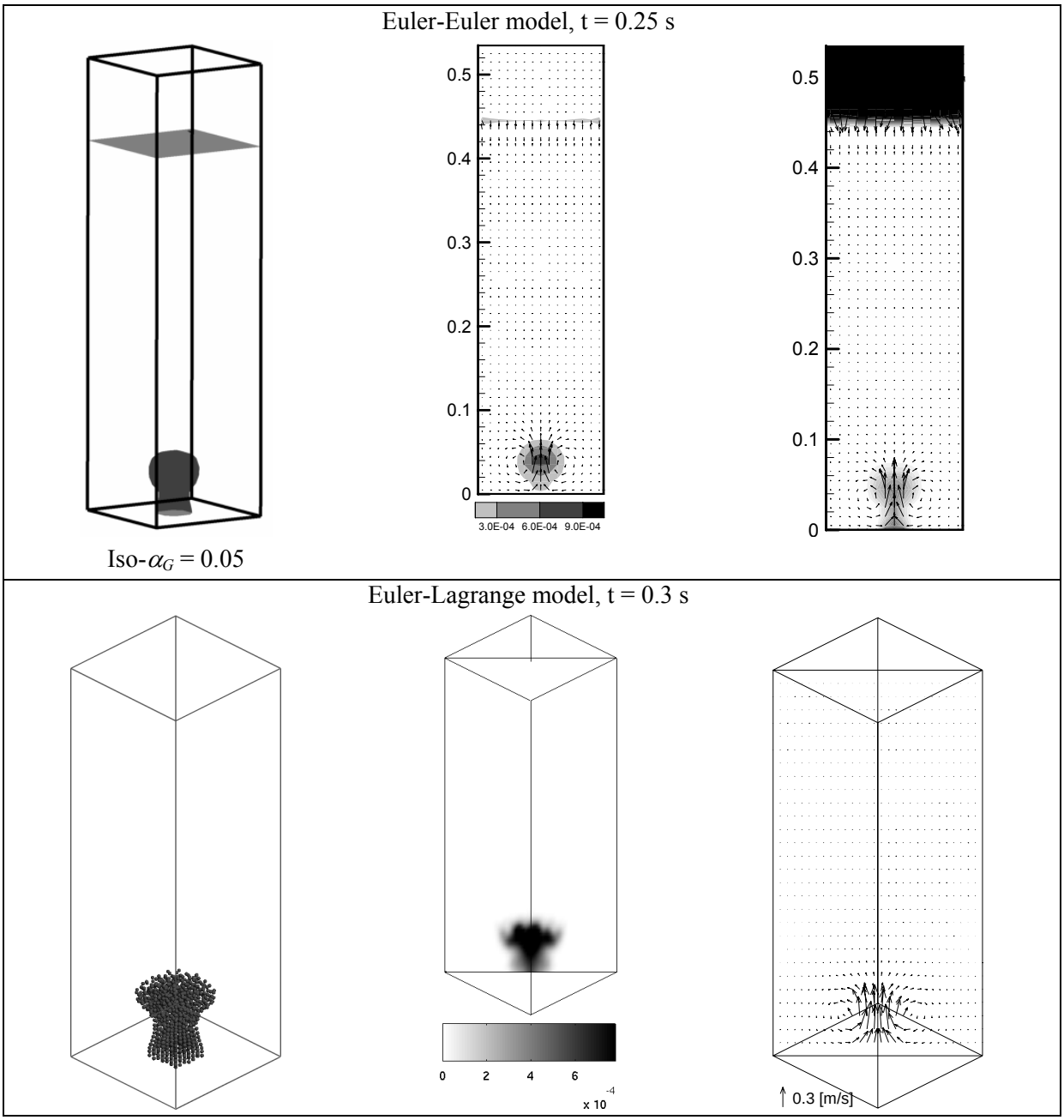

Figure 5.8: Comparison of instantaneous results of gas distribution (left), dissolved CO_2 concentration in kmol/m^3 (middle) and liquid velocity field (right) obtained from the Euler-Euler model (top row) and an Euler-Lagrange model (bottom row, after Darmana et al., 2005) at three different instances.

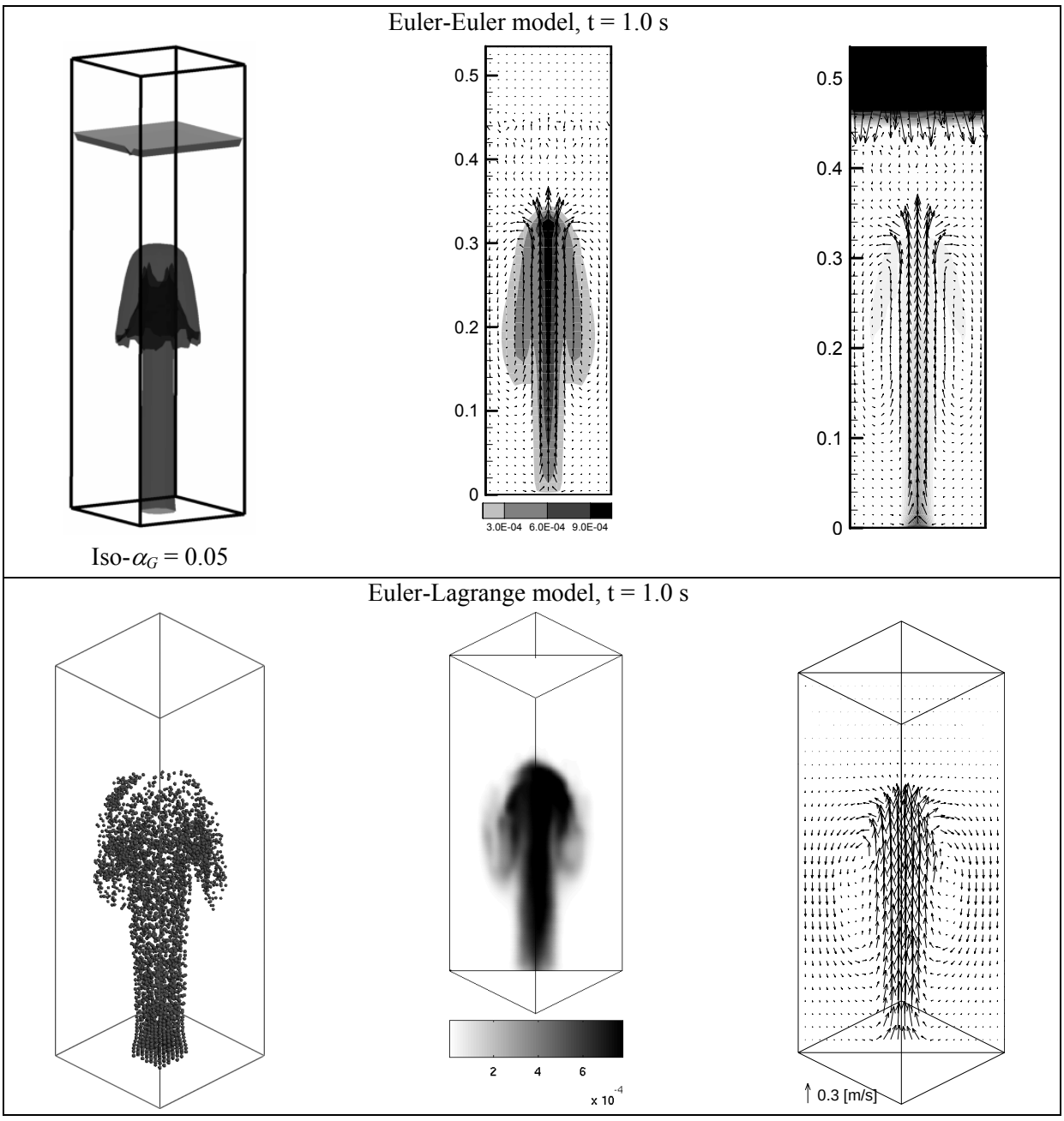

Figure 5.8: Continued.

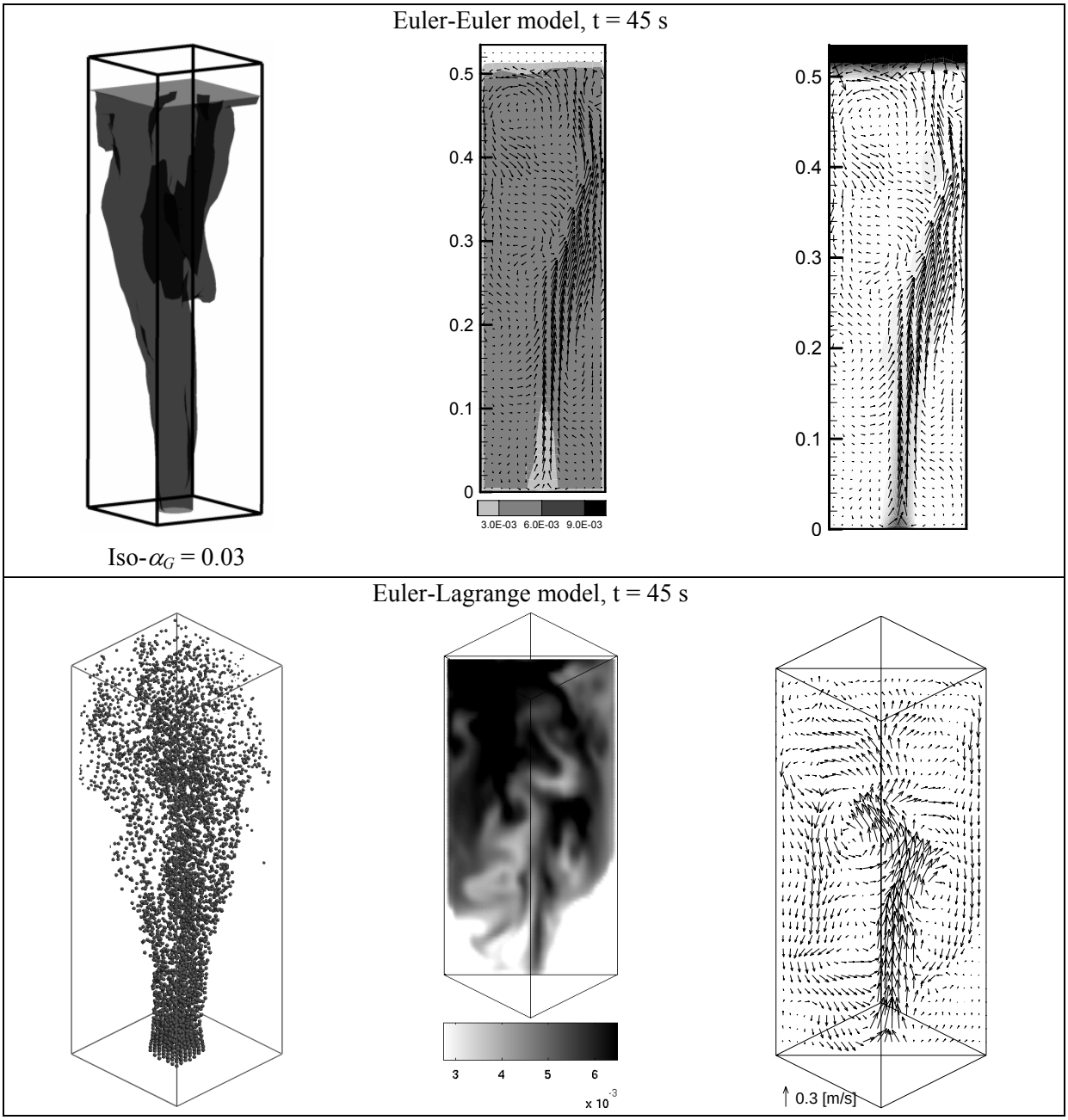

Figure 5.8: Continued.

Figure 5.8 displays the comparison of transient behavior in the column after the CO_2 bubbles are introduced into the column obtained from Euler-Euler and Euler-Lagrange (Darmana, 2006)models. It is observed that the hydrodynamics and flow pattern obtained from Euler-Euler models are relatively similar to those obtained from Euler-Lagrange model; and obviously, in this case a high fraction of aqueous CO_2 is found near the bubble plume before the bubble plume reaches the free surface. After the bubble plume has arrived at the free surface, it becomes dynamic, and the liquid phase CO_2 is transported to the lower part of the column along the walls. At the free surface, the liquid mixture moves laterally and meanwhile, the bubbles are spread to the wall. After 20 s, the mass fraction of aqueous CO_2 is relatively high in the entire column.

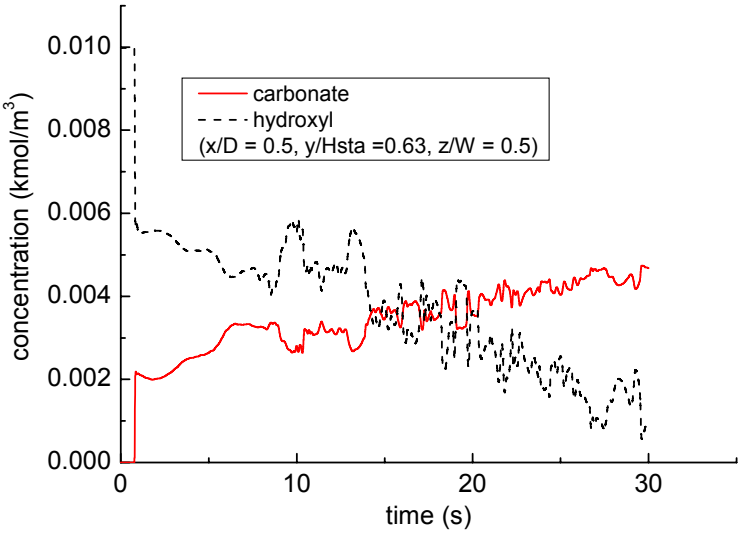

Figure 5.9: Concentration history of CO_3^{2-} and OH^- species involved in the chemical reaction process resulting from the numerical simulation at the point x/D = 0.5, y/H_{sta} = 0.63 and z/W = 0.5.

5.5.5 Chemisorption of pure CO_2 bubbles in aqueous NaOH solution

In this sub-section, we study the chemisorption of pure CO_2 in aqueous NaOH solution with an initial pH value of 12. As in the top part of column, CO_2 and N_2 are mixed, one additional species transport equation is used to compute the mass fraction of CO_2 in the gas phase. Transport equations for the mass fractions of aqueous CO_2, OH^-, HCO_3^- and CO_3^{2-} are solved as well (see Eq. 5.22).

In the early stages, the chemisorption process of CO_2 into an aqueous NaOH solution is characterized by the consumption of OH^- ions and formation of CO_3^{2-}. Figure 5.9 shows the predicted evolution of the concentrations of these two species during the chemisorption process. As observed in Figure 5.9, in the very beginning of the process, as no CO_2 bubbles reach the monitoring point, no OH^- is consumed and neither is CO_3^{2-} formed. The CO_2 bubbles arrive at the monitoring point after about 0.8 s, very much of the OH^- is consumed within a short time; correspondingly, CO_3^{2-} is produced very rapidly. After this short period of high chemical reaction rate, due to the low local concentration of OH^-, the chemical reaction is reduced; the consumption of OH^- or production of CO_3^{2-} becomes slower. Subsequently, the local species concentration shows an oscillatory behavior, which can be attributed to the local or even large scale mixing caused by convection. Only small traces of CO_2 (aq) and HCO_3^- are observed, which means that all the absorbed CO_2 is immediately consumed by the chemical reaction and bi-carbonate, HCO_3^- is only an intermediate product.

Figure 5.10 demonstrates the transient behavior in the column after the CO_2 bubbles are introduced into the column. It is seen that the gas bubbles agitate the liquid mixture and clearly, a lower pH value is obtained near the bubble plume before the bubble plume reaches the free surface, which implies that the absorbed CO_2 is consumed locally; after the bubble plume arrives at the free surface, as found earlier, the reaction products are transported to the lower part of the column along the walls, so the pH value decreases correspondingly. With the development of time, more OH^- is consumed, and lower pH values are observed in the entire column.

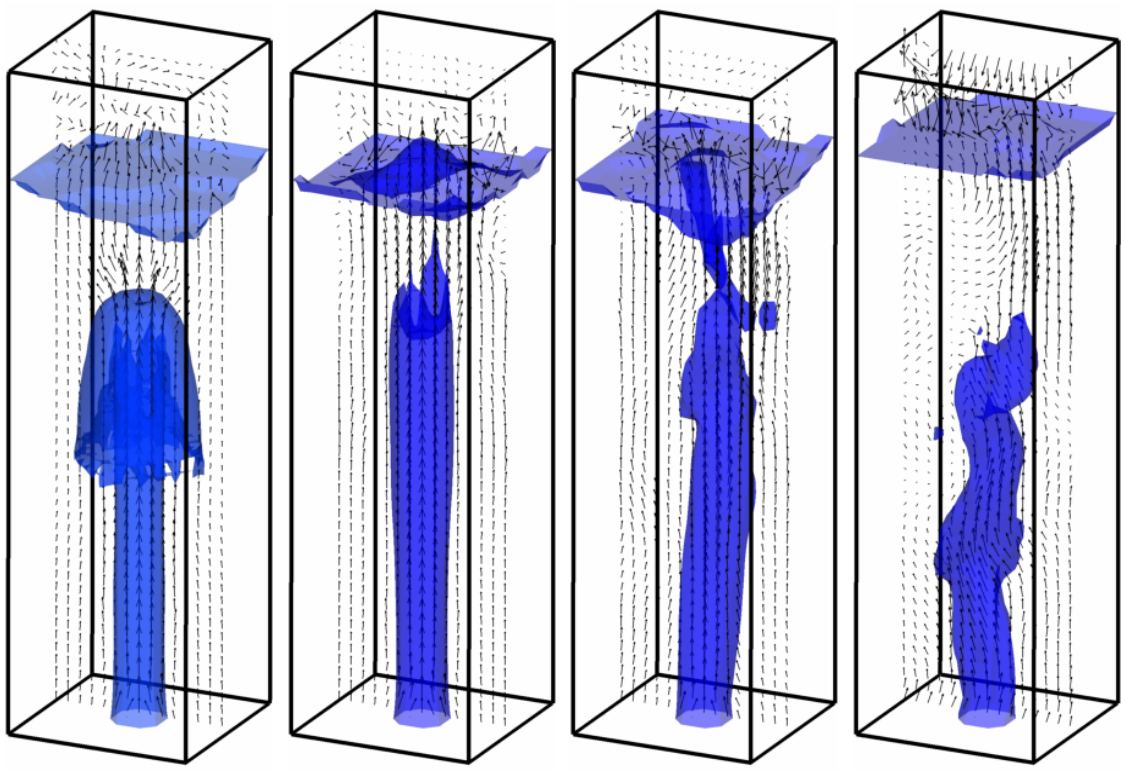

t = 0.50 s
iso-α_G = 0.05

t = 2.50 s
iso-α_G = 0.05

t = 10.00 s
iso-α_G = 0.05

t = 30.00 s
iso-α_G = 0.05

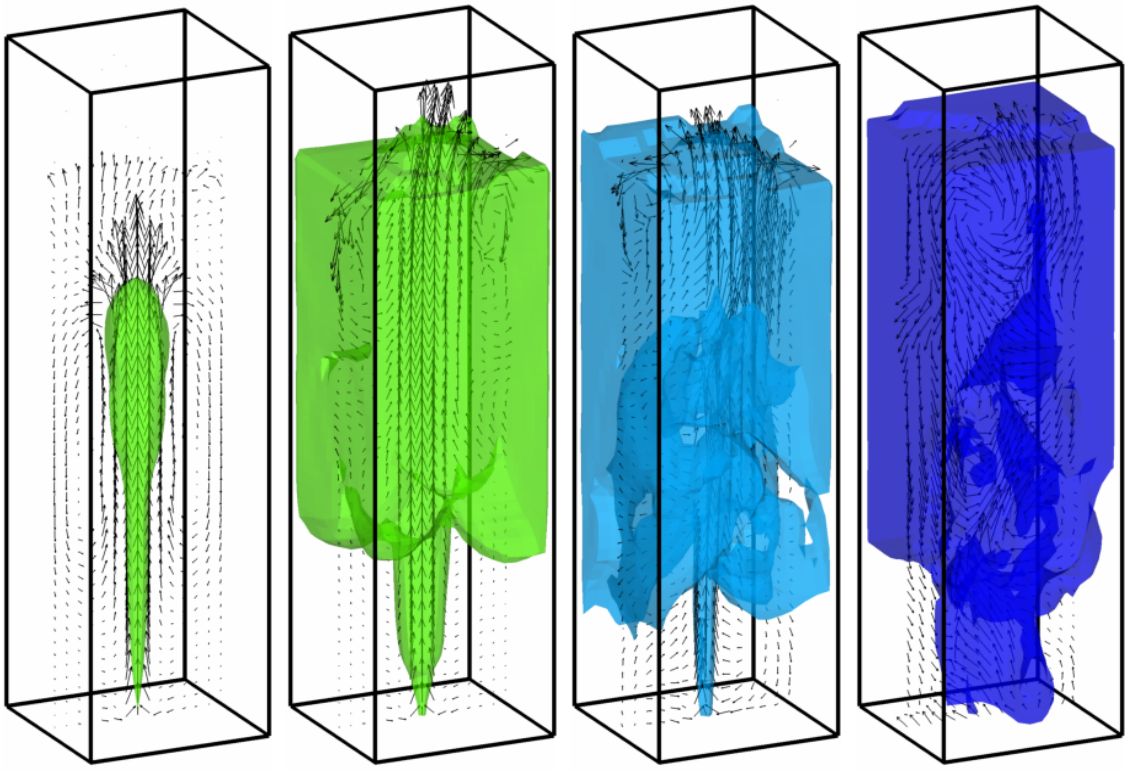

t = 0.50 s
iso-pH = 11.90

t = 2.50 s
iso-pH = 11.90

t = 10.00 s
iso-pH = 11.80

t = 30.00 s
iso-pH = 11.00

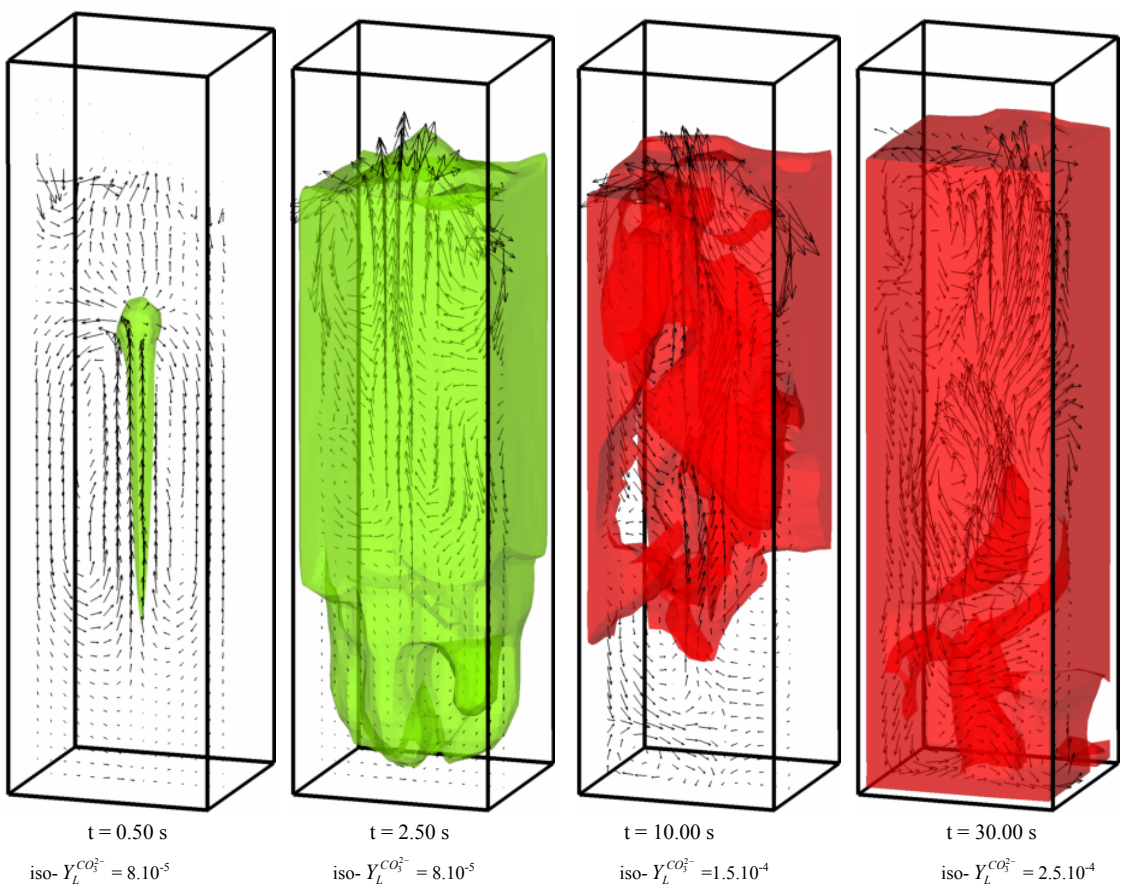

Figure 5.10: Snapshots of the simulated iso-surface of α_G = 0.05 and gas phase velocity field in the plane of z/W = 0.5 (top) and different iso-surfaces of pH and liquid phase velocity field in the plane of x/D = 0.5 (middle) and different iso-surfaces of $Y_L^{CO_3^{2-}}$ and liquid phase velocity field in the plane of z/W = 0.5 (bottom) at different times during the chemisorption of pure CO_2 bubbles in an aqueous NaOH solution.

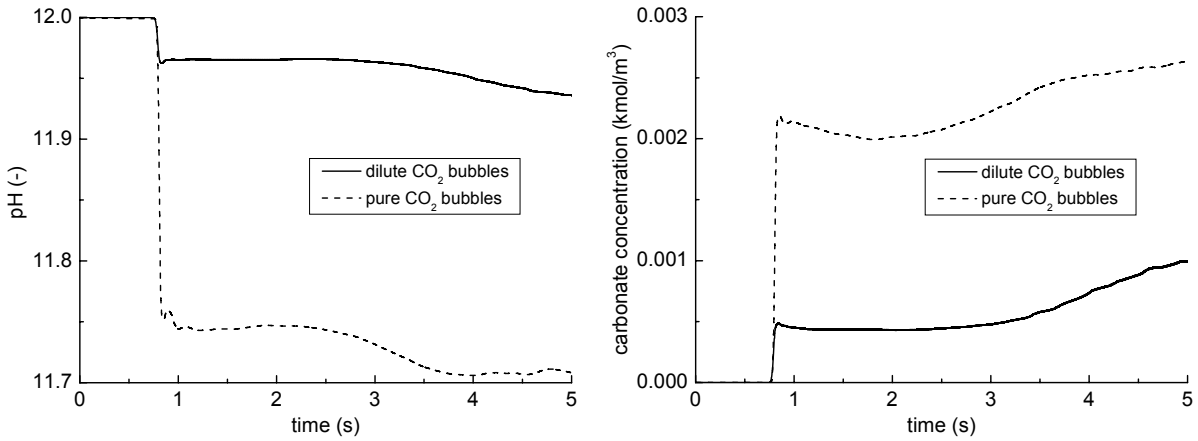

Figure 5.11: Comparison of history of pH and carbonate concentration during the chemical reaction process resulting from the numerical simulation at the point x/D = 0.5, y/H_{sta} = 0.63 and z/W = 0.5. Dilute and pure CO_2 bubbles are used here.

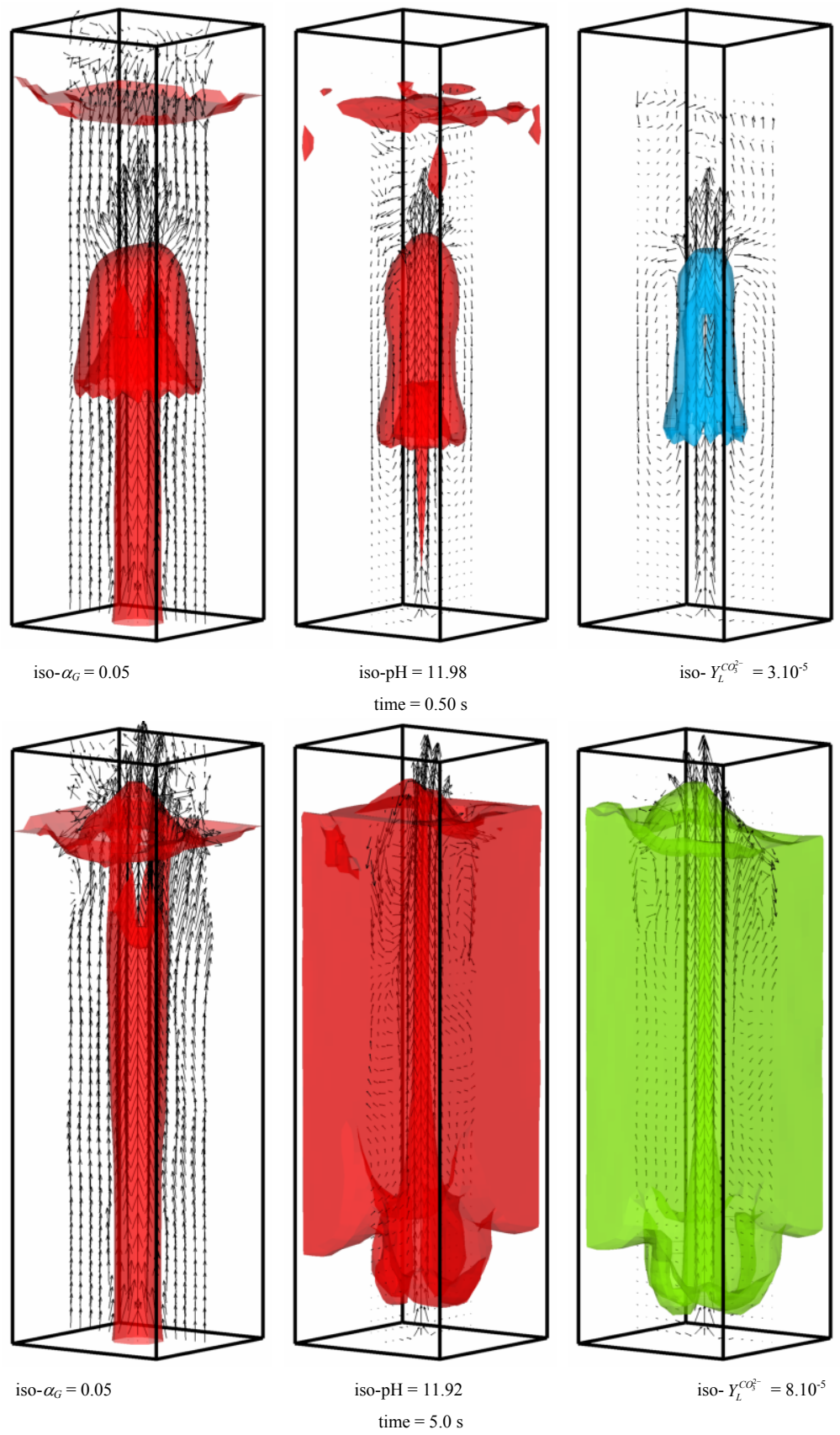

Figure 5.12: Snapshots of the simulated iso-surface of α_G = 0.05 and gas phase velocity field in the plane of z/W = 0.5 (left) and iso-surface of pH and liquid phase velocity field in the plane of x/D = 0.5 (middle) and iso-surfaces of $Y_L^{CO_3^{2-}}$ and liquid phase velocity field in the plane of z/W = 0.5 (right) at different times during the chemisorption of dilute CO_2 bubbles in aqueous NaOH solution.

5.5.6 Chemisorption of diluted CO_2 bubbles in an aqueous NaOH solution

In this sub-section, we study the chemisorption of diluted CO_2 in aqueous NaOH solution with an initial pH value of 12. The same mass fractions as in the previous case were solved for according to Eqs. 5.22 and 5.23. Figure 5.11 shows the difference between the chemisorption of pure and diluted CO_2 bubbles in aqueous NaOH solution. Obviously, compared with the diluted CO_2 bubbles, in the case of pure CO_2 bubbles, the mass transfer rate is higher and more carbonate is produced. Transient behavior in the column is displayed in Figure 5.12. It is seen that the pH value drops slower in the diluted case.

5.7 Conclusions

Numerical simulations of the gas-liquid two-phase flow with mass transfer in a square cross-sectioned bubble column were carried out with the use of the commercial software package CFX-4.4. The sub-grid scale (SGS) turbulence model of Vreman (2004) was employed to evaluate the shear-induced turbulent viscosity in the liquid phase. Both "Pressure" and "Opening" boundary conditions are applied at the outlet, while the previously used interfacial coefficients (Zhang et al., 2006) were used in the simulations.

Through a simple analysis, it is concluded that the overall mass transfer coefficient k_L changes less than 10% when the bubble diameter is in the range of 2 to 4 mm. Provided that the pH value of the alkaline solution is lower than 12, the bubble diameter decreases approximately linearly with the time. Due to the short residence time, the bubble diameter remains within the range of 2 to 4 mm, which is still acceptable to satisfy the aforementioned criterion for k_L.

When pure CO_2 is absorbed into water or aqueous NaOH solution, the "Pressure" boundary condition at the outlet is not suitable, since the so-called "Pressure" boundary condition allows gas CO_2 to enter the column from the outlet; or even other liquid chemical species enter into the column from the outlet, which alters the components in the solution and this is unphysical. When the "Opening" boundary condition is applied at the outlet, special measurements should be taken in the gas cap to avoid high rate mass transfer and chemical reaction due to high gas fraction.

When pure CO_2 is absorbed into water, the hydrodynamics is quite similar to the gas-liquid flow without mass transfer, and high CO_2 concentrations in the liquid phase are found in the vicinity of the bubble plume. When the bubble plume arrives at the free surface, the aqueous CO_2 is transported from the top part of the column to the bottom part along the walls due to the down flow of the liquid phase.

Chemisorption of pure CO_2 into aqueous NaOH solution with an initial pH value of 12 has been simulated as well. Initially most of the CO_2 is consumed in the center region of the column, where the bubble plume rises. As a consequence, the OH^- concentration is reduced in this area. Subsequently the fluid with low pH (i.e. OH^- concentration) is transported with the bubbles to the top of the column and finally flows back along the walls. After a while, the system is well mixed and the pH is homogeneous.

Finally chemisorption of (20 m% CO_2 and 80 m% N_2) dilute CO_2 bubbles in alkaline solutions was studied as well. Due to the lower mass fraction of CO_2 in the gas phase, the local pH value drops slower compared with the pure CO_2 bubbles, the flow structure and hydrodynamics are similar to the chemisorption of pure CO_2 into NaOH solution.

All the numerical results are only qualitatively presented; a more detailed comparison of the E-E results with available E-L simulated results is planned for the near future.

5.8 Notation

a	interfacial area (m^2); strain rate (s^{-1})
B	Sub-grid scale model parameter (m^4 s^{-4})
d	diameter (m)
c	species concentration(kmol m^{-3})
C	model coefficient, dimensionless
D	depth (m); diffusivity (m^2 s^{-1})
g	gravitational constant (m s^{-1})
E	enhancement factor, dimensionless
$Eö$	Eötös number, dimensionless
H	Henry constant, dimensionless; height (m)
Ha	Hatta number, dimensionless
I	ionic concentration (kmol m^{-3})
k_{11}	forward reaction rate constant (m^3 $kmol^{-1}$ s^{-1})
k_{12}	backward reaction rate constant (s^{-1})
k_{21}	forward reaction rate constant (m^3 $kmol^{-1}$ s^{-1})
k_{22}	backward reaction rate constant (s^{-1})
k_l	overall mass transfer coefficient (m s^{-1})
K_1	equilibrium constant for reaction 1 (m^3 $kmol^{-1}$)
K_2	equilibrium constant for reaction 2 (m^3 $kmol^{-1}$)
M	interfacial force (kg m s^{-2})
$\dot{m}$	mass transfer from gas(single bubble) (kg s^{-1})
m	mass of single bubble (kg)
P	pressure (Nm^{-2})
R	reaction rate (kmol m^{-3} s^{-1})
Re	Reynolds number, dimensionless
S	source term in the species balance equation, kg m^{-3} s^{-1}
S	stress tensor
Sh	Sherwood number, dimensionless
t	time (s)
T	temperature (K)
u	velocity vector (m s^{-1})
u	velocity component in x direction (m s^{-1})
v	slip velocity (m s^{-1})
v	velocity component in y direction (m s^{-1})
w	velocity component in z direction (m s^{-1})
Y	mass fraction, dimensionless
z	ionic charge, dimensionless
[.]	concentration (kmol m^{-3})

Greek letters

Δ	subgrid length scale (m)
Γ	species diffusion coefficient (m^2 s^{-1})
ρ	density (kg m^{-3})
β	Sub-grid scale model parameter (m^2 s^{-2})
σ	interfacial tension (N m^{-1})
μ	viscosity (kg m^{-1} s^{-1})
τ	Stress tensor (N m^{-2})

Subscripts

aq	aqueous
B	bubble
BIT	Bubble-induced turbulence
D	drag
e	equilibrium
eff	effective
G	gas
GL	Gas-liquid
h	horizontal direction
i	Cartesian ordinate direction index
j	Cartesian ordinate direction index
k	phase indicator
L	lift, liquid
Lam	laminar
rel	relative velocity
S	subgrid scale model
Tur	shear-induced turbulence
v	vertical direction
VM	virtual mass

Superscripts

w	water

5.9 Bibliography

Bauer, M. and Eigenberger, G., 1999. A concept for multi-scale modeling of bubble columns and loop reactors. *Chem. Eng. Sci.,* 54, 5109-5117.

Bauer, M. and Eigenberger, G., 2001. Multiscale modeling of hydrodynamics, mass transfer and reaction in bubble columns reactors. *Chem. Eng. Sci*., 56, 1067-1074.

Bauer, M., 2001. On the multiscale modeling of bubble column reactors. PhD thesis, University of Stuttgart, Germany.

Becker, S., Sokolichin, A. and Eigenberger, G., 1994. Gas-liquid flow in bubble columns and loop reactors:Part II. Comparison of detailed experiments and flow simulations. *Chem. Eng. Sci.,* 49, 5747-5762.

Brauer, H., 1981. Particle/fluid transport processes. Progress in *Chemical Engineering,* 19, 81-111.

Darmana, D., Deen, N. G. and Kuipers, J. A. M., 2005. Detailed modeling of hydrodynamics, mass transfer and chemical reactions in a bubble column using a discrete bubble model. *Chem. Eng. Sci.*, 60, 3383-3404.

Darmana, D., 2006. On the multiscale modeling of hydrodynamics, mass transfer and chemical reactions in a bubble columns. PhD thesis, University of Twente. Enschede, The Netherlands.

Deen, N. G., Solberg, T. and Hjertager, B. H., 2001. Large eddy simulation of the gas-liquid flow in a square cross-sectioned bubble column. *Chem. Eng. Sci.*, 56, 6341-6349.

Delnoij, E., Kuipers, J. A. M. and Van Swaaij, W. P. M, 1997. Dynamic simulation of gas-liquid two-phase flow: effect of column aspect ratio on the flow structure. *Chem. Eng. Sci.*, 52, 3759-3772.

Delnoij, E., Kuipers, J. A. M. and Van Swaaij, W. P. M, 1999. A three-dimensional model for gas-liquid bubble columns. *Chem. Eng. Sci.*, 54, 2217-2226.

Drew, D. A. and Passman, S. L., 1999. Theory of multicomponent fluids, Applied Mathematical Sciences 135, Springer.

Edwards, T. J., Maurer, G., Newman, J. and Prausnitz, J. M., 1978. Vapor-liquid equilibrium in multicomponent aqueous solutions of volatile weak electrolytes. *AIChE J.*, 24, 966-976.

Eigen, M., 1954. Method for investigation of ionic reactions in aqueous solutions with half times as short as 10^{-9} sec. Discussions of the Faraday Society, 17, 194-205.

Fleischer, C., Becker, S. and Eigenberger, G., 1996. Detailed modeling of the chemisorption of CO_2 into NaOH in a bubble column. *Chem. Eng. Sci.,* 51, 1715-1724.

Hikita, H., Asai, S. and Takatsuka, T., 1976. Absorption of carbon dioxide into aqueous sodium hydroxide and sodium carbonate-bicarbonate solutions. Chemical Engineering Journal, 11, 131-141.

Jakobsen, H. A., Sannæs, B. H., Grevskott, S. and Svendsen, H. F., 1997. Modeling of vertical bubble-driven flows. *Ind. Eng. Chem. Res*., 36, 4052-4074.

Márquez, M. A., Amend, R. J., Carbonell, R. G., Sáez, A. E. and Roberts, G. W., 1999a. Hydrodynamics of gas-lift reactors with a fast, liquid-phase reaction. *Chem. Eng. Sci.*, 54, 2263-2271.

Márquez, M. A., Sáez, A. E., Carbonell, R. G. and Roberts, G. W., 1999b. Coupling of hydrodynamics and chemical reaction in gas-lift reactors. *AIChE, J.*, 45, 410-423.

Mudde, R. F. and Simonin, O., 1999. Two- and three dimensional simulations of a bubble plume using a two-fluid model. *Chem. Eng. Sci.*, 54, 5061-5069.

Pohorecki, R. and Moniuk, W., 1988. Kinetics of reaction between carbon dioxide and hydroxyl ions in aqueous electrolytic solutions. *Chem. Eng. Sci*, 43, 1677-1684.

Ratcliff, G. A. and Holdcroft, J. G., 1963. Diffusivities of gases in aqueous electrolyte solutions. Transaction of the Institution of Chemical Engineers and the Chemical Engineer, 41, 315-319.

Rigopoulos, S. and Jones, A., 2003. A hybrid cfd-reaction engineering framework for multiphase reactor modeling: basic concept and application to bubble column reactors. *Chem. Eng. Sci*., 58, 3077-3089.

Sato, Y. and Sekoguchi, K., 1975. Liquid velocity distribution in two-phase bubble flow. *Int. J. Multiphase Flow*, 2, 79-95.

Tomiyama, A., 2004. Drag, lift and virtual mass forces acting on a single bubble. 3rd International Symposium on Two-Phase Flow Modeling and Experimentation. Pisa, Italy. 22-24 Sept.

Tsonopolous, C., Coulson, D. M. and Inman, L. W., 1976. Ionization constants of water pollutants. Journal of Chemical & Engineering Data, 190-193.

Versteeg, G. F. and van Swaaij, W. P. M., 1988. Solubility and diffusivity of acid gases (CO_2 and N_2O) in aqueous alkaloamine solutions. *J. Chem. Eng. Data*, 33, 29-34.

Vreman, A. W., 2004. An eddy-viscosity subgrid-scale model for turbulent sher flow: Algebraic theory and applications. *Phys. Fluids*, 16, 3670-3681.

Westerterp, K. R., van Swaaij, W. P. M. and Beenackers, A. A. C. M., 1984. Chemical Reactor Design and Operation. John Wiley & Sons Ltd., 411.

Weisenberger, S. and Schumpe, A., 1996. Estimation of gas solubility in salt solutions at temperatures from 273 K to 363 K. *AIChE J.*, 42, 298-300.

Zhang, D., 2005. Numerical simulation of dynamic flow behavior in a bubble column: grid and time-independent solution. *Technical report*. University of Twente, March.

Zhang, D., Deen, N. G. and Kuipers, J. A. M., 2006. Numerical simulation of dynamic flow behavior in a bubble column: A study of closures for turbulence and interface forces. *Chem. Eng. Sci.*, 61, 7593-7608.

Zhang, D., Deen, N. G. and Kuipers, J. A. M., 2007. Numerical Modeling of Hydrodynamics, Mass transfer and Chemical Reaction in Bubble Columns. International Conference on Multiphase Flow, ICMF 2007, Leipzig, Germany, July 9 – 13.

Appendix A Kinetics

The forward rate constant k_{11} of reaction Eq. 18 is calculated via the relation presented by Pohorecki and Moniuk (1988):

$$\log(\frac{k_{11}}{k_{11}^{\infty}}) = 0.221I - 0.016I^2 \tag{A1}$$

where the reaction rate constant at infinitely diluted solution (m^3/kmol. s), is given by:

$$\log(k_{11}^{\infty}) = 11.895 - \frac{2382}{T} \tag{A2}$$

This equation is valid in the temperature range of 291- 314 K.
The ionic strength, I, is calculated as:

$$I = \frac{1}{2}([Na^+]z_{Na^+}^2 + [OH^-]z_{OH^-}^2 + [HCO_3^-]z_{HCO_3^-}^2 + [CO_3^{2-}]z_{CO_3^{2-}}^2) \tag{A3}$$

where $z_{Na^+} = 1$, $z_{OH^-} = -1$, $z_{HCO_3^-} = -1$ and $z_{CO_3^{2-}} = -2$.

The backward rate constant k_{12} (s^{-1}) is calculated via the equilibrium constant K_3 and K_w. K_3 is calculated according to Edwards et al. (1978):

$$K_3 = \frac{[HCO_3^-][H^+]}{[CO_2]} = \exp(\frac{-12092.1}{T} - 36.786\ln(T) + 235.482) \tag{A4}$$

The solubility product, K_w, was taken from Tsonopolous et al. (1976):

$$K_w = [H^+][OH^-] = 10^{(-5839.5/T + 22.4773\log(T) - 61.2062)} \tag{A5}$$

The backward reaction is then obtained using the following relation:

$$K_1 = \frac{k_{11}}{k_{12}} = \frac{K_3}{K_w} \tag{A6}$$

Since the second reaction involves a proton transfer, it is very rapid. Eigen (1954) determined the rates of reactions involving protons or hydroxyl ions in aqueous solution to be in the order of 10^{10} - 10^{11} m^3/kmol s. The backward reaction rate k_{22} (1/s) is calculated using the equilibrium constant K_2 (m^3/kmol) as suggested by Hikita et al. (1976):

$$K_2 = \frac{k_{21}}{k_{22}} \tag{A7}$$

with:

$$\log K_2 = \log K_2^{\infty} + \frac{1.01\sqrt{[Na^+]}}{1+1.27\sqrt{[Na^+]}} + 0.125[Na^+] \tag{A8}$$

where:

$$\log K_2^{\infty} = \frac{1568.94}{T} + 0.4134 - 0.00673T \tag{A9}$$

6

Detailed modeling of flow, mass transfer and chemical reaction in a bubble column

Abstract

Physical and chemical absorption of pure CO_2 bubbles in water and aqueous sodium hydroxide (NaOH) solution has been studied in a square-sectioned bubble column using the commercial software package CFX-4.4. The sub-grid scale (SGS) turbulence model of Vreman (2004) was employed to evaluate the shear-induced turbulent viscosity in the liquid phase. An "Opening" boundary condition was applied at the outlet, whereas the previously studied interfacial coefficients (see Chapter 2) were used in the simulations. Full coupling of fluid flow, mass transfer and chemical reaction is achieved through the incorporation of a bubble number density equation.

The capability of the bubble number density model to predict the bubble size is investigated first. Physical absorption of pure CO_2 in water and chemisorption of pure CO_2 bubbles in aqueous NaOH solution are numerically studied.

It was verified for test cases that the predicted bubble size agrees well with the assumed ones and that the bubble number density equation is capable of predicting the bubble size in the gas-liquid flow.

For the physical absorption of CO_2 in water, it is found that generally, the size of the bubbles in the core of the bubble plume is larger than that of the bubbles trapped in the down flow along the wall. In this test case, the bubble size ranges from 3 to 4 mm. As time proceeds, the differences in bubble size become smaller both in horizontal and vertical directions.

When pure CO_2 is absorbed into aqueous NaOH solution with an initial pH value of 12, the bubble size does not change very much: also in this case the bubble size ranges from 2.7 to 4 mm as the mass transfer enhancement factor is in the order of one, due to the relatively low pH. The pH history resulting from the numerical model is compared to that obtained from a simple macroscopic model. It is found that numerical results obtained from the case in which the bubble size is solved agrees well with the simple model. The observed differences between the simple model and the simulated results obtained with constant bubble size are due to the lack of coupling of mass transfer and fluid flow.

All the numerical results are only qualitatively presented, a more detailed comparison of the E-E results with the available E-L simulated results or experimental data is still required. Currently, only relatively low pH values of the alkaline solution are used. In the future, higher initial pH values leading to enhancement factors substantially larger than one should be tested.

6.1 Introduction

Bubble column reactors are widely used in chemical, petrochemical and biological processes. Many processes involve gas-liquid mass transfer with accompanying reactions between the gas and the liquid phase itself or with components dissolved or suspended in it. Despite the widespread application of bubble columns and intensive research efforts devoted to understand their complex behaviour, detailed knowledge on the fluid flow, mass transfer and chemical reactions as well as their interactions is currently very limited.

Experimental investigation and numerical simulations are widely used to study and analyze gas-liquid flow processes. In the last two decades, two approaches were frequently used to simulate the flow in bubble columns: the Euler-Euler model (E-E) (Becker et al., 1994; Deen et al., 2001) and Euler-Lagrange model (E-L) (Delnoij et al., 1997,1999; Darmana et al. 2005). Detailed descriptions of the E-L and E-E models are found in the previous chapters. Figure 6.1 schematically shows how the two models account for the bubble shrinkage due to physical absorption or chemisorption. In the Euler-Lagrange approach bubble shrinkage can be monitored for each individual bubble, while accounting for the properties of the individual bubbles. In the Euler-Euler approach, detailed information of the bubble size distribution can be obtained by solving additional equation which accounts for the breakage and coalescence of bubbles as well as the growth or shrinkage of bubbles due to mass transfer. The MUSIG (Multiple Size Group) model (Lo, 1996), the interfacial area concentration (Wu et al., 1998; Ishii and Kim, 2001; Yao and Morel, 2004; Ishii et al., 2005) and the recently developed S_γ model (Lo and Pao, 2007) were found to track the bubble size distribution, which will be discussed later. Though it is easier to track the bubble size change in the E-L model, due to its high computational effort and memory requirements, it is less suited to study gas-liquid flow in large-scale bubble columns or at high gas hold-up. In this study, the E-E model is adopted to investigate mass transfer in bubbly flows.

When a chemical reaction is considered in a gas-liquid system, the interactions between the prevailing processes are very complex as schematically depicted in Figure 6.2: the chemical reaction rate depends on the local concentration of the species, which is determined by the inter-phase mass transfer process and the mixing induced by the dispersed bubbles. The interphase mass transfer rate depends on the mass transfer coefficient, the interfacial area concentration and chemical reaction rate; meanwhile the mass transfer coefficient is a function of the local hydrodynamics, which itself is influenced by the bubble shrinkage due to physical or chemical absorption and variation of physical properties due to the inhomogeneous distributions of the chemical species. These complex interactions make the overall prediction of the performance and scale-up of this kind of reactor very difficult.

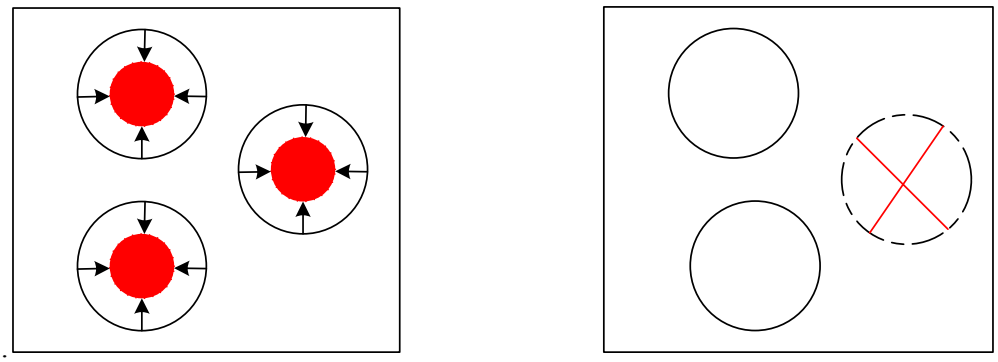

(a) reality (E-L) (b) E- E model

Figure 6.1: Treatment of bubble shrinkage due to mass transfer.

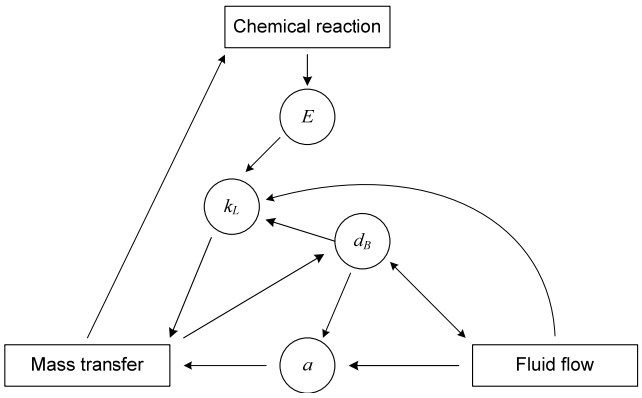

Figure 6.2: Schematic representation of inter-dependency of fluid flow, mass transfer and chemical reaction.

Due to the complexity of gas-liquid systems, some researchers have simplified the modeling in the E-E approach to steady state conditions or adopted one-dimensional or two-dimensional models (Fleischer et al., 1996; Márquez et al., 1999a, b); the so-called hybrid method is used as well to solve these kinds of problems, in which CFD is employed only for the simulation of hydrodynamics, and the chemical reactions are accounted for by a custom-build compartment models (Bauer and Eigenberger, 1999, 2001; Rigopoulos and Jones, 2003). Though the model of Fleischer et al. (1996) is capable to qualitatively predict the transient behaviour of a chemisorption process in a slender bubble column, many authors (Becker et al., 1994; Darmana et al., 2005; Zhang et. al., 2007) found that bubble columns inherently exhibit unsteady three-dimensional flow characteristics. In the so-called hybrid model, the interactions between hydrodynamics, mass transfer, chemical reactions is decoupled, each sub-problem is solved with a separate model, and consequently, the interaction among hydrodynamics, mass transfer and chemical reaction process are not necessarily accounted for. Furthermore, the influence of the mass transfer and chemical reaction on the hydrodynamics is not accounted for and due to limitations to represent a change in bubble size the predictive capabilities will be limited.

In the Euler-Euler model, fully coupling of mass transfer, fluid flow and chemical reaction can be achieved when the local bubble size distribution is known. Though the MUSIG model (Lo, 1996) is capable of predicting a bubble size distribution, its computational effort and the assumption of the same slip velocity for all bubble size classes constrains its application to small scale geometries. As found in previous chapters, interfacial transfer terms appear in each of the conservation equations of mass, momentum and species in each phase. The interfacial transfer terms are strongly related to the interfacial area concentration, a and the local transfer mechanisms such as the degree of turbulence near the interfaces. This makes the interfacial area concentration a very important quantity. Hence, it is pointed out by Isshi (1990) that accurate modeling of the local interfacial area concentration is the first step to be taken for the development of reliable two-fluid (E-E) model closure relations. In the past two decades, much attention (Wu et al., 1998; Millies and Mewes, 1999; Hibiki and Ishii, 2000; Ishii and Kim, 2001; Lehr and Mewes, 2001; Ishii et al., 2002; Kim et al., 2002; Yao and Morel, 2004; Ishii et al.; Lo and Pao, 2007) has been concentrated towards developing an interfacial area concentration transport equation to describe the temporal and spatial evolution of the two-phase geometrical structure. Local Sauter mean diameter d_{32} is obtained through local gas holdup, α_G and interfacial area concentration, a. The main difference among the aforementioned interfacial area concentration models is the closures for breakup and coalescence. Furthermore, the transport equation of interfacial area concentration can be easily transformed to the bubble number density equation as

found in the work of Yeoh and Tu (2004). It is more straightforward to use the bubble number density to track the bubble size, since the bubble number is not changed due to mass transfer, which makes the bubble number density a passive scalar. Therefore, it is adopted in the current work.
The chemisorption of CO_2 into aqueous NaOH solution is chosen as the test case for this work, because it exhibits all important phenomena encountered in practice while its reaction mechanism is well understood and the reaction kinetics are well established.
In this work, simulations were performed with the use of a E-E model for the flow with mass transfer and chemical reaction in a square cross-sectioned gas-liquid bubble column ($W \times D \times H$ = $0.15 \times 0.15 \times 0.55$ m^3) that was aerated with pure CO_2 gas through the bottom plane with a superficial gas velocity of V_S = 0.005 m/s. Drag, virtual mass and lift forces are considered for the interfacial momentum transfer. The Sub-grid scale (SGS) turbulence model proposed by Vreman (2004) was employed to evaluate the shear-induced turbulent viscosity in the continuous phase. Specifically, we study the feasibility and applicability of the bubble number density equation for the numerical simulation of the fully coupled mass transfer, fluid flow and chemical reactions in a reactive gas-liquid flow. Chemisorption of CO_2 into aqueous NaOH solutions with an initial pH value of 12 is studied.

6.2 Governing equations

The equations of the two-fluid model can be obtained by ensemble-averaging of the local instantaneous equations for single-phase flow (Drew, 1999). Two sets of balance equations for mass and momentum are obtained. The generic conservation equations for mass and momentum respectively take the following form:

$$\frac{\partial(\alpha_k \rho_k)}{\partial t} + \nabla \cdot (\alpha_k \rho_k \mathbf{u}_k) = -\dot{m}_{k \to l} \tag{6.1}$$

$$\frac{\partial(\alpha_k \rho_k \mathbf{u}_k)}{\partial t} + \nabla \cdot (\alpha_k \rho_k \mathbf{u}_k \mathbf{u}_k + \alpha_k \boldsymbol{\tau}_k) = \alpha_k \rho_k \mathbf{g} - \alpha_k \nabla p_k + \mathbf{M}_k - \dot{m}_{k \to l} \mathbf{u}_k \tag{6.2}$$

where the index k refers to the phase under consideration (L for liquid, G for gas) and l to the other phase. $\mathbf{u} = (u,v,w)$ is the velocity vector. The volume fraction of each phase is denoted by α, whereas $\dot{m}_{k \to l}$ is the mass transfer rate from phase k to phase l. $\mathbf{M}_k$ represents the inter-phase momentum exchange between phase k and all other phases, and accounts for the interface forces.
For phase k, the stress tensor τ_k appearing in Eq. 6.2 reads:

$$\tau_k = -\mu_{k,eff} (\nabla \mathbf{u}_k + (\nabla \mathbf{u}_k)^T - \tfrac{2}{3} I \nabla \cdot \mathbf{u}_k) \tag{6.3}$$

$\mu_{k,eff}$ is the effective viscosity for phase k. For the liquid phase ($k = L$) is composed of three contributions: the molecular viscosity $\mu_{L,Lam}$, the shear-induced turbulent viscosity $\mu_{L,Tur}$, and an extra term due to bubble-induced turbulence μ_{BIT} :

$$\mu_{L,eff} = \mu_{L,Lam} + \mu_{L,Tur} + \mu_{BIT} \tag{6.4}$$

According to Jakobsen et al. (1997), the effective viscosity of the gas phase ($k = G$) is calculated as follows:

$$\mu_{G,eff} = \frac{\rho_G}{\rho_L}\mu_{L,eff} \tag{6.5}$$

The liquid phase shear-induced turbulent viscosity is evaluated by the SGS model proposed by Vreman (2004):

$$\mu_{L,Tur} = 2.5\rho_L C_S^2 \sqrt{\frac{B_\beta}{S_{ij}S_{ij}}} \tag{6.6}$$

where $B_\beta = \beta_{11}\beta_{22} - \beta_{12}^2 + \beta_{11}\beta_{33} - \beta_{13}^2 + \beta_{22}\beta_{33} - \beta_{23}^2$, $S_{ij} = \partial u_j / \partial x_i$, $\beta_{ij} = \Delta_m^2 S_{mi} S_{mj}$ and Δ_i is the filter width in the i^{th} direction. C_S is a model constant; and $C_S = 0.1$ is used based on the findings in Chapter 3.

The bubble-induced turbulent viscosity appearing in Eq. 6.4 is accounted for through the model of Sato and Sekoguchi (1975):

$$\mu_{BIT} = \rho_L \alpha_G C_{\mu,BIT} d_B |\mathbf{u}_G - \mathbf{u}_L| \tag{6.7}$$

where $C_{\mu,BIT}$ is a model constant which is set to 0.6.

When we assume that there is no coalescence and breakup , the bubble number density equation is given by:

$$\frac{\partial n}{\partial t} + \nabla \cdot (\mathbf{u}_g n) = 0 \tag{6.8}$$

The Sauter mean diameter can be obtained from the bubble number density and the local gas fraction and is expressed as:

$$d_{32} = \left(\frac{6\alpha_G}{\pi n}\right)^{1/3} \tag{6.9}$$

The term $\mathbf{M}_k$ in Eq. 6.2, describing the interface forces, is given by the following expression:

$$\mathbf{M}_L = -\mathbf{M}_G = \mathbf{M}_{L,D} + \mathbf{M}_{L,L} + \mathbf{M}_{L,VM} \tag{6.10}$$

where the terms on the right hand side represent forces due to drag, lift and virtual mass, respectively. They are calculated as:

$$\mathbf{M}_{L,D} = \frac{3}{4}\alpha_G \rho_L \frac{C_D}{d_B} |\mathbf{u}_G - \mathbf{u}_L| (\mathbf{u}_G - \mathbf{u}_L) \tag{6.11}$$

$$\mathbf{M}_{L,L} = \alpha_G \rho_L C_L (\mathbf{u}_G - \mathbf{u}_L) \times \nabla \times \mathbf{u}_L \tag{6.12}$$

$$\mathbf{M}_{L,VM} = \alpha_G \rho_L \mathbf{C}_{VM} (\frac{D_G \mathbf{u}_G}{Dt} - \frac{D_L \mathbf{u}_L}{Dt}) \tag{6.13}$$

According to Tomiyama (2004), the virtual mass coefficient vector $\mathbf{C}_{VM}$ takes the form ($C_{VM,h}$, $C_{VM,v}$, $C_{VM,h}$). Based on our previous study, the following interfacial coefficients are used in this work:

$$C_L = 0.5 \tag{6.14}$$

$$C_{VM,h} = \frac{E\cos^{-1}E - \sqrt{1-E^2}}{E^2\sqrt{1-E^2} - E\cos^{-1}E} \quad C_{VM,V} = \frac{\cos^{-1}E - E\sqrt{1-E^2}}{(2E^{-1} - E)\sqrt{1-E^2} - \cos^{-1}E} \tag{6.15}$$

where E is the bubble aspect ratio as found in Chapter 2.
When the bubble size is changing, the drag coefficient is modeled with the correlation of Tomiyama (2004):

$$C_D = \max[\min[\frac{16}{\mathrm{Re}}(1 + 0.15\,\mathrm{Re}^{0.687}), \frac{16}{\mathrm{Re}}], \frac{8}{3}\frac{E\ddot{o}}{E\ddot{o} + 4}] \tag{6.16}$$

The chemisorption of CO_2 in aqueous alkaline solutions takes place via two reactions. Before these reactions take place, CO_2 gas has to be absorbed in water physically first:

$$CO_2(g) \rightarrow CO_2(aq) \tag{6.17}$$

Subsequently, the elementary reactions then proceed as follows:

$$CO_2(aq) + OH^- \underset{k_{12}}{\overset{k_{11}}{\rightleftharpoons}} HCO_3^- \tag{6.18}$$

$$HCO_3^- + OH^- \underset{k_{22}}{\overset{k_{21}}{\rightleftharpoons}} CO_3^{2-} + H_2O \tag{6.19}$$

Where k_{11} and k_{12} respectively are the forward and backward rate constants for the first reaction (Eq. 6.18) and k_{21} and k_{22} represent the forward and backward rate constants for the second reaction (Eq. 6.19). The reaction rates are consequently written as follows:

$$R_{11} = k_{11}[CO_2(aq)][OH^-] \tag{6.20}$$

$$R_{12} = k_{12}[HCO_3^-] \tag{6.21}$$

$$R_{21} = k_{21}[HCO_3^-][OH^-] \tag{6.22}$$

$$R_{22} = k_{22}[CO_3^{2-}] \tag{6.23}$$

The expressions for the rate constants are provided in appendix A in Chapter 5.

The mass fraction of a chemical species A in the liquid mixture is represented by Y_L^A. The chemical species transport equations for the liquid phase are given by:

Table 6.1: Source terms used in the species transport equations.

Species	Sources (kg/(m^3 s))
CO_2(aq)	$\dot{m}_{G\to L} + \alpha_L(R_{12} - R_{11})M_{CO_2}$
OH^-	$\alpha_L(R_{12} - R_{11} + R_{22} - R_{21})M_{OH^-}$
HCO_3^-	$\alpha_L(R_{11} - R_{12} + R_{22} - R_{21})M_{HCO_3^-}$
CO_3^{2-}	$\alpha_L(R_{21} - R_{22})M_{CO_3^{2-}}$
CO_2(g)	$-\dot{m}_{G\to L}$

$$\frac{\partial(\alpha_L\rho_L Y_L^A)}{\partial t} + \nabla\cdot(\alpha_L\rho_L\mathbf{u}_L Y_L^A - \alpha_L\Gamma_L^A\nabla Y_L^A) = S_A \tag{6.24}$$

whereas the gas phase transport equation for CO_2 is given by:

$$\frac{\partial(\alpha_G\rho_G Y_G^{CO_2})}{\partial t} + \nabla\cdot(\alpha_G\rho_G\mathbf{u}_G Y_G^{CO_2} - \alpha_G\Gamma_G^{CO_2}\nabla Y_G^{CO_2}) = S_G^{CO_2} \tag{6.25}$$

The relevant chemical species and their source terms are listed in Table 6.1.
The mass transfer rate of species CO_2 per unit volume, $\dot{m}_{G\to L}$, from the dispersed phase to the continuous phase, is defined as:

$$\dot{m}_{G\to L} = k_L a E \rho_L (Y_{GL,e}^{CO_2} - Y_L^{CO_2}) \tag{6.26}$$

where k_L is the overall mass transfer coefficient for the chemical species CO_2(aq), $a = 6\alpha_G/d_{32}$ is the interfacial area concentration , E is the enhancement factor due to the chemical reaction, and $Y_{GL,e}^{CO_2}$ is the equilibrium mass fraction of CO_2(aq) in the liquid phase. Detailed information of k_L, E and $Y_{GL,e}^{CO_2}$ can be found in Chapter 5.

6.3 Numerical solution method

All the numerical simulations are carried out with the commercial CFD package CFX-4.4 of AEA Technology, Harwell, UK. The total domain is subdivided into uniform computational grid cells with $\Delta x = \Delta y = \Delta z = 0.01$ m. Eqs. 6.1 and 6.2 are solved in a transient fashion. Different time steps are used for each of the cases and these are listed in Table 6.2. The curvature compensated convective transport (CCCT) scheme is used for the discretization of all convective terms. "Opening" boundaries are applied at the outlet and it requires that:

$$\alpha_L = 0;\ \alpha_G = 1 \tag{6.27}$$

In the gas cap, special measures need to be taken to prevent numerical problems due to the high gas volume fraction. This is accomplished as follows:

$$\alpha_L < 0.55 \quad \begin{cases} C_D = 0.05 \\ C_L = 0 \\ C_{VM} = 0 \end{cases} \tag{6.28}$$

With these measures, Eqs. 6.1 and 6.2 in approximation reduce to those for single phase flow. A small finite value for C_D is required in Eq. 6.28 to guarantee proper coupling of the two phases.
It should also be noted that, an unrealistically large bubble size might be obtained from Eq. 6.9 when the local bubble number density is very small ($nV_{\text{cell}} << \varepsilon$, $\varepsilon = 10^{-6}$). To prevent this from happening, a bubble size cutoff is exerted in our simulation, which takes a value of $d_{B,cutoff} = 4.05$ mm:

$$d_B = \max\left(d_{B,cutoff}, d_{32}\right) \tag{6.29}$$

6.4 Physical problem

A sketch of the bubble column studied in this work is shown in Figure 6.3. The column is initially filled to a height of 0.45 m with pure water or aqueous NaOH solution with an initial pH value of 12. Air or pure CO_2 is used as the dispersed gas phase and injected in the center of the bottom plane with $A_{in} = 0.03 \times 0.03$ m^2 and $V_{G,in} = 0.1225$ m/s corresponding to a superficial gas velocity of 4.9 mm/s. Initially, the gas cap above the liquid is filled with inert N_2 gas. The gas-liquid flow is assumed to be homogeneous (bubbly) flow and break-up and coalescence are not accounted for. The width, depth and height of the column are respectively set to $W = 0.15$ m, $D = 0.15$ m, and $H = 0.55$ m. The gas distributor is located in the bottom wall of the column at a distance of 0.06 m from each of the surrounding walls of the column. All the simulation parameters and physical properties are presented in Table 6.2. Diffusivities of the four species were obtained from the work of Bauer (2001). An initial bubble size of 4 mm is used and the bubble number density equation is incorporated to obtain the bubble size, which is used to calculate the interfacial closure coefficients and the overall mass transfer coefficient.

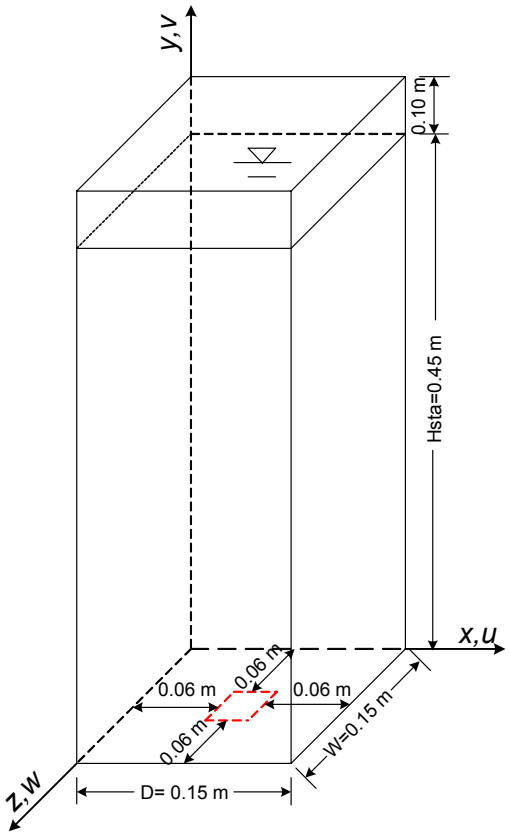

Figure 6.3: Schematic representation of the investigated bubble columns. "Opening" boundary conditions is applied at the outlet.

Table 6.2: Case definition and involved parameters.

Case	Liquid mixture	Initial pH of liquid mixture	inlet gas	d_B	Drag coefficient	with species equation
1	pure water	7	air	4 mm	1.071	no
2	pure water	7	Pure CO_2	4 mm	Tomiyama (2004)	yes
3	pure water	7	Pure CO_2	Eq. 6.29	Tomiyama (2004)	yes
4	aqueous NaOH solution	12	Pure CO_2	4 mm	Tomiyama (2004)	yes
5	aqueous NaOH solution	12	Pure CO_2	Eq. 6.29	Tomiyama (2004)	yes
$\rho_L = 1000$ kg/m^3, $\rho_G = 1.98$ kg/m^3, $\mu_{L,Lam} = 0.001$ kg/(m.s), $\mu_{G,Lam} = 1.812\times10^{-5}$ kg/(m.s). $\sigma = 0.07275$ N/m. $D_{CO_2} = 1.699\times10^{-9}$ m^2/s; $D_{OH^-} = 5.3\times10^{-9}$ m^2/s; $D_{HCO_3^-} = 1.1\times10^{-9}$ m^2/s; $D_{CO_3^{2-}} = 1.5\times10^{-9}$ m^2/s						

6.5 Results and Discussion

The implementation of the number density model in CFX4.4 is first tested with the aid of a case without absorption. Subsequently the model is applied to the cases of physical absorption of pure CO_2 into pure water and chemisorption of pure CO_2 into aqueous NaOH solution with an initial pH value of 12.

6.5.1 No absorption

Case 1 is employed to verify the implementation of the bubble number density model in CFX-4.4. In this case, a constant bubble diameter and drag coefficient (C_D = 1.071) are assumed, the Sauter diameter is obtained through Eq. 6.9. Figure 6.4 shows the predicted local bubble diameter history at a monitoring point in the center of the column. Clearly, a constant bubble size is achieved in this case, i.e. the error in the predicted bubble diameter is less than 0.1%. Figure 6.5 presents the simulated instantaneous bubble diameter in horizontal and vertical directions. It is found here that the predicted bubble diameter is consistent with the assumed bubble diameter, which proves the correctness of the current implementation.

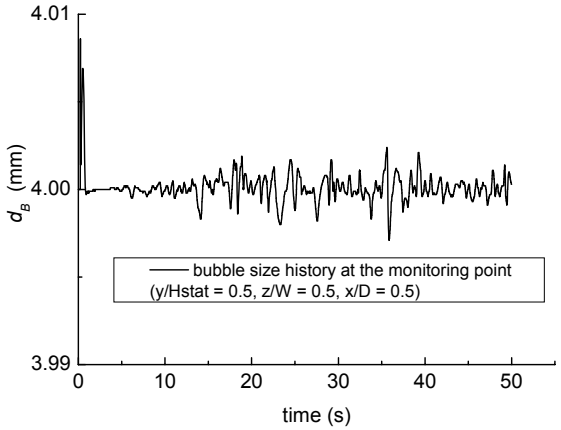

Figure 6.4: Local bubble diameter history obtained from numerical simulation.

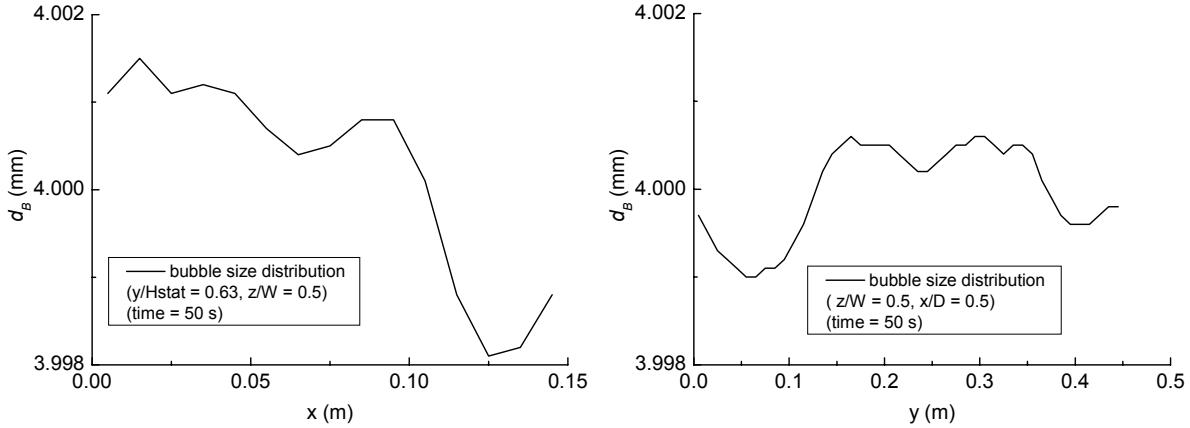

Figure 6.5: Instantaneous bubble Sauter diameter distribution in horizontal (left) and vertical (right) directions.

6.5.2 Physical absorption of pure CO_2 bubbles in water

During physical absorption of pure CO_2 in water, dispersed CO_2 bubbles are shrinking. A number density equation is solved here to keep track of the bubble size change in order to couple the mass transfer and flow dynamics. The bubble diameter obtained from Eq. 6.9 is used to calculate drag coefficient (Eq. 6.16), bubble-induced turbulence (Eq. 6.7) and mass transfer rate (Eq. 6.26). Figure 6.6 displays the instantaneous predicted bubble diameter in horizontal and vertical directions. It is seen that vertically the bubble diameter shrinks from 4 mm to about 3.6 mm due to the physical absorption. Along the column walls the bubble residence time is longer than in the center of the bubble column, leading to a smaller bubble diameter in those regions.

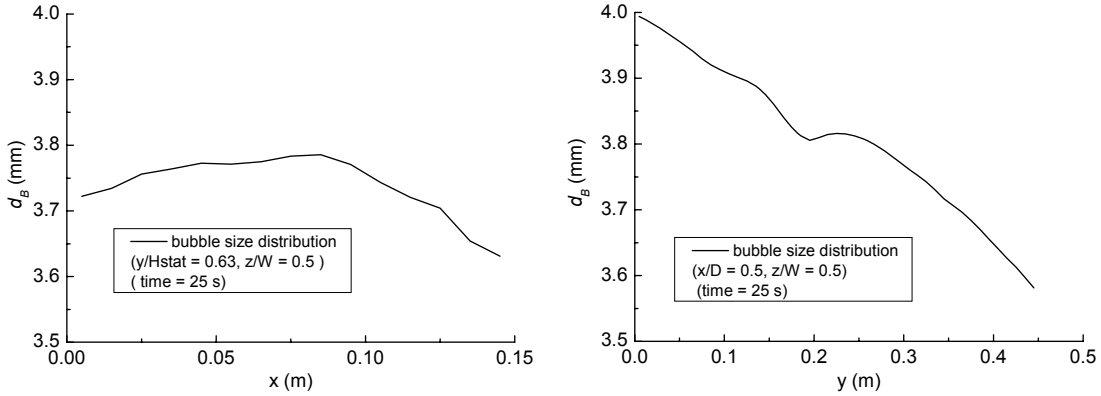

Figure 6.6: Instantaneous bubble size distribution in horizontal (left) and vertical (right) directions during physical absorption of pure CO_2 in water.

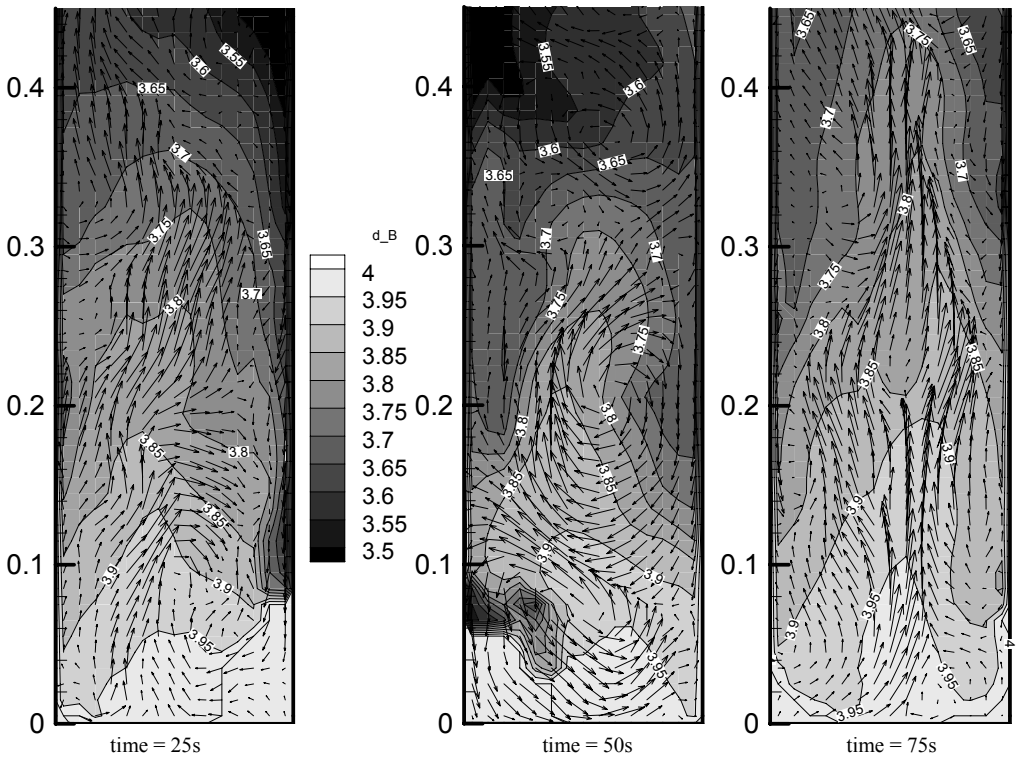

Figure 6.7: Snapshots of the instantaneous bubble diameter distribution and liquid phase velocity field in the plane of z/W = 0.5 obtained from numerical simulation during physical absorption of pure CO_2 in water at different times.

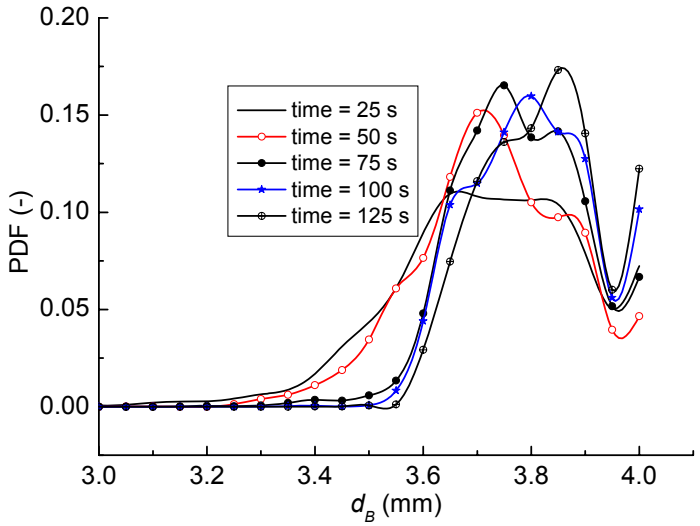

Figure 6.8: Probability density function of the bubble size in the entire column at different times.

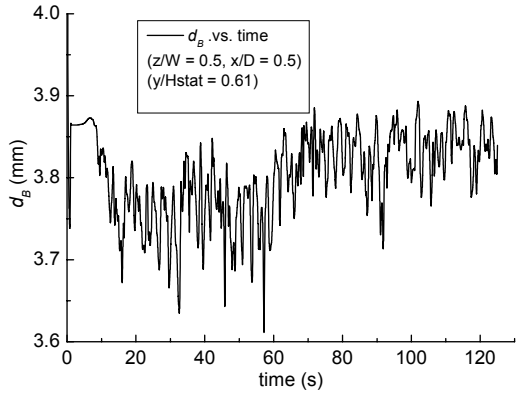

Figure 6.9: Local bubble diameter history obtained from numerical simulation during physical absorption of pure CO_2 in water.

Figure 6.7 illustrates the instantaneous bubble size distribution and liquid phase velocity field. As expected, the flow in the column is quite dynamic, and the bubble size is decreasing with the increase of distance from the sparger. As found earlier, the bubble size along the confining walls is relatively small.

Figure 6.8 demonstrates the probability distribution function of the bubble size averaged in the entire column at different times during the physical absorption of pure CO_2 in water. As expected, with time the liquid gets saturated with CO_2 (aq) and reduction in bubble size is less, thus as found in Figure 6.8, the bubble size distribution in the entire column is shifting towards larger bubble sizes. Due to the small and large scales of mixing induced by convection and the meandering behavior of the bubble plume, the local bubble size increasing behavior shows an oscillatory behavior, which is shown in Figure 6.9.

The comparison of the overall normalized dissolved CO_2 concentration of the entire column obtained from the constant bubble size (Case 4) and dynamic bubble size (Case 3) has also been made and is displayed in Figure 6.10. In case 3, the bubble size is smaller due to the mass transfer, which leads to a longer residence time, and thus the predicted dissolved CO_2 concentration is a little bit higher than that from case 4, where a constant bubble size is used. The discrepancy between the macroscopic model (see Darmana et al., 2005) and cases 3 and 4 comes from the fact, that in the detailed model, the gas volume fraction and bubble size are changing with time.

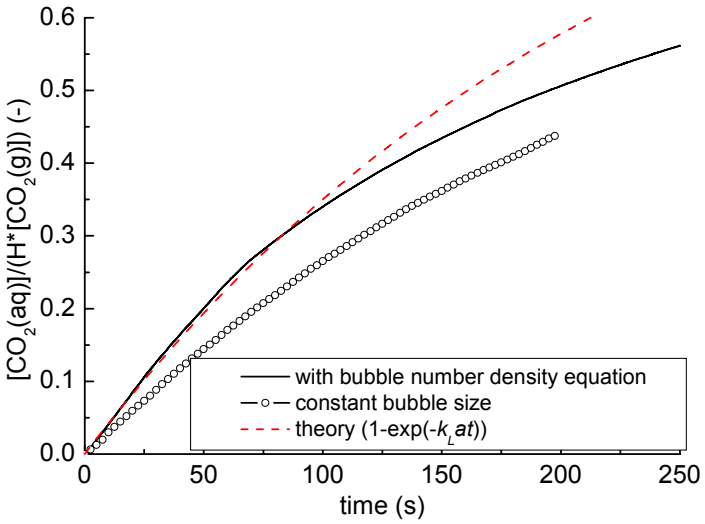

Figure 6.10: Comparison of the normalized dissolved CO_2 concentration in the entire column obtained from different cases during physical absorption of pure CO_2 in water.

6.5.3 Chemisorption of pure CO_2 bubbles in aqueous NaOH solution

In this section, we study the chemisorption of pure CO_2 in aqueous NaOH solution with an initial pH value of 12. Transport equations for the mass fractions of aqueous CO_2, OH^-, HCO_3^- and CO_3^{2-} are solved as well as the mass fraction of CO_2 in the gas phase.

As the chemisorption of CO_2 is characterized by the consumption of gas CO_2 and liquid OH^- and production of CO_3^{2-}, Figure 6.11 shows the evolution of the local bubble diameter and the instantaneous species concentration of OH^- and CO_3^{2-} at a monitoring point. It is observed here that the bubble size decreases dramatically shortly after CO_2 bubbles arrive at the monitoring point. Subsequently, OH^- is consumed immediately after the CO_2 bubbles arrive at the monitor point, and correspondingly, CO_3^{2-} is produced quickly. Then, the local bubble size is rather constant for a short period as the local gas hold-up is also constant. Due to the consumption of CO_2 and the subsequent meandering behavior of the bubble plume, the bubble size history shows an oscillating pattern, which leads to an oscillatory decrease of the OH^- concentration.

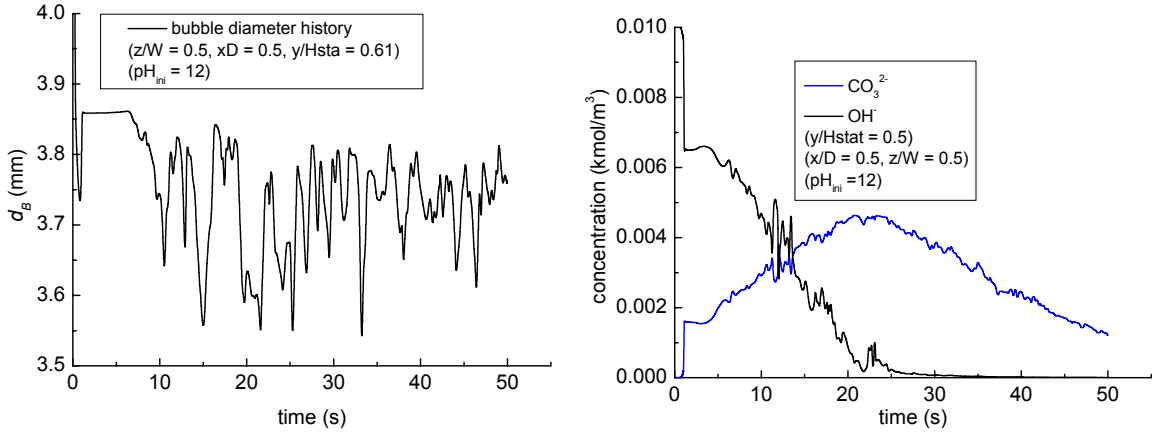

Figure 6.11: Local bubble diameter (left) and concentration history of CO_3^{2-} and OH^- species (right) evolution history obtained from numerical simulation during chemisorption of pure CO_2 in aqueous NaOH solution with an initial pH = 12. A bubble number density equation is used to obtain the bubble size.

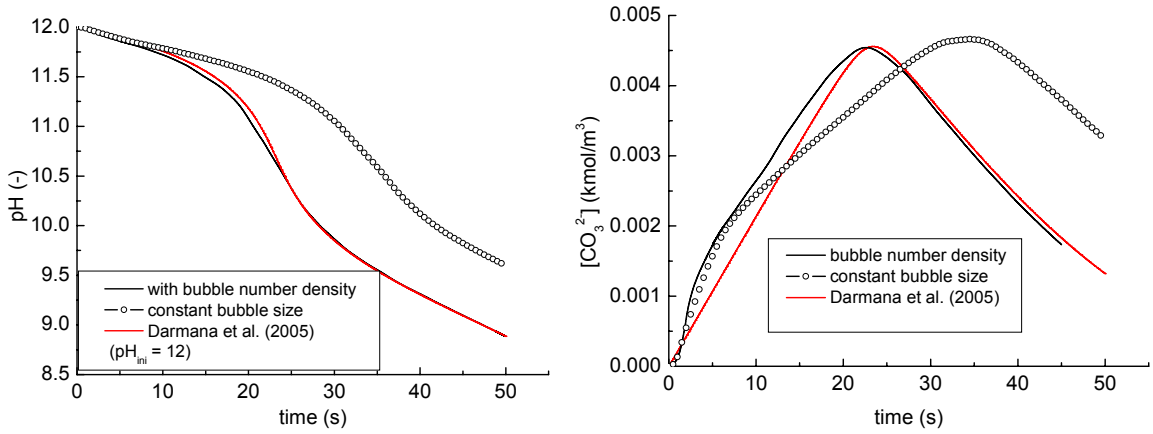

Figure 6.12: Comparison of the overall pH history (left) and concentration history of the CO_3^{2-} species (right) in the entire column involved in the chemical reaction process resulting from different the numerical simulations.

In Figure 6.12, the predicted histories of pH and the CO_3^{2-} species concentration averaged over the entire column obtained from cases 4 and 5 are compared with those obtained from a simple macroscopic model, employing the average bubble size and gas holdup obtained from the detailed numerical simulation (Darmana et al., 2005). It is found that when bubble size is tracked (Case 5), numerical simulated results agree well with the simple model, whereas with the constant bubble size assumption, the difference between the detailed numerical results and those obtained from the simple model is larger, which in turn implies that it is important to use a dynamic bubble size.

Figure 6.13 displays snapshots for bubble size and gas phase velocity field, liquid phase volume fraction and velocity field and pH distribution in the column. As found in Figure 6.13, the bubble size distribution greatly depends on the local flow structure. Furthermore, the bubble size change is still within 1 mm, which is caused by the short residence time of bubbles. After 40 s the pH is distributed uniformly around a value of about 9.2, which is due to the fact that the reactive system is past the first acidity constant of $pK_{a,1} = 10.3$.

Figure 6.14 shows the instantaneous predicted bubble diameter in horizontal direction at different heights and the variation of the entire column bubble size distribution with times. It is found again that in the beginning, the bubble size decreases with the increasing of height; and always, the bubble diameter in the column center is larger than along the walls due to differences in residence times. Furthermore, contrary to the case of physical absorption the bubble size distribution hardly changes with time. This can be explained by the fact that all transferred CO_2 immediately reacts, leading to an approximately constant mass transfer rate.

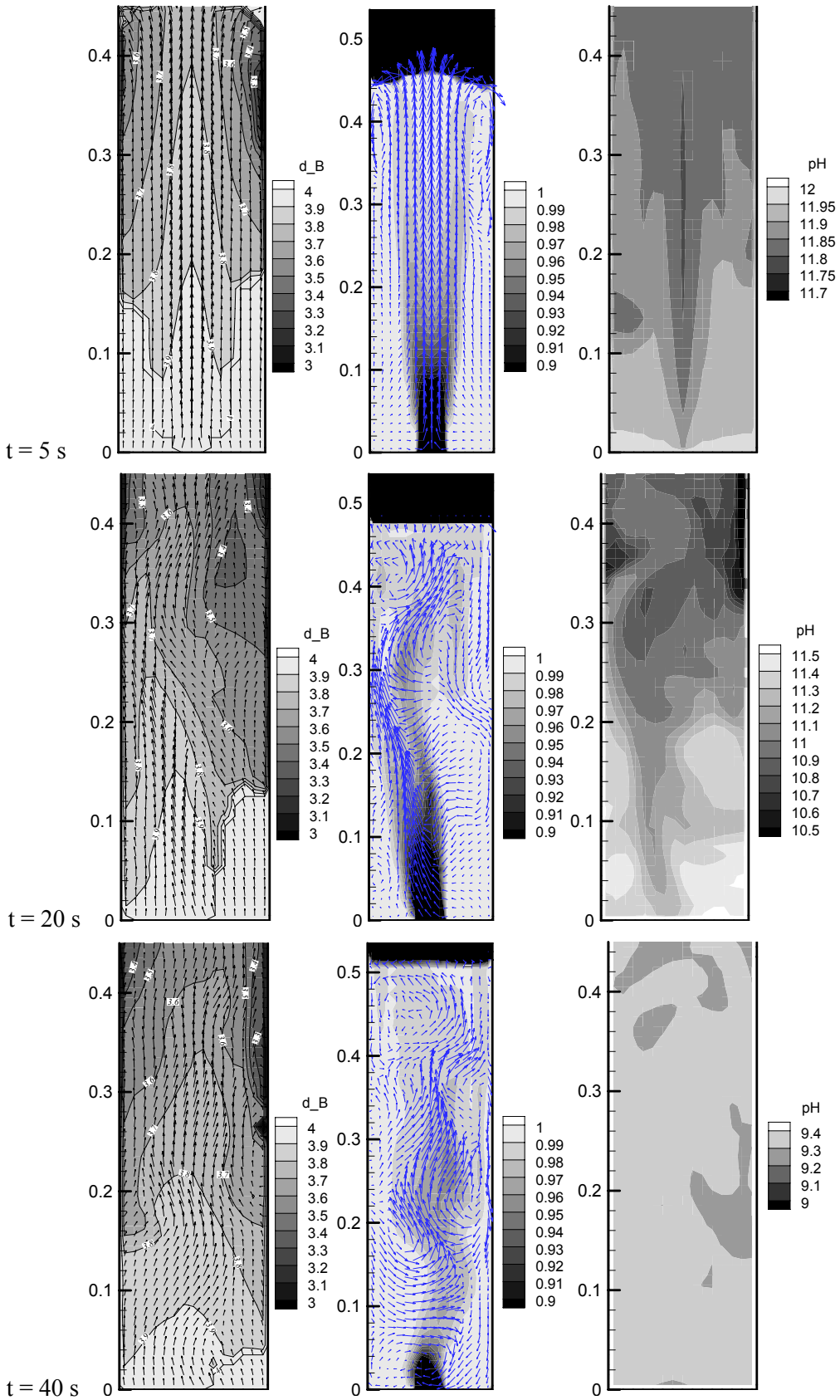

Figure 6.13: Snapshots of instantaneous bubble size distribution and gas phase velocity field (left), liquid phase volume fraction and velocity field (middle) and pH distribution (right) in the plane of z/W = 0.5 at different times during chemisorption of pure CO_2 in aqueous NaOH solution with an initial pH = 12.

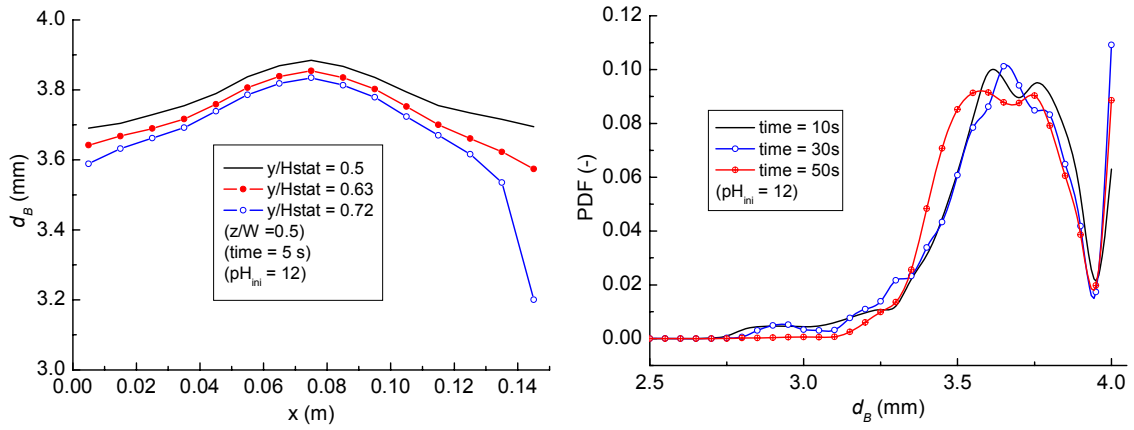

Figure 6.14: Instantaneous bubble size distribution in horizontal direction at different heights (left) and entire column averaged bubble size distribution at different times (right) during chemisorption of pure CO_2 in aqueous NaOH solution with an initial pH = 12. A bubble number density equation is used to obtain the bubble size.

6.6 Conclusions

Numerical simulations of the gas-liquid two-phase flow with mass transfer in a square cross-sectioned bubble column were carried out, by incorporating a bubble number density equation. First a simulation without mass transfer was carried out to verify that the bubble size that follows from this equation is the same as the assumed bubble size. The error in the predicted bubble size was less than 0.1%, which makes the model suited for application to systems with mass transfer.

When pure CO_2 is absorbed into water, the flow is quite dynamic, and the bubble size does not change much, bubble size ranges from 3 to 4 mm in the entire column. Generally, the bubble size inside the bubble plume is larger than those close to the walls, where the bubbles that are trapped in strong down flow have more time to transfer species. .

Chemisorption of pure CO_2 into aqueous NaOH solution with an initial pH value of 12 has been simulated as well. Fully coupling of fluid flow, mass transfer and chemical reaction is achieved by employing the bubble number density model. As the mass transfer is not chemically enhanced (E = 1), the bubble size ranges from 2.7 to 4 mm in this test case. The simulated column averaged pH agrees well with that obtained from a simple macroscopic model (Darmana et al., 2005). The differences between the macroscopic model and the numerical results obtained with the constant bubble size are due to the decoupling of fluid flow and mass transfer in the latter model. This indicates the necessity to account for changes in bubble size and proves the added value of the bubble number density equation.

All the numerical results are only presented qualitatively; a more detailed comparison of the E-E results with available E-L simulated results and/or experimental data is still required. Also, numerical simulation of chemisorption of pure CO_2 in NaOH solution with higher pH should be carried out.

6.7 Notation

a	interfacial area (m^2); strain rate (s^{-1})
B	Sub-grid scale model parameter (m^4 s^{-4})
d	diameter (m)
c	species concentration (kmol m^{-3})
C	model coefficient, dimensionless
D	depth (m); diffusivity (m^2 s^{-1})

g	gravitational constant (m s^{-1})
E	enhancement factor, dimensionless
Eö	Eötös number, dimensionless
H	Henry constant, dimensionless; height (m)
Ha	Hatta number, dimensionless
I	ionic concentration (kmol m^{-3})
k_{11}	forward reaction rate constant (m^3 $kmol^{-1}$ s^{-1})
k_{12}	backward reaction rate constant (s^{-1})
k_{21}	forward reaction rate constant (m^3 $kmol^{-1}$ s^{-1})
k_{22}	backward reaction rate constant (s^{-1})
k_l	overall mass transfer coefficient (m s^{-1})
K_1	equilibrium constant for reaction 1 (m^3 $kmol^{-1}$)
K_2	equilibrium constant for reaction 2 (m^3 $kmol^{-1}$)
M	interfacial force (kg m s^{-2})
$\dot{m}$	mass transfer from gas(single bubble) (kg s^{-1})
m	mass of single bubble (kg)
n	bubble number density (m^{-3})
P	pressure (Nm^{-2})
PDF	probability distribution function
R	reaction rate (kmol m^{-3} s^{-1})
Re	Reynolds number, dimensionless
S	source term in the species balance equation, kg m^{-3} s^{-1}
Sh	Sherwood number, dimensionless
t	time (s)
T	temperature (K)
u	velocity vector (m s^{-1})
u	velocity component in x direction (m s^{-1})
v	slip velocity (m s^{-1})
v	velocity component in y direction (m s^{-1})
w	velocity component in z direction (m s^{-1})
Y	mass fraction, dimensionless
z	ionic charge, dimensionless
[.]	concentration (kmol m^{-3})

Greek letters

Δ	subgrid length scale (m)
Γ	species diffusion coefficient (m^2 s^{-1})
ρ	density (kg m^{-3})
β	Sub-grid scale model parameter (m^2 s^{-2})
σ	interfacial tension (N m^{-1})
μ	viscosity (kg m^{-1} s^{-1})
τ	Stress tensor (N m^{-2})

Subscripts

aq	aqueous
B	bubble
BIT	Bubble-induced turbulence
D	drag
e	equilibrium

eff	effective
G	gas
GL	Gas-liquid
h	horizontal direction
i	Cartesian ordinate direction index
j	Cartesian ordinate direction index
k	phase indicator
L	lift, liquid
Lam	laminar
rel	relative velocity
S	subgrid scale model
Tur	shear-induced turbulence
v	vertical direction
VM	virtual mass
32	The Sauter mean diameter

Superscripts

w	water

6.8 Bibliography

Bauer, M. and Eigenberger, G., 1999. A concept for multi-scale modeling of bubble columns and loop reactors. *Chem. Eng. Sci.,* 54, 5109-5117.

Bauer, M. and Eigenberger, G., 2001. Multiscale modeling of hydrodynamics, mass transfer and reaction in bubble columns reactors. *Chem. Eng. Sci*., 56, 1067-1074.

Bauer, M., 2001. On the multiscale modeling of bubble column reactors. PhD thesis, University of Stuttgart, Germany.

Becker, S., Sokolichin, A. and Eigenberger, G., 1994. Gas-liquid flow in bubble columns and loop reactors:Part II. Comparison of detailed experiments and flow simulations. *Chem. Eng. Sci.,* 49, 5747-5762.

Darmana, D., Deen, N. G. and Kuipers, J. A. M., 2005. Detailed modeling of hydrodynamics, mass transfer and chemical reactions in a bubble column using a discrete bubble model. *Chem. Eng. Sci.*, 60, 3383-3404.

Deen, N. G., Solberg, T. and Hjertager, B. H., 2001. Large eddy simulation of the gas-liquid flow in a square cross-sectioned bubble column. *Chem. Eng. Sci.*, 56, 6341-6349.

Delnoij, E., Kuipers, J. A. M. and Van Swaaij, W. P. M, 1997. Dynamic simulation of gas-liquid two-phase flow: effect of column aspect ratio on the flow structure. *Chem. Eng. Sci.*, 52, 3759-3772.

Delnoij, E., Kuipers, J. A. M. and Van Swaaij, W. P. M, 1999. A three-dimensional model for gas-liquid bubble columns. *Chem. Eng. Sci.*, 54, 2217-2226.

Drew, D. A. and Passman, S. L., 1999. Theory of multicomponent fluids, Applied Mathematical Sciences 135, Springer.

Fleischer, C., Becker, S. and Eigenberger, G., 1996. Detailed modeling of the chemisorption of CO_2 into NaOH in a bubble column. *Chem. Eng. Sci.,* 51, 1715-1724.

Hibiki, T. and Ishii, M., 2000. One-group interfacial area transport of bubbly flow in vertical round tubes. *Int. J. Heat Mass Transfer*, 43, 2711-2726.

Ishii, M., 1990. Two-fluid model for two-phase flow. *Multiphase Sci. Tech.*, 5, 1-58.

Ishii, M., Kim, S. and Uhle, J., 2002. Interfacial area transport equation:One-group interfacial area transport model development and benchmark experiments. *Int. J. Heat Mass Transfer*, 45, 3111-3123.

Ishii, M., Kim, S. and Kelly, J., 2005. Development of interfacial area transport equation. Nuclear Engineering and Technology, 37, 525-536.

Jakobsen, H. A., Sannæs, B. H., Grevskott, S. and Svendsen, H. F., 1997. Modeling of vertical bubble-driven flows. *Ind. Eng. Chem. Res*., 36, 4052-4074.

Kim, S., Ishii, M., Sun, X. and Beus, S. G., 2002. Interfacial area transport and evaluation of source terms for confined air-water bubbly flow. *Nucl. Eng. Des.*, 219, 61-65.

Lehr, F. and Mewes, D., 2001. A transport equation for the interfacial area density applied to bubble columns. *Chemical Engineering Science*, 56, 1159-1166.

Lo, S., 1996. Application of Population Balance to CFD Modelling of Bubbly Flow via the MUSIG model, AEA Technology, *AEAT-1096*.

Lo, S. and Rao, P.,2007. Modelling of droplet breakup and coalescence in an oil-water pipeline. Poster paper PS2_6, 6th International Conference on Multiphase Flow, Leipzig, Germany, July 9-13.

Márquez, M. A., Amend, R. J., Carbonell, R. G., Sáez, A. E. and Roberts, G. W., 1999a. Hydrodynamics of gas-lift reactors with a fast, liquid-phase reaction. *Chem. Eng. Sci.*, 54, 2263-2271.

Márquez, M. A., Sáez, A. E., Carbonell, R. G. and Roberts, G. W., 1999b. Coupling of hydrodynamics and chemical reaction in gas-lift reactors. *AIChE, J.*, 45, 410-423.

Millies, M. and Mewes, D.,1999. Interfacial area density in bubbly flow. *Chemical Engineering and Processing*, 38, 307-319.

Rigopoulos, S. and Jones, A., 2003. A hybrid cfd-reaction engineering framework for multiphase reactor modeling: basic concept and application to bubble column reactors. *Chem. Eng. Sci*., 58, 3077-3089.

Sato, Y. and Sekoguchi, K., 1975. Liquid velocity distribution in two-phase bubble flow. *Int. J. Multiphase Flow*, 2, 79-95.

Tomiyama, A., 2004. Drag, lift and virtual mass forces acting on a single bubble. 3rd International Symposium on Two-Phase Flow Modeling and Experimentation. Pisa, Italy. 22-24 Sept.

Vreman, A. W., 2004. An eddy-viscosity subgrid-scale model for turbulent sher flow: Algebraic theory and applications. *Phys. Fluids*, 16, 3670-3681.

Wu, Q., Kim, S., Ishii, M. and Beus, S. G., 1998. One-group interfacial area transport in vertical bubbly flow. *Int. J. Heat Mass Transfer*, 41, 1103-1112.

Yao, W., and Morel, C., 2004. Volumetric interfacial area prediction in upward bubbly two-phase flow One-group interfacial area transport in vertical bubbly flow. *Int. J. Heat Mass Transfer*, 47, 307-328.

Yeoh, G. H. and Tu, J. Y., 2004. Modeling gas-liquid bubbly flows. 15th Australasian Fluid Mechanics Conference. The University of Sydney, Sydney, Australia, 13-17 December.

Zhang, D., 2005. Numerical simulation of dynamic flow behavior in a bubble column: grid and time-independent solution. *Technical report*. University of Twente, March.

Zhang, D., Deen, N. G. and Kuipers, J. A. M., 2006. Numerical simulation of dynamic flow behavior in a bubble column: A study of closures for turbulence and interface forces. *Chem. Eng. Sci.*, 61, 7593-7608.

Zhang, D., Deen, N. G. and Kuipers, J. A. M., 2007. Numerical Modeling of Hydrodynamics, Mass transfer and Chemical Reaction in Bubble Columns. International Conference on Multiphase

Flow, ICMF 2007, Leipzig, Germany, July 9 – 13.

Zhang, D., 2007. Numerical simulation of dynamic flow behavior in a bubble column: bubble number density equation and the S_γ model. *Technical report*. University of Twente, June.

Publication list

1. D. Zhang**,** N. G. Deen and J. A.M. Kuipers. Numerical Simulation of the Dynamic Flow Behavior in a Bubble Column: A Study of Closures for Turbulence and Interface Forces. Chemical Engineering Science, Vol.61: 7593-7608, 2006.

2. D. Zhang, N. G. Deen and J.A.M. Kuipers. Numerical Simulation of the Dynamic Flow Behavior in a Bubble Column: Comparison of the Bubble-Induced Turbulence Models in k-ε Model. CFD 2005 - 4th International Conference on Computational Fluid Dynamics, Trondheim, Norway, June 5 – 7. 2005.

3. D. Zhang, N.G. Deen and J.A.M. Kuipers. Numerical Simulation of Small bubble-Big bubble-Liquid Three-Phase Flows. CHISA 2006, Prague, Czech Republic, August 27 – 31, 2006.

4. D. Zhang, N.G. Deen and J.A.M. Kuipers. Numerical Modeling of Hydrodynamics, Mass transfer and Chemical Reaction in Bubble Columns. International Conference on Multiphase Flow, ICMF 2007, Leipzig, Germany, July 9 – 13, 2007.

Presentations

1. D. Zhang, N.G. Deen and J.A.M. Kuipers. Bubble column modeling: Comparison of the Bubble-Induced Turbulence Models in the k-ε model. Numerical Simulation of small-Bubble Big-Bubble Liquid Three-Phase Flows. NPS 5, 26 October, 2005, Veldhoven, The Netherlands.

2. D. Zhang, N.G. Deen and J.A.M. Kuipers. Numerical Simulation of small-Bubble Big-Bubble Liquid Three-Phase Flows. Benelux ANSYS en CFX User meeting, 3 November 2006, Breda, The Netherlands.

Acknowledgements

And now I have arrived at the final part of the thesis!

During the past four years studying the reactive gas-liquid flow in the research group Fundamentals of Chemical Reaction Engineering group, Faculty of Science and Technology, University of Twente, I have received a lot of support from my colleagues, family and friends. Here I would like to express my sincere thanks to you all for your help, support, discussion and friendship.

First of all, I wish to thank my supervisor, Professor Hans Kuipers for hosting me in his group as a PhD student, as this will greatly change my career life. His patient guidance and discussions with him and his kind help in all aspects have made the past years an ever-good memory in my life. Furthermore, I would like to mention that his ability to understand my English (especially at the beginning of my study) is impressive! I would like to express my sincere thanks to his wife, Liesbeth for generating the homely stay in Enschede through managing the social side of the group and organizing bowling and Waarbeek festivals.

Special thanks goes to Dr. ir. Niels Deen who coached me in the past four years. I will long-remember our fruitful weekly discussions and your encouragement, tolerance and understanding! You motivated and encouraged me during the research and the writing of the thesis, especially the last chapter would not have been possible without your kind help! I would like to thank you for helping me prepare the concept thesis, for all the grammatical correction work of the papers and thesis and for translating the summary into Dutch and all other things you did for me. I have learned quite a lot from your extensive knowledge in chemical engineering and fluid flow and software use and many brilliant and creative ideas!

Then I want to thank dr. ir. Martin van Sint Annaland for his kind help and support. Your working style and spirit always encourage me to work harder. My sincere thanks also for Martin van der Hoef for his kind help and discussions in the code developing.

Furthermore, I would like to thank Professor Lohse and and Professor van der Vegt for their kind encouragements and for reading and reviewing my thesis.

I am grateful to Gerrit and Wim, the technicians in the group for their help in small experimental tests. Robert, thanks very much for your help in PC installing, email settings and cluster settings and maintaining.

A warm thank you goes to Eduard Bos in the Telecommunication Engineering group, University of Twente, who was always willing to help me and my wife at any time. Your kind translating of Dutch letters, life suggestions and so on always made our stay in the Netherlands comfortable.

I like to thank all other members of the Fundamentals of Chemical Reaction Engineering group: Albert, Charu, Christiaan, Dadan, Esther, Jan Albert, Jeroen, Joris, Mao Ye, Martin Tuinier, Maureen, Renske, Sabita, Sander, Sebastian, Tymen, Wei Bai, Wenxing, Willem and Wouter for bringing the friendly and creative atmosphere, nice X'mas parties and memorable sailing events and borrels.

Special thanks for warm-hearted Chris for all his kind help. Genius Wouter, thanks very much for offering me your most recent front tracking results. Albert, thanks for your introduction to the Euler-Euler model. It has been a pleasure to talk with goal keeper Jan Albert about the Dutch national soccer team, though it always was annoying him. Tymen and Sander, it was very interesting and joyful to talk with you during lunch time and learn more about Dutch society. Jeroen, it was very nice to talk with you about China and joke with you. Dadan, I still remember my beginning days in FAP and it was nice to argue with you about the advantages of the Euler-Euler model. Dear Martin and Ivo, it will be a good memory of our Chinese talking. Beauty Maureen and sailor Willem, thanks very much for becoming my paranimfen. Bai, thanks for your help. Renske, you are the first and only Internationale Chemie Olympiade winner I ever knew and worked with! Sebastian, thanks very much for organizing FCRE parties and borrels and maintaining OSCAR clusters. All the poker guys, Wouter, Baco, Wessel, Tom, it has been very funny and joyful to play poker during lunch time! Roy, it was very nice to talk with you about chemical reaction and your help to get back my luggage will be long remembered.

I wish to express my thanks to Nicole Haitjema for her help in many administrative matters and Dutch translations and other kinds of help. All the things you did made my stay in the Netherlands feel like home.

I like to thank Simon Lo in CD-adapco for his kind offering of the most recent developed s-gamma model and our nice talking in Prague and Leipzig.

Special thanks is given to my mother-in-law, Cuilan Luan for all her kind help and support. You hold the whole family and are always there when we need help. Many thanks to you for taking care of Evan and doing the house work for us, especially in my final stage of thesis. Dear mother, I am indebted to you for all my life!

Many new friendship were born during my stay in Twente: Jia Tian, Jing Song, landlord Zhou, Wei Zhou, Wenxing Zhang, Xinhui Wang, Yang Zhang, beauty Zeng (in ITC). The small family parties, dinners, borrels and memorable outings made my life in Enschede colorful. Landlord, our cycling along the highway will be long-remembered! Zeng, your kind and supportive words in my stressful job hunting times are appreciated with utmost gratitude! Yuanqing Guo and Jianbo Zhang, we are very lucky to know you, especially after we realized that you already know Hong and her story. Thanks a lot to all your help, suggestions and support. I would like to thank Jiahua Chen and Mao Ye, Yizhi He and Xiaoquan Zhao; Yu Wang and Jian Wu and Xia Bian and Pengxiang Xu for all your help and happy times we had.

I owe many thanks to my family. I am grateful to my parents for giving me their deep love, encouragement and support during my years of education. I want to thank my sisters Lifang Zhang, Liqin Zhang and brother, Qisheng Zhang and their families for taking care of our parents and all the support, which made my stay in the Netherlands possible.

There are a lot of thanks I want to mention to my deeply loved wife, Hong He. Thank you for giving the most patient and loving support and encouragement, especially giving me my lovely son, Evan. Many thanks to you for your patient listening tomy complex and sometimes boring stories about my work, which always sparks me and leads me out of difficulty.

Now to my very important person, my cute and healthy son, Evan! You brought and are bringing lots of happiness, fresh air of life, hope and good luck to us! Your brilliant smiles always made me go forward in my stressful job-hunting times. I hope you will be happy and healthy all days of your life.

I like to thanks the user committee members in the project: Bob, thanks very much for your encouragement and kind suggestions. Maurice, thanks a lot for talking with me about gas-liquid flow. Piotr, thanks for your suggestions and remarks, your advices were finally realized in this thesis. Mathijs, thanks for your critical remarks and suggestions. Peter, it was very nice to talk with you about gas-liquid flow in industrial scale. Wouter, thanks very much for your advices. Lars and Hanneke, our cooperation and free talk will be a good memory for me. The mutual communications and suggestions during the user meetings improved my work.

Finally, I want to acknowledge the funding from STW, FOM, Shell, DSM, Akzo Nobel and MARIN.

Dongsheng Zhang
August 12, 2007, Enschede

About the author

Dongsheng Zhang was born on October 25th 1974 in Fugu, Shaanxi, China.

After completing his secondary education in Mazhen High school in 1992, he attended Xi'an University of Technology, where he acquired his B.Sc degree of Engineering of Cropland Irrigation Works in July 1996. He obtained his M.Sc degree in the specialty of Hydraulics and River Mechanics Engineering in Xi'an University of Technology in April 1999.

In September 1999, he joined the group led by Professor Wenquan Tao in the school of Energy and Power Engineering, Xi'an Jiaotong University and there earned his first doctorate degree in Power Engineering and Engineering Thermophysics with a thesis titled with "Numerical and Experimental Investigation of Fluid Flow and Heat Transfer with Moving boundary".

On November 20, 2000 he married Hong He. On June 24 2006, they had a baby named Evan Zhang.

In September 2003, he joined the Fundamentals of Chemical Reaction Engineering group led by Professor Kuipers in the Faculty of Science and Technology, University of Twente. During his research on two phase flows with free surfaces, he was supervised by Prof. dr. ir. Hans Kuipers and Dr. ir. Niels Deen. The main results are described in this thesis.

In October 2007, he joined CD-adapco in Didcot office, Oxfordshire UK as a software development engineer.

Prepositions

1. There are no universal interfacial closure laws for bubble columns. (Chapter 2)

2. The performance of a k-ε turbulence model in numerical modeling of multiphase flow can be improved with a proper bubble-induced turbulence model. (Chapter 3)

3. In the gas-liquid heterogeneous flow regime, the extended k-ε turbulence model works well as it implicitly accounts for the bubble-induced turbulence. (Chapter 4)

4. The hydrodynamics of the flow in a bubble column is not affected by the outlet boundary condition, but it is wise to use a so-called "Opening" boundary condition when the system involves mass transfer. (Chapter 5)

5. The incorporation of a bubble number density equation helps to obtain an accurate solution in gas-liquid bubbly flow with substantial mass transfer. (Chapter 6)

6. The difference between "war for Iraq" and "war in Iraq" is when they were proposed.

7. Football game should be abolished as 23 running persons keep another 23 million sitting.

8. As Mr. Zhu led all the pigs in China to Kuala Lumpur to play football there, pork price increased dramatically in China in July 2007. In Chinese, pig pronounces as "Zhu".

9. If eating fish can make me smarter, I think I need a pair of whales.

Prepositions

1. There are no universal interfacial closure laws for bubble columns. (Chapter 2)

2. The performance of a k-ε turbulence model in numerical modeling of multiphase flow can be improved with a proper bubble-induced turbulence model. (Chapter 3)

3. In the gas-liquid heterogeneous flow regime, the extended k-ε turbulence model works well as it implicitly accounts for the bubble-induced turbulence. (Chapter 4)

4. The hydrodynamics of the flow in a bubble column is not affected by the outlet boundary condition, but it is wise to use a so-called "Opening" boundary condition when the system involves mass transfer. (Chapter 5)

5. The incorporation of a bubble number density equation helps to obtain an accurate solution in gas-liquid bubbly flow with substantial mass transfer. (Chapter 6)

6. The difference between "war for Iraq" and "war in Iraq" is when they were proposed.

7. Football game should be abolished as 23 running persons keep another 23 million sitting.

8. As Mr. Zhu led all the pigs in China to Kuala Lumpur to play football there, pork price increased dramatically in China in July 2007. In Chinese, pig pronounces as "Zhu".

9. If eating fish can make me smarter, I think I need a pair of whales.